

**Characterisation of a Carbon/Carbon Multi-Plate Clutch for a
High Energy, Race Car Application**

Ranvir Singh Kalare

Submitted in accordance with the requirements for the degree of
Doctor of Philosophy

The University of Leeds

School of Mechanical Engineering

March 2015

The candidate confirms that the work submitted is his own, except where work which has formed part of jointly authored publications has been included. The contribution of the candidate and the other authors to this work has been explicitly stated below. The candidate confirms that appropriate credit has been given within the thesis where reference has been made to the work of others.

The work in Chapters 3, 5, 6 & 7 of this thesis have appeared in publication as follows:

Proceedings of FISITA EuroBrake 2013 Conference, Dresden, Germany, June 2013, Kalare, R.S., Brooks, P.C., Barton, D.C.

I was responsible for the work presented in the paper and writing the paper (~80%). The contribution of the other authors was supervisory and advisory (~20%).

This copy has been supplied on the understanding that it is copyright material and that no quotation from the thesis may be published without proper acknowledgement.

© 2015 The University of Leeds and Ranvir Singh Kalare

The right of Ranvir Singh Kalare to be identified as Author of this work has been asserted by him in accordance with the Copyright, Designs and Patents Act 1988.

Acknowledgements

First and foremost I would like to express my sincerest gratitude to my supervisors Professor David Barton and Dr Peter Brooks. Their support, guidance and motivation has been crucial not only over the course of this research but also during my time as an undergraduate in the School of Mechanical Engineering at Leeds University.

I would like to thank my industrial supervisors who gave me the chance to work on such a fascinating project

I also owe a huge debt of gratitude to Mr Tony Wiese and Mr David Readman whose hard work and assistance helped to commission the clutch-plate dynamometer and complete my objectives despite circumstances seeming to constantly conspire against it.

Thanks to Mr Adrian Eagles, Dr Tim Comyn and Mr Stuart Micklethwaite for their help in carrying out the surface characterisation work undertaken in this research.

I would also like to thank Mr Graham Brown and the staff in the Faculty of Engineering Workshop as well as the staff at P H Engineering for manufacturing the components of the clutch-plate dynamometer.

Thank you to Dr Abdulwahab Alnaqi with whom I shared ideas about the methods for executing the finite element analyses. The divulgence of his experiences saved me countless hours by starting me off in the right direction.

Last, but certainly not least, I would like to thank my parents for more than I can say here as I would probably go over the word limit well before I had gone through everything they have done for me.

Abstract

The carbon/carbon multi-plate clutch is an essential part of the drivetrain of a Formula One race car. However, the performance of the clutch has proved unstable and inconsistent during race starts. The torque output can vary significantly during a single clutch engagement and then behave in a very different manner during the successive engagement despite no change in input energy level or clamp load.

A unique single clutch-plate interface dynamometer has been designed and commissioned to allow the torque behaviour of an individual clutch-plate pair to be investigated. Using a series of initial rotational speed and clamp load combinations, the previously reported torque output behaviour was replicated, showing stability and consistency at low speed/load combinations but having high instability and inconsistency at high speed/load combinations.

A high speed thermal imaging camera was used to measure the friction surface temperature of the rotating clutch plate during dynamometer tests, showing the formation of extreme hot bands up to 1650°C during the highest clamp load tests. The high localised temperatures suggest that only a small proportion of the friction surface is doing work and the location of the hot band represents the effective friction radius. The radial position of the hot bands, and hence effective friction radius, were observed to move between successive engagements but not during single engagements. The effective friction radius migration can only happen if wear occurs, eliminating the original contact area so that contact is established elsewhere.

The clutch-plate friction surfaces were examined before and after dynamometer testing using scanning electron microscopy. Distinct wear tracks were apparent on the clutch-plate friction surfaces subjected to the highest clamp loads. Distortion of the carbon fibres could be seen in these areas but a definitive wear mechanism could not be determined.

Both 1D heat transfer and fully coupled thermomechanical axisymmetric finite element models were developed to simulate the loading of the clutch plates during dynamometer tests. Both types of model predicted similar levels of contact localisation, and as a result, similar maximum friction surface temperatures. The finite element models best approximated the dynamometer results using a temperature-coefficient of friction relationship where the coefficient of friction increased with temperature and a wear model in which the wear rate increased exponentially with temperature.

The experimental and numerical results suggest that torque instability during a single engagement is due purely to surface morphology effects (which change the coefficient of friction) whilst the torque inconsistency between engagements is due to a combination of both effective friction radius migration and surface morphology effects. These results have important implications for the design of such carbon/carbon clutches for F1 applications.

Contents

Acknowledgements	i
Abstract	ii
Contents	iii
List of Tables and Figures	vii
List of Abbreviations	xviii
1. Introduction	1
1.1 The Function of Clutches	1
1.1.1 Uniform Pressure Model	4
1.1.2 Uniform Wear Model	5
1.2 F1 Application	9
1.3 Aims and Objectives	18
2. Literature Review	19
2.1 Introduction	19
2.2 Clutch Performance and Modelling	19
2.3 Processing and Structures of Carbon/Carbon Composites	25
2.4 Structural Characterisation of Carbon/Carbon Composites	27
2.5 Physical and Chemical Properties of Carbon/Carbon Composites	28
2.6 Surface Morphologies of Carbon/Carbon Composites and Their Effect on Friction and Wear Performance	30
2.7 Thermoelastic Instabilities	40
2.8 Summary	44
3. Design of Single Clutch-Plate Interface Dynamometer (SCID)	45
3.1 Introduction	45
3.2 The Need for an In-House Dynamometer	45
3.3 SCID Design Parameters	46
3.4 SCID Layout	47

3.4.1	Electric Motor Assembly	52
3.4.2	Intermediate Shaft Assembly	53
3.4.3	Driving Shaft Assembly	54
3.4.4	Main Shaft Assembly	55
3.4.5	Sleeve Assembly	56
3.4.6	Lever Arm Assembly	58
3.5	Design Process	59
3.5.1	Non-Rotating Parts	59
3.5.2	Rotating Parts	62
3.6	Summary	66
4.	Clutch-Plate Engagement Tests Using SCID	67
4.1	Introduction	67
4.2	Test Programme	67
4.3	Thermal Imaging Camera	68
4.4	Experimental Procedure	73
4.5	Torque Profiles	76
4.6	Thermal Imaging Results	83
4.7	Summary	95
5.	Clutch-Plate Friction Surface Characterisation	96
5.1	Introduction	96
5.2	Characterisation Techniques	96
5.2.1	White Light Interferometry	96
5.2.2	Contact Profilometry	99
5.2.3	Scanning Electron Microscopy	100
5.2.4	X-Ray Diffraction	102
5.3	New Clutch Plates – Initial Examination	104
5.4	Race-Conditioned Clutch Plates – Initial Examination	108
5.5	New Clutch Plates – Prior to SCID Testing	112
5.5.1	Surface Condition	112
5.5.2	Roughness and Waviness Characteristics	113
5.5.3	Surface Structure & Morphology	115
5.6	Used Clutch Plates – After SCID Testing	117

5.6.1	Surface Condition	117
5.6.2	Roughness and Waviness Characterisation	120
5.6.3	Surface Structure & Morphology	123
5.7	Summary	130
6.	1D Heat Transfer Model	131
6.1	Introduction	131
6.2	Purpose of the 1D Model	131
6.3	Finite Difference Method	132
6.4	Heat Transfer Equations	133
6.5	Model Assumptions	135
6.6	Model Structure	138
6.7	Heat Flux Input	140
6.8	Sensitivity Analysis	143
6.9	Uniform Pressure Model vs. Uniform Wear Model	146
6.10	Taguchi Design of Experiment	147
6.11	The Signal-to-Noise Ratio	150
6.12	Summary	154
7.	Thermomechanically Coupled Finite Element Analysis (TCFEA)	155
7.1	Introduction	155
7.2	Abaqus Thermomechanical Model	155
7.3	Matlab-Abaqus Coupling	159
7.3.1	Input File Setup	161
7.3.2	Full Analysis	166
7.4	Mesh Sensitivity Analysis	170
7.5	Initially Flat Surface Results	173
7.6	Initially Non-Flat Surface Results	182
7.7	Wear Model	190
7.7.1	Initially Flat Friction Surface Results	193
7.7.2	Initially Non-Flat Friction Surface Results	196
7.7.3	Wear Constant Sensitivity Analysis	198
7.7.4	Asymmetric Friction Surface Profiles	203
7.7.5	Consecutive Clutch-Plate Engagements	207

7.8 Modifications Made to TCFEA Based on SCID Results	209
7.9 Alternative TCFEA Models	214
7.9.1 Alternative Temperature-COF Relationship	214
7.9.2 Alternative Wear Equation	219
7.10 Summary	224
8. Discussion	226
8.1 Introduction	226
8.2 The Problem – Further Understanding	226
8.3 Computational Modelling	228
8.4 Contact Localisation	233
8.5 Wear Mechanism	236
8.6 Further Investigations	238
8.7 Summary	239
9. Conclusions	240
References	245

List of Tables and Figures

Figure 1.1	Typical Vehicle Drivetrain Layout (DIFF – Differential)	Page 2
Figure 1.2	Basic Layout of an Axial Friction Clutch [2]	Page 2
Figure 1.3	Friction Surface of Clutch Plate	Page 3
Figure 1.4	Schematic Diagram of Multi-Plate Wet Clutch [4]	Page 8
Figure 1.5	Two Types of Clutch Plates Used in F1 Clutch	Page 10
Figure 1.6	Clutch Hub and Clutch Basket	Page 11
Figure 1.7	F1 Clutch-Plate Pack Assembly	Page 12
Figure 1.8	Multi-Plate F1 Clutch Assembly	Page 12
Figure 1.9	Race Start Procedure	Page 14
Figure 1.10	Clutch torque Output Results from Dynamometer Tests [7]	Page 15
Figure 1.11	Possible Friction surface Temperature-Morphology-COF Relationship	Page 15
Figure 1.12	Temperature and Torque Profiles for a Single Full Clutch Engagement at 1400N Clamp Load and 110kJ Energy Dissipation	Page 16
Figure 2.1	Linear 1D Thermal Clutch Model [11]	Page 20
Figure 2.2	Power Flow Through 1D Model [11]	Page 20
Figure 2.3	Temperature Distributions in Multi-Plate Clutch at Discrete Times [13]	Page 22
Figure 2.4	Contact Pressure Distribution Evolution [17]	Page 24
Figure 2.5	Process for the Production of Carbon/Carbon Composites [20]	Page 25
Figure 2.6	Process for the Production of PAN-Based Carbon Fibres [20]	Page 26
Table 2.1	Typical Properties of Carbon/Carbon Composites [13]	Page 29
Figure 2.7	Typical Friction Characteristics of Carbon/Carbon Composites [9]	Page 30

Figure 2.8	SEM Images of Wear Debris from Dynamometer Tests Simulating (a) Taxiing Cycles, (b) Normal Landing Cycles and (c) Rejected Take-Off [33]	Page 33
Figure 2.9	COF Variation During Sliding Tests for High Initial Sliding Speed [27]	Page 34
Figure 2.10	SEM Micrographs of a Carbon/Carbon Brake Disc Showing (a) Initial Surface, (b) Type I Morphology and (c) Type II and Type III Morphology [27]	Page 35
Figure 2.11	Dusting Wear in Ambient Air and Dry Nitrogen [26]	Page 37
Figure 2.12	Friction and Temperature Profiles as a Function of Sliding Distance for Different Load Levels [41]	Page 38
Figure 2.13	Weight Loss of Carbon/Carbon Composite as a Function of Temperature in a Helium/Oxygen Gas Mixture [41]	Page 39
Figure 2.14	Experimental Setup to Demonstrate and Investigate TEI [8]	Page 40
Figure 2.15	Surface Separation During TEI Experiment [8]	Page 42
Figure 2.16	Contact Pressure Distribution Predicted by Non-Wear FE Model [43]	Page 43
Table 3.1	Range of Race Start Parameters [7]	Page 46
Figure 3.1	Plan View of SCID	Page 50
Figure 3.2	Side View of SCID	Page 51
Figure 3.3	Electric Motor Assembly	Page 52
Figure 3.4	Intermediate Shaft Assembly	Page 53
Figure 3.5	Driving Shaft Assembly	Page 54
Figure 3.6	Main Shaft Assembly	Page 55
Figure 3.7	Sleeve Assembly	Page 57
Figure 3.8	Lever Arm Assembly	Page 58
Figure 3.9	Design Process for Non-Rotating SCID Components	Page 60
Figure 3.10	Design Process for Sizing of SCID Power Transmission Shafts	Page 63
Figure 3.11	Final SCID Assembly	Page 66
Table 4.1	Initial Speed/Clamp Load Combinations Used in SCID Tests	Page 67

Figure 4.1	IR Thermographs of Railway Brakes Rotor During Braking Tests [52]	Page 69
Figure 4.2	Thermal Imaging Camera Setup for SCID Engagement Tests	Page 70
Table 4.2	Thermal Imaging Camera Temperature Range Configuration	Page 71
Table 4.3	Thermal Imaging Camera Post-Processing Parameters	Page 72
Figure 4.3	Test Procedure for SCID Engagement Tests	Page 73
Table 4.4	States and Conditions of State-Machine LabVIEW Program for Executing SCID Engagement Tests	Page 75
Figure 4.4	rpm, Clamp Load and Torque Traces for Engagement Test 7000rpm/1000N-1	Page 76
Figure 4.5	Torque Output Results for 7000rpm/1000N Engagement Tests	Page 77
Figure 4.6	Torque Output Results for 7000rpm/1200N Engagement Tests	Page 77
Figure 4.7	Torque Output Results for 7000rpm/1400N Engagement Tests	Page 78
Figure 4.8	Torque Output Results for 8000rpm/1000N Engagement Tests	Page 80
Figure 4.9	Torque Output Results for 8000rpm/1200N Engagement Tests	Page 81
Figure 4.10	Torque Output Results for 8000rpm/1400N Engagement Tests	Page 81
Figure 4.11	Maximum Temperature Recorded During Engagement ⁴ Occurring at 1.650s for 7000rpm/1000N Speed/Load Combination	Page 84
Figure 4.12	Maximum Temperature Recorded During Engagement ⁷ Occurring at 1.580s for 7000rpm/1200N Speed/Load Combination	Page 85
Figure 4.13	Maximum Temperature Recorded During Engagement ⁵ Occurring at 1.160s for 8000rpm/1400N Speed/Load Combination	Page 86

Figure 4.14	Maximum Temperatures Recorded for 1000N Load Case	Page 87
Figure 4.15	Maximum Temperatures Recorded for 1200N Load Case	Page 88
Figure 4.16	Maximum Temperatures Recorded for 1400N Load Case	Page 88
Figure 4.17	Hot Band Evolution During Engagement ⁵ for 8000rpm/1400N Speed/Load Combination	Page 90
Figure 4.18	Thermal Camera Images of Maximum Friction Surface Temperatures for 1400N Load Case at (a) 7000rpm and (b) 8000rpm	Page 92
Figure 4.19	Effective Friction Radius for 1400N Engagement Tests	Page 93
Table 4.5	Effect of Effective Friction Radius Migration on Torque Output	Page 93
Figure 5.1	Schematic of Key Interferometer Components [54]	Page 97
Figure 5.2	Intensity of Recombined Light Wave as a Function of Optical Path Difference [55]	Page 98
Table 5.1	Surface Roughness Parameters	Page 98
Figure 5.3	Key Components of Contact Profilometer [56]	Page 99
Table 5.2	Surface Waviness Parameters	Page 100
Figure 5.4	Key Components of a Scanning Electron Microscope	Page 101
Figure 5.5	Setup and Operation of XRD Machine	Page 103
Figure 5.6	Measurement Regions for White Light Interferometry (72° Apart) and Contact Profilometry	Page 104
Table 5.3	Roughness Parameter Values for New Clutch Plates (Initial Examination)	Page 105
Figure 5.7	Processed Image of Typical New Clutch Plate Friction Surface (Initial Examination, Isometric View)	Page 106
Figure 5.8	Processed Image of Typical New Clutch Plate Friction Surface (Initial Examination, Plan View)	Page 106
Table 5.4	Waviness Parameter Values for New Clutch Plates (Initial Examination)	Page 107
Figure 5.9	Friction Surface Profile of Clutch Plate NI-DR1-1W (Initial Examination)	Page 107
Table 5.5	Roughness Parameter Values for Used (Race- Conditioned) Clutch Plates (Initial Examination)	Page 108

Figure 5.10	Processed Image of a Typical Used (Race-Conditioned) Clutch-Plate Friction Surface (Initial Examination, Isometric View)	Page 109
Figure 5.11	Processed Image of a Typical Used (Race-Conditioned) Clutch-Plate Friction Surface (Initial Examination, Plan View)	Page 110
Table 5.6	Waviness Parameter Values for Used (Race-Conditioned) Clutch Plates (Initial Examination)	Page 111
Figure 5.12	Typical Friction Surface Profile of a Used (Race-Conditioned) Clutch Plate (Initial Examination)	Page 111
Figure 5.13	Clutch-Plate Pair B2 Prior to SCID Testing	Page 113
Table 5.7	Roughness Parameter Values of Clutch Plates (Pre-SCID Testing)	Page 113
Table 5.7	Waviness Parameter Values of Clutch Plates (Post-SCID Testing)	Page 114
Figure 5.14	BSE SEM Image of Clutch Plate A3-DN (x100 Magnification)	Page 116
Figure 5.15	Clutch Plate Pair B2 After SCID Testing	Page 117
Figure 5.16	Clutch-Plate Pair A4 After SCID Testing	Page 118
Table 5.9	Summary of Wear Track on All Clutch-Plate Pairs	Page 119
Table 5.10	Roughness Parameter Values of Clutch Plates (Post-SCID Testing)	Page 120
Figure 5.17	Clutch Plate Roughness Values Before and After SCID Testing	Page 121
Table 5.11	Waviness Parameter of Clutch Plates (Post-SCID Testing)	Page 122
Figure 5.18	Clutch Plate B4-DR After SCID Testing	Page 123
Figure 5.19	Section of SEM Image of Clutch-Plate B4-DR After SCID Testing (72° Clockwise to Reference Point, x100 Magnification)	Page 124
Figure 5.20	SEM Images of Clutch Plate A2-DN Before (Left) and After (Right) SCID Testing (x100 Magnification)	Page 125

Figure 5.21	SEM Images of Clutch Plate A3-DN Before (Left) and After (Right) SCID Testing (x100 Magnification)	Page 126
Figure 5.22	SEM Image of Wear Tack on Friction Surface of Clutch Plate A4-DN After SCID Testing (x100 Magnification)	Page 127
Figure 5.23	XRD Curves for Clutch-Plate B4-DN Before and After SCID Testing	Page 128
Table 5.12	Interlaying Spacing of Graphite Crystal Structures	Page 129
Figure 6.1	Single Clutch-Plate Nodal Network [60]	Page 131
Figure 6.2	Overall 1D Heat Transfer Model Structure	Page 137
Figure 6.3	Clutch Plate Divided Into Annuli of Equal Width	Page 139
Table 6.1	Sensitivity Analysis Results for 1D Heat Transfer Model	Page 141
Figure 6.4	Time Step Size Sensitivity Analysis Results for 1D Heat Transfer Model	Page 142
Figure 6.5	Mesh Density Sensitivity Analysis Results for 1D Heat Transfer Model	Page 143
Table 6.2	Inputs and Material Properties Used in 1D Models	Page 143
Figure 6.6	Mesh Used in 1D Abaqus Model	Page 144
Figure 6.7	Application of Heat Flux in 1D Model	Page 144
Figure 6.8	Clutch-Plate Temperature Predicted by Matlab and Abaqus 1D Models	Page 145
Figure 6.9	Temperature Differences Between Matlab and Abaqus 1D Models	Page 145
Table 6.3	L_8 Orthogonal Array	Page 148
Table 6.4	Factors Investigated in Design of Experiment Analysis	Page 149
Table 6.5	Factor Values Used in Design of Experiment Analysis	Page 149
Table 6.6	S/N Ratio and Main Effect Results	Page 151
Figure 6.10	Main Effect Results	Page 152
Table 7.1	Key Parameters in Abaqus Thermomechanical Model	Page 155
Table 7.2	Material Properties Used in Abaqus Thermomechanical Model	Page 156
Figure 7.1	Abaqus Axisymmetric Finite Element Model of Clutch Plates	Page 156
Figure 7.2	Matlab-Abaqus Coupling for TCFEA	Page 160

Figure 7.3	Process for Modifying Input Files	Page 162
Figure 7.4	Default Surface Numbering of Elements in Abaqus	Page 163
Figure 7.5	Default Node and Element Numbering in Abaqus	Page 163
Figure 7.6	Sine Wave Profile Parameters	Page 165
Figure 7.7	Node Set Definitions for Slave Friction Surface	Page 165
Table 7.3	Temperature-COF Reference Values Used in TCFEA	Page 167
Figure 7.8	TCFEA Friction Surface Mesh Sensitivity Analysis Results	Page 170
Figure 7.9	Computing Time for Friction Surface Mesh Sensitivity Analysis	Page 171
Figure 7.10	Through-Thickness Mesh Sensitivity Analysis Results	Page 172
Figure 7.11	Computing Time for Through-Thickness Mesh Sensitivity Analysis	Page 172
Figure 7.12	Contact Pressure and Friction Surface Temperature Profiles at $t=0.01s$	Page 173
Figure 7.13	Contact Pressure and Friction Surface Temperature Profiles at $t=0.02s$	Page 174
Figure 7.14	Contact Pressure and Friction Surface Temperature Profiles at $t=0.10s$	Page 175
Figure 7.15	Contact Pressure and Friction Surface Temperature Profiles at $t=0.20s$	Page 175
Figure 7.16	Maximum Contact Pressure and Friction Surface Temperature Profiles at $t=0.42s$ (Contact Pressure) and $t=0.45s$ (Surface Temperature)	Page 176
Figure 7.17	Temperature Contour Plot of Clutch Plates at $t=0.45s$	Page 177
Figure 7.18	Hot Banding Mechanism	Page 178
Figure 7.19	Contact Pressure and Friction Surface Temperature Profiles at $t=1.00s$	Page 179
Figure 7.20	Temperature Contour Plot of Clutch Plates at $t=1.00s$	Page 179
Figure 7.21	Contact Pressure and Friction Surface Temperature Profiles at $t=1.33s$	Page 180
Figure 7.22	Temperature Contour Plot of Clutch Plates at $t=1.33s$	Page 180
Figure 7.23	Torque Output Predicted During Clutch-Plate Engagement (Non-Wear Model)	Page 181

Figure 7.24	Effective Friction Radius Migration Predicted During Clutch-Plate Engagement (Non-Wear Model)	Page 182
Table 7.4	Surface Profiles Used in TCFEA	Page 183
Figure 7.25	Initial Contact Pressure Distributions for Profiles 1-3	Page 184
Figure 7.26	Initial Contact Pressure Distributions for Profile 2 & Profiles 4-6	Page 185
Figure 7.27	Initial Contact Pressure Distributions for Profiles 7-9	Page 186
Figure 7.28	Results of Varying Peak Amplitude on Maximum Friction Surface Contact Pressure and Maximum Temperature	Page 187
Figure 7.29	Results of Varying Number of Peaks (Wavelength) on Maximum Contact Pressure and Maximum Friction Surface Temperature	Page 187
Figure 7.30	Results of Varying Phase Angle on Maximum Contact Pressure and Maximum Friction Surface Temperature	Page 188
Table 7.5	Values Used to Calculate Wear Constant	Page 191
Figure 7.31	Wear Rate as a Function of Temperature at Pressure and Sliding Velocity Values Presented in Table 7.5	Page 193
Figure 7.32	Contact Pressure and Friction Surface Temperature Profiles at $t=0.20s$	Page 194
Figure 7.33	Contact Pressure and Friction Surface Temperature Profiles at $t=0.34s$	Page 194
Figure 7.34	Contact Pressure and Friction Surface Temperature Profiles at $t=0.39s$	Page 195
Figure 7.35	Contact Pressure and Friction Surface Temperature Profiles at $t=0.75s$	Page 195
Figure 7.36	Maximum Contact Pressure and Friction Surface Temperature Profiles at $t=0.31s$ (Contact Pressure) and $t=0.28s$ (Surface Temperature)	Page 197
Figure 7.37	Contact Pressure Distribution at $t=0.75s$ (Non-Wear and Wear Models)	Page 197
Figure 7.38	Contact Pressure Distribution at $t=1.00s$ (Non-Wear and Wear Models)	Page 198

Figure 7.39	Torque Output Predicted by Non-Wear Model Using Profile 2	Page 199
Figure 7.40	Torque Output Predicted by Wear Model Using Profile 2	Page 199
Figure 7.41	Wear Constant Sensitivity Analysis for Flat-to-Flat Surfaces (Profile 0)	Page 200
Figure 7.42	Wear Constant Sensitivity Analysis for Flat-to-Sine Surfaces (Profile 2)	Page 201
Figure 7.43	Clutch-Plate Engagement Times as a Function of Wear Constant Order of Magnitude	Page 202
Figure 7.44	Initial Contact Pressure Distribution for Profiles 10 and 11	Page 203
Figure 7.45	Contact Pressure Distribution at $t=0.20s$ (Profiles 10 and 11)	Page 204
Figure 7.46	Contact Pressure Distribution at $t=0.40s$ (Profiles 10 and 11)	Page 204
Figure 7.47	Contact Pressure Distribution at $t=0.60s$ (Profiles 10 and 11)	Page 205
Figure 7.48	Contact Pressure Distribution at Completion of Clutch-Plate Engagement ($t=1.08s$ for Profile 10, $t=1.10s$ for Profile 11)	Page 205
Figure 7.49	Effective Friction Radius History for Profile 10	Page 206
Figure 7.50	Effective Friction Radius History for Profile 11	Page 206
Figure 7.51	Torque Output History for Ten Consecutive Clutch-Plate Engagements (RS)	Page 208
Figure 7.52	Effective Friction Radius History for Ten Consecutive Clutch-Plate Engagements (RS)	Page 209
Figure 7.53	Modified Time-Clamp Load and Temperature-COF Relationships	Page 210
Table 7.6	Results of TCFEA Simulations (Original and Modified)	Page 211
Figure 7.54	Torque Outputs Predicted by TCFEA Simulations Listed in Table 7.6	Page 211
Table 7.7	Alternative Temperature-COF Relationship Used in TCFEA	Page 214

Figure 7.55	Contact Pressure and Friction Surface Temperature Profiles at t=0.20s (Non-Wear Model, Alternative Temperature-COF Relationship)	Page 215
Figure 7.56	Contact Pressure and Friction Surface Temperature Profiles at t=0.25s (Non-Wear Model, Alternative Temperature-COF Relationship)	Page 215
Figure 7.57	Torque Outputs Predicted by Modified TCFEA Non-Wear Model and Non-Wear Model With Alternative Temperature-COF Relationship	Page 217
Figure 7.58	Torque Outputs Predicted by Modified TCFEA Wear Model and Wear Model With Alternative Temperature-COF Relationship	Page 218
Figure 7.59	Alternative Wear Rate as a Function of Contact Pressure and Sliding Velocity	Page 219
Figure 7.60	Contact Pressure and Friction Surface Temperature Profiles at t=0.20s (Alternative Wear Model, Original Temperature-COF Relationship)	Page 220
Figure 7.61	Contact Pressure and Friction Surface Temperature Profiles at t=0.40s (Alternative Wear Model, Original Temperature-COF Relationship)	Page 221
Figure 7.62	Contact Pressure and Friction Surface Temperature Profiles at t=0.70s (Alternative Wear Model, Original Temperature-COF Relationship)	Page 221
Figure 7.63	Contact Pressure and Friction Surface Temperature Profiles at t=1.00s (Alternative Wear Model, Original Temperature-COF Relationship)	Page 222
Figure 7.64	Contact Pressure and Friction Surface Temperature Profiles at t=1.30s (Alternative Wear Model, Original Temperature-COF Relationship)	Page 222
Figure 7.65	Torque Outputs Predicted by TCFEA Wear Models	Page 223
Figure 8.1	Torque and COF Traces for Engagement ⁷ at 8000rpm/1400N Speed/Load Combination	Page 227

Table 8.1	Summary of Results Based on Modified TCFEA Models (Flat-to-Flat Surface Condition)	Page 228
Figure 8.2	Friction Surface Temperature Distribution Predicted by Modified TCFEA Wear Model at Time of Maximum Temperature Occurring (t=0.73s)	Page 229
Figure 8.3	Torque Output Predicted by Modified TCFEA Wear Model	Page 231
Figure 8.4	Torque Output Traces for 8000rpm/1400N Speed/Load Combination SCID Tests	Page 231
Figure 8.5	Clutch-Plate Friction Surface Temperatures Predicted by 1D Heat Transfer Model as a Function of Proportion of Full Friction Surface Area	Page 234
Figure 8.6	Maximum Friction Surface Temperature-Proportion of Full Friction Surface Area in Contact Relationship Predicted by 1D Heat Transfer Model	Page 235
Figure 8.7	Contact Pressure Distribution at Moment When Maximum Contact Pressure is Predicted by Modified TCFEA Wear Model	Page 236
Figure 8.8	Torque Output Results from SCID Tests Carried Out at 7000rpm/1400N Speed/Load Combination With (a) Holes and (b) No Holes Drilled Through Driving Clutch Plate	Page 237

List of Abbreviations

Acronyms

- 1D – One Dimensional
- 2D – Two Dimensional
- 3D – Three Dimensional
- BSE – Backscattered Electrons
- CCD – Charge-Coupled Device
- COF – Coefficient of Friction
- CVD – Chemical Vapour Deposition
- CVI – Chemical Vapour Infiltration
- DET – Distortion Energy Theory
- ECU – Engine Control Unit
- EFR – Effective Friction Radius
- EM – Electromagnetic
- F1 – Formula One
- FE – Finite Element
- GUI – Graphical User Interface
- IR – Infrared
- MSD – Mean Square Deviation
- MSST – Maximum Shear Stress Theory
- OPD – Optical Path Difference
- OTI – Optical Texture Index
- PAN – Polyacrylonitrile
- rpm – Revolutions per Minute
- RS – Race Start

SCID – Single Clutch-Plate Interface Dynamometer
S/N – Signal-to-Noise Ratio
SE – Secondary Electrons
SEM – Scanning Electron Microscopy
SF – Scale Factor
STEM – Scanning Transmission Electron Microscopy
TCFEA – Thermomechanically Coupled Finite Element Analysis
TEI – Thermoelastic Instabilities
TEM – Transmission Electron Microscopy
VSI – Vertical Scanning Interferometry
XRD – X-Ray Diffraction

Symbols

A – Cross-Sectional Area (m^2)
 $A_{\%}$ – Proportion of Full Friction Surface Area (%)
 A_s – Amplitude (m)
 b – Cross-Sectional Width (m)
 B_s – $1/\text{Wavelength}$ (m^{-1})
 c – Specific Heat Capacity ($\text{Jkg}^{-1}\text{K}^{-1}$)
 C_s – Phase Shift (rad)
 C_{Press} – Contact Pressure (Pa)
 d – Shaft Diameter (m)
 d_{min} – Minimum Shaft Diameter (m)
 d_a – Atomic Spacing (m)
 F – In-plane Friction Force (N)
 g – Acceleration due to Gravity (ms^{-2})

h – Incremental Wear (m)
 h_c – Convective Heat Transfer Coefficient ($\text{Wm}^{-2}\text{K}^{-1}$)
 h_k – Key Cross-Section Height (m)
 I – Inertia (kgm^2)
 I_A – Second Moment of Area (m^4)
 I_f – Flywheel Inertia (kgm^2)
 k – Wear Constant (m^2N^{-1})
 k_c – Through-Thickness Thermal Conductivity ($\text{Wm}^{-1}\text{K}^{-1}$)
 KE – Kinetic Energy (J)
 k_f – Finish Factor
 k_m – Miscellaneous Factor
 k_r – Reliability Factor
 k_s – Size Factor
 k_t – Temperature Factor
 l_{min} – Minimum Key Length (m)
 M – Bending Moment (Nm)
 M_{crit} – Bending Moment at Critical Point (Nm)
 m_f – Mass of Flywheel (kg)
 n – Number of Data Points
 n_r – Order of Reflection
 n_s – Safety Factor
 P – Clamp Load (N)
 p_c – Contact Pressure (Pa)
 P_p – Clamp Load (N) (Uniform Pressure Model)
 P_w – Clamp Load (N) (Uniform Wear Model)
 Q – Shear Load (N)

q'' – Heat Flux Input (Wm^{-2})

R – Yield Strength:Max Stress Ratio

r – Friction Radius (m)

r_{eff} – Effective Friction Radius (m)

R_i – Clutch Plate Inner Radius (m)

r_i – Inner Radius of Flywheel (m)

R_m – Mean Clutch Plate Radius (m)

R_o – Clutch Plate Outer Radius (m)

r_o – Outer Radius of Flywheel (m)

S^2 – Variance

S_e – Modified Endurance Limit (MPa)

S'_e – Endurance Limit (MPa)

S_y – Yield Strength (Nm^{-2})

T – Torque (Nm)

t – Time (s)

Δt – Time Step (s)

T'_0 – Surface Node Temperature at Current Time Step (K)

T_0 – Surface Node Temperature at Previous Time Step (K)

T_∞ - Ambient Temperature (K)

T_1 – Adjacent Internal Node Temperature at Previous Time Step (K)

T_{crit} – Transmitted Torque at Critical Point (Nm)

t_f – Flywheel Thickness (m)

T_k – Transmitted Torque (Nm)

T_{max} – Maximum Friction Surface Temperature ($^{\circ}\text{C}$)

T'_n – Current Temperature at Internal Node (K)

T_n – Previous Temperature at Internal Node (K)

T_{n+1}/T_{n-1} – Previous Temperature at Adjacent Internal Node (K)
 T_p – Torque Generated (Nm) (Uniform Pressure Model)
 T_w – Torque Generated (Nm) (Uniform Wear Model)
 u – Sliding Velocity (ms^{-1})
 w_k – Key Cross-Section Width (m)
 W_i – Weight of Mass i (kg)
 x – Radial Position (m)
 Δx – Distance Between Nodes (m)
 y – Height of Surface Above Origin (m)
 \bar{y} – Mean
 y_i – Value of Data Point i
 y_{max} – Maximum Distance from Neutral Axis (m)
 Z – Temperature (K)
 Z_o – Reference Temperature (K)
 \emptyset – Diameter
 α - Thermal Diffusivity (m^2/s)
 δ_i – Deflection at Point i due to Mass i only (m)
 $\delta_{i,max}$ – Total Deflection at Point i due to all Masses (m)
 θ – Angle of Incidence Between X-Rays and Sample Surface (deg)
 λ – Wavelength of X-Rays (m)
 μ – Coefficient of Friction
 ν – Poisson’s Ratio of Material
 ρ – Material Density (kgm^{-3})
 σ – Bending Stress (Nm^{-2})
 $\sigma_{1,2}$ – Principal Stresses (Nm^{-2})
 $\sigma_{\theta,max}$ – Maximum Hoop Stress (Nm^{-2})

$\sigma_{r,max}$ – Maximum Radial Stress (Nm^{-2})

σ_{des} – Maximum Allowable Compression Stress (Nm^{-2})

τ – Shear Stress (Nm^{-2})

τ_{des} – Maximum Allowable Shear Stress (Nm^{-2})

ω – Rotational Speed (rads^{-1})

ω_{crit} – Critical Shaft Speed (rads^{-1})

ω_i – Shaft Critical Speed if only Mass i Existed (rads^{-1})

ω_{op} – Shaft Operating Speed (rads^{-1})

1. Introduction

A clutch performs a vital role within a vehicle drivetrain and its performance during a vehicle launch is a critical factor in the overall quality of the launch. In motor racing, the quality of the vehicle launch is judged by how quickly the vehicle accelerates from a standing start. A good launch can potentially win a race whilst a bad launch could lose one. The ideal clutch must therefore perform well and perform well consistently.

Consistent performance of the Formula One (F1) clutch in this investigation has proven difficult to achieve and has led to a number of poor vehicle launches which have had a negative effect on the overall race result. Possible sources of the inconsistency have previously been identified but further understanding is required in order to determine potential control measures that could improve the consistency of performance of the clutch.

1.1 The Function of Clutches

A clutch is used to connect two shafts initially rotating at different speeds and gradually and smoothly bring the speed of the output shaft up to the same speed as the input shaft [1]. In a motor vehicle, the clutch is engaged in order to couple the engine and drivetrain to achieve forward motion of the vehicle. Figure 1.1 shows where the clutch is situated within the vehicle drivetrain.

During a clutch engagement from a standing start, the speed of the gearbox input shaft is gradually increased to match the speed of the engine crankshaft. The clutch is disengaged when the vehicle is brought to a halt in order to decouple the engine from the drivetrain to prevent the engine from stalling. The clutch is also used to decouple and recouple the engine and drivetrain whenever gear changes are made.

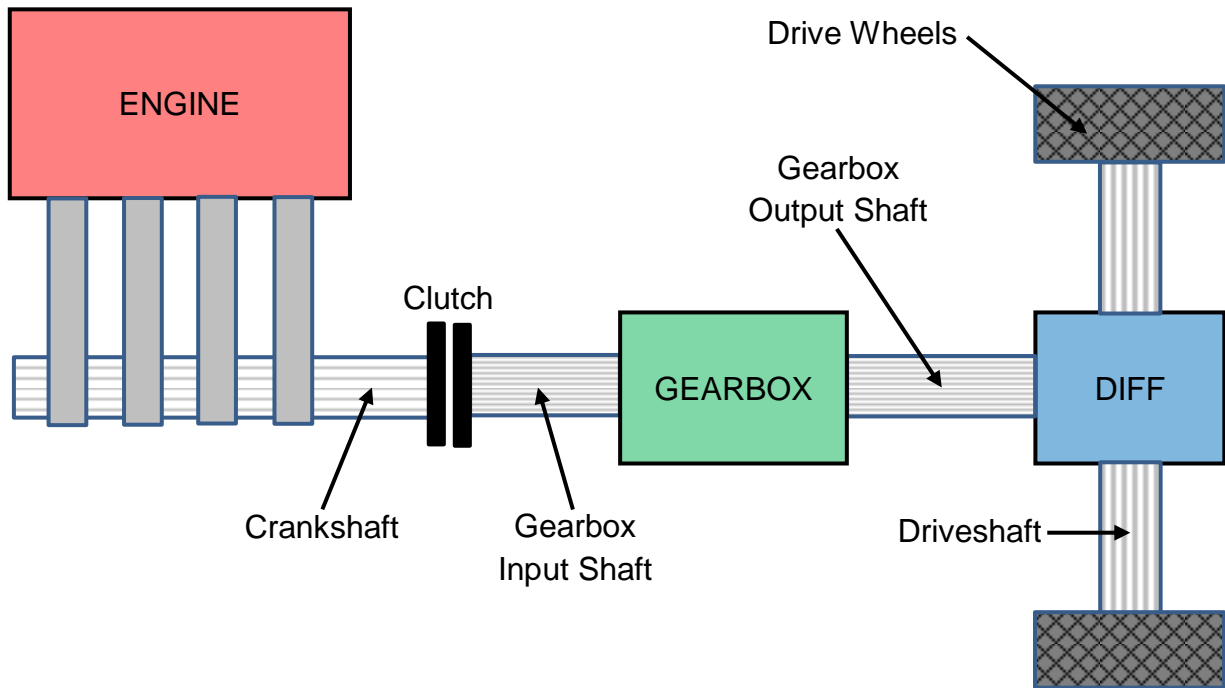


Figure 1.1 – Typical Vehicle Drivetrain Layout (DIFF – Differential)

Friction clutches are the most commonly used type of clutch where two opposing surfaces, rotating at different speeds, are forced into frictional contact, generating a torque which is utilised to accelerate the drivetrain inertia. Figure 1.2 shows the basic layout of an axial friction clutch [2] where plates E and F are mounted on shafts A and B via keys or splines that transmit the torque. The two shafts are carried in bearings C and D and the entire assembly rotates about axis XY.

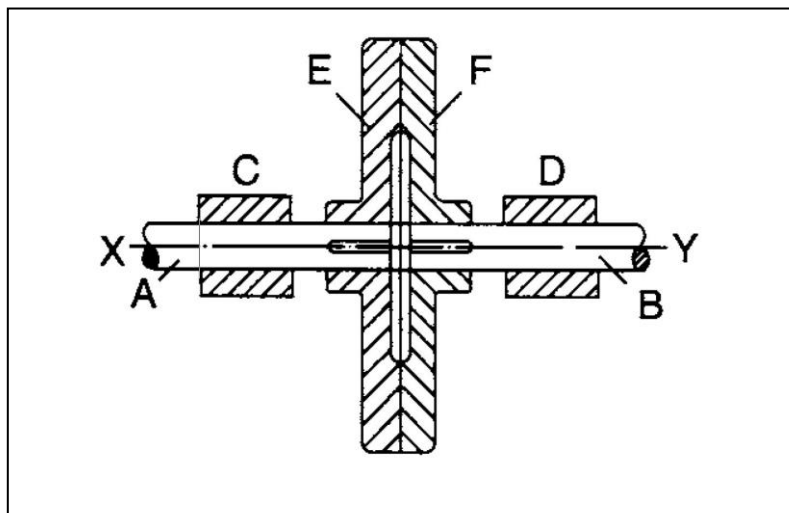


Figure 1.2 – Basic Layout of an Axial Friction Clutch [2]

If plate E is axially constrained on shaft A, plate F will be free to move axially on shaft B. The clutch is engaged by applying an axial force to the back face of plate F pushing it against plate E. This load is termed the clamp load and is usually generated by springs and the clutch is disengaged through a driver-controlled linkage which pulls the springs away to release the clamp load. The magnitude of the clamp load directly affects the amount of torque that the clutch can generate. Figure 1.3 shows the friction surface of a single clutch plate where a small arbitrary surface element has been selected for analysis.

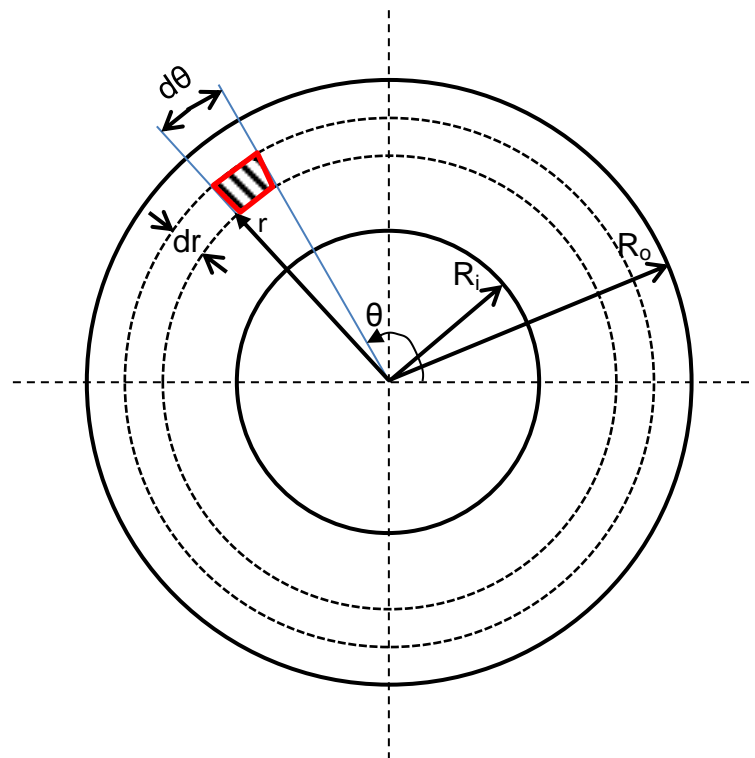


Figure 1.3 – Friction Surface of Clutch Plate

The surface area dA of the element shown in Figure 1.3 is given by Equation 1.1:

$$dA = (rd\theta)dr \quad (1.1)$$

The normal load, dP , acting on the element is a product of the elemental area and the interface pressure p :

$$dP = prd\theta dr \quad (1.2)$$

The frictional force dF is calculated using Equation 1.3:

$$dF = \mu dP \quad (1.3)$$

The torque produced by the whole clutch can be derived using Equation 1.4:

$$T = \int rdF = \int \mu rdP = \iint \mu pr^2 drd\theta \quad (1.4)$$

Using Equation 1.4, the torque generated over the entire friction interface can be calculated based on either the assumption of uniform pressure or uniform wear as discussed in the following sections [3].

1.1.1 Uniform Pressure Model

If it is assumed that when the clutch plates are new their friction surfaces are perfectly flat and, if they are accurately aligned, the interface pressure will be uniform ($p = p_o$). Substituting into Equation 1.2 gives:

$$dP = p_o rd\theta dr \quad (1.5)$$

Integrating between the limits of $0 < \theta < 2\pi$ and $R_i < r < R_o$ gives the normal load acting across the friction interface:

$$P_p = \int_0^{2\pi} \int_{R_i}^{R_o} r d\theta dr = \pi p_o (R_o^2 - R_i^2) \quad (1.6)$$

The torque generated is calculated by integrating Equation 1.4:

$$\begin{aligned} T_p &= \int_0^{2\pi} \int_{R_i}^{R_o} \mu p_o r^2 dr d\theta = 2\pi p_o \int_{R_i}^{R_o} r^2 dr \\ &= 2\pi \mu p_o \left(\frac{R_o^3}{3} - \frac{R_i^3}{3} \right) = \frac{2\pi \mu p_o (R_o^3 - R_i^3)}{3} \end{aligned} \quad (1.7)$$

Finally, rearranging Equation 1.6 and substituting into Equation 1.7 gives:

$$T_p = \frac{2\mu P_p (R_o^3 - R_i^3)}{3(R_o^2 - R_i^2)} \quad (1.8)$$

Where: T_p – Torque Generated (Nm) (Uniform Pressure Model)

μ – Coefficient of Friction

P_p – Clamp Load (N) (Uniform Pressure Model)

R_o – Clutch Plate Outer Radius (m)

R_i – Clutch Plate Inner Radius (m)

1.1.2 Uniform Wear Model

If the clutch plates are considered to be rigid, it can be assumed that the wear across the friction surface of the plates is uniform. If the wear is proportional to the amount of work done in sliding at the friction surface, the rate of energy conversion, h_w , is given by Equation 1.9:

$$h_w = Fu = \mu Pu = \mu A p u \quad (1.9)$$

If it is assumed that wear is uniform across the friction surface, the rate of energy conversion must be uniform over the friction surface. The coefficient of friction μ and friction surface area A are constants but the sliding velocity u increases linearly in relation to the radius. Therefore, from Equation 1.9, the product of the pressure p and sliding velocity must be constant to maintain a uniform rate of energy conversion. The pressure must therefore be inversely proportional to the radius. Equation 1.10 represents this relationship where an arbitrary constant of proportionality c is introduced:

$$p = \frac{c}{r} \quad (1.10)$$

Rearranging to make the constant of proportionality the subject of Equation 1.10 and substituting into Equation 1.5 gives:

$$dP = prd\theta dr = cd\theta dr \quad (1.11)$$

Integration of Equation 1.11 gives the normal force acting on the friction surface:

$$P_w = \int_0^{2\pi} \int_{R_i}^{R_o} cd\theta dr = 2\pi c(R_o - R_i) \quad (1.12)$$

As the pressure has been assumed to be inversely proportional to the radius, the maximum pressure must occur at the inner radius:

$$c = p_{max}R_i \quad (1.13)$$

Substituting into Equation 1.12 leads to the expressions for the normal load P_w :

$$P_w = 2\pi p_{max} R_i (R_o - R_i) \quad (1.14)$$

The torque generated can be calculated by substituting Equation 1.10 into Equation 1.4:

$$T_w = \int r dF = \int \mu r dP = \iint \mu c r d r d\theta \quad (1.15)$$

Integration of Equation 1.15 and simplifying leads to the desired expression for torque based on the assumption of uniform wear:

$$\begin{aligned} T_w &= \pi \mu p_{max} R_i (R_o^2 - R_i^2) = 2\pi \mu p_{max} R_i (R_o - R_i) \frac{(R_o + R_i)}{2} \\ &= \mu P_w R_m = \frac{\mu P_w (R_o + R_i)}{2} \end{aligned} \quad (1.16)$$

Where: T_w – Torque Generated (Nm) (Uniform Wear Model)

P_w – Clamp Load (N) (Uniform Wear Model)

R_m – Mean Clutch Plate Radius (m)

Equations 1.8 and 1.16 can be used to calculate the torque generated at a single friction interface. It can clearly be seen from these equations that there are several ways to increase the level of torque that the clutch can generate. The coefficient of friction (COF) can be increased by using alternative friction plate linings whilst the torque can also be increased by using a clutch plate with a larger mean friction radius. Simply increasing the clamp load would also result in greater levels of torque generation. Another way of increasing torque would be to increase the number of friction interfaces. The overall torque would then be the sum of the torque generated at each friction interface.

Figure 1.4 shows a schematic diagram of a multi-plate wet clutch design [4]. A wet clutch differs from a dry clutch in that the clutch components are bathed in lubricating fluid which reduces the amount of friction at the clutch plate interfaces but improves the level of cooling of the clutch plates. In the clutch shown in Figure 1.4, hydraulic pressure in the piston forces the stacked clutch plates and friction discs against the fixed pressure plate in order to engage the clutch. The friction discs have teeth on their outer radial edge that mesh with the clutch drum spline. The clutch drum is connected to the gearset that receives the generated torque. The clutch is disengaged by reducing the piston hydraulic pressure allowing the piston springs to relax thereby reducing the clamp load on the clutch pack and pressure plate.

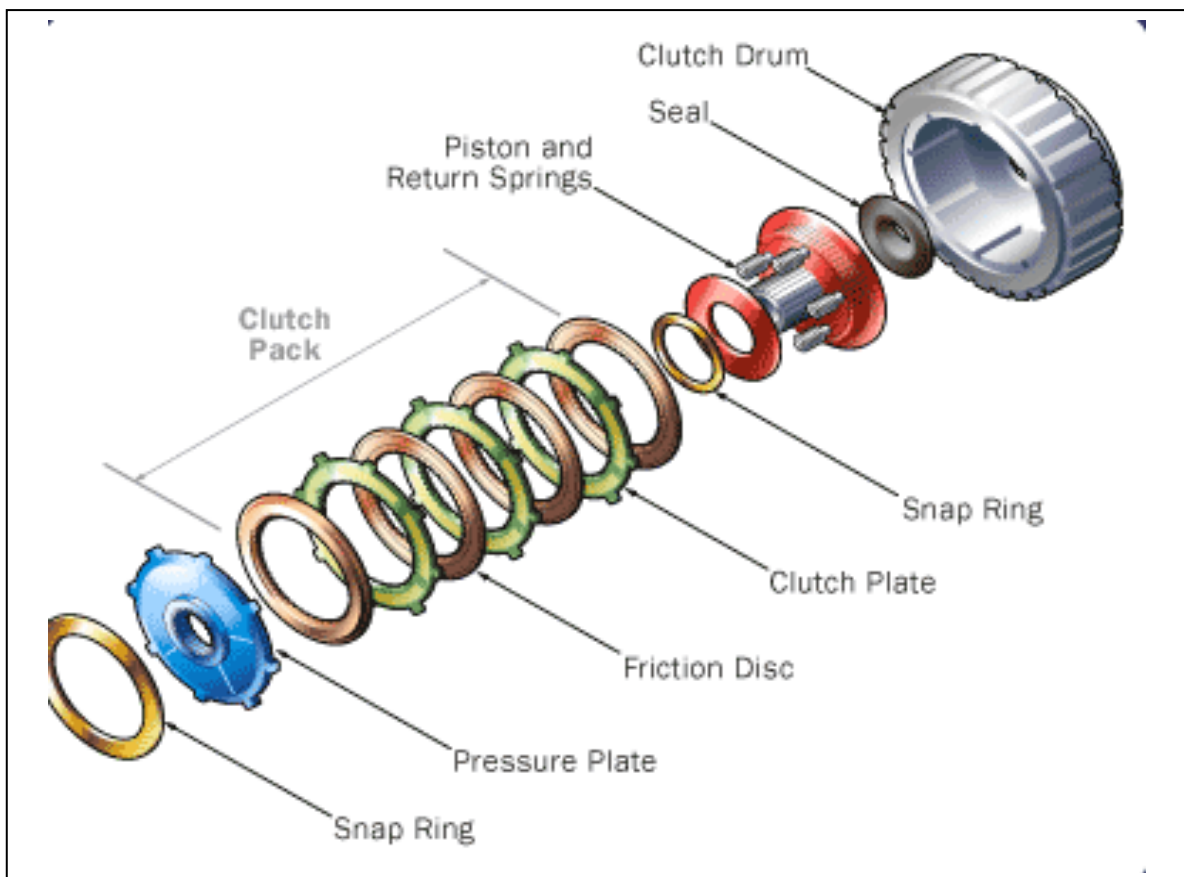


Figure 1.4 – Schematic Diagram of Multi-Plate Wet Clutch [4]

1.2 F1 Application

F1 is the world's top tier of open-wheel, single-seater racing in which teams spend hundreds of millions of pounds every season to compete. It is therefore understandably extremely competitive. Teams want to win not only for the glory of sporting achievement, but also for the financial rewards to justify the huge investments. The performance difference between the slowest and fastest cars has become less in recent years and overtaking during a race can be extremely difficult, hence a good grid position is critical for achieving a good race result.

F1 cars start a race from a stationary grid so in order to take advantage of a good grid position, it is vital to get a good launch away from the grid. A bad start may result in losing places and, by falling back into the crowded midfield, increases the likelihood of being involved in a race-ending first corner collision. Even if the first corner is negotiated, the driver will have to overtake to regain places and thus the risks of a race-ending collision, either through contact or a driver error, are greatly increased. There is no doubt that a strong start is of huge benefit to race performance and a bad start can result in the loss of championship points and therefore prize money.

Gibson et al. [5] and Lawrence et al. [6] (working with AP Racing who develop clutches for F1) have both presented a brief history of the development of carbon/carbon clutches for F1 applications. The first carbon/carbon clutch was introduced in 1982 but was abandoned due to the low coefficient of friction at low temperatures. In 1984 a modified hub was developed to better distribute loads and in 1987, the first race victory using a carbon/carbon clutch was achieved. By 1988 most teams were using carbon/carbon clutches. The next major development came in 1999 when the 2D carbon weave then being used was replaced by a 3D carbon weave to more effectively conduct heat away from the friction surface. This prevents heat saturation at the friction surface leading to excessive temperatures which strongly affect the frictional performance. Oxidation of the carbon/carbon material occurs at temperatures above 400°C and increases exponentially thereafter. Despite this, carbon/carbon clutches can last up to 16 times longer than traditional materials due to their high structural integrity at high speeds.

Carbon/carbon multi-plate clutches have since been standard technology within F1. The high coefficient of friction (0.2-0.5 [7]) that the material offers combined with its low density (offering weight saving opportunities) makes it an ideal clutch plate friction material. The arrangement of the F1 carbon/carbon multi-plate clutch in this investigation is similar to that shown in Figure 1.4. The two types of clutch plates used are shown in Figure 1.5. The friction surfaces of the two types of clutch plate are equal in size and both types of clutch plate are manufactured from a PAN-CVI carbon/carbon composite where the type of resin used to form the matrix is not specified (discussed further in Literature Review). The driving plates are thicker (3.5mm) than the driven plates (3mm) and the way they are mounted within the clutch assembly differs, reflected by the differences in their overall shape.

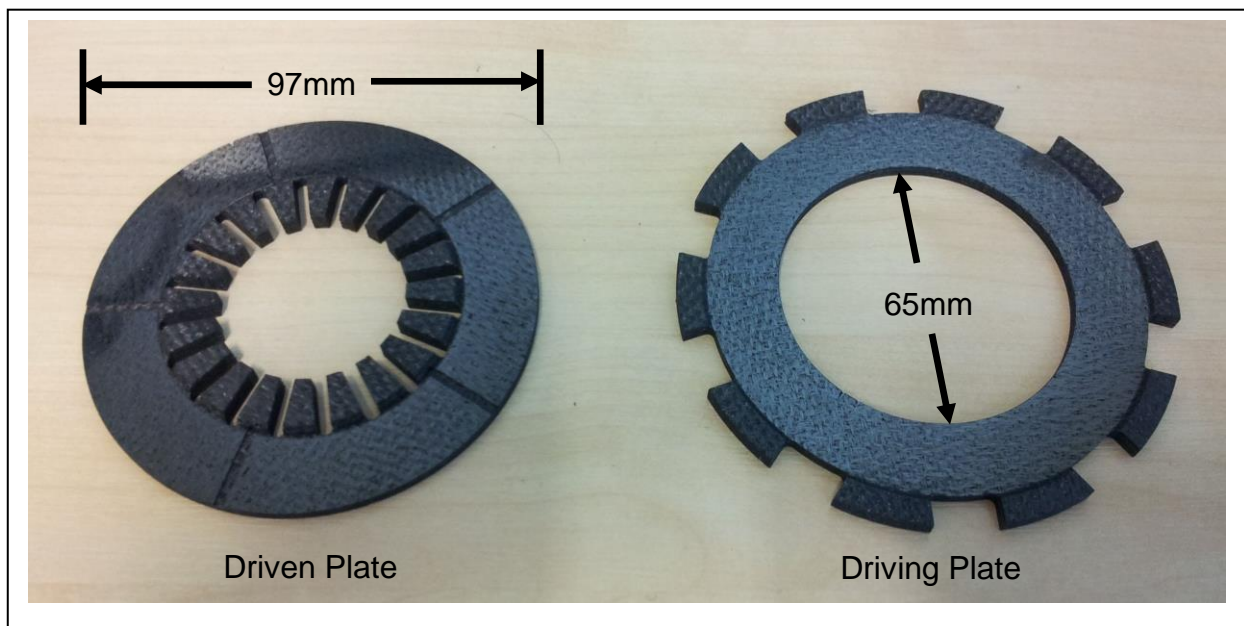


Figure 1.5 – Two Types of Clutch Plates Used in F1 Clutch

Figure 1.6 shows the clutch hub and clutch basket that are used in the clutch assembly. The driven plates are mounted on the clutch hub via their internal teeth and the clutch hub is then connected to the gearbox input shaft via a splined shaft. The driving plates are mounted within the clutch basket, radially constrained by their external teeth and the arms of the clutch basket. The back of the clutch basket has an internal spline profile machined into it which facilitates connection to the engine crankshaft via another splined shaft.

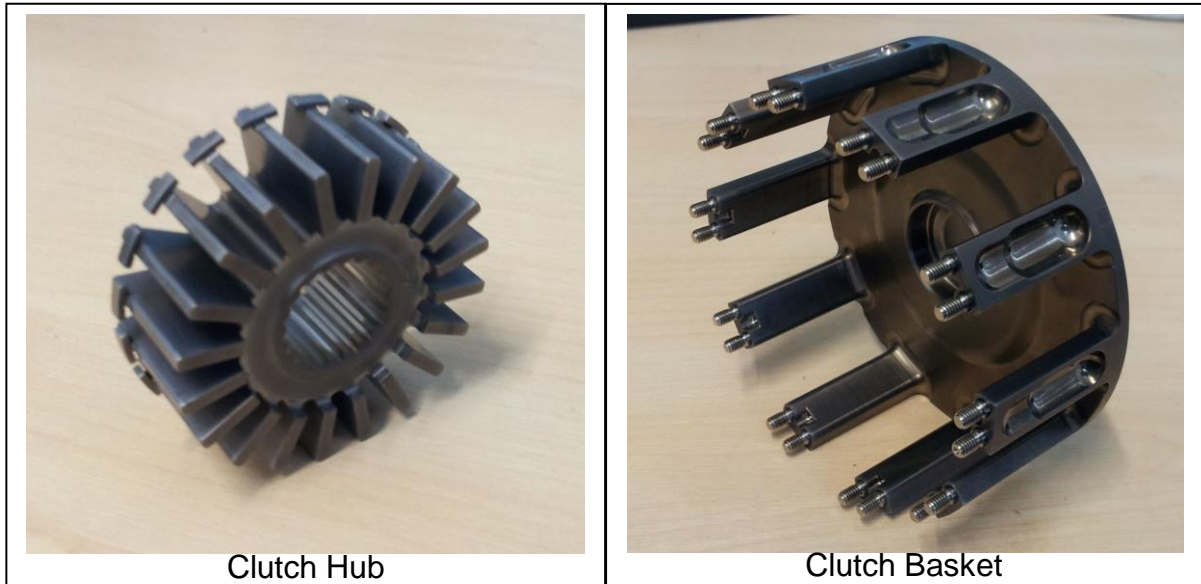


Figure 1.6 – Clutch Hub and Clutch Basket

Figure 1.7 illustrates how the clutch-plate pack is assembled within the clutch and the whole clutch assembly is shown in Figure 1.8. The driving and driven clutch plates are arranged alternately within the clutch with 5 driving and 4 driven clutch plates in total. During the race start the engine speed is held anywhere between 8000rpm and 10000rpm whilst the drivetrain on the output side of the clutch is not rotating. The relative velocity between the driving and driven plates is therefore very large. The Belleville spring provides the clamp load with the static clamp load (~20kN) being applied by tightening the lock nuts to a defined torque (only 8 shown in Figure 1.8 but a full set of 20 lock nuts would be used). The clamp load is varied through the use of a hydraulic linear actuator which pulls the Belleville spring away from the clutch plate pack. A pressure plate between the Belleville spring and clutch pack ensures that the applied pressure is uniform across the back face of the first clutch plate. The torque generated at the clutch plate interfaces is transferred via the clutch hub and gearbox input shaft to the gearbox and to the drive wheels through the remainder of the drivetrain.

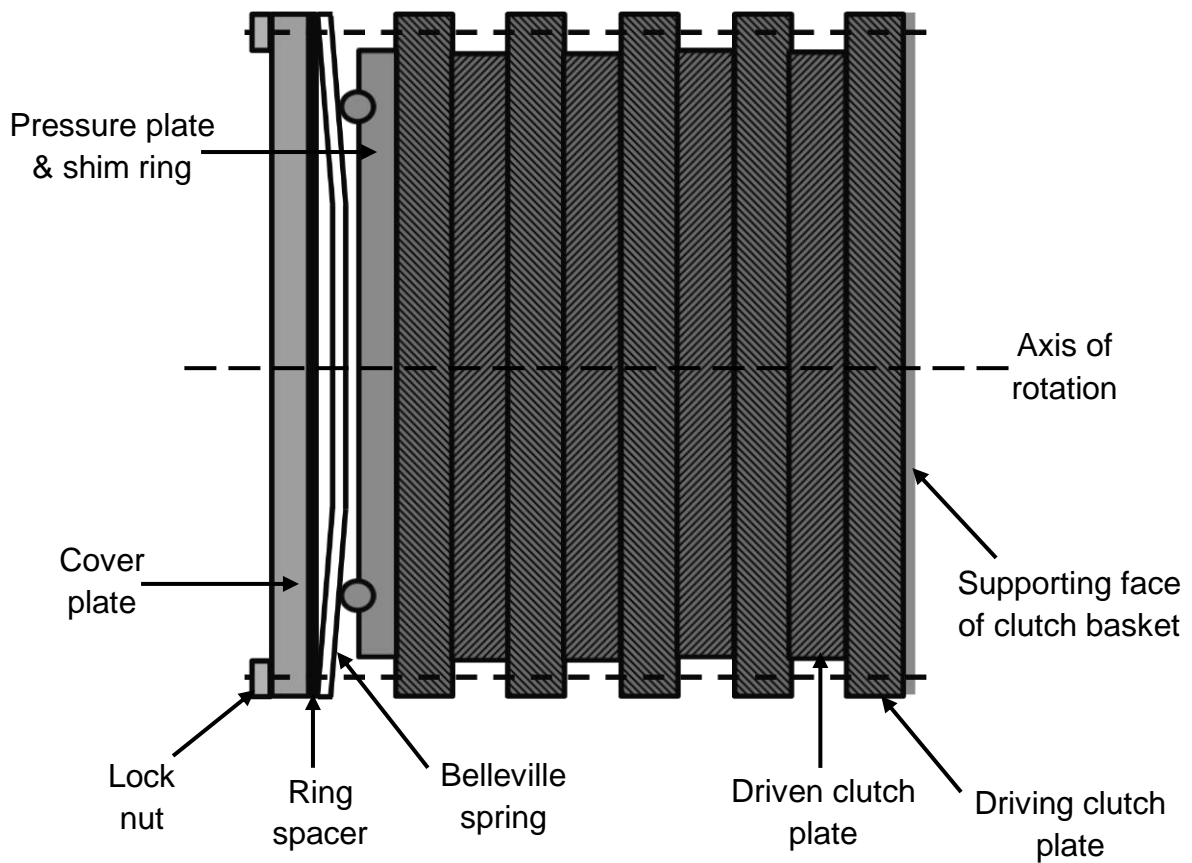


Figure 1.7 – F1 Clutch-Plate Pack Assembly

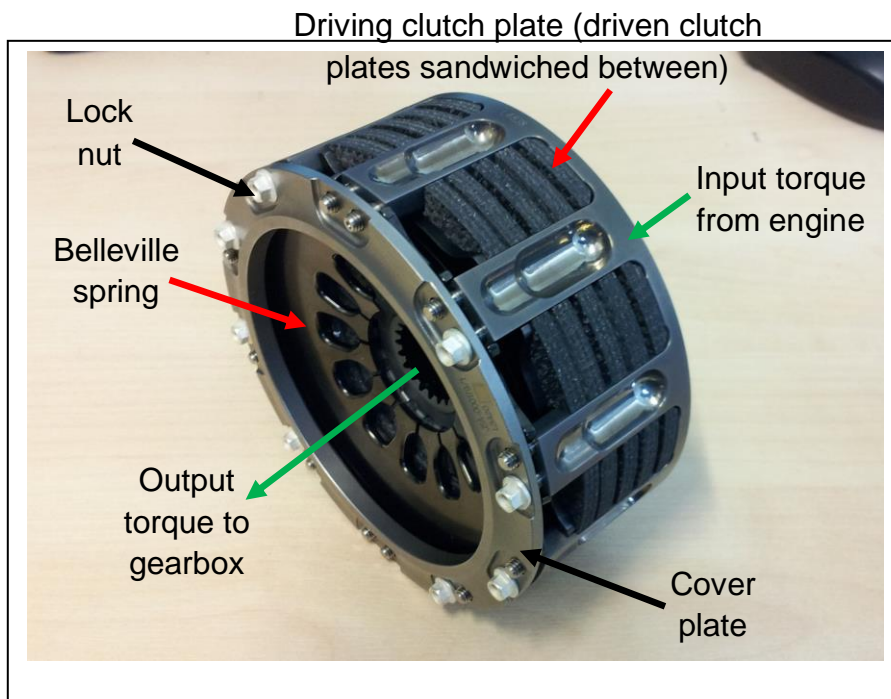


Figure 1.8 – Multi-Plate F1 Clutch Assembly

Figure 1.9 shows how the race start is carried out. The race start procedure begins at the start of the warm-up (formation) lap with the driver performing a practice launch away from the grid. The vehicle dynamics data during the practice launch is transmitted back to the engineers in the pit lane who then analyse the results and calculate the clutch COF. Based on this calculation, the value of clamp load required to generate the desired clutch torque (based on road conditions) for an optimal launch is determined. Upon finishing the warm-up lap and taking up their grid position, the driver sets the launch clamp load using a control on the steering wheel (F1 rules dictate that vehicle settings cannot be controlled from the pit lane). Prior to the race start, the driver holds the throttle at a constant engine speed and when the lights go out, the clutch is engaged in two distinct stages. The steering wheel has two clutch paddles which the driver squeezes as they pull into their grid slot. At this point there is no clamp load acting on the clutch as the Belleville spring is pulled away by the hydraulic clutch actuator. When the race begins, the driver releases the first clutch paddle which partially releases the Belleville spring to apply the launch clamp load. The vehicle then accelerates from the grid. The driver can use the first clutch paddle and throttle to vary the clamp load and engine rpm to achieve the best possible start. Once the clutch is fully engaged, the driver releases the second clutch paddle which fully releases the Belleville spring applying the full clamp load of approximately 20kN.

This race start procedure however has proved to be inconsistent in terms of the quality of vehicle launch it provides [7]. It was found that the torque output for the proper race start can be dramatically different from the torque output from the practice race start even if the clamp load setting and initial engine rpm are consistent. If the torque output is greater than expected for the proper race start, the excess torque generated will result in a rapid fall of the engine speed. The engine control unit (ECU) will then override the clutch engagement electronics and disengage the clutch to prevent the engine from stalling. The vehicle will therefore temporarily lose drive whilst the engine speed is recovered. The opposite scenario where the clutch torque is lower than expected for the proper race start would result in excessive slip within the clutch, increasing the clutch engagement time and resulting in a low level of vehicle acceleration. If either of these scenarios occurs, the driver does their best to recover the situation but by the time they have, several

positions may have been lost. All forms of vehicle launch control are prohibited by F1 rules so the vehicle launch is an entirely manual, driver-controlled event.

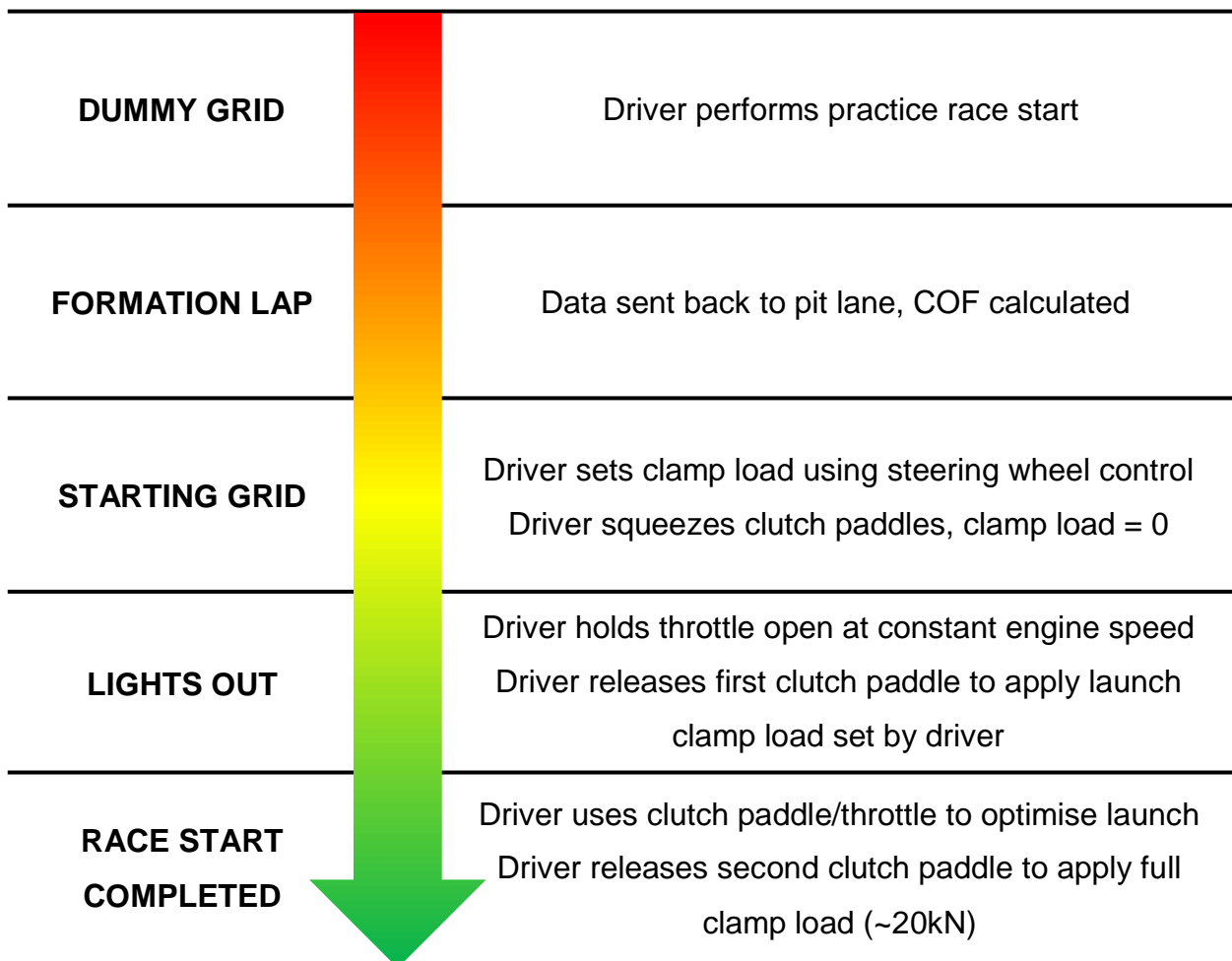


Figure 1.9 – Race Start Procedure

Further investigation of the clutch performance revealed the extent of the problem. Figure 1.10 shows torque output results from dynamometer tests [7] using the same carbon/carbon multi-plate clutch at two different clamp load and energy dissipation combinations. At both clamp load/energy combination, seven consecutive engagements were carried out and the traces shown are the clutch torque outputs measured. For each test the bulk temperature of the clutch plate pack was allowed to cool to 200°C before commencing the next engagement. The measured temperature was the surface temperature which was measured on the outer through-thickness surface of the clutch pack using an infrared camera.

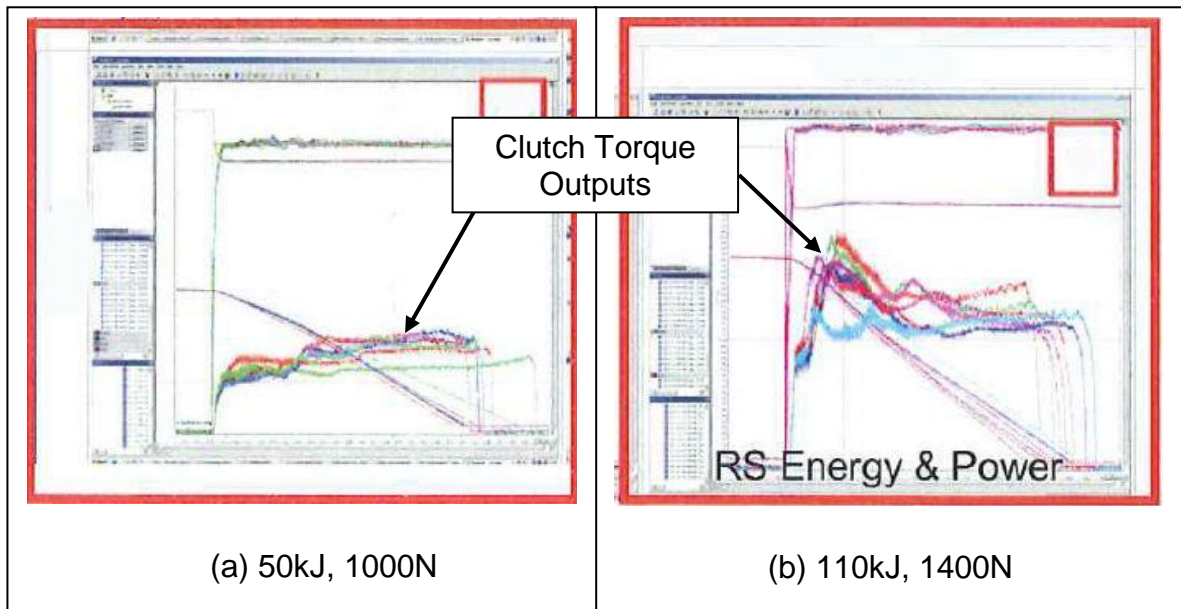


Figure 1.10 – Clutch Torque Output Results from Dynamometer Tests [7]

Figure 1.10 shows that the torque output of the clutch is stable and consistent at a low clamp load and low energy combination but at input levels typical of the race start, the torque output is highly unstable and inconsistent. With reference to Equations 1.8 and 1.16, the cause of this inconsistency could be due to the COF changing from test to test as the surface morphology (discussed further in literature review) of the friction surface is altered as a direct result of the energy dissipation taking place. Figure 1.11 shows the relationship that is believed to exist between the friction surface temperature, surface morphology and COF.

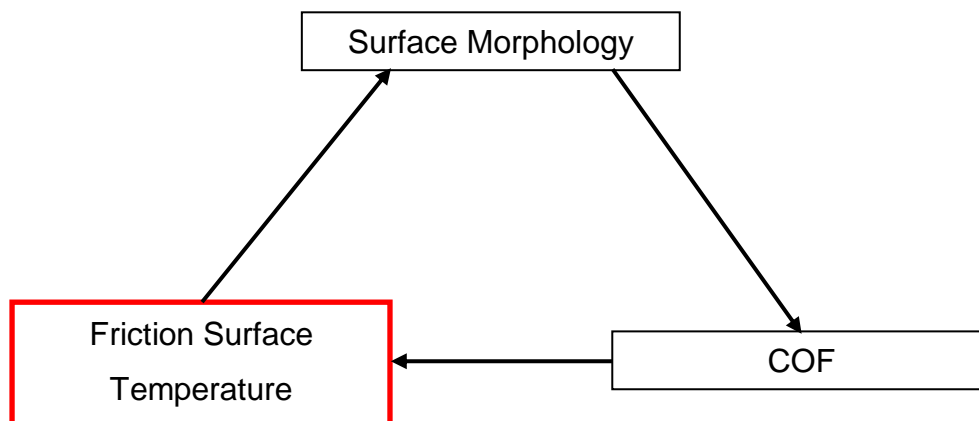


Figure 1.11 – Possible Friction Surface Temperature-Morphology-COF Relationship

The temperature and torque profiles of a single engagement test carried out at the race start clamp load and energy combination illustrates this potential relationship. Figure 1.12 shows that the sudden rise in torque during the clutch engagement is accompanied by a rapid rise in the friction surface temperature. An increase in COF would lead to increased torque and greater energy dissipation as a result. The friction surface temperature would then increase causing a surface morphology change which in turn would affect the COF and torque which would then influence the surface temperature. A closed-loop system is thus formed as shown in Figure 1.11.

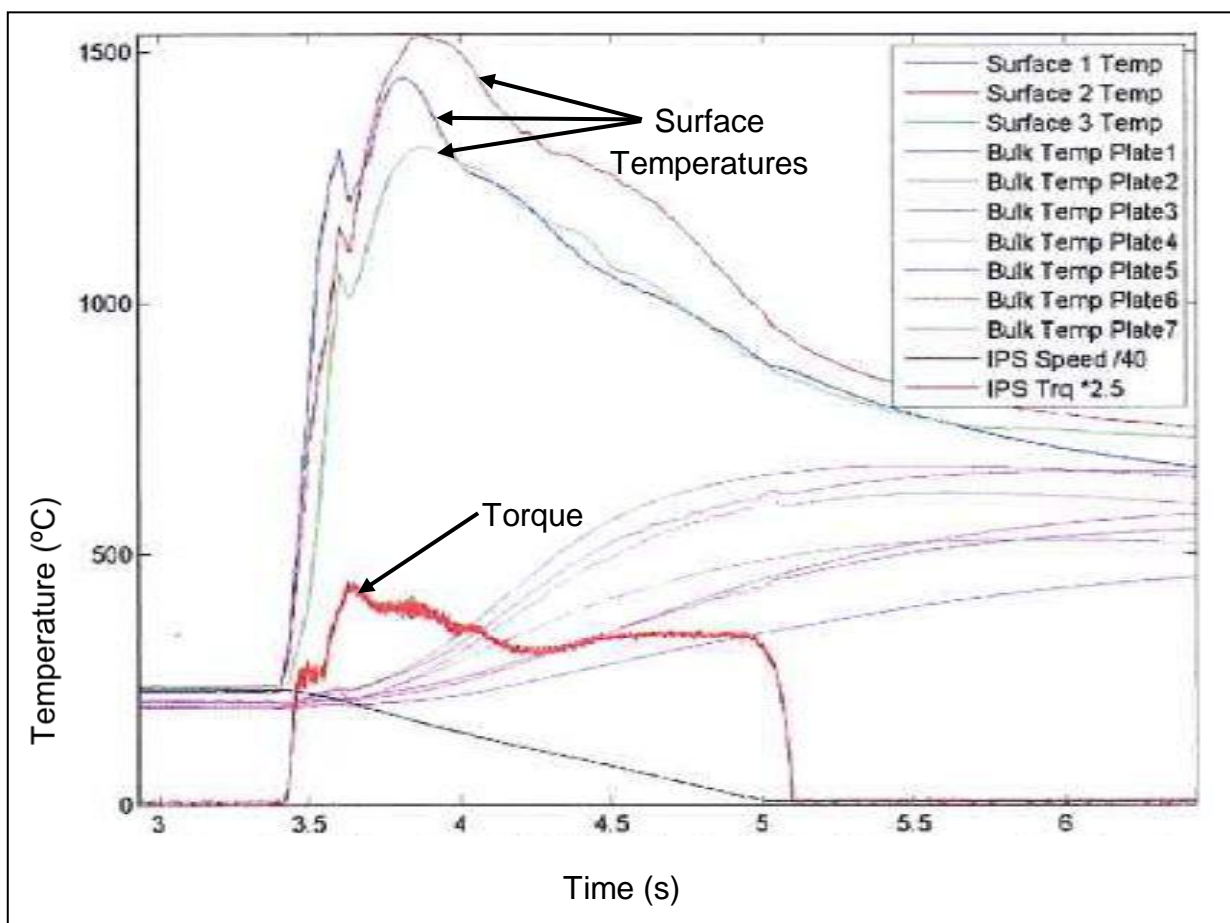


Figure 1.12 – Temperature and Torque Profiles for a Single Full Clutch Engagement at 1400N Clamp Load and 110kJ Energy Dissipation

Equations 1.8 and 1.16 however assume that the two friction surfaces are in perfect contact and hence the effective friction radius is simply equal to the mean geometric radius of the clutch plate friction surfaces. This is extremely unlikely to be case in

reality as the friction surfaces will have initial surface asperities which localise contact to a few discrete regions of the friction surfaces. If these contact regions lie anywhere except the mean geometric radius, the torque output will deviate from that given by Equations 1.8 and 1.16. In particular, this would affect the value of COF calculated during the race start procedure leading to an incorrect clamp load setting. A phenomenon known as thermoelastic instability (TEI) could then lead to hot banding [8]. Due to the initial surface asperities, the pressure distribution will be non-uniform leading to higher temperatures in regions of higher pressure. These regions will then experience larger amounts of thermal expansion and become further proud of the surface thus intensifying the effect. However these regions will wear quicker than the rest of the friction surface and contact will then be lost, moving to a different part of the surface. Hot spots will occur at the real contact areas where the pressure and temperatures and ultimately thermal expansion levels are higher. In the case of disc-on-disc contact, banding will occur whereby contact only occurs over a small circumferential band of the friction surfaces. Based on the geometry of the clutch plates in this investigation, the clutch torque could increase by 50% solely based on if the point of contact (and therefore effective friction radius) between the clutch plates shifted from the inner radius to the outer radius.

It is yet unclear whether surface morphology changes, hot banding or a combination of both cause the clutch torque behaviour shown in Figures 1.10 and 1.12. This investigation aims to lead to an understanding of the cause of the clutch torque instability and inconsistency by establishing the influence surface morphology changes and hot banding have on clutch torque output. A strategy for achieving an at least consistent torque output (driver can compensate for instability) can then be recommended based on either controlling the surface morphology, hot banding or both.

1.3 Aim and Objectives

Aim

To increase understanding of clutch-plate friction behaviour in order to make recommendations for design or procedure changes to ensure consistent and predictable torque output of the Formula One carbon/carbon multi-plate clutch.

Objectives

1. Understand research problem and gain knowledge of previous research findings.
2. Design single clutch-plate interface dynamometer (SCID), produce engineering drawings and submit for manufacture.
3. Carry out friction performance testing of clutch-plate pairs using SCID.
4. Develop 1D heat transfer model to gain understanding of influence of system and material properties on clutch plate friction surface temperatures.
5. Develop fully thermomechanically coupled finite element models of a single clutch plate pair under SCID operating conditions in order to predict clutch plate temperatures and extent of hot banding.

2. Literature Review

2.1 Introduction

A literature review has been carried out to assess areas of research into carbon/carbon friction materials, their applications and the key findings to date. The principal areas are summarised as clutch performance modelling, processing and structure of carbon/carbon composites, characterisation techniques, physical and chemical properties and carbon/carbon surface morphologies and how these relate to friction and wear performance. The phenomenon of thermoelastic instabilities (TEI) is also discussed as it can strongly affect friction and thermal performance.

Blanco et al. [9] present a literature review summarising research into carbon/carbon composite brake materials. They note that published papers are limited due to much of the research in this area being carried out by industry and many of the findings being protected by patents. The review also highlights that most published research is associated with the development of aircraft brakes, a point that is reiterated by Savage [10]. Aircraft brakes are similar in construction to the multi-plate carbon/carbon clutch used in this investigation in that friction is generated via disc-on-disc contact. The fact that they are also used in a high energy application means that much of the research findings can be related directly to multi-plate clutches.

2.2 Clutch Performance and Modelling

The pressure and temperature at the friction surface of clutch plates has a direct effect on coefficient of friction (COF) levels and hence torque output, as well as influencing the wear of the friction surfaces. Clutch modelling allows prediction of the evolution of pressure and temperature profiles during clutch operation and is hence an important tool in predicting the performance of a clutch. The models developed to predict friction surface behaviour vary in complexity from simple 1D analytical models predicting clutch-plate temperatures to 3D fully coupled thermomechanical finite element models predicting transient temperature behaviour and wear.

Velardocchia et al. [11] developed a one-dimensional linear model to estimate temperatures on the slipping surface of a clutch plate. The model consists of three

masses: the mass located between the push plate and clutch disc (m_{sv}), the mass located in the clutch disc (m_i) and the mass located at the interface between the flywheel and the clutch disc (m_{ss}). The model neglects the energy exchanged between the engine and clutch and the radial temperature distribution is not considered in order to reduce complexity which is justified given the model's aim. The analysis is carried out for the outer radius as this is where the highest temperature changes occur and the model also considers the clutch in both open and closed states. Figure 2.1 represents the thermal model whilst Figure 2.2 shows how the dissipated power is modelled.

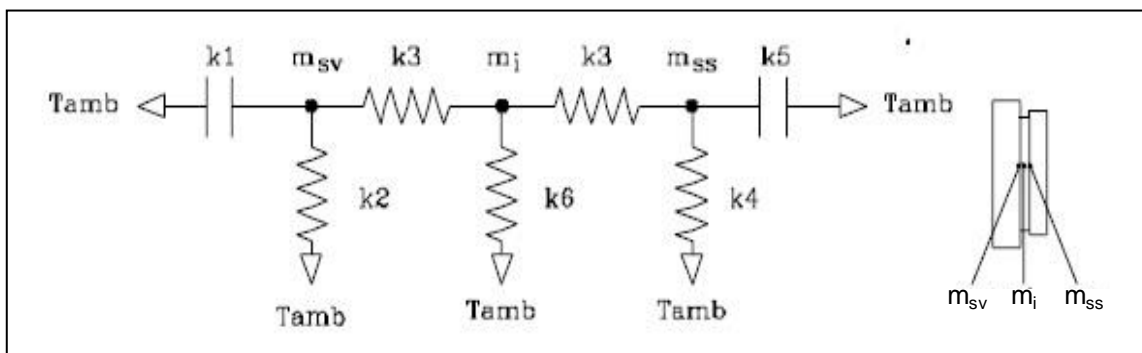


Figure 2.1 – Linear 1D Thermal Clutch Model [11]

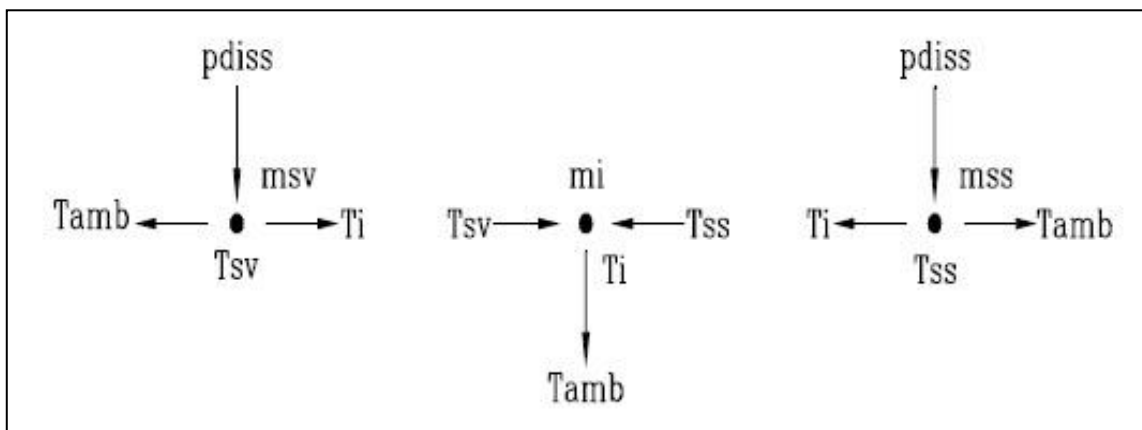


Figure 2.2 – Power Flow Through 1D Model [11]

The parameters k_1 - k_6 represent combined conductive and convective heat transfer coefficients and were determined experimentally. The temperatures at the inner, middle and outer radii of the clutch plate were measured during a sequence of open and closed clutch cycles. The results were typical of a first order system and the parameters were calculated using associated homogeneous equations. The most

significant outcome of this model was that test conditions used to determine the parameters were critical in affecting the accuracy of the model. The model overestimated the slipping surface temperatures when the power dissipated in the model was less than the power dissipated during the experiments and vice versa. The model also overestimated the slipping surface temperature when the open clutch (cooling) period used in the experiments was decreased and when the closed clutch (heating) period was increased. The model also overestimated temperature if a worn clutch was used for parameter determination.

Using a two-dimensional model allows the stresses in the clutch plate to be estimated. Zagrodzki [12] presents a numerical analysis of the temperature fields and thermal stresses in the friction disc of a multi-plate wet clutch. It is important to note the assumptions made in this analysis. It was assumed that the heat flux on all friction plate surfaces within the multi-plate clutch were equal and the temperature distribution through the plates was axisymmetric. The coefficient of friction was assumed to be constant with radius but increased with sliding speed (experimentally determined). The pressure was assumed to be constant and cooling was included at the inner and outer radii. The heat flux input to the plates was modelled as being proportional to the radius and hence the model predicted radial temperature gradients due to the non-uniform heat flux over the friction surface resulting in a dominance of hoop stresses. It is therefore important to keep the heat flux as constant as possible over the friction surface in order to minimise these stresses.

Zhao et al. [13] developed a fully coupled thermomechanical finite element model to investigate the transient temperature behaviour of an aircraft multi-plate clutch under normal operating conditions. An axisymmetric model was developed in which a finer mesh is used at the friction surfaces to better capture the temperature profiles in this region. The clutch model consists of a pressure plate, two rotors, a stator and a back plate. Pressure is applied uniformly to the pressure plate and the back plate is constrained from moving in the axial direction. The heat flux is equal to the product of the coefficient of friction, sliding speed and contact pressure and convective cooling is included in the model. During engagement, the results initially show very high temperature gradients at the friction surfaces. These temperature gradients rapidly reduce as heat is conducted through the clutch and the energy input is decreased as sliding speed decreases as shown in Figure 2.3.

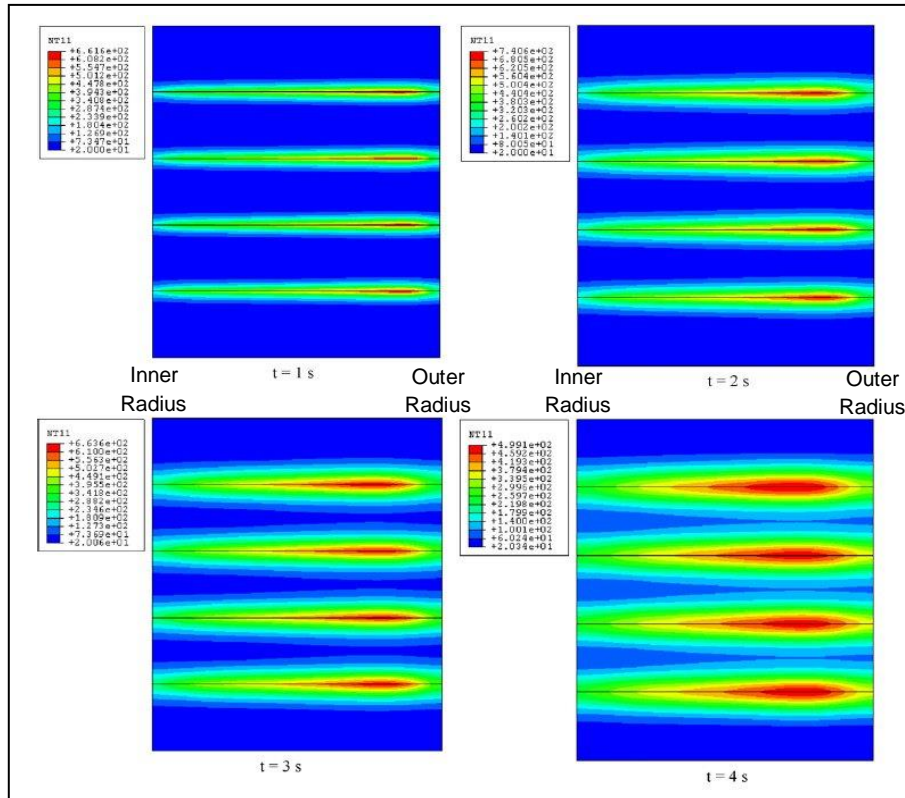


Figure 2.3 – Temperature Distributions in Multi-Plate Clutch at Discrete Times [13]

The model also showed that temperatures towards the outer radii were significantly higher than towards the inner radii, which contradicts the experimental results found by Lawrence et al. [6]. However, lower pressures due to thermal expansion and loss of contact were predicted at the very inner and outer radii resulting in low temperatures. Upon disengagement the temperature distribution became more uniform both radially and axially. Hoop stresses were predicted to be dominant (as predicted by Zagrodzki [12]). A parametric study was carried out and it was found that increasing disc thickness, specific heat, and transverse conductivity reduces clutch-plate temperatures.

Further work was carried out by Zhao et al. [14] to predict the wear of the multi-plate clutch simulated in the previous work [13]. The same geometry and finite element model were used to determine pressure distribution and accumulative wear with the surface geometry changing accordingly on each iteration. The model was validated against open literature for disc-on-disc sliding tests. The model showed that the level of wear is highest at the beginning of the clutch-plate engagement when the heat flux and sliding velocity are high and then decreases as the engagement progresses.

Zagrodzki [15] developed a 2D finite element model to analyse thermomechanical phenomena in multi-plate clutches and brakes. The phenomenon of thermoelastic instabilities is known to occur on sliding surfaces and cause non-uniform pressure distributions [8] (discussed further in Section 2.7). However, another cause of non-uniform pressure distribution can arise from the one-sided heating of the clutch plates at the ends of a multi-plate clutch pack. The plates at the end of a clutch pack have only one friction interface and so heat input is from one side only. The model showed that should any non-uniformity in pressure distribution arise at the end of the clutch-plate pack, the non-uniformity would propagate through the clutch pack, further compounding the problem.

Abdullah et al. [16] developed a 3D finite element model of a clutch-plate pair in which the heat flux distribution at the friction surfaces was proportional to the sliding velocity. The results showed that the heat flux increases linearly from the inner to the outer radius with the temperature and pressure fields following the same trend. All three parameters were circumferentially uniform.

However, further work by Abdullah et al. [17, 18] using an axisymmetric model that takes into account the process of thermoelastic instabilities, produced significantly different results to their previous work [16]. The finite element model incorporated a heat flux that was equal to the product of the coefficient of friction (constant), contact pressure and sliding velocity. However, if at any node no contact pressure was calculated due to any separation of the friction surfaces, the temperature of the node was set equal to its temperature at the previous time step. Ten friction surfaces were modelled between the piston and pressure plate of the clutch. The pressure plate was constrained to be unable to displace in the axial direction. Figure 2.4 shows the contact pressure evolution of the third friction surface which is typical of the other friction surfaces. The simulations predicted a uniform pressure distribution at the start of the engagement but expansion of the clutch plates led to loss of contact at the inner and outer radii. This caused the pressure to increase towards the centre of the clutch plates. The heat flux and thus temperature followed the same pattern which led to more and more localisation of the pressure distribution towards the centre of the clutch plates as the engagement progressed. The maximum temperature was therefore recorded at the centre of the clutch plate at around 900K for an initial sliding speed of 3000rpm. Several sliding speeds were investigated and

the results showed that the degree of localisation became stronger with increased sliding speed and hence the maximum pressure and temperature also increased. The highest pressures and temperature were predicted at the friction surface nearest to the pressure plate.

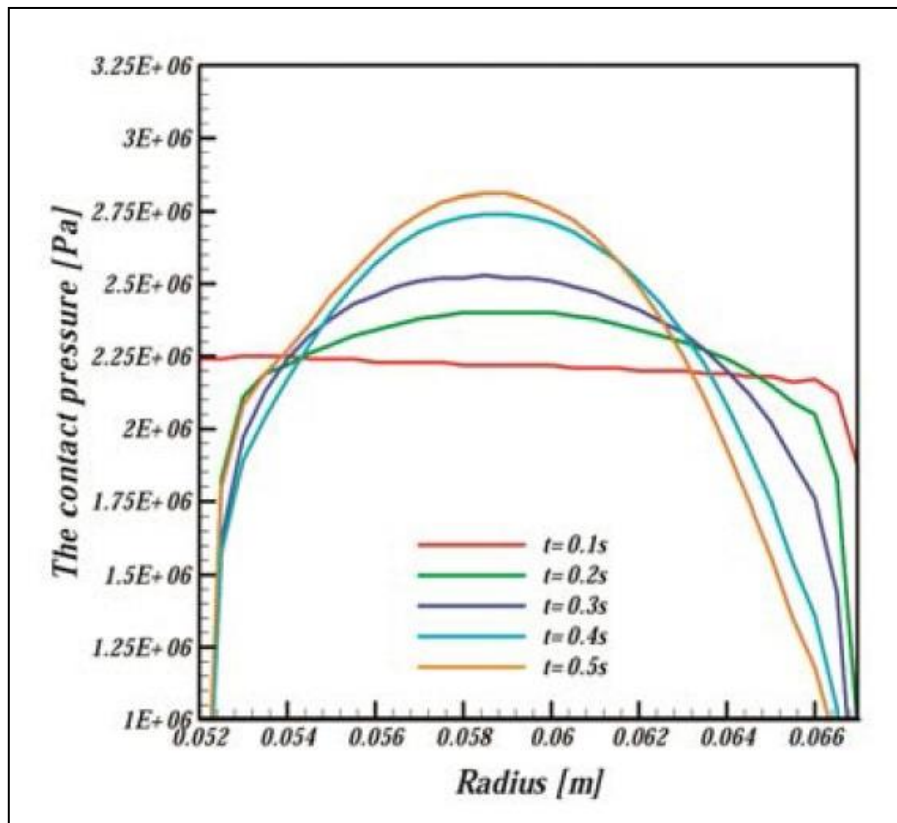


Figure 2.4 – Contact Pressure Distribution Evolution [17]

Abdullah et al. [19] also developed a 3D finite element model to model the effect of cleaning grooves on the thermal behaviour of dry clutch plates. The clutch plates were modelled with one circumferential groove at the clutch-plate centre with a series of equally spaced radial grooves. The relative area of the grooves to the overall friction surface (groove ratio) was varied and the surface temperature predicted for each case. A uniform wear model was used where full contact area was assumed. Convection was included in the model. The models predicted that the maximum surface temperature during the clutch-plate engagement was not affected by the groove ratio. However, the increased convective cooling with increased groove ratio did reduce the overall thermal energy within the clutch plate, meaning that sub-surface temperatures were reduced by increasing the groove ratio.

2.3 Processing and Structure of Carbon/Carbon Composites

The basic structure of a carbon/carbon composite is described by Inagaki [20]. The two major parts of a carbon/carbon composite are the filler and matrix where the matrix is the binder for the filler. The filler consists of carbon fibres which give a wide range of variation in properties by selecting either strand, yarn or chopped forms. The purpose of the matrix is to assist in utilising the high strength of the fibres. The structure and texture of the matrix are the most important factors in determining the properties of carbon/carbon composites such as fracture behaviour, strength, toughness and thermal expansion. A flow chart showing how carbon/carbon composites are produced, presented by Inagaki, is shown in Figure 2.5.

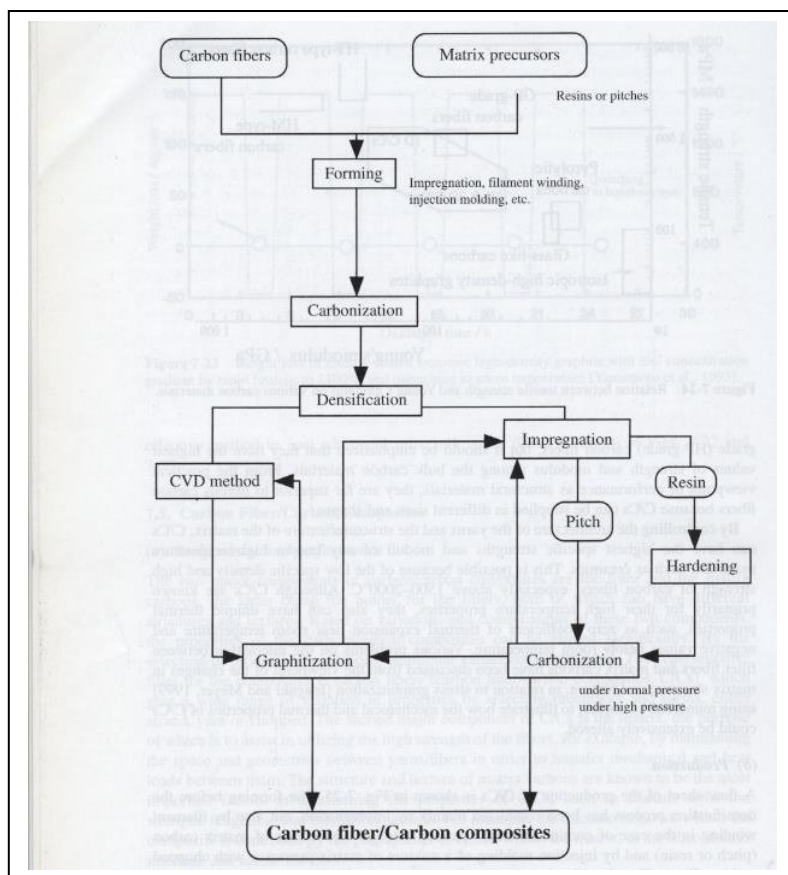


Figure 2.5 – Process for the Production of Carbon/Carbon Composites [20]

As can be seen from Figure 2.5, there are different densification methods which can be used. Byrne [21] divides carbon/carbon composites into two categories based on their densification method: matrix phases in fibre preforms formed by either liquid infiltration/deposition methods followed by carbonisation or those formed by chemical

vapour infiltration/deposition (CVI/CVD). The fibre preforms can either be 2D random tows (untwisted bundles of continuous filaments) pressed together, stacked weaves, a woven 3D structure, needle felts or some combination of these structures. Byrne states that three distinct areas affect the properties of the carbon/carbon materials with these being: phase structure and orientation, fibre architecture and fibre-matrix interface.

Savage [10] discusses the three different precursors for carbon fibres: rayon, polyacrylonitrile (PAN) and pitch, with PAN being the most widely used. PAN fibres are non-graphitisable. The production of PAN fibres is discussed by Inagaki [20] who presents a flow chart for the production of these fibres which is shown in Figure 2.6.

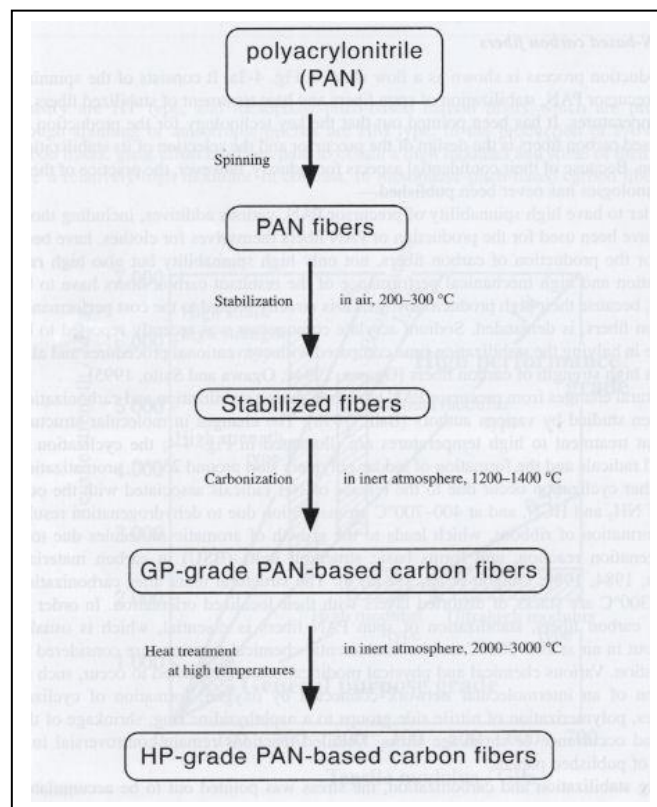


Figure 2.6 – Process for the Production of PAN-Based Carbon Fibres [20]

Another important aspect in the processing of carbon/carbon composites is the level of graphitisation which can be affected by the heat treatment temperature (HTT). As discussed by Savage [10], increasing the HTT will increase the modulus of the fibres and the level of graphitisation as the graphite structures align more preferentially to the fibre axis. This effect is limited to a HTT of approximately 1500°C, above which

defects develop on the surface. However, as reported by Luo et al. [22], high HTT also weakens the fibre-matrix bond leading to an increased tendency for delamination of the composite surface to occur. A similar result is also reported by Marinkovic et al. [23] being attributed to an increase in crystallite dimensions and decrease in interlayer spacing (also found by Luo et al. [22]) which results in less cross-linking therefore increasing delamination tendency. This affects the friction and wear performance of the carbon/carbon material.

It is clear from the literature presented regarding the processing and structure of carbon/carbon composites that the overall properties of a carbon/carbon composite are affected by many factors ranging from the carbon fibre precursors to the processing conditions. Through careful control of these factors, carbon/carbon composites with specific properties can be produced to suit their purpose such as orienting fibres perpendicular to the material friction surface to increase transverse thermal conductivity (discussed further in Section 2.5).

2.4 Structural Characterisation of Carbon/Carbon Composites

Savage [24] discusses the common techniques used to characterise the structure of carbon/carbon composites. These techniques fall into three categories: optical microscopy, electron microscopy and x-ray diffraction.

Optical microscopy uses light transmission through or reflected from the surface of a material to obtain information about the material. Magnification values can be up to 1000x with a limit of resolution of 1 μ m. The surface must be polished before examination. Polarised light is used to produce interference colours which arise due to the orientation of the graphite layers. Analysis of the interference patterns are used to calculate an Optical Texture Index (OTI). The OTI gives a measure of the level of graphitisation and orientation of the graphite layers at the surface. Optical microscopy can therefore be used to measure shape, size and degree of porosity, level of graphitisation and estimate the sizes of graphitic/non-graphitic regions.

Scanning Electron Microscopy (SEM) is used to study surface topography. The resolution of SEM is approximately three times greater than optical microscopy. An electron beam is passed through the sample and the scattering of the electrons

reveals rough topographical features and void content of the sample. Etching of the surfaces is required in order for full detail to be revealed.

Transmission Electron Microscopy (TEM) differs from SEM as it uses the diffraction and transmission intensities of the electron beam to reveal information about the structure and morphology of a material. The spacing of the lattice structures can be determined by the diffraction patterns whilst the transmitted beam can be used to produce a magnified image of the sample. The magnified image can provide information about the size and shape of the microstructure up to a resolution of 0.2 μm . Scanning Transmission Electron Microscopy (STEM) allows the electron beam to sweep over a small predetermined area and as the electron beam interacts with the sample, characteristic x-rays are emitted. Regions as small as 0.05 μm can be studied using STEM.

X-ray diffraction (XRD) is used to determine the bulk structure of carbon/carbon materials. The sample is prepared as a powder and diffracts x-rays that are passed through the sample. The diffraction pattern produced is unique for different crystallite structures hence this technique allows crystallite structure to be determined. A reference compound (usually a crystalline salt) is added to the powder to allow for calibration of the diffraction pattern. The amount of order and disorder may also be examined by measuring the amount of background scatter which is an indication of disorder. Measurement of the broadening of the diffraction peaks allows mean particle size to be estimated.

2.5 Physical and Chemical Properties of Carbon/Carbon Composites

The physical properties that make carbon/carbon composites suitable for friction applications are mentioned by many authors [9, 13, 21, 22, 25, 26, 27, 28]. Carbon materials have low density, low coefficients of thermal expansion, high specific heat capacity, high thermal conductivity, are self-lubricating, have high wear resistance, are strong and stiff and can withstand temperatures of over 2000°C. Some typical material properties are presented in Table 2.1.

As can be seen from Table 2.1, it is possible to have different properties in the z-direction (axial) of the carbon/carbon composite. The effect of varying the z-fibre content on the properties and performance of a carbon/carbon composite has been

investigated by Byrne et al. [29]. It was found that increasing z-fibre content resulted in higher density composites with lower open porosity and increased through-thickness diffusivity values. Dynamometer tests were carried out to determine the effect this had on the temperature through aircraft brakes disc with varying z-fibre content. It was found that those with highest z-fibre content had the lowest near-surface temperatures for comparative tests.

Material properties	Value
Density, ρ (kg/m ³)	1800
Elastic modulus, E_r (GPa)	50.2
Elastic modulus, E_z (GPa)	5.89
Shear modulus, G_{rz} (GPa)	2.46
Poisson's ratio, $\nu_{r\theta}$	0.3
Poisson's ratio, ν_{rz}	0.33
Thermal conductivity, k_r (W/m K)	50
Thermal conductivity, k_z (W/m K)	10
Specific heat, c (J/kg K)	1420
Thermal expansion, α_r (10^{-6} K ⁻¹)	0.31
Thermal expansion, α_z (10^{-6} K ⁻¹)	0.29
Friction coefficient, μ	0.2
Heat convection coefficient, h (W/m ² K)	100

Table 2.1 – Typical Properties of Carbon/Carbon Composites [13]

r – Radial Direction, z – Through-Thickness Direction

The chemical properties of carbon/carbon composites are very different from traditional materials. Blanco et al. [9] discuss the gasification of the carbon/carbon material surface at high temperature and the adsorption of water at low temperatures. The carbon/carbon material is not completely inert to oxygen present in air such that at temperatures above 1000°C, oxidation of carbon to carbon monoxide and carbon dioxide occurs. Below these temperatures, oxygen complexes are formed on the surface and particularly in the wear dust. These oxygen complexes allow water to be adsorbed onto the surface at low temperatures. Increasing the level of graphitisation decreases the ability of oxygen complexes to form.

2.6 Surface Morphologies of Carbon/Carbon Composites and Their Effect on Friction and Wear Performance

The friction performance of carbon/carbon materials in ambient conditions has been investigated by several authors [9, 26, 30, 31] and the same general trends have been observed. Initially the coefficient of friction is low due to water being present on the friction surface. Once a certain temperature is reached (approximately 150°C) the water is desorbed from the surface and a rapid increase in COF is observed along with a rapid rise in temperature. As the temperature rises further however, the COF falls from its peak value and remains fairly constant at a higher value than the COF at ambient temperature. These friction characteristics are due to changes in surface morphology which are strongly affected by level of energy input and ambient conditions. The typical friction characteristics shown in Figure 2.7 are presented in work by Blanco et al. [9].

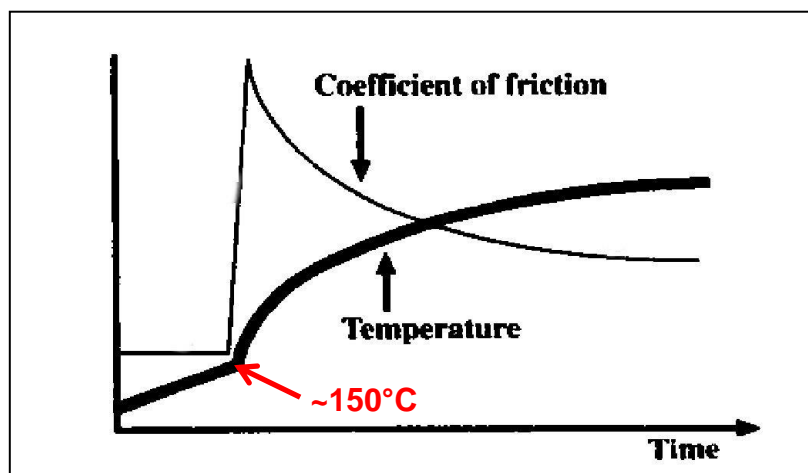


Figure 2.7 – Typical Friction Characteristics of Carbon/Carbon Composites [9]

It is generally accepted that there are three types of surface morphology which form on carbon/carbon composites. Type I morphology is characterised by a thin, smooth, bright film. Thick, rough, dark powdery debris is indicative of type II morphology. Type III morphology consists of a smooth, dense, bright debris film. The transition from low COF to high COF occurs when type I morphology is transformed to type II and wear dust is formed. The fall thereafter in COF is the result of the transformation of type II morphology to type III which forms a protective film reducing COF and wear.

The formation of type I morphology results from physically adsorbed water present on the friction surface, the adsorption of which is facilitated by the presence of chemically bonded oxygen complexes [9]. The hydrophilic oxygen complexes allow a film of water to be established on the surface of the carbon/carbon composite. The film of water present on the friction surface has a lubricating effect resulting in the initially low COF shown in Figure 2.7, but when the water is desorbed (a physical process similar to evaporation), the lubricating effect is lost.

Work by Kasem et al. [31] established the physical mechanism that causes the transition from type I to type II morphology. Pin-on-disc tests were carried out where external heaters were used to maintain the temperature of the pin and disc at 150°C. At this temperature water is already desorbed from the friction surface. Any small defect on the friction surface leads to contact localisation and high local pressure. Abrasion of the friction surface in these regions causes 1st body (friction material) degradation resulting in 3rd body (detached) particles being produced. The 3rd body particles that remain in the contact region greatly reduce the real contact area leading to further increased local pressure resulting in increased stress and temperature leading to further particle detachment. However, not all 3rd body particles remain in the contact region and some may either be ejected from the contact region or fill surface porosities. Based on their observations, Kasem et al. then attempted to force the COF transition at low temperature by artificially introducing 3rd body particles onto the friction surface. The COF transition did not occur until the water desorption temperature had been exceeded, demonstrating that the COF transition is a function of both mechanical and physiochemical actions.

Yen et al. [32] carried out a ring-on-ring test to simulate aircraft brakes and used optical and scanning electron microscopy to examine the sliding surfaces. Type II morphology was observed at the inner and central radii on the rings whilst type I morphology was observed at the outer radius. At a fixed sliding speed, the percentage of type I to type II morphology decreased with increasing load and eventually only type II morphology was present. The difference in morphologies is attributed to non-uniform pressure distribution where there is a higher pressure at the inner radius (type II morphology) and lower pressure at the outer radius (type I morphology).

Hutton et al. [33] carried out similar work to investigate the mechanism that leads to the formation of type III morphology from type II morphology. Scanning electron microscopy, x-ray diffraction and optical microscopy were used to examine the wear surfaces and wear debris from dynamometer tests carried out at three different energy levels. It was found that the type II particulate wear debris comprised of a disordered carbon phase formed mainly by shear deformation of the CVI matrix as well as containing small fragments of the PAN carbon fibres. Type III morphology was observed after high energy stops where shear-stress assisted graphitisation of the friction film takes place, forming a fine mosaic texture which is very different to the CVI matrix. Figure 2.8 shows SEM images of the collected wear debris. It can be seen that the wear debris from the low energy test (a) consists mainly of particulate debris (type II morphology) whilst the wear debris from high energy tests (c) consists mainly of large flat platelets (type III morphology). The intermediate energy level test (b) shows evidence of both particulate and platelet debris.

Further work by Hutton et al. [34] confirmed that shear deformation is the main mechanism for the formation of friction films. Different fibre orientations at the surface were investigated and it was found that orientations parallel to the surface favour formation of a friction film due to easier shear deformation of the CVI matrix.

As well as the fibre orientation, the type of fibres within the carbon/carbon composite affects the transition between surface morphologies and therefore the friction performance of the composite. Hao et al. [35] carried out disc-on-disc tests simulating normal landing and rejected take-off conditions. Two different carbon/carbon materials were used and the hardness of each material was determined through nanoindentation tests. The composite containing PAN fibres was softer than the composite containing carbon fibre felts. The harder composite exhibited a less stable COF at higher energy loads and also showed a higher level of wear. It is thought that the harder fibres destroy the type III friction film whereas the softer PAN fibres deform more easily and contribute to the friction film.

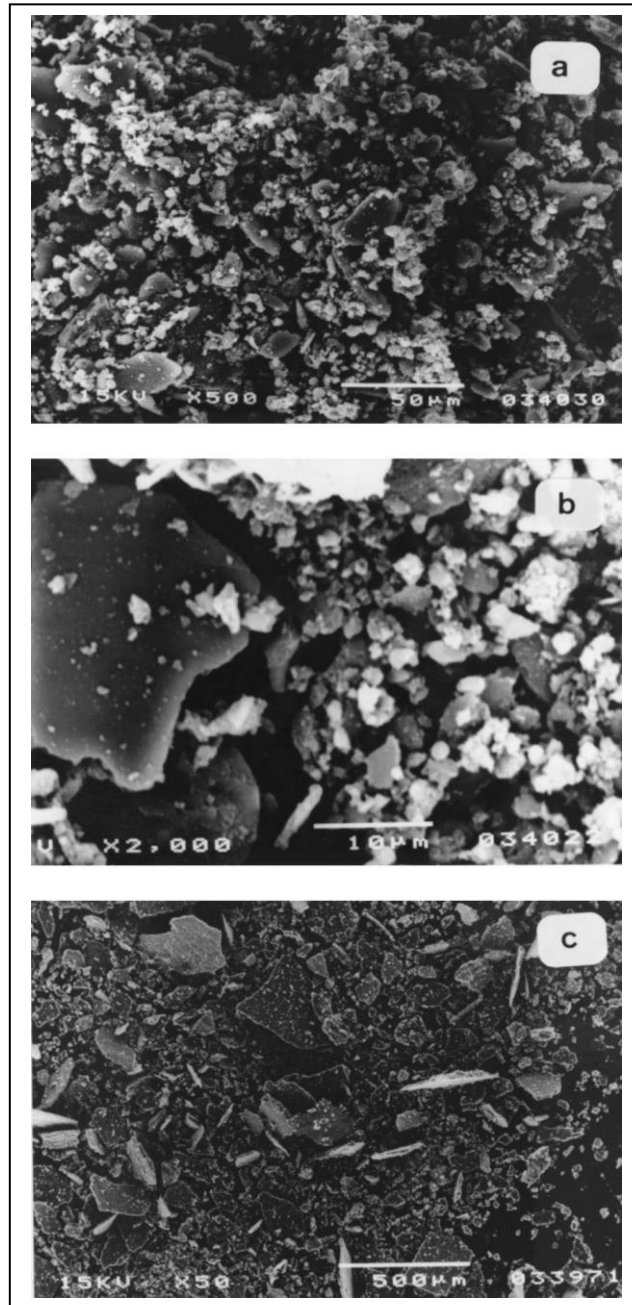


Figure 2.8 – SEM Images of Wear Debris from Dynamometer Tests Simulating (a) Taxiing Cycles, (b) Normal Landing Cycles and (c) Rejected Take-Off [33]

Francois et al. [36] examined wear debris from disc-on-disc tests simulating aircraft brakes under taxiing conditions. The investigation found that the wear debris from high energy tests consisted mainly of platelets (type III morphology) with some fibre fragments present. This result is consistent with the surface morphology evolution of carbon/carbon composites. It was found that the platelets were formed mostly at

high sliding speeds but not necessarily at high temperatures, suggesting that mechanical work is the main factor in forming type III morphology from type II morphology.

Lee et al. [27] investigated the effect of surface condition on tribological performance and found that bedded-in carbon/carbon brake discs always had higher COF than new discs during simulated braking tests. However, it is the result that was observed in relation to initial sliding speed that is more important to the present investigation. It was found that at low initial sliding speeds the COF remained almost constant with no transition occurring to a high COF. However, at higher initial sliding speeds, a transition did occur followed by a V-shaped variation in COF with a final rise as the sliding speed reached zero as shown in Figure 2.9. It was also found that wear was proportional to COF.

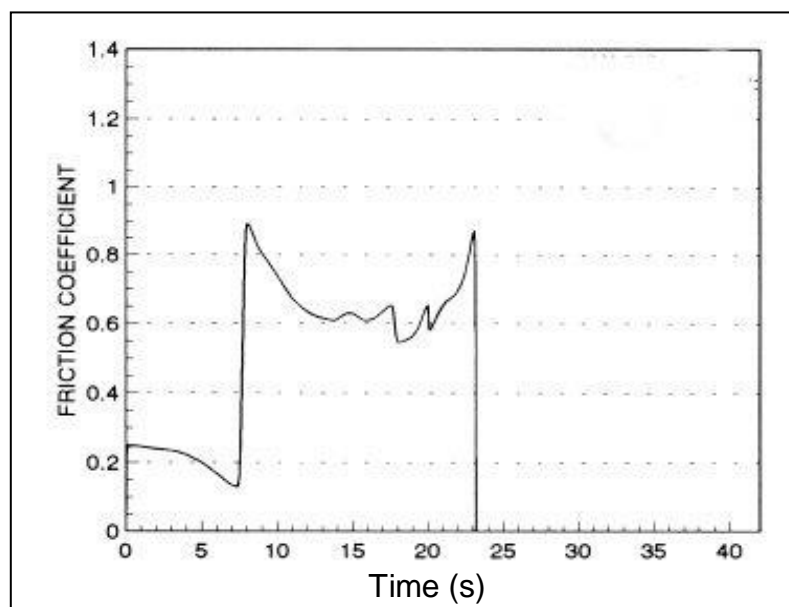


Figure 2.9 – COF Variation During Test for High Initial Sliding Speed [27]

Examination of the surfaces by Lee et al. [27] showed that initially small cracks and pores were present on the composite surface. After low speed sliding, the surface became smooth with the small pores filled with wear debris (type I morphology). After high speed sliding, the surface was covered with non-uniformly distributed rough, dark regions and smooth, light regions (type II and type III morphologies respectively). These three different surfaces are shown in Figure 2.10. Type III morphology is more lubricating than type II causing the fall in COF seen after the

initial transition and is formed by the compacting of type II debris. The formation of type III morphology from type II is in a constant state of formation, breaking down and re-forming which causes the V-shaped variation in COF observed. The final rise in COF is attributed to the low energy input being insufficient to maintain type III morphology and type II is formed again. This investigation showed that type III morphology cannot be formed without type II which in turn requires a minimum energy input to form from type I morphology.

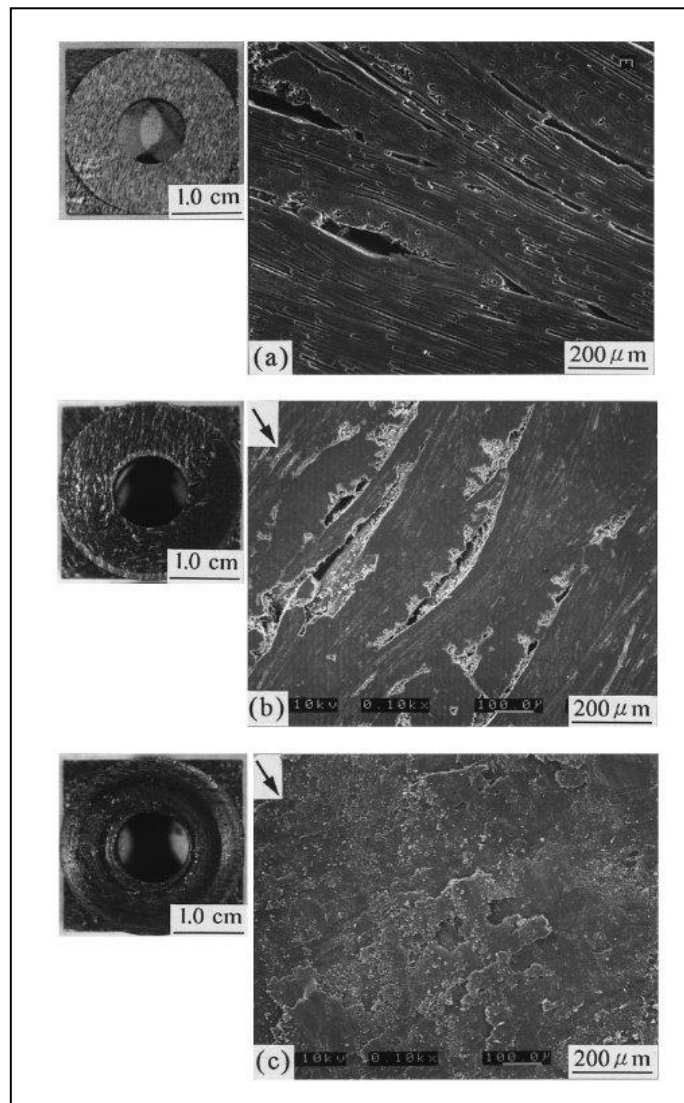


Figure 2.10 – SEM Micrographs of a Carbon/Carbon Brake Disc Showing (a) Initial Surface, (b) Type I Morphology and (c) Type II and Type III Morphology [27]

The observation that high energy levels are required for surface morphology changes is further corroborated by work carried out by Kasem et al. [25]. At low temperatures, type II morphology was observed whilst at high temperatures, type III was observed accompanied by a reduced wear rate.

As well as investigating the formation of surface morphologies, Kasem et al. [37, 38, 39] have also carried out work to investigate the wear mechanisms of carbon/carbon composites. They found that when tested at relatively low temperatures (when the COF is still high), abrasion causes scratches and grooves on the friction surface where the 3rd body particles trapped between the surfaces contribute to the wear. When tested at relatively high temperatures (when the COF has fallen), the surfaces are much smoother with shallow scratches and grooves. Micro-cracks lead to the detachment of small particles which are readily oxidised. They also found that at high temperatures, plastic deformation of the matrix surrounding the z-fibres can occur.

As discussed by Tanner et al. [40], the friction performance of carbon/carbon composites is affected by the environment within which they operate as the formation of surface morphologies is dependent upon ambient conditions. Krkoska et al. [30] investigated the effect of humidity on the frictional performance of these composites. High humidity led to no COF transition occurring at low energies but at higher energies, the COF transition was stronger and longer in duration. Also at high energy levels, wear decreased with increasing levels of humidity as observed by Chen et al. [28]. Low humidity accelerates the formation of type II debris as water desorption can occur more easily whilst high humidity levels increase the formation of type III morphology particularly at high speeds. This accounts for the reduced wear observed by Krkoska et al. [30] as type III morphology is more lubricative.

Yen et al. [26] carried out an investigation operating a carbon/carbon composite in dry nitrogen and in ambient air. It was found that in dry nitrogen, dusting wear (type I to type II morphology) occurs quicker due to the lack of lubricating vapour in the environment. In ambient air, dusting wear only occurs after the initial COF transition, once water has been desorbed from the surface. Once dusting wear has formed on the surface, the subsequent COF levels in ambient air were found to be lower than in dry nitrogen suggesting that oxygen in the air has a small lubricating effect. It is this self-lubricating effect that reduces the wear of carbon/carbon composites making them attractive as friction materials. This result is shown in Figure 2.11.

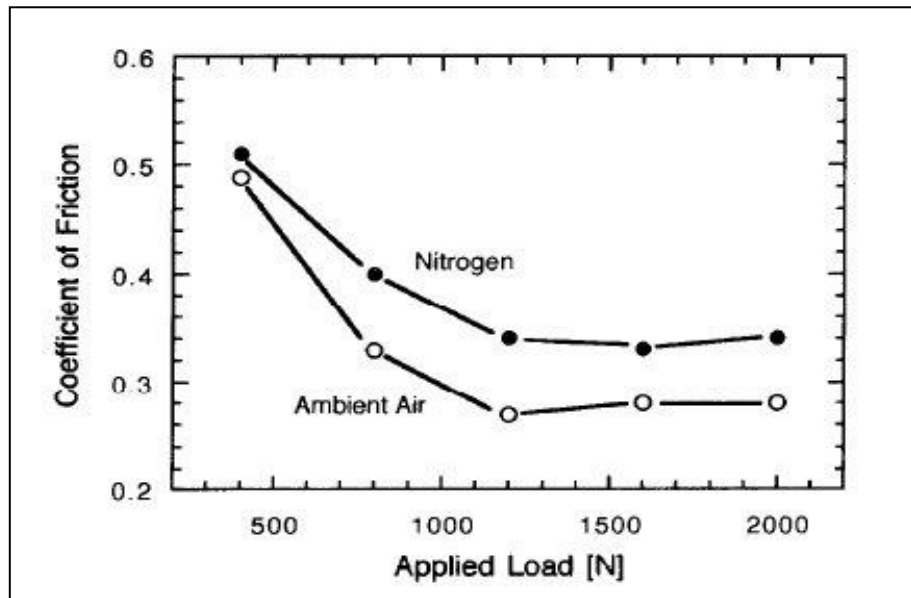


Figure 2.11 – Dusting Wear COF in Ambient Air and Dry Nitrogen [26]

Yen et al. [41] showed that oxygen in the environment can also have a detrimental effect on the wear of a carbon/carbon composite at very high energy input levels. A ring-on-ring test procedure was carried out at a range of applied loads and sliding speeds. Figure 2.12 shows the results from this experiment where three different loading cases have been investigated.

Type A loading shows the typical temperature and COF profiles expected. However, for Type B loading, which has a higher clamp load and hence higher energy input, a second COF transition is observed with a corresponding temperature increase. The second transition is attributed to oxidation which results in further dusting wear (type II morphology) to be formed causing an abrupt rise in COF and temperature. This is similar to dusting wear formed by water desorption at the first COF transition. To validate this theory, a thermogravimetric test was carried out to determine the critical temperature at which rapid oxidation occurs. The results shown in Figure 2.13 indicate that rapid oxidation occurs at around 650-700°C which corresponds to the temperature at the second transition shown for Type B loading in Figure 2.12. CO₂ was also detected in the test chamber at 700°C and above, confirming that oxidation was occurring.

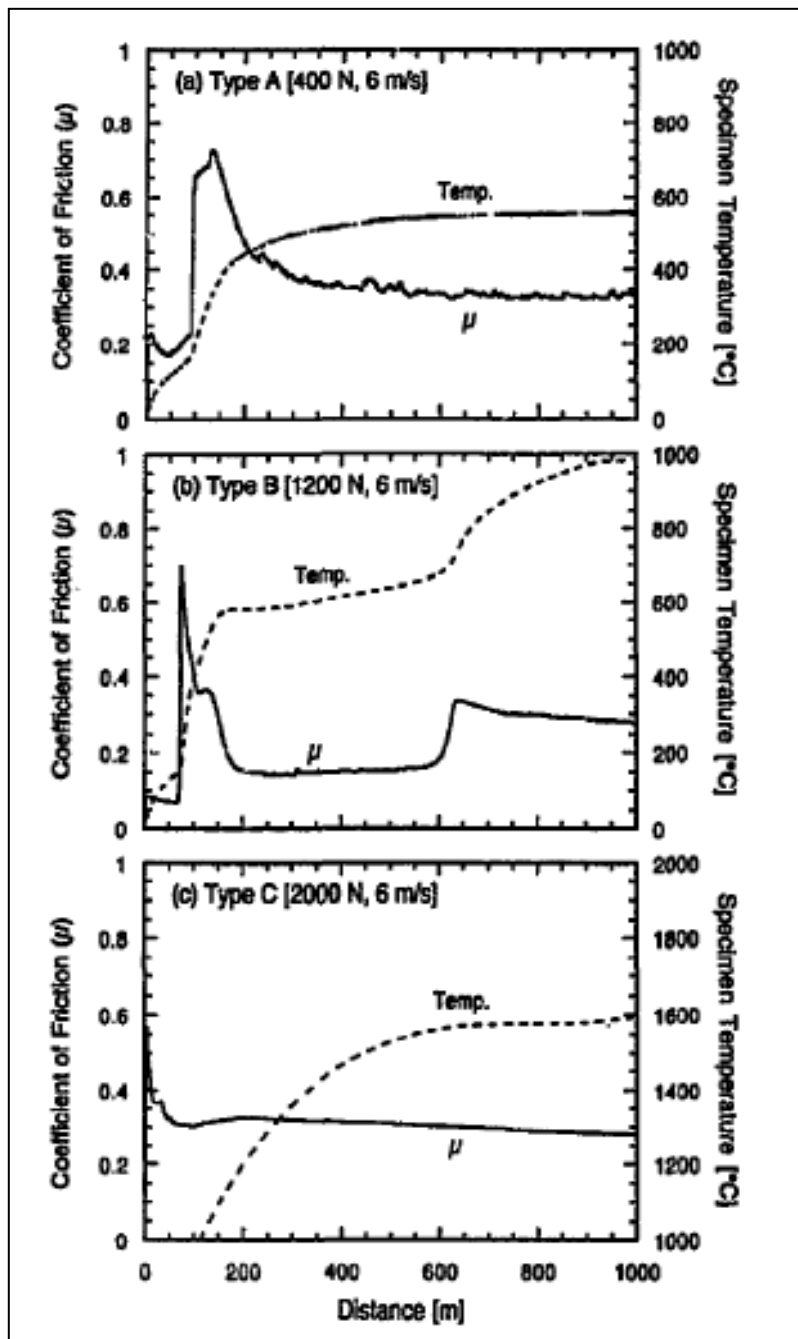


Figure 2.12 – Friction and Temperature Profiles as a Function of Sliding Distance for Different Load Levels [41]

The Type C loading profile shown in Figure 2.12 occurs for very high energy inputs where the level of energy input is so high that the first transition occurs very rapidly and the temperature increase is such that oxidation occurs immediately after the first transition. This effectively bypasses the regime between the two transitions seen in the Type B loading profile.

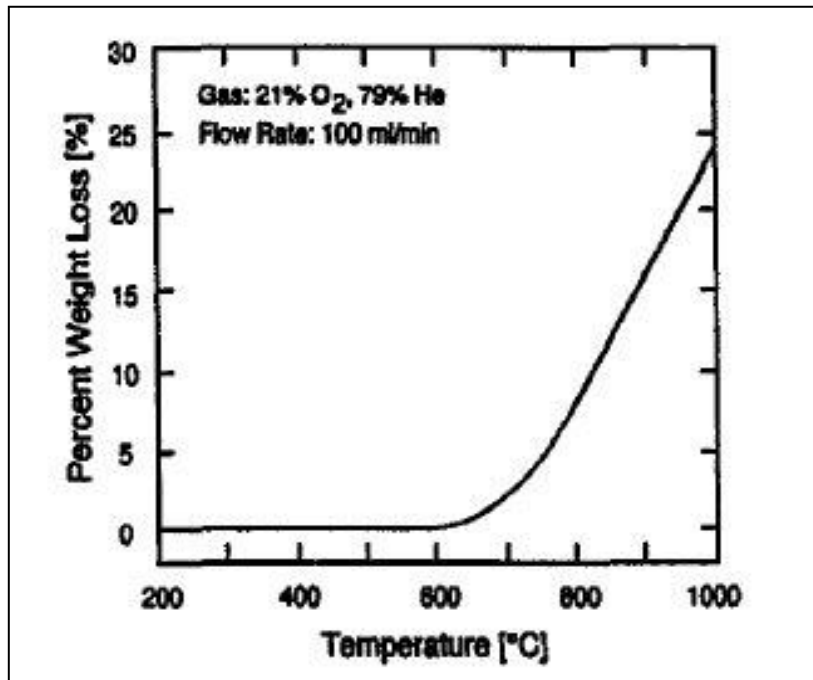


Figure 2.13 – Weight Loss of Carbon/Carbon Composite as a Function of Temperature in a Helium/Oxygen Gas Mixture [41]

Karmi [42] attempted to develop a numerical model to predict the COF during the transition from type I to type II morphology for an aircraft brake. By doing so it was hoped that the brake torque could be calculated and could then be used, in conjunction with the control systems, to achieve smooth braking during landing. Results from dynamometer tests were used to form an initial equation to calculate the COF based on pressure and temperature. The equation was validated against aircraft deceleration performance data and the integration constant of the equation was calculated so that the data fitted correctly. However, from test to test, the value of the integration constant had to be changed as the friction behaviour during the COF transition was inconsistent. This was attributed to the relationship between temperature and COF and the reciprocal effect these two factors have on each other.

2.7 Thermoelastic Instabilities

The phenomenon of thermoelastic instabilities (TEI) is well established as occurring in sliding contact applications. Barber [8] states that any irregularities on the contacting surfaces of sliding solids will cause a non-uniform pressure distribution. The heat input distribution will mirror the non-uniformity and lead to preferential thermal expansion in the area of high temperatures. The pressure will then increase in these areas, concentrating the heat input and causing further temperature increase and greater thermal expansion. The thermal distortion tends to exaggerate the original surface irregularities.

Barber [8] carried out a number of experiments to demonstrate TEI where a cast iron block on a load arm was pressed against a rotating mild steel wheel as shown in Figure 2.14a. The non-uniform heat input was apparent as red hot areas were seen on the sides of the block. These areas were transient, lasting only a few seconds. On the block, the areas of high temperature appeared as hot spots as the points of contact are stationary on the block. This spot corresponds to a specific radius on the outer face of the wheel which is constantly receiving a heat input as it rotates and hence the area of high temperature appeared as a circumferential hot band.

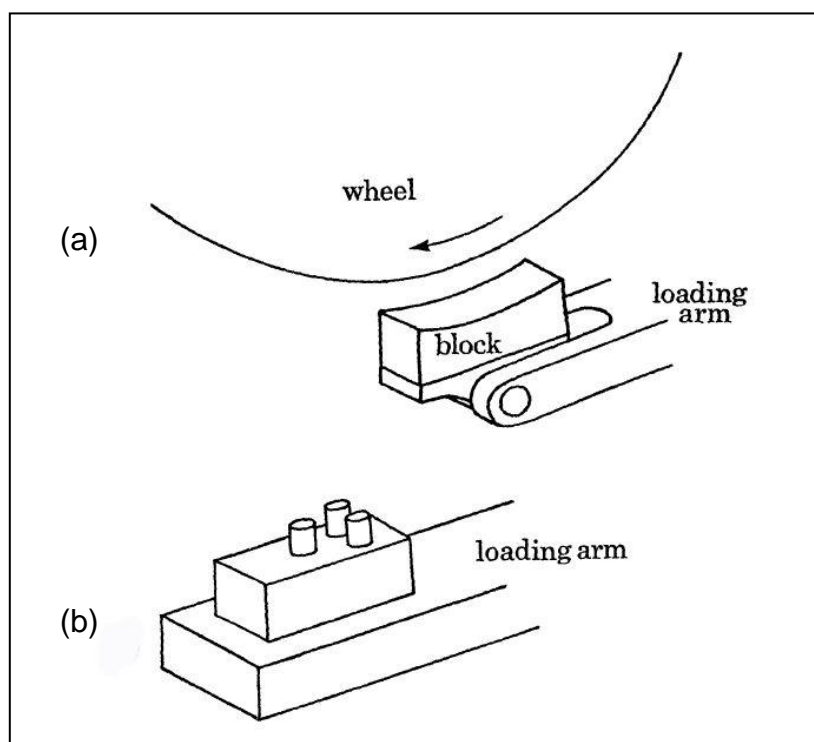


Figure 2.14 – Experimental Setup to Demonstrate and Investigate TEI [8]

Thermocouples were inserted into the block at four different positions (locations not provided in literature). The recorded temperatures remained largely stable except for small periods when the temperature at one thermocouple would suddenly rise before falling again. It was calculated that the peak temperatures could only arise if at least half of the total normal load was concentrated above that particular thermocouple.

It was noted that the time between temperature peaks at any particular thermocouple was relatively constant suggesting that the concentration of load is cyclic and once a point has been in contact, it remains out of contact until all other parts of the surface go through a period of load concentration. Measurement of the surface profile revealed surface recesses where high temperatures had been recorded immediately before the end of the experiment. When the normal load is concentrated due to a surface asperity, the thermal expansion at that point causes the surfaces to separate, exaggerating the effect. Contact only moves to a different area once that contact point has worn away and, in the absence of heat input due to contact loss, the area contracts as it cools leaving a surface recess.

An experimental verification of this theory was carried out using the experimental setup shown in Figure 2.14b. Three cast iron pins were placed on the block with thermocouples inserted into them. This system is comparable to a block of large nominal area with contact localised to three small circular areas. The recorded temperatures showed that contact was isolated to one pin for a period of time before very quickly moving to another which sustained contact for a similar period of time. The contact order was a function of the original pin heights.

To confirm that this behaviour was due to TEI, the separation of the surfaces was measured and showed an initial separation as contact was established at a new point which then fell away as the wear rate became greater than the rate of thermal expansion as shown in Figure 2.15.

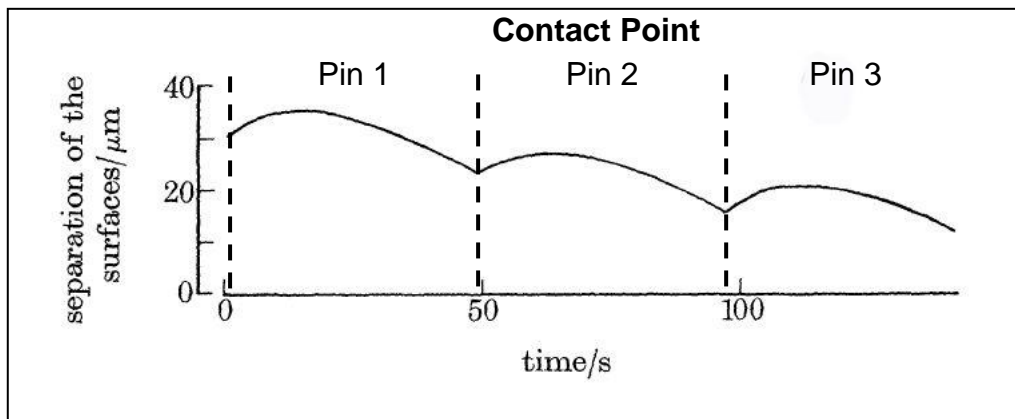


Figure 2.15 – Surface Separation During TEI Experiment [8]

A computational model was developed to simulate this phenomenon, the results of which showed that even a 1nm height difference between the pins, causing less than 0.1% difference in normal load between the pins, would be enough to initiate TEI.

Thureson [43] developed a 2D finite element model to establish the effect of the material properties on the extent of TEI. The model consisted of a simple block in contact with a rigid foundation. Figure 2.16 shows the results of the contact pressure results for the initial non-wear model. It can clearly be seen that as the simulation time progresses, TEI causes contact localisation to occur leading to high localised contact pressures.

Thureson [43] found that a material with a lower Young's modulus leads to lower contact pressures but also noted that the practical disadvantage of this could be that the softer material wears away unacceptably quickly. The simulations also showed that if the wear rate is low, thermal expansion becomes dominant and leads to higher localised contact pressure as the block 'rides' on a small number of contact areas. A high wear rate results in a smoother contact pressure distribution as material subject to large thermal expansion is worn away as the temperature increases.

A similar result regarding the material stiffness was reported by Vernersson et al. [44] where a fully coupled temperature-displacement analysis was carried out using Abaqus to simulate railway brakes under repeated braking cycles. Vernersson et al. simulated a range of elastic moduli and found that for the lowest material stiffness, TEI was negligible.

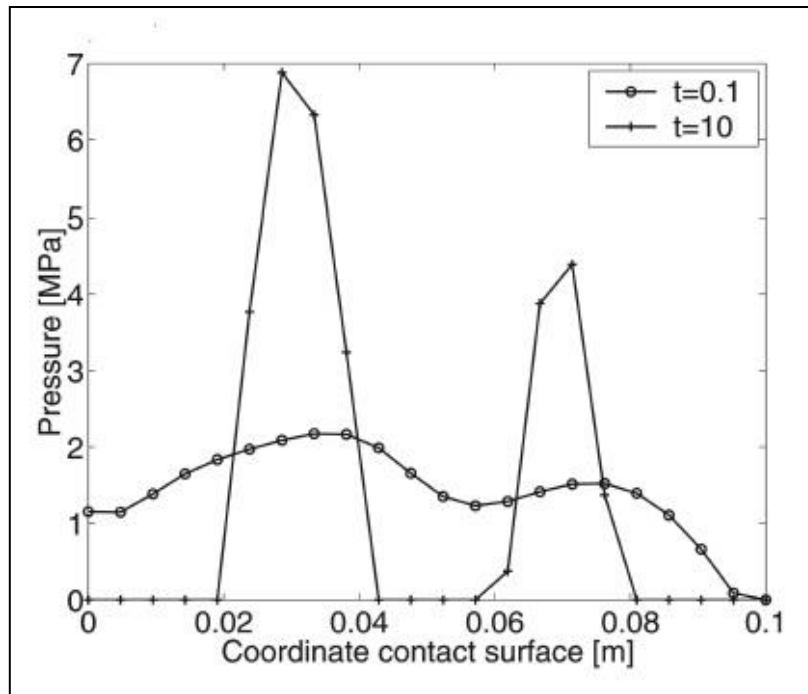


Figure 2.16 – Contact Pressure Distribution Predicted by Non-Wear FE Model [43]

Graf et al. [45] used numerical models in order to carry out a parametric study of an automotive brake friction pair and identify potential strategies for limiting TEI. It was predicted that reducing the stiffness of the brake pad and backing plate would reduce TEI whilst changing the thermal properties of the brake disc could also offer improvements. Cooling makes very little difference but the geometry of the sliding path and contact area have a strong potential for optimisation.

Not only is TEI important from a friction performance point of view, it is also of great significance from the perspective of safety. Day et al. [46, 47] discuss that for cast iron brake rotors, TEI can lead to plastic deformation and also result in the formation of cracks. In the area of the hot spot or hot band, the cast iron material may cool so quickly after the braking event that martensite may form. As martensite occupies a larger volume than pearlitic cast iron, cracks may initiate around the martensite. Day et al. also noted that hot spots can often be regularly spaced. On drum brakes, hot spots have been observed to follow the pattern of rivet holes whilst for brake rotors, the fit on the brake rotor hub can affect rotor expansion causing the brake rotor to distort. A regular hot spot pattern may form, where the pattern is dependent on the fit of the rotor and hub. It is therefore not only important to have a well machined friction surface to limit TEI but aspects of the friction-pair system must also be considered.

Barber [8] showed that even a surface height difference as small as 1nm can initiate TEI. However, work carried out by Zhao et al.[13], Zagrodzki [15], and Abdullah et al. [17,18] predicted contact localisation and high localised temperatures even though the friction surfaces were modelled as initially perfectly flat. This is because a surface height difference was effectively induced as the clutch engagement progressed. Very early in the engagement, the clutch plates expanded radially and contact was lost at the inner and outer radii. This established a non-uniform contact pressure distribution analogous to a non-flat friction surface thus initiating TEI and the temperature and contact pressure profiles shown in Figures 2.3 and 2.4 arose. These profiles were steady-state as wear was not included in the models so no contact point migration occurred as thermal expansion was completely dominant.

2.8 Summary

The process of manufacturing carbon/carbon materials is a lengthy one, requiring large amounts of energy which results in carbon/carbon composites being very expensive. These two factors go some way to explaining why published research regarding these materials is limited

The trends in surface COF of carbon/carbon composites has however been well documented as well as the fact that the formation and transitions of surface morphologies (and hence COF) are affected by many factors including mechanical, thermal and environmental effects. Accurate prediction of the frictional behaviour has therefore proved difficult with the added complication that carbon/carbon materials can vary greatly in their composition and can be highly heterogeneous.

Numerical models and finite element analyses have also shown that, because carbon/carbon friction materials are often used in high energy applications, thermoelastic instabilities can have a significant impact on the thermal performance of the material. This of course will affect the surface morphology of the friction surface and affect the COF levels thus influencing the friction performance.

It has been shown that TEI arises in sliding contact to different extents dependent on material and system properties. The contact localisation resulting from TEI means that the actual contact area is less than the nominal area and this must be taken into account when developing a friction material and associated system components.

3. Design of Single Clutch-Plate Interface Dynamometer (SCID)

3.1 Introduction

A single clutch-plate interface dynamometer (SCID) has been designed and commissioned to facilitate testing of the friction performance of a number of clutch plate pairs. The SCID replicates race-start conditions in the laboratory where the temperature of the rotating clutch plate friction surface and torque output of the clutch plates during an engagement are measured and recorded to assess the friction and thermal performance of the clutch-plate pairs..

3.2 The Need for an In-House Dynamometer

The F1 team, for whom the clutch plates are being investigated, offered access to their full-scale dynamometer if required but it was decided that an in-house dynamometer would be the best option for two reasons:

1. It allows the friction performance of a single clutch-plate pair to be investigated.
2. The in-house dynamometer can be used locally at the convenience of the user who has control of procedures and inputs and also has immediate access to results.

The first reason is fundamental to this study in that an attempt was being made to understand the clutch-plate behaviour at the clutch-plate interface. The dynamometer that the F1 team has developed does not allow testing of a single clutch-plate pair but instead the whole clutch-plate pack has to be used. When the whole pack is used, it is impossible to ascertain what is occurring at each clutch-plate interface as the torque produced is an amalgamation of the torque produced at each interface. It is also difficult to take temperature measurements of the clutch-plate pairs in the middle of the pack so little understanding can be gained for those clutch-plate pairs. Developing a single clutch-plate interface dynamometer allows a

single interface to be carefully investigated and simplifies the practical issues involved in measuring the clutch-plate temperatures.

The second reason greatly reduces the time between a decision being made as to what tests should be carried out and getting the results from these tests. If the F1 dynamometer was used, it could potentially be a long time between sending a request and receiving the results. The request would first need to be approved before a time slot was booked for using the dynamometer to carry out the tests. There could also be potential issues regarding the release and transfer of data and intellectual property. A dedicated in-house dynamometer negates these potential issues.

Bearing these issues in mind, it was decided that the benefits of developing an in-house dynamometer outweighed the time and financial costs of designing, manufacturing and commissioning the SCID.

3.3 SCID Design Parameters

Table 3.1 lists the range of values that the SCID had to be capable of achieving in order to replicate race start conditions. These values have been taken from previous work carried out by the F1 team [7] (see Chapter 1.2):

Race Start Parameter	Range
Engine Rotational Speed	8000-10000rpm
Clamp Load	1000-1400N
Typical Energy Dissipation per Clutch-Plate Interface	13.75kJ (at 10000rpm)

Table 3.1 – Range of Race Start Parameters [7]

As there are a total of eight clutch-plate interfaces in the complete clutch assembly, the value stated in Table 3.1 equates to a total of 110kJ of energy dissipated by the full clutch-plate pack (same total energy level as previous dynamometer tests [7]).

The overall component design and layout of the SCID was dictated by the parameters listed in Table 3.1. The overall layout was subject mainly to the need to

utilise equipment used on existing rigs in order to minimise costs and time in developing new hardware and software. The design of components for the SCID required careful consideration to ensure that they were strong enough to withstand the large static and dynamic loads they will carry. Consideration of how the SCID would be assembled and operated also influenced both the layout and component design.

3.4 SCID Layout

The overall layout of the SCID is shown in Figures 3.1 and 3.2. Due to limited resources, several parts of the SCID have been a compromise in order to reduce costs by utilising existing resources:

1. A spare 2kW electric motor has been incorporated into the SCID rather than purchasing a new bespoke electric motor. The electric motor has a maximum operating speed of 4000rpm requiring pulleys and friction belts to achieve the required maximum clutch plate rotational speed of 10000rpm.
2. The SCID was originally designed based on the use of an electric motor with a maximum output speed of 1700rpm. Due to the size of commercially available pulleys, the required speed ratio could not be achieved in one stage using this motor. The maximum achievable ratio was 5:1 resulting in a maximum clutch-plate rotating speed of 8500rpm. A second stage of speed increase was therefore required, achieved through the use of an intermediate shaft. Problems with the original electric motor meant that the electric motor detailed above had to be used instead. The required speed ratio could be achieved in one stage using the alternative motor but the SCID components had already been manufactured so the original layout was retained, with the electric motor assembly being modified to allow the alternative motor to be mounted on the existing components.
3. It became clear as the design developed that the table being used was not long enough to mount all components on so an aluminium base plate was

mounted on the table and all SCID assemblies were mounted on the base plate. Although this increased costs, it provided two advantages. All holes for mounting components could be drilled during the plate manufacture rather than by hand during assembly in the lab and it provided a flat, machined surface upon which to mount the components.

4. A mini-electromagnetic (EM) clutch has been included in order to decouple the inertia of the driving shaft, intermediate shaft and electric motor assembly from the main shaft inertia when the clutch plates are engaged. By decoupling the main shaft from the preceding assemblies, only the energy stored in the main shaft assembly inertia is dissipated at the clutch plate interface. As the main shaft assembly is an original design within this investigation, its inertia value is known and hence the energy stored at any rotational speed can be calculated. The mini-EM clutch is controlled by a 24V DC power supply. When a current is supplied to the mini-EM clutch, a magnetic field is created pulling the armature plate at the front of the armature into contact with the rotor to couple the clutch. When the current is switched off, a spring in the armature pulls the armature plate back, decoupling the mini-EM clutch
5. The clutch basket and clutch hub supplied by the F1 team have been utilised in the SCID. As opposed to their operation within the vehicle during a race start, the clutch basket and driving clutch plate (mounted on the end of the sleeve assembly) remain stationary whilst the clutch hub and driven plate (mounted on the end of main shaft) rotate.
6. A 5kN tension/compression load cell mounted between the lever arm assembly and sleeve assembly is used to measure the clamp load applied to the clutch plates.
7. A $\text{Ø}12\text{mm}$ hole has been machined through the clutch basket, clutch plate spacer and stationary clutch plate to allow the friction surface of the rotating clutch to be viewed using a thermal imaging camera (discussed further in Chapter 4). The use of an infrared (IR) mirror is required as a direct line of sight between the thermal imaging camera and back of the clutch basket is

not available. The IR mirror can be retracted away from the main assembly along its aluminium base to allow removal and replacement of the clutch plates.

8. As a linear electric actuator had already been purchased for use on other dynamometers, it was decided that this actuator could be shared between applications. The limitation of using this actuator is that it has a maximum output force of 500N hence a lever arm has been incorporated in order to scale-up the output force. The lever arm has a force ratio of 5:1 chosen so that the actuator is operated well below its maximum output force leaving spare capacity to run high clamp load tests should they become relevant. The length of the base plate (which was manufactured externally) was significantly reduced as the electric actuator no longer needed to be mounted on the base plate and could instead be housed underneath the table. The actuator is powered by a 24V DC power supply resulting in a maximum output force of 500N at 5A. The actuator is an ACME screw type requiring 767 pulses per 100mm of stroke. The positional resolution of the push rod is therefore 0.130mm. The push rod has a travelling speed of 53-30mm/s linearly varying from 0-500N.

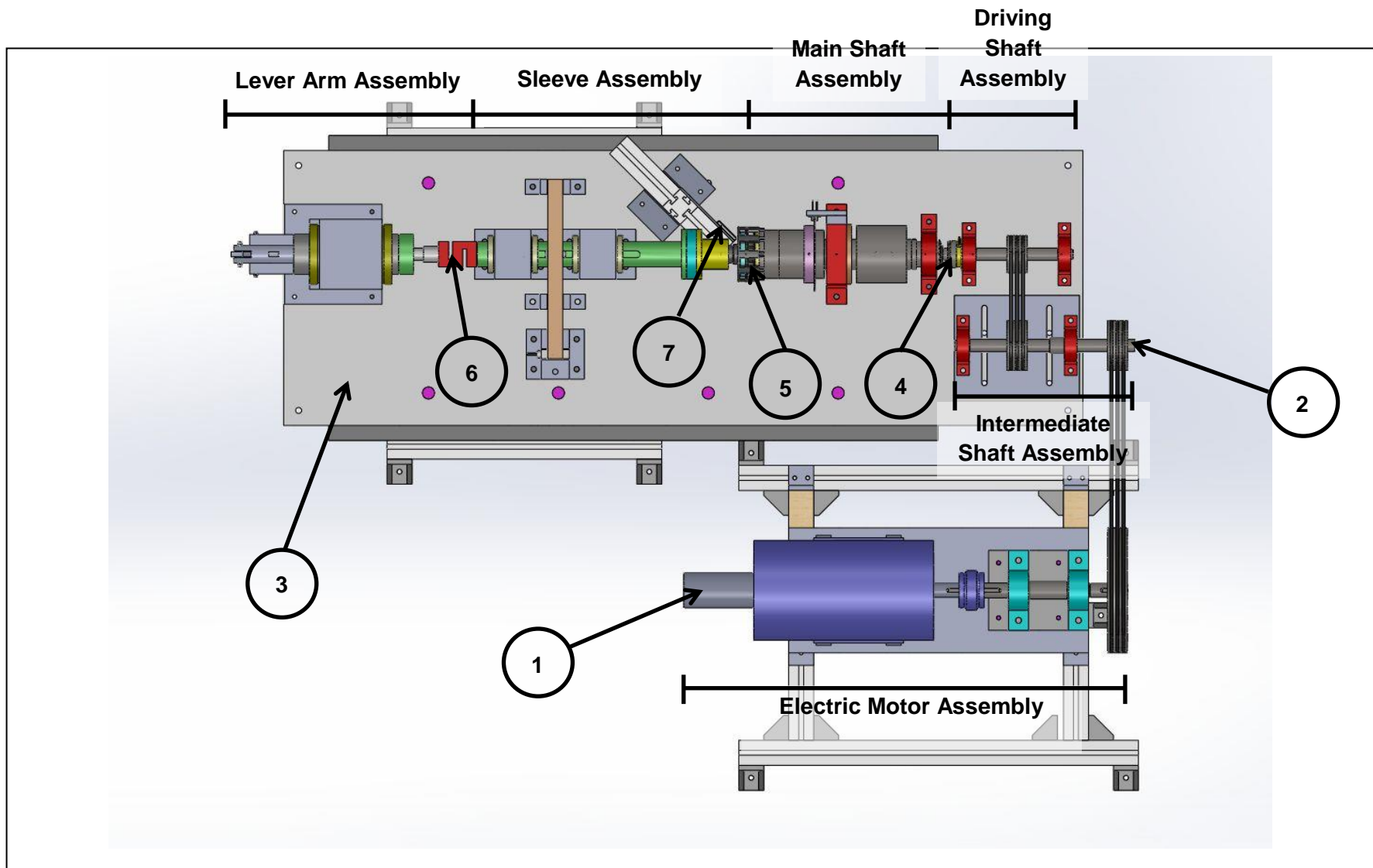


Figure 3.1 – Plan View of SCID

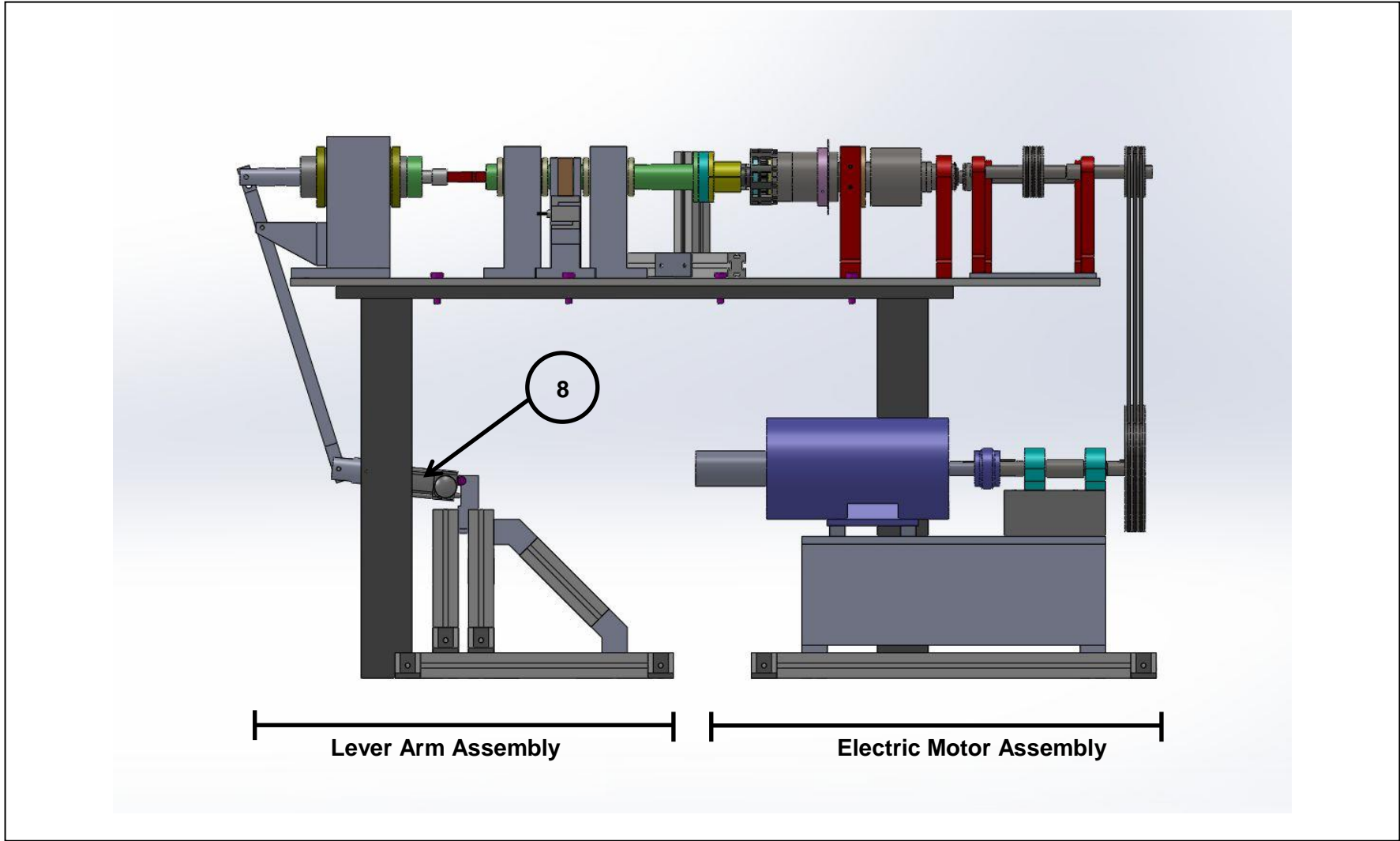


Figure 3.2 – Side View of SCID

3.4.1 Electric Motor Assembly

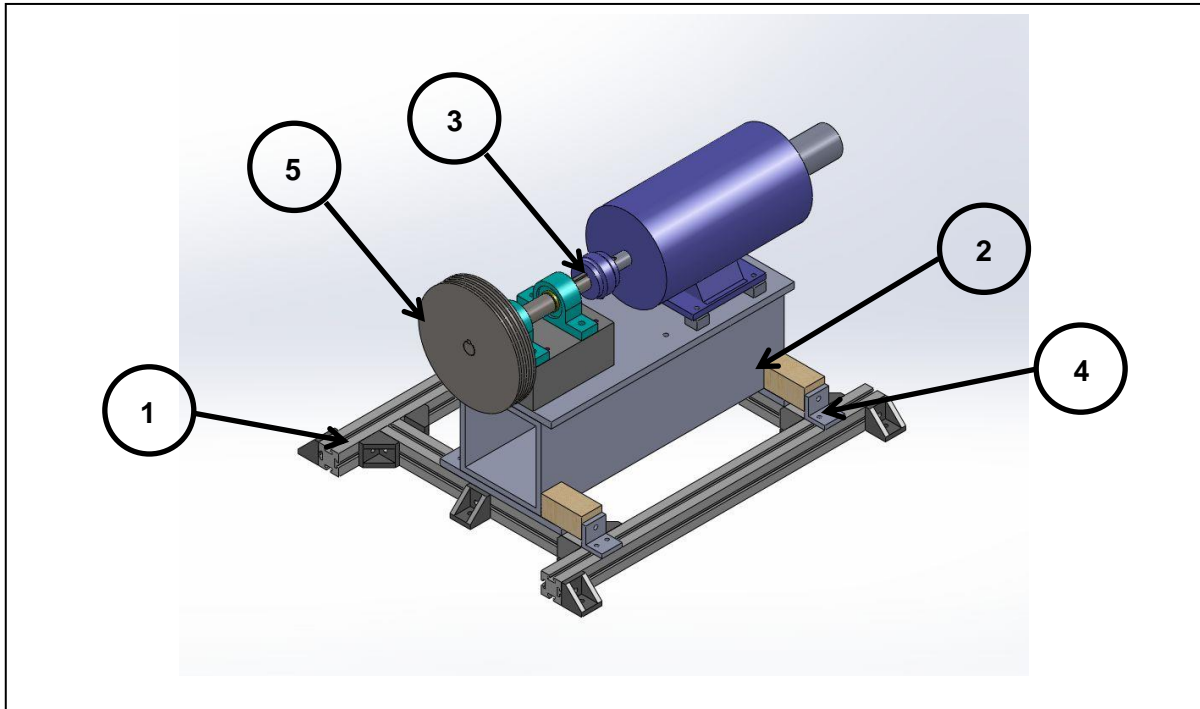


Figure 3.3 – Electric Motor Assembly

1. The electric motor assembly is mounted on an aluminium frame constructed from Bosch Rexroth struts which have been salvaged from old test rigs. The frame is easily assembled and adjusted. The frame is bolted to the laboratory floor via the angle brackets located around the aluminium frame.
2. Using the original electric motor, a 500mm diameter pulley was required to achieve the desired speed ratio. The centre height of the axis of rotation had to be raised to allow sufficient ground clearance for the pulley. The electric motor is therefore mounted on a box section which in turn is bolted on to the aluminium frame.
3. The pulley is not mounted directly on to the electric motor output shaft in order to eliminate applying large radial loads to the motor bearings which could affect its performance. A shaft supported by two bearings has been placed between the electric motor and pulley and these bearings react the weight of the pulley. The two shafts are connected using a taper lock coupling.

4. The friction belts are tensioned by pushing the box section sideways on the aluminium frame. The tensioner blocks shown have two threaded holes through their vertical face. Two M10 bolts are then used to push the wooden blocks, pushing the box section along.
5. For the original electric motor, a 500mm pulley was used but as the alternative electric motor has a greater speed capacity, a smaller pulley has been used in the final SCID layout. An overall speed ratio of 3.33:1 is achieved so that the maximum speed at which the electric motor has to operate is 3000rpm which is well below its maximum of 4000rpm.

3.4.2 Intermediate Shaft Assembly

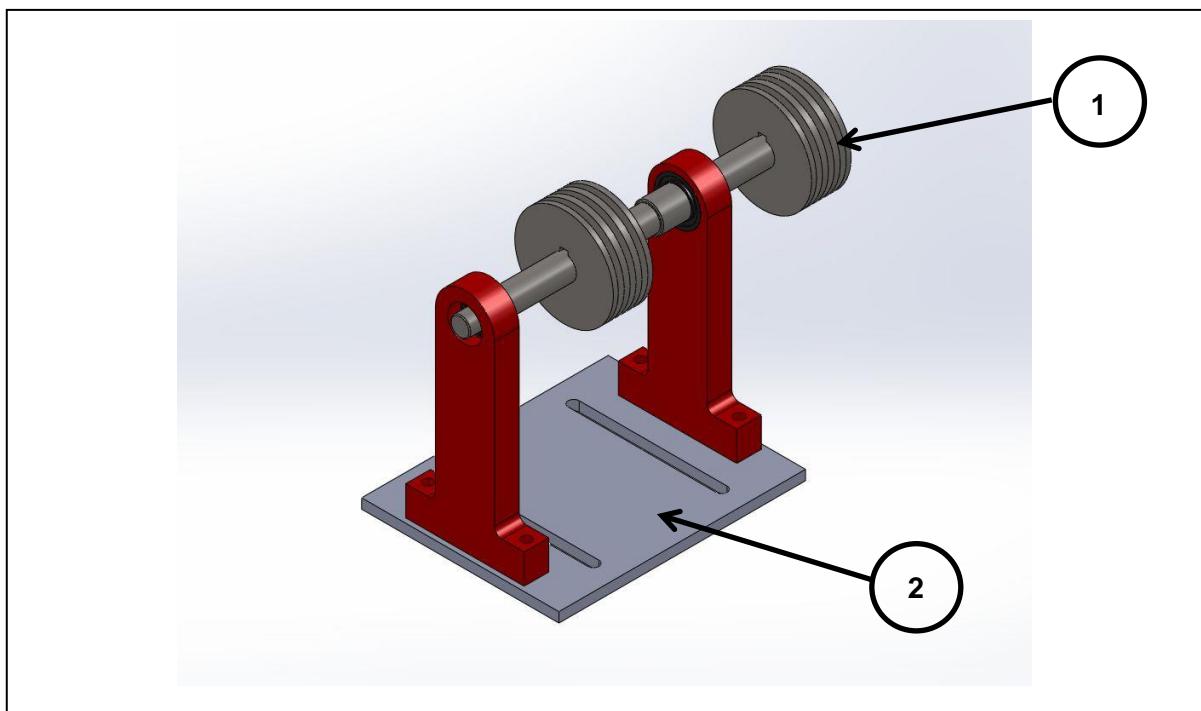


Figure 3.4 – Intermediate Shaft Assembly

1. The pulley at the end of the shaft overhangs the table so that the friction belts connecting this pulley to the electric motor pulley cannot touch the table. The assembly has been positioned as close as possible to the end of the table/base plate in order to reduce the length of the overhang and consequently the amount of deflection caused by the pulley. The shaft critical

speed is therefore higher for any given shaft diameter allowing the shaft diameter to be kept to a minimum.

2. The bearing housings are not bolted directly to the base plate but are instead bolted on to an intermediate base plate which is then bolted to the main base plate. The slots in the intermediate base plate allow the assembly to be moved sideways to tension the friction belts before the assembly is bolted down.

3.4.3 Driving Shaft Assembly

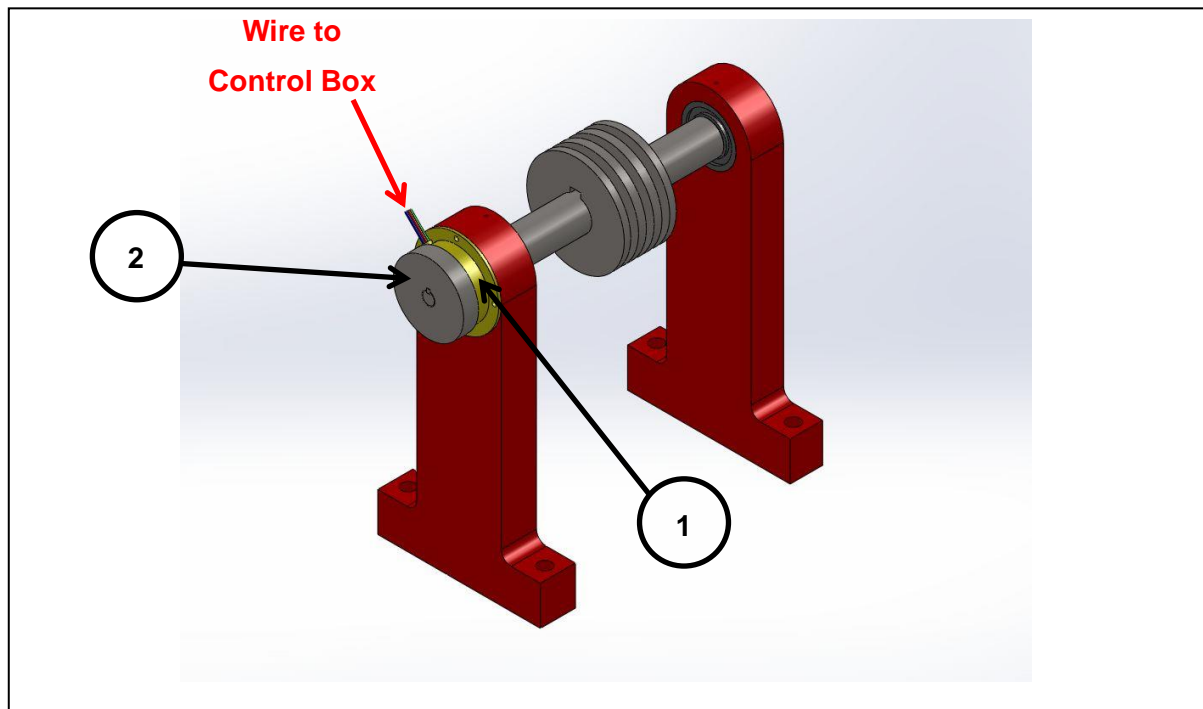


Figure 3.5 – Driving Shaft Assembly

1. The stator of the mini-EM clutch is bolted directly to the bearing housing and does not rotate with the shaft. The stator receives current from the power supply and creates the magnetic field required to engage the clutch.
2. The rotor of the mini-EM clutch is mounted on the end of the driving shaft and rotates with the shaft. Torque (up to 3.6Nm) is transmitted via a key and keyway.

3.4.4 Main Shaft Assembly

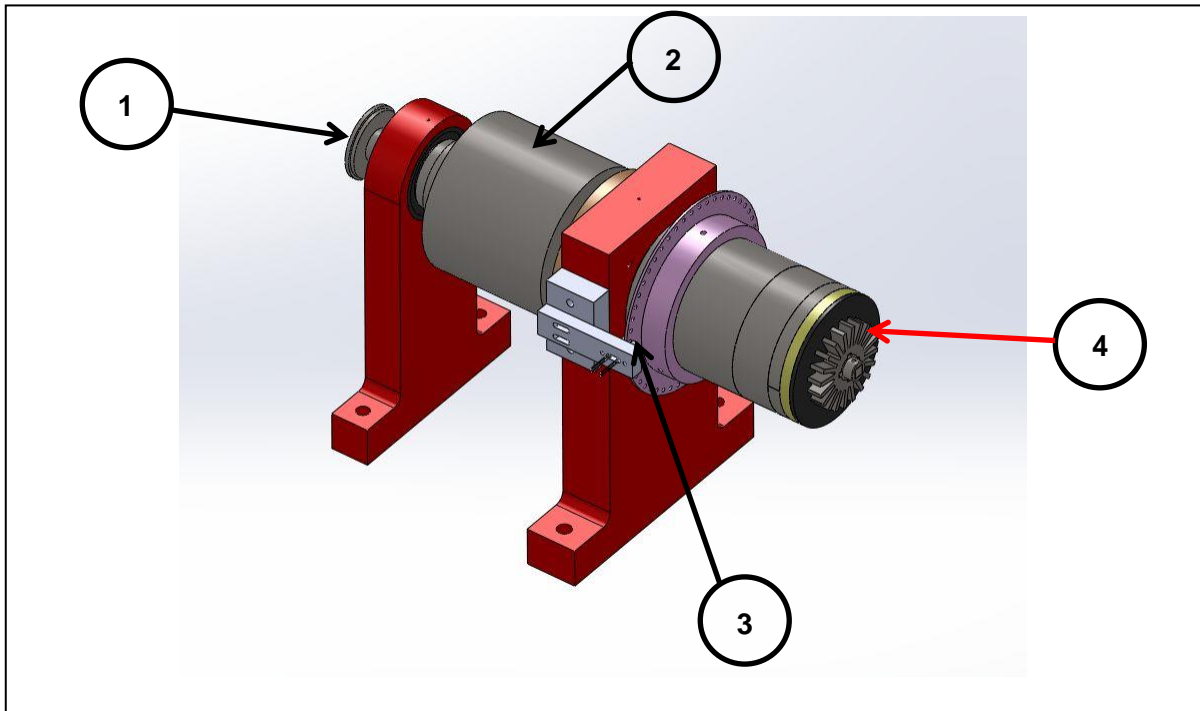


Figure 3.6 – Main Shaft Assembly

1. The armature of the mini-EM clutch is attached to the end of the main shaft and torque is transmitted via a key and keyway. Axial location is achieved through the use of a grub screw and a flat on the main shaft. This allows the axial location of the armature to be adjusted in order to set the required 0.2mm air gap between the rotor and armature.
2. The flywheel was sized such that its inertia, combined with that of the other rotating parts of the main shaft assembly, stores the required level of energy to be dissipated at the clutch-plate interface according to Equation 3.1.

$$KE = \frac{I\omega^2}{2} \quad (3.1)$$

Where: KE – Kinetic Energy (J)

I – Inertia (kgm^2)

ω – Rotational Speed (rads^{-1})

The flywheel is circumferentially constrained via two keys and keyways and axially constrained by the two bearings which are axially constrained by either their bearing housing or a lock nut.

3. The rotational speed of the main shaft is measured through the use of an infrared photoemitter and an encoder ring with a series of regularly spaced holes at a constant pitch circle diameter. The infrared photoemitter outputs a voltage only if the infrared light from the emitter reaches the detector. The shaft encoder ring is therefore placed in the 3mm gap between the emitter and detector. As the main shaft and shaft encoder ring rotate (constrained using grub screws), the detector outputs a voltage if a hole in the encoder ring passes through the photoemitter and emits no voltage if a solid section of the encoder ring passes through the photoemitter. A square waveform output voltage is thus established and by measuring the time between the leading edges of the pulses, the rotational speed of the shaft can be calculated.
4. The driven clutch plate (rotating in the SCID) is mounted on the clutch hub (see Chapter 1.2) which is mounted onto the main shaft via an intermediate splined component as the main shaft itself could not have a splined end due to manufacturing limitations. The end of the main shaft has a square profile on to which a specially manufactured component mates. This component has a spline profile on its outer circumference on to which the clutch hub is mounted. The circular cross-section length at the end of the intermediate component locates inside a bearing in the clutch basket.

3.4.5 Sleeve Assembly

1. The driving plate (stationary in the SCID) is mounted in the clutch basket. The clutch basket has a splined hole at its rear and is connected to the sleeve via a shaft with a splined section on its end that mates with the clutch basket and two keys and keyways that mate with the sleeve. The end of the main shaft mates with a small bearing inserted into the clutch basket to ensure concentricity between the clutch plates.

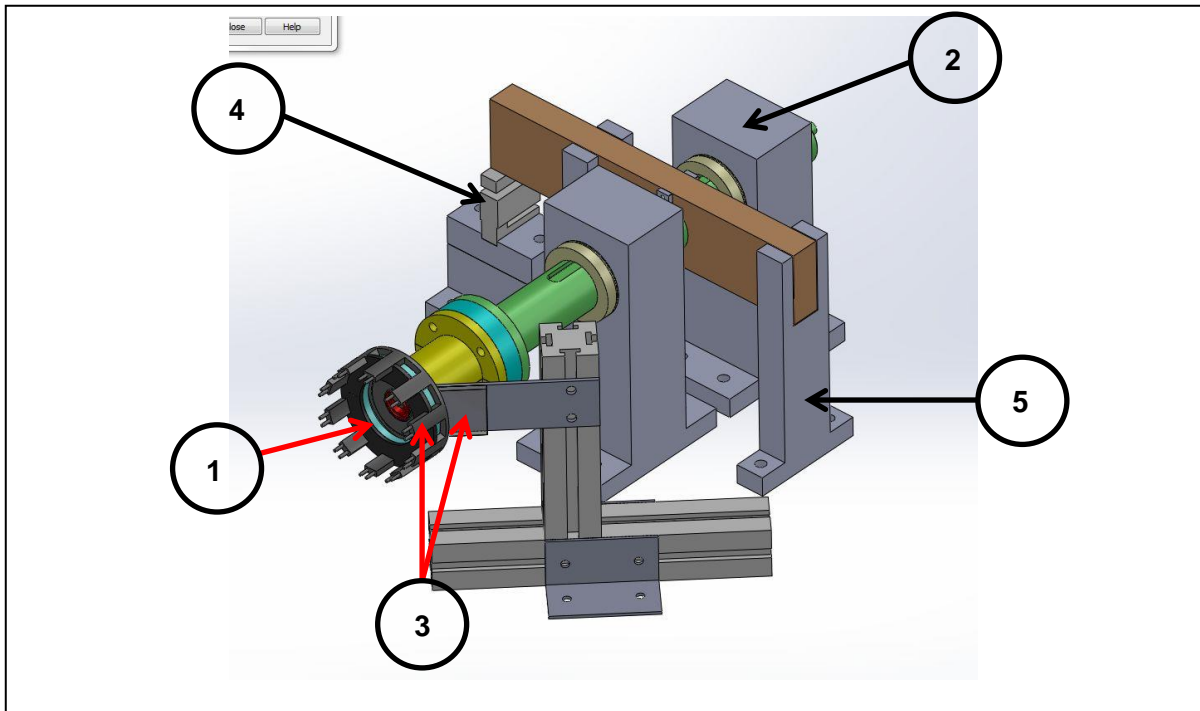


Figure 3.7 – Sleeve Assembly

2. The sleeve is located in two linear bearings which allow the sleeve, and hence clutch basket, to be retracted in order to remove and replace the clutch plate. The clutch plates are then engaged by pushing the assembly on to the end of the main shaft.

3. An IR mirror set at 45° to the back of the clutch basket allows a thermal imaging camera to view the friction surface of the rotating clutch plate via a $\text{Ø}12\text{mm}$ hole drilled through the stationary clutch plate, clutch-plate spacer and clutch basket. The setup of the thermal camera is discussed in Chapter 4.3.

4. When the clutch plates are engaged, the torque generated is transmitted via the clutch basket to the sleeve. The sleeve will then try to rotate. The torque arm (coloured brown) rotates with the sleeve but only rotates slightly before coming into contact with the 30kg load cell. Torque is transmitted from the sleeve to the torque arm via keys and keyways and this torque can be calculated from the product of the normal load measured by the load cell and the distance from the radial centre of the sleeve to the load cell contact point.

5. Two backlash stops are used to prevent the torque arm from moving axially when the sleeve is retracted or pushed forward. The two stops prevent the torque arm from twisting around the vertical axis so that the sleeve can travel smoothly without becoming stuck. The backlash stop on the opposite side to the load cell also prevents the torque arm from swinging back excessively when the clutch-plate engagement is complete and torque ceases to be generated.

3.4.6 Lever Arm Assembly

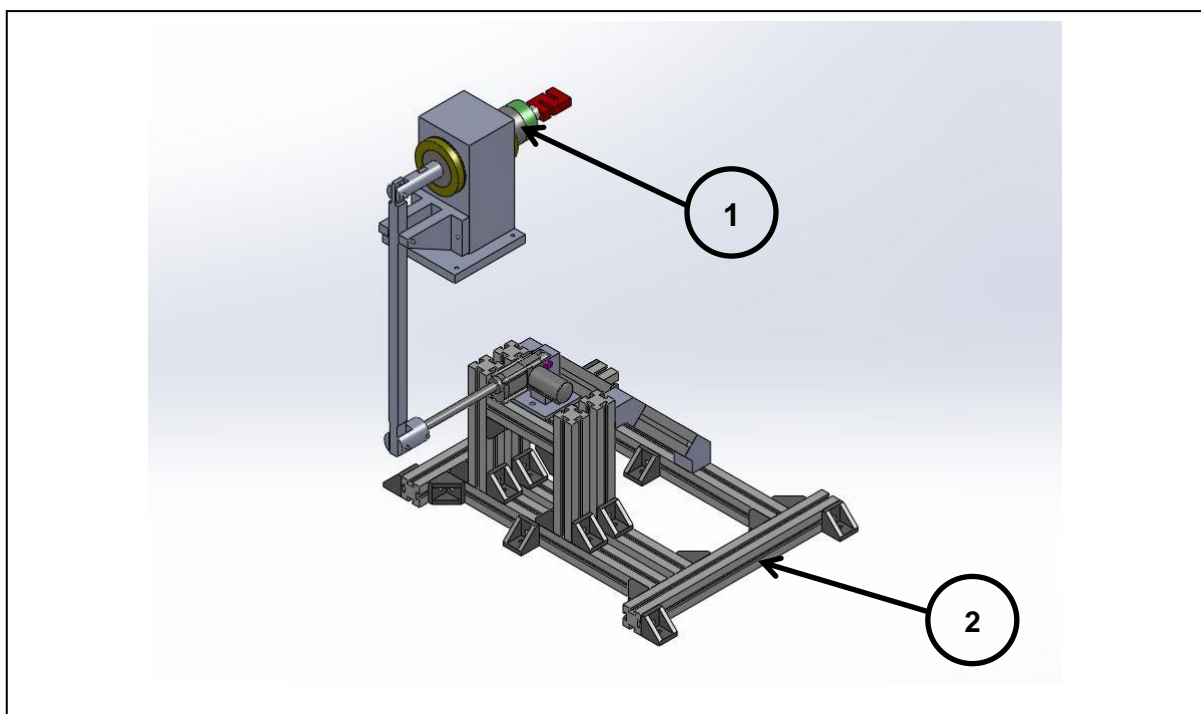


Figure 3.8 – Lever Arm Assembly

1. The load cell measuring the clamp load is fastened to a push rod via a threaded section on the end of the push rod. The push rod sits within a cylindrical component that runs in a linear bearing. Within the cylinder is a compression spring which contacts with the push rod and the spring is compressed when the actuation force (clamp load) is applied. The spring has been included to smooth any actuation force fluctuations that may occur.

2. As with the electric motor assembly, the actuator is mounted on an aluminium strut frame with the frame bolted to the laboratory floor. The use of the frame was necessary as the actuator needs to be mounted at a height above the floor due to the length of the lever arm.

3.5 Design Process

As the SCID consists of both rotating and non-rotating components, two different design processes were required for the two types of component. The non-rotating components, such as bearing housings, are subject to loads causing bending or shear stress or a combination of both. The rotating components, such as power transmission shafts, are subject to the same loading considerations as that of the non-rotating components but as the components are rotating, the stress of the components fluctuates, resulting in cyclic loading. Ensuring that the rotating parts are designed to prevent fatigue failure due to cyclic loading is important from a practical perspective but is critical from a safety standpoint. Failure of the rotating components (some of which may rotate at up to 10000rpm) could have catastrophic consequences. Full consideration of safety was taken into account when designing the SCID components.

Although the SCID's initial use is to facilitate friction and thermal performance testing of a single clutch-plate pair, the SCID has been designed to allow a full clutch to be tested should this be required in future investigations. The components have hence been designed with the load demands associated with a full clutch.

3.5.1 Non-Rotating Parts

Figure 3.9 shows the design process used for the non-rotating components of the SCID. The design of components such as the bearing housings were dictated by shaft and bearing diameters and therefore the design process shown in Figure 3.9 was used as a check to ensure the component designs were suitable. For other component such as the lever arm, the design was dictated purely on strength considerations and therefore the design process could be used in an iterative manner to produce a component with sufficient strength to withstand the loads applied to it whilst minimising its size and hence cost.

Key:



Design



Calculation



Critical

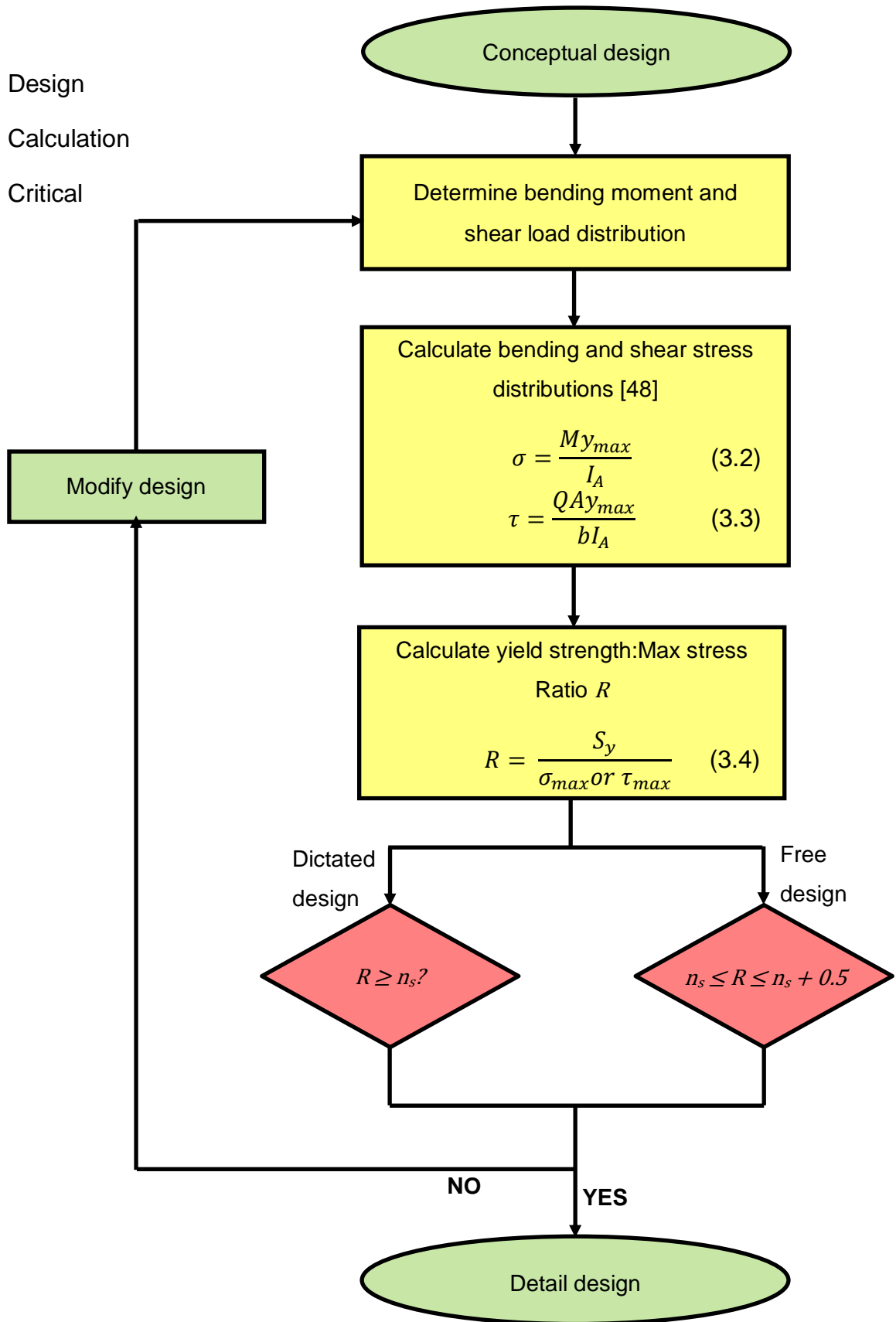


Figure 3.9 – Design Process for Non-Rotating SCID Components

Where: σ – Bending Stress (Nm^{-2})
 τ – Shear Stress (Nm^{-2})
 M – Bending Moment (Nm)
 y_{max} – Maximum Distance from Neutral Axis (m)
 I_A – Second Moment of Area (m^4)
 Q – Shear Load (N)
 A – Cross-Sectional Area (m^2)
 b – Cross-Sectional Width (m)
 S_y – Yield Strength (Nm^{-2})
 n_s – Safety Factor

The minimum length of the keys and keyways used to transmit torque between various components of the SCID were calculated via a separate process. The following equations were used to determine the minimum key length to prevent shear and compression failure [49]. The cross-sectional dimensions of the keys are dependent upon the shaft diameter and are quoted in standard sizes:

$$\tau_{des} = \frac{0.4S_y}{n_s} \quad \sigma_{des} = \frac{0.9S_y}{n_s} \quad (3.5,3.6)$$

$$l_{min} = \frac{2T_k}{dw_k\tau_{des}} \quad l_{min} = \frac{4T}{dh_k\sigma_{des}} \quad (3.7,3.8)$$

Where: τ_{des} – Maximum Allowable Shear Stress (Nm^{-2})
 σ_{des} – Maximum Allowable Compression Stress (Nm^{-2})
 l_{min} – Minimum Key Length (m)
 T_k – Transmitted Torque (Nm)
 d – Shaft Diameter (m)

w_k – Key Cross-Section Width (m)

h_k – Key Cross-Section Height (m)

3.5.2 Rotating Parts

Figure 3.10 shows the design process used to size the power transmission shafts. Once this process was completed, suitable bearings were chosen which then allowed the design of bearing housings to be carried out according to Figure 3.9 as well as determining the length of the keys used to transmit torque.

Where:

- d_{min} – Minimum Shaft Diameter (m)
- M_{crit} – Bending Moment at Critical Point (Nm)
- T_{crit} – Transmitted Torque at Critical Point (Nm)
- ω_{crit} – Critical Shaft Speed (rads^{-1})
- g – Acceleration due to Gravity (ms^{-2})
- W_i – Weight of Mass i (N)
- $\delta_{i,max}$ – Total Deflection at Point i due to all Masses (m)
- ω_i – Shaft Critical Speed if only Mass i Existed ($\omega_i = \sqrt{g/\delta_i}$) (rads^{-1})
- δ_i – Deflection at Point i due to Mass i only (m)
- ω_{op} – Shaft Operating Speed (rads^{-1})
- S_e – Modified Endurance Limit (MPa)
- S'_e – Endurance Limit (MPa) (Function of Loading Type)
- k_f – Finish Factor
- k_s – Size Factor
- k_r – Reliability Factor
- k_t – Temperature Factor
- k_m – Miscellaneous Factor
- $\sigma_{1,2}$ – Principal Stresses (Nm^{-2})

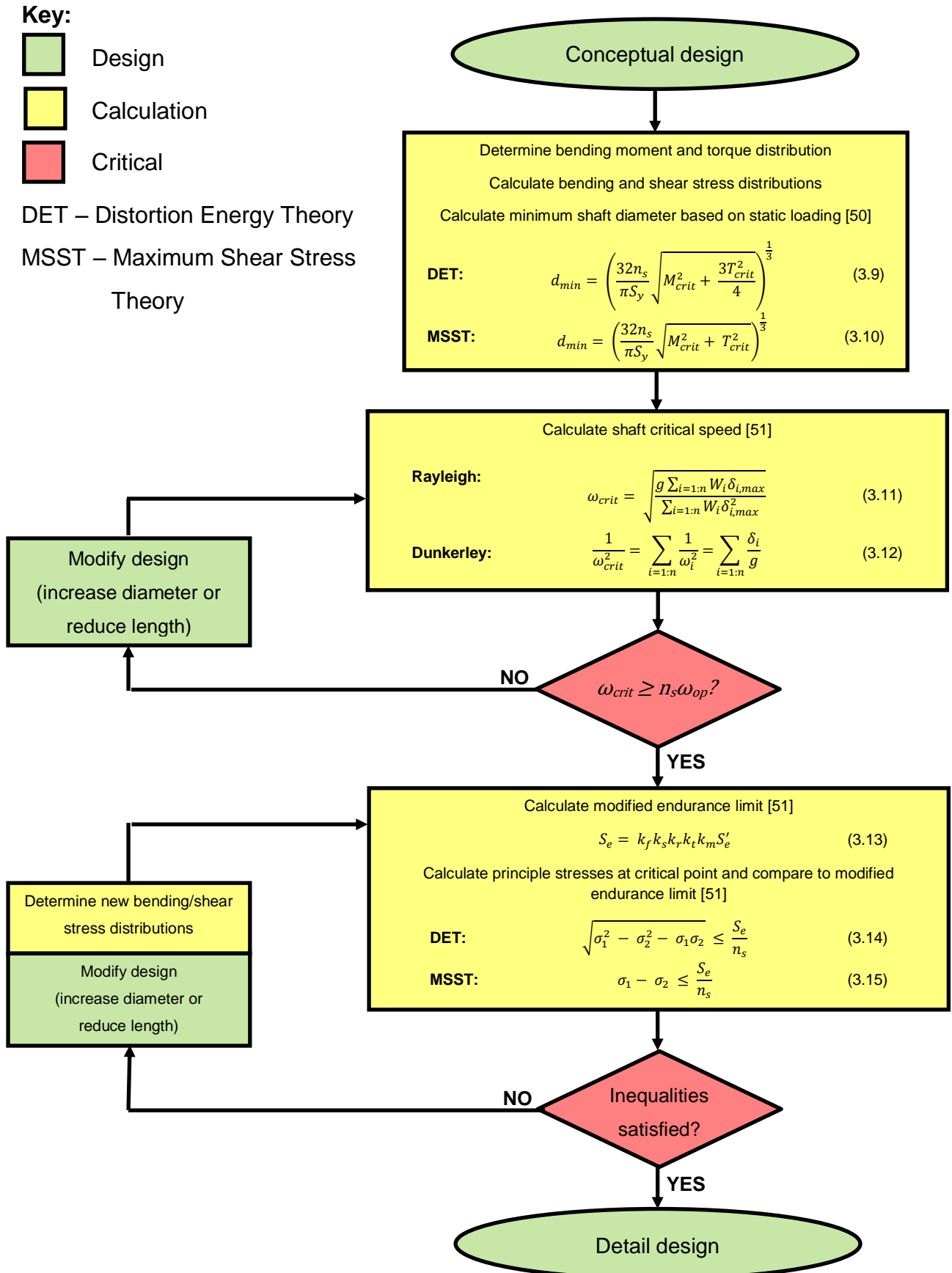


Figure 3.10 – Design Process for Sizing of SCID Power Transmission Shafts

The flywheel was sized after the power transmission shafts were sized as the shaft diameter and length of the main shaft dictated the inner radius and thickness of the flywheel. Equation 3.1 is used to calculate the required inertia of the flywheel which is related to the dimensions of the flywheel according to Equation 3.16 with the mass of the flywheel calculated using Equation 3.17:

$$I_f = \frac{m_f(r_o^2 + r_i^2)}{2} \quad (3.16)$$

$$m_f = \rho\pi(r_o^2 - r_i^2)t_f \quad (3.17)$$

Where: I_f – Flywheel Inertia (kgm^{-2})
 m_f – Mass of Flywheel (kg)
 r_o – Outer Radius of Flywheel (m)
 r_i – Inner Radius of Flywheel (m)
 ρ – Material Density (kgm^{-3})
 t_f – Flywheel Thickness (m)

Substituting Equation 3.17 into 3.16 and rearranging allows the outer radius to be calculated using Equation 3.18:

$$r_o = \sqrt[4]{\frac{2I_f}{\rho\pi t} + r_i^4} \quad (3.18)$$

After determining the flywheel dimensions, the maximum hoop and radial stresses within the flywheel were determined [48]. Provided that the stresses do not exceed S_y/n_s , the flywheel dimensions calculated are suitable. If the stresses are too high, the outer radius has to be reduced but in order to maintain the same value of inertia, the mass of the flywheel would need to be increased by using a thicker flywheel. This would require increasing the length of the main shaft which would require the

design process shown in Figure 3.10 to be carried out to ensure that the main shaft can be lengthened without a risk of failure. An iterative process would then be required to size both the main shaft and flywheel to ensure failure of neither component occurs. This iterative process was carried out and a suitable solution was found. This iterative process was also required as the initial detail design of the main shaft was completed using an estimated flywheel mass and it was therefore necessary to carry out the shaft sizing design process at least once to ensure the main shaft was correctly sized.

Hoop Stress:
$$\sigma_{\theta,max} = \frac{3 + \nu}{4} \rho \omega_{op}^2 \left(r_o^2 - \frac{1 - \nu}{3 + \nu} r_i^2 \right) \quad (3.19)$$

Radial Stress:
$$\sigma_{r,max} = \frac{3 + \nu}{8} \rho \omega_{op}^2 (r_o - r_i)^2 \quad (3.20)$$

Where: ω_{op} – Shaft Operating Speed (rads^{-1})
 $\sigma_{\theta,max}$ – Maximum Hoop Stress (Nm^{-2})
 $\sigma_{r,max}$ – Maximum Radial Stress (Nm^{-2})
 ν – Poisson’s Ratio of Material

3.6 Summary

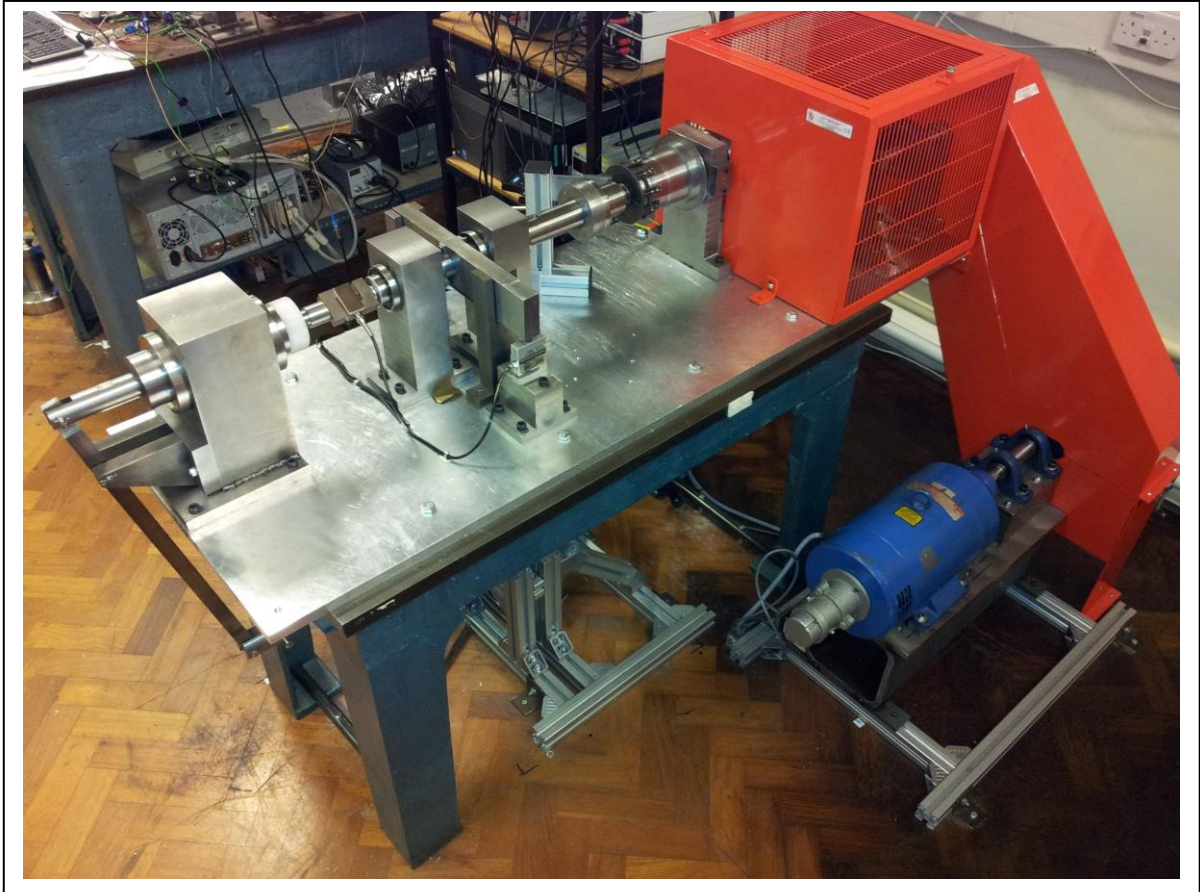


Figure 3.11 – Final SCID Assembly

The SCID has been designed to facilitate friction and thermal performance testing of single clutch-plate pairs under representative race start conditions. Considerations have also been made with regards to possible future use of a SCID as a full clutch dynamometer. Compromises were made in order to save manufacturing time and costs but the critical race start parameters listed in Table 3.1 have been replicated within the finished SCID shown in Figure 3.11. The guarding shown surrounds the rotating components in order to absorb the energy of any flying debris in the unlikely event that the shafts fail or the friction belts break. The guarding was designed and manufactured externally by Procter Machine Guarding.

4. Clutch-Plate Engagement Tests Using SCID

4.1 Introduction

The SCID was used to carry out a series of engagement tests at several clamp load and initial rotational speed combinations. The clamp load, rotational speed and torque during the engagement tests were measured, recorded and compared in order to establish at what level of energy input the torque output behaviour of the clutch plates becomes unstable and inconsistent.

A thermal imaging camera was used to record the friction surface temperature of the rotating clutch plate during the engagement tests. The maximum temperatures were recorded along with the location and size of any hot bands in order to establish the possible effect of TEI on the torque output of the clutch-plate pairs.

4.2 Test Programme

Table 4.1 shows the combinations of clamp loads and initial rotational speeds used, the total amount of energy dissipated and which clutch-plate pairs (discussed further in Chapter 5) were used for each speed/load combination. The speed and load combinations at 8000rpm are identical to those carried out in a previous investigation [7] but the total energy dissipation is lower. This is because the SCID was designed to dissipate 13.75kJ (Table 3.1) at the friction interface, when operated at 10000rpm. However, the electric motor was not capable of operating above 8000rpm and as such the total energy dissipation levels were lower than originally intended. Seven engagement tests were carried out at each speed/load combination as per the previous investigation [7],

	Clamp Load (N)	1000	1200	1400
Initial rpm/ Total Energy Dissipation (kJ)				
7000/6.74		A2	A3	A4
8000/8.80		B2	B3	B4

Table 4.1 – Initial Speed/Clamp Load Combinations Used in SCID Tests

4.3 Thermal Imaging Camera

This investigation required the measurement of the temperature profile across the rotating clutch-plate friction surface during an engagement. Due to the high relative rotational speeds and full area contact, the use of rubbing thermocouples was impossible. The possible options were therefore embedded thermocouples or thermal imaging.

The use of a thermal imaging camera offers several distinct advantages over the use of embedded thermocouples. Firstly, the thermocouples must be embedded within the clutch-plate material and as such, the measurement tip of the thermocouple would be a small distance below the actual friction surface and therefore not measure its true temperature value. Due to the short length of time of the engagement and the high energy concentration at the friction surface, the measured temperature could be far below that of the friction surface due to the finite time it takes for the heat to conduct through the thickness of the clutch plate.

The radial and circumferential positioning of the embedded thermocouples is also problematic as it was anticipated that hot bands on the friction surfaces would cover potentially only a small proportion of the total friction surface area. If a thermocouple was embedded directly below where a hot band will form, the temperature of the band would be measured (but with the through-thickness conduction error). If the thermocouple was however embedded well away from the location of a hot band, a much lower temperature would be recorded. There would be no way of knowing if the measured temperature represented that of the friction surface or whether it was simply a function of the thermocouple location. The hot bands could therefore go undetected unless a large number of thermocouples were used. The thermocouples would have to be spaced a finite distance apart which raises the problem of radial conduction in a similar sense to that of through-thickness conduction.

Finally, thermocouples have an inherent measurement lag (thermal inertia) and therefore even if the thermocouple was embedded at the correct radial position as close to the friction surface as possible, the hot band phenomenon may still not be captured if the high temperatures persist for only a very short period of time.

The SCID has been designed with a 12mm diameter hole through the clutch basket, clutch-plate spacer and stationary clutch plate (see Chapter 3.4) such that the

thermal imaging camera can view the friction surface of the rotating clutch plate and record its true temperature. The thermal camera can also view a large area of the friction surface at the same time and offers a rapid measurement rate, overcoming the issues associated with the use of embedded thermocouples.

An infrared (IR) thermal imaging camera was used by Thevenet et al. [52] to measure the temperature of railway brakes during braking tests. The use of the IR camera permitted the observation of hot band formation (Figure 4.1a) and, as the test progressed, migration of the hot band on the surface of the brake rotor (Figures 4.1b & 4.1c). This result is shown in Figure 4.1 where the temperatures were calculated using an emissivity value of 1.

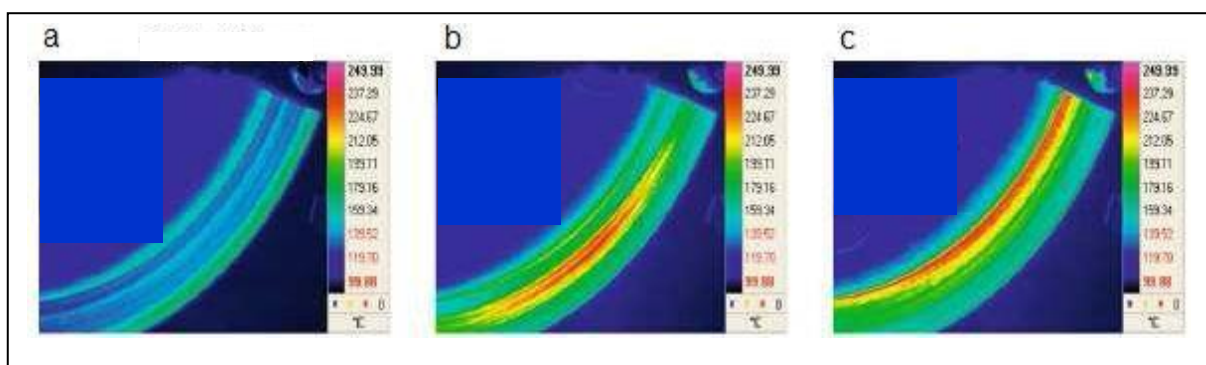


Figure 4.1 – IR Thermographs of Railway Brake Rotor During Braking Tests [52]

The value of emissivity used to calculate the temperatures is very important. If a body absorbs all of the radiation incident upon it, it is known as a blackbody and through the application of thermal equilibrium, a blackbody must also emit the same amount of radiation otherwise its temperature would constantly increase. The ratio of the total incident radiation energy absorbed, and hence emitted, is known as the emissivity and is equal to 1 for a blackbody. If the emissivity of the object is lower than 1 but the temperatures calculated via thermal imaging are computed using a value equal to 1, the calculated temperatures will be lower than the real temperature of the body. Essentially, using an emissivity of 1 assumes that the maximum possible amount of energy via radiation is being emitted. Using an emissivity of 1 therefore gives the lowest potential temperature of the body being viewed.

A FLIR X6540SC thermal imaging camera was used to record the temperature of the rotating clutch-plate friction surface during SCID engagement tests. The physical

setup of the camera in relation to the rig is shown in Figure 4.2. A 12mm extension ring was used to focus the image at short distance. The camera was controlled and videos recorded using FLIR R&D software. The camera was armed so that recording was triggered by a 5V input controlled by an output from the SCID LabVIEW program.

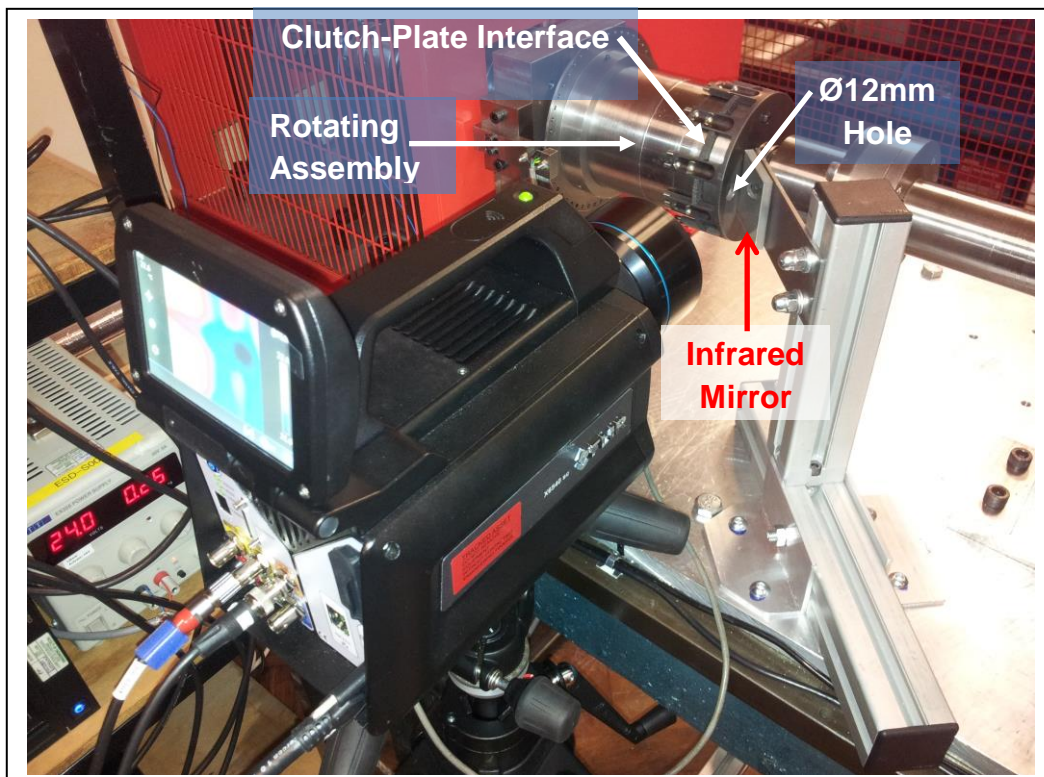


Figure 4.2 – Thermal Imaging Camera Setup for SCID Engagement Tests

The camera detects infrared radiation using an IR Focal Plane Array consisting of detectors and pixels. The camera has 640x480 pixels where each pixel receives incident radiation which is then converted to an electrical signal. The higher the temperature, the more radiation energy is received by each pixel. The integration time dictates how long the pixels absorb radiation for before the detector shuts off and convert the electrical signal to a temperature value before switching on again. The integration time must be set appropriately for the temperature of the scene that the camera is viewing. If the integration time is too long, the detector becomes saturated and cannot absorb any more energy via radiation. The recorded temperature may then be much lower than the actual temperature. The temperature

is calculated for each pixel by substitution of the radiation energy levels into Planck's equation and the temperature of the scene is presented to the user.

Due to limitations of thermal imaging camera technology, only discrete bands of the electromagnetic (EM) spectrum can be viewed. This means that a continuous measurement from room temperature to very high temperature is not possible. The FLIR X6540SC has two calibration settings from 5-300°C and 300-1500°C. Table 4.2 lists the configurations used to record the expected high temperatures of the clutch-plate friction surface. Any temperature under 300°C can therefore not be measured and recorded, although due to the noise caused by objects at room temperature viewed by the thermal imaging camera, any temperatures under 450°C could not in fact be recorded. Using more than one temperature range reduces the maximum possible frame rate of recording but results in more accurate temperature measurements. The configuration in Table 4.2 gave the best compromise allowing a frame rate of 200Hz to be used.

Temperature Range (°C)	Integration Time (µs)
300-842	149
757-1500	14

Table 4.2 – Thermal Imaging Camera Temperature Range Configuration

The settings in Table 4.2 must be applied prior to recording but the values shown in Table 4.3 can be changed in the results post-processing stage. The values shown in Table 4.3 were used to obtain all the thermal imaging results presented in this chapter.

Incident radiation from surrounding objects may fall on the clutch-plate friction surface which will then be emitted and viewed by the thermal camera. The reflected apparent temperature compensates for this. The value entered is the temperature of any bodies from which the incident radiation may originate. Any incident radiation on the clutch-plate friction surface would have to travel through the Ø12mm hole in the clutch basket and clutch-plate spacer. As such, only a small amount of incident radiation can reach the clutch-plate friction surface and will therefore be insignificant compared to the amount of radiation emitted by the hot clutch-plate friction surface.

Molecules in the atmosphere (H₂O, O₂, CO, CO₂) absorb infrared radiation and will therefore affect the thermal imaging results [53]. Due to the short distance between the clutch-plate friction surface and the thermal camera detector, the atmosphere is unlikely to absorb a large amount of the radiation so a transmission value of 1 has been used.

The temperature and transmission of the external optics, such as the viewing window of an oven, can also have an effect on the measurements. As no external optics were used in this investigation, the values were set to room temperature and an emissivity of 1.

The emissivity of the carbon/carbon clutch-plate material and its variation with temperature was unknown and no literature regarding the emissivity of carbon/carbon materials could be found. An emissivity value of 1 was hence used. In conjunction with the other parameter values presented in Table 4.3, the lowest possible temperature of the clutch-plate friction surface has been calculated as it has been assumed that 100% of the radiation energy is emitted and no losses occur due to atmospheric factors.

Parameter	Value
Emissivity	1
Reflected Apparent Temperature	20°C
Atmospheric Temperature	20°C
Transmission	1
Distance	0.1m
External Optics Temperature	20°C
External Optics Transmission	1

Table 4.3 – Thermal Imaging Camera Post-Processing Parameter Values

4.4 Experimental Procedure

Figure 4.3 shows the experimental procedure followed to carry out the engagement tests. The tests were executed using LabVIEW in conjunction with a National Instruments PXI chassis. The load and speed data were written directly to a Microsoft Excel spreadsheet.

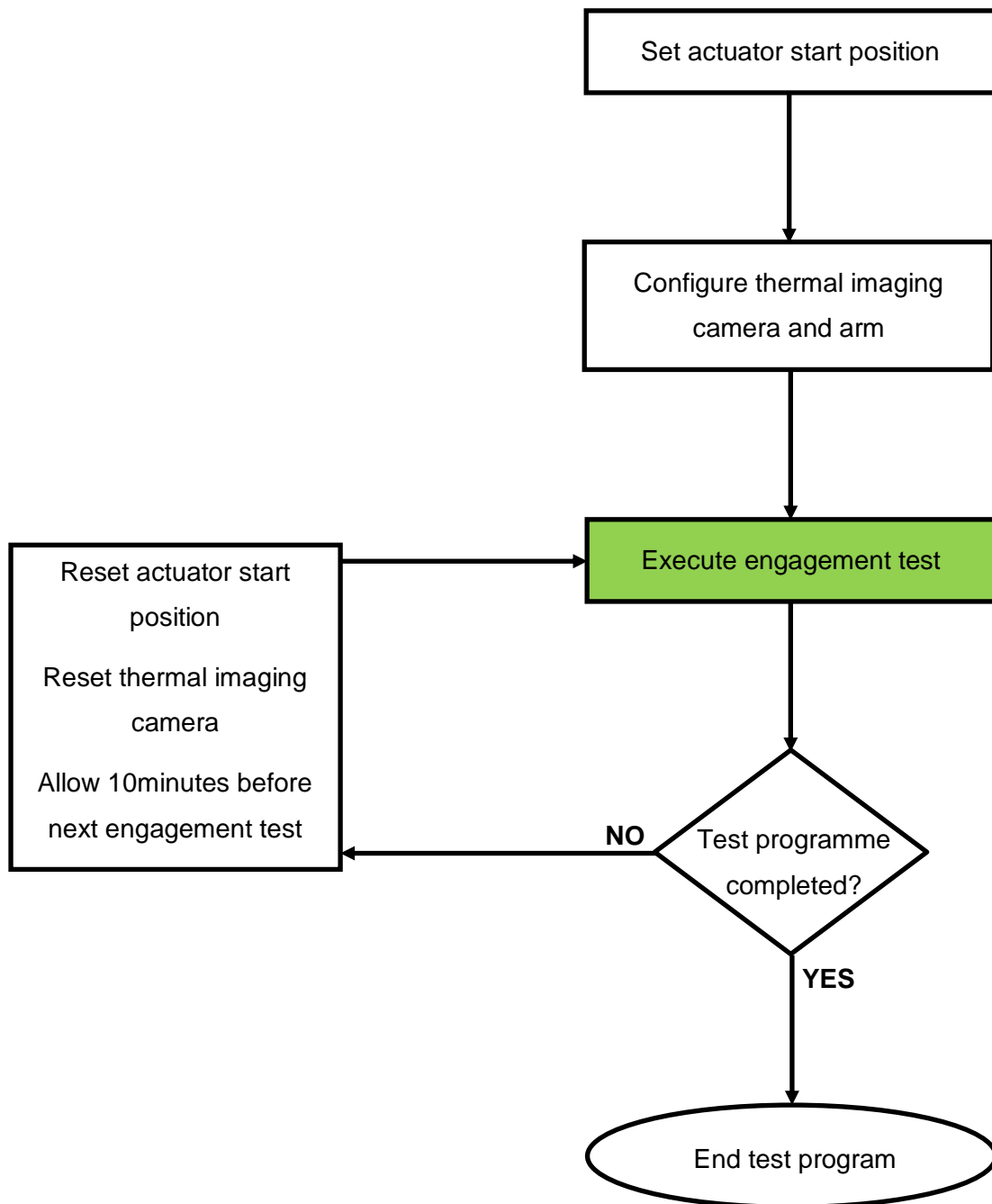


Figure 4.3 – Test Procedure for SCID Engagement Tests

The actuator initial position is set in order to leave a small gap (~1mm) between the stationary clutch plate and the rotating clutch plate so that the rotating clutch plate can spin up to speed freely. The small gap between the plates also means that the clamp load can be built up as quickly as possible because the actuator only has a small distance to move forward. As a result, there is a minimal loss of rotational speed in the time between the main shaft of the SCID being disconnected from the electric motor and drive assemblies, and the clutch-plate engagement occurring.

Ideally, consecutive engagements would have been carried out two and a half minutes apart to best replicate the race start procedure. However, issues with the reliability of some SCID hardware components meant that this was not possible. Intervals of ten minutes were chosen to allow time to fix any potential issues and also for the clutch plates to cool down to room temperature before the next engagement thereby ensuring the same initial conditions.

The engagement tests were executed using a LabVIEW program which utilises a state-machine architecture. Table 4.4 lists the states within the state-machine. The program executes continuously within a while loop and remains in a single state until a condition is met. Once the condition is met, the program switches to the next state dependent upon which condition has been met. Once the final state is entered, the while loop is stopped and the program finishes executing, saving the results to a spreadsheet file.

For the initialise and shutdown stages, one second was chosen to give sufficient time for the software and hardware to initialise or shutdown. A total of 0.1seconds in the EM Clutch state ensured that the mini-EM clutch fully disengaged before the clamp load was applied whilst ensuring that a minimal amount of rotational speed is lost during this phase. Due to the method of measuring rotational speed, speeds below 200rpm cannot be reliably measured due to a trade-off between measurement resolution and the time between pulses output from the IR photoemitter used to measure rotational speed. Speeds below 200rpm cannot be recorded as the time between pulses becomes greater than the measurement interval.

State	Description	Next State	Condition
Initialise	Initialises all software and hardware	Spin	1s has elapsed
Spin	Spins rotating clutch plate up to target speed	EM Clutch	Target speed has been reached
EM Clutch	Disengages mini-EM clutch to decouple excess inertia	Engagement	0.1s have elapsed
Engagement	Moves actuator forward at full speed to apply PID-controlled clamp load	Cooldown	Rotational speed of rotating clutch plate has fallen below 200rpm
Cooldown	Clamp load is maintained as clutch plates cool down to a safe temperature	Pullback	10s have elapsed
Pullback	Pulls actuator back to release clamp load	Shutdown	Clamp load < 0
Shutdown	Shuts down all software and hardware	None	1s has elapsed

Table 4.4 – States and Conditions of State-Machine LabVIEW Program for Executing SCID Engagement Tests

4.5 Torque Profiles

Due to the vibrations resulting from the high rotational speeds of the SCID components, the clamp load and torque traces recorded were very noisy. A first order Savitzky-Golay smoothing filter was applied to the data using Matlab. Figure 4.4 shows the results for engagement test 7000rpm/1000N-1 after applying the filter.

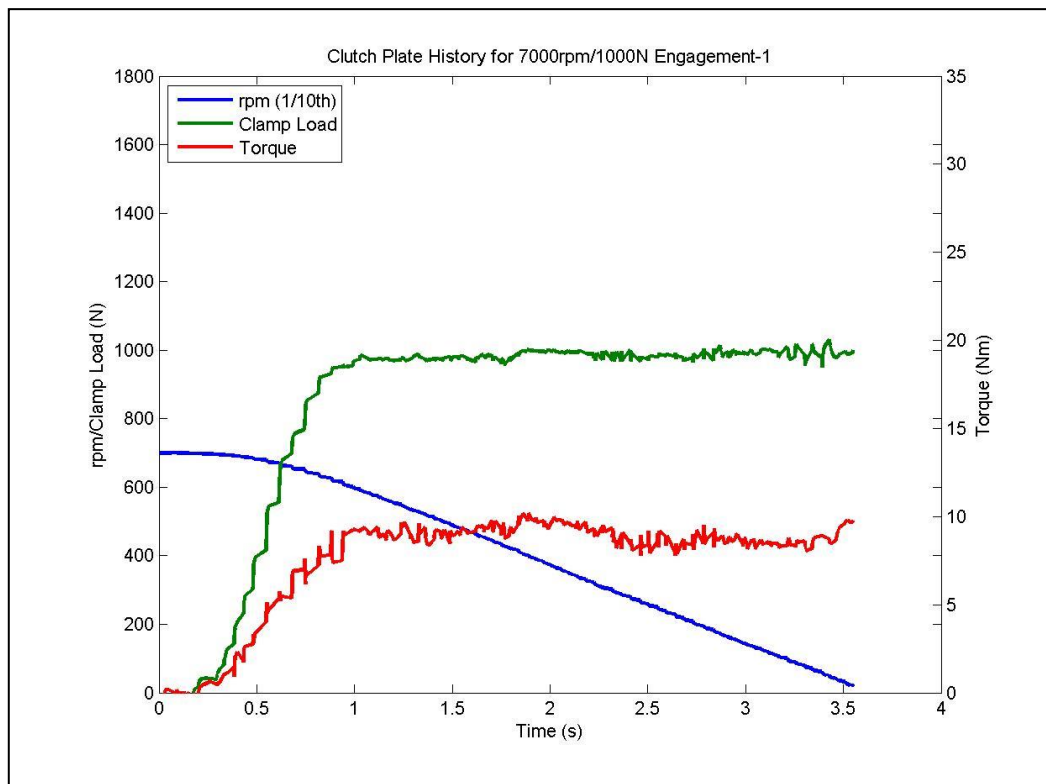


Figure 4.4 – rpm, Clamp Load and Torque Traces for Engagement Test 7000rpm/1000N-1

The results are recorded from the start of the EM Clutch state to the end of the Engagement state. The delay in full clamp load build-up is due to three distinct phases. The first 0.1s are spent in the EM Clutch state where the actuator is held stationary and during the next ~0.1s, the actuator is moved forward so that the clutch plates come into contact with each other. No clamp load and hence no torque is generated during this time. It then takes ~0.8-1.0s for the clamp load to build up to the target clamp load. Figures 4.5-4.7 show the torque outputs for the engagement tests carried out at 7000rpm. It is important to note that the time scales are not identical but are scaled to the maximum engagement time recorded for that particular speed and clamp load combination. The torque scales are identical.

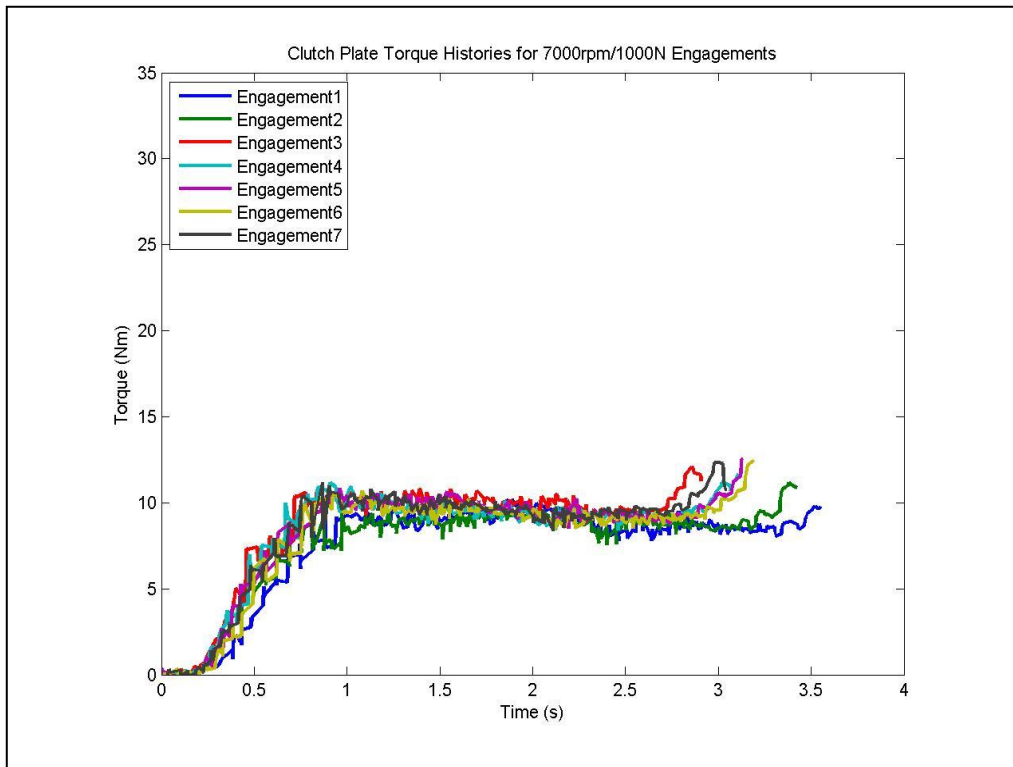


Figure 4.5 – Torque Output Results for 7000rpm/1000N Engagement Tests

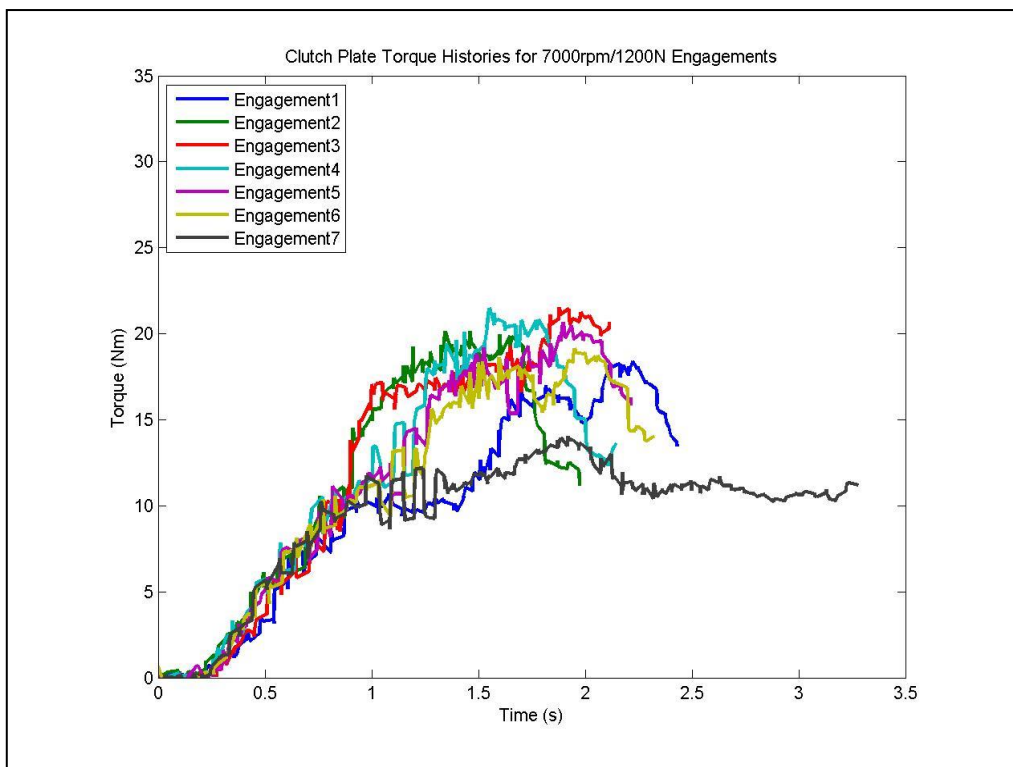


Figure 4.6 – Torque Output Results for 7000rpm/1200N Engagement Tests

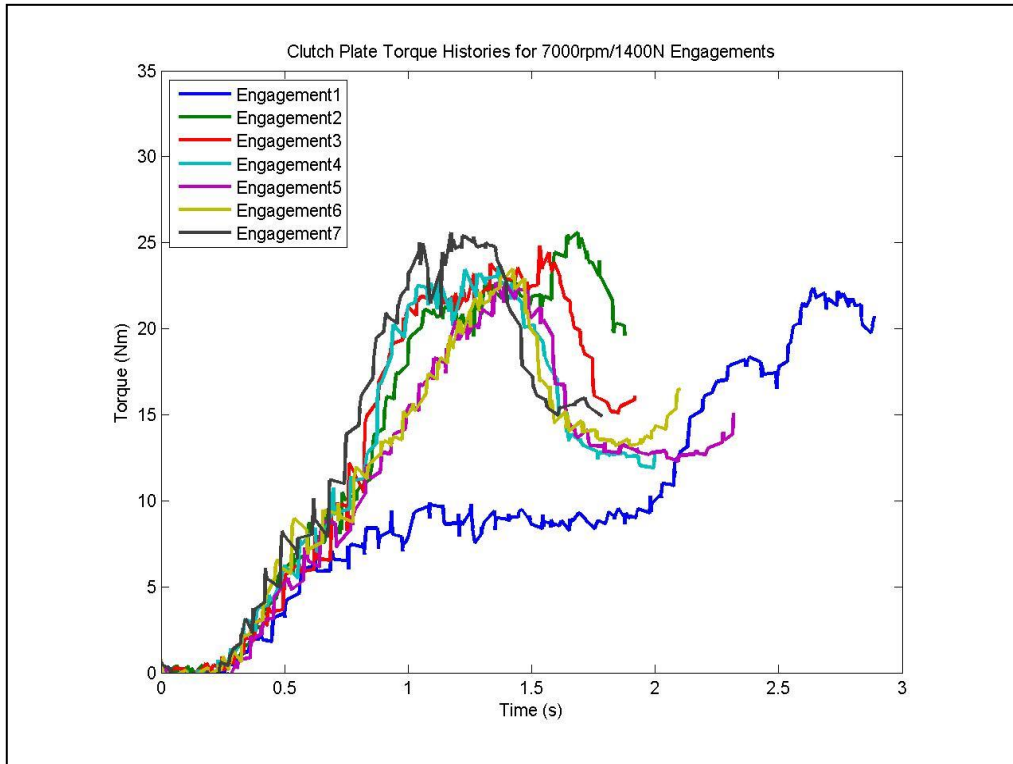


Figure 4.7 – Torque Output Results for 7000rpm/1400N Engagement Tests

At the lowest energy and lowest clamp load combination (Figure 4.5), the torque output is consistent between engagements and is also very stable once the full clamp load has been built up. The torque level is quite low however and as a result the engagements take at least three seconds to complete. The consistent but low torque output suggests a predominance of type I morphology on the friction surfaces. As discussed in the literature review (Chapter 2.6), it has been established that a minimum amount of power is required to affect a morphology change suggesting that a clamp load of 1000N is insufficient to cause type II morphology to form for an initial rotational speed of 7000rpm. Equation 4.1 can be used to calculate the power dissipation at the friction interface. The power dissipation level is simply the rate at which the energy is dissipated at the friction interface.

$$Power = P\mu\omega r \quad (4.1)$$

Where: P – Clamp Load (N)
 μ – Coefficient of Friction
 ω – Rotational Speed (rads^{-1})
 r – Friction Radius (m)

As the clamp load is increased for the same total overall energy dissipation level (Figure 4.6), the torque output levels increase as expected as the torque generated is proportional to the clamp load (see Chapter 1.1). However, the increase in peak torque from the engagement tests at 1000N to 1200N is disproportionate to the clamp load increase alone. In most cases, the torque output is approximately double for the 1200N engagement tests. As a result the engagements take less time to complete. However the evolution of the torque output is much less stable at 1200N whereby the torque reaches a peak value before decreasing again towards the end of the engagement. This behaviour is a strong indication of type II morphology forming on the friction surfaces leading to a high COF and therefore high torque, before type III morphology is formed reducing the COF. The disproportionate increase in peak torque can be explained via Equation 4.1 where the clamp load increase accounts for part of the increase in power dissipation and the remaining increase is due to the increase in COF. As the COF increases, the power dissipation will increase and cause further morphology changes and initially increases the COF as type II morphology becomes dominant. The effect is self-exacerbating until the power dissipation level becomes sufficient to convert the type II morphology to type III and lower the COF and power dissipation level. Although unstable for individual engagement tests, the torque outputs appear to show some consistency between tests except for the final engagement which shows similar behaviour to that of the engagement tests carried out at 1000N, possibly due to type III morphology becoming predominant.

When the clamp load is increased to 1400N, a further increase in peak torque is observed and the same fall in torque towards the end of the engagement is seen. The mechanisms for this behaviour are similar to those at 1200N where the increased torque is due to the greater clamp load and possibly a greater proportion of type II morphology being formed leading to a higher COF. As a result of the higher

torque outputs, the engagements times are shorter at 1400N. The first engagement shows an initially low torque output before rising sharply later in the engagement. At this point, the clamp load is stable and hence the increase must be due to a change in the COF. As this is the first engagement, this behaviour is most likely due to water being desorbed from the friction surface and type II morphology resulting thereafter. As for the 1200N load case, the torque outputs are highly unstable for individual engagements but show a reasonable level of consistency between engagements.

Figures 4.8-4.10 show the torque outputs for the engagement tests carried out at 8000rpm. It is again important to note that the time scales are not identical but are scaled to the maximum engagement time recorded for that particular speed and clamp load combination. The torque scales are identical.

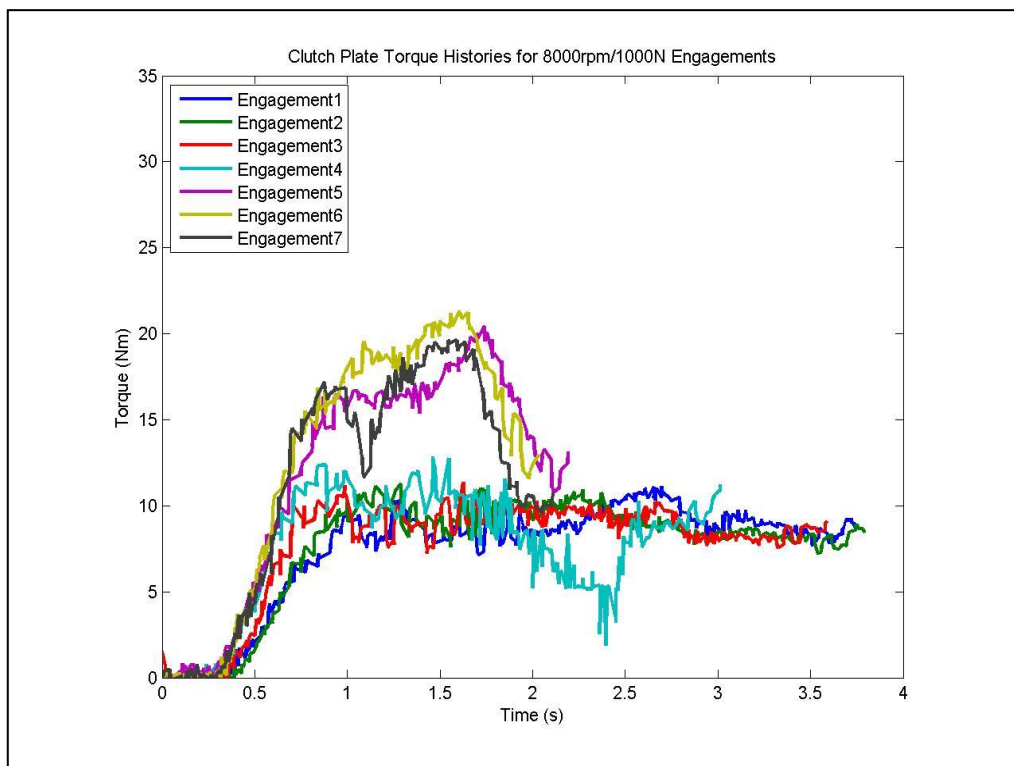


Figure 4.8 – Torque Output Results for 8000rpm/1000N Engagement Tests

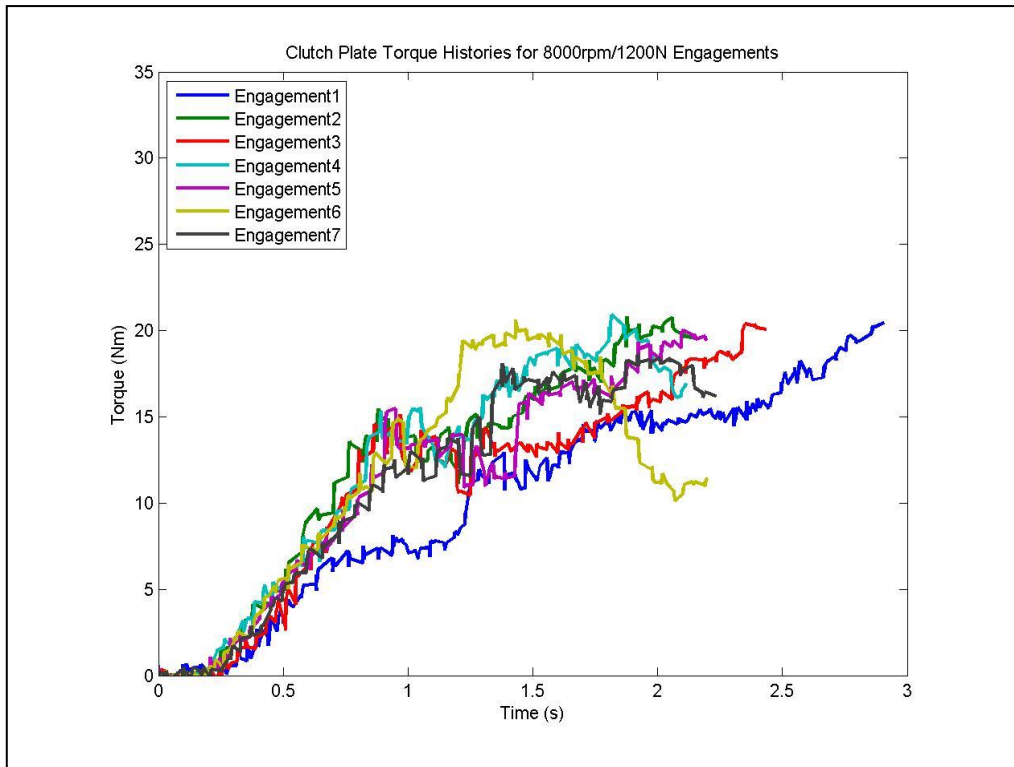


Figure 4.9 – Torque Output Results for 8000rpm/1200N Engagement Tests

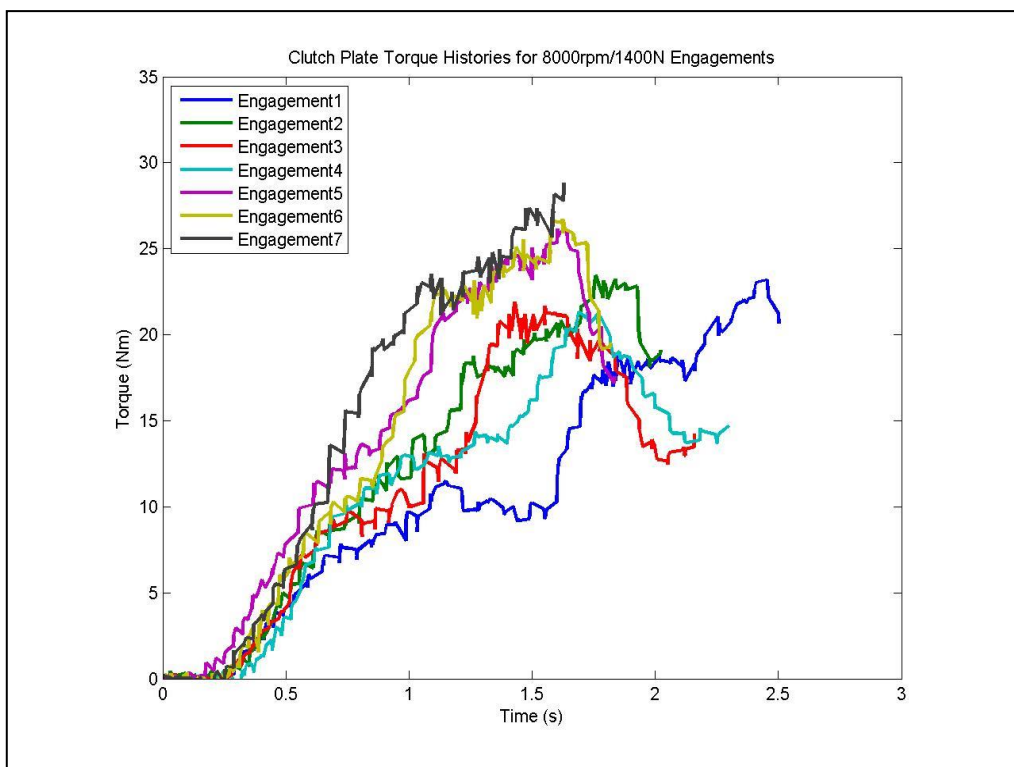


Figure 4.10 – Torque Output Results for 8000rpm/1400N Engagement Tests

At a clamp load of 1000N (Figure 4.8), the first four torque outputs are very similar for the engagement tests at 8000rpm to those at 7000rpm whereby a stable, low torque output is produced with high consistency between engagements. The sudden dip in torque for Engagement4 (light blue trace) at around 2.4s was caused by an unknown source of noise that affected the recorded load cell signal. The dip in torque is therefore not a function of a sudden friction surface change and can be ignored. The final three engagements show similar behaviour to those carried at 7000rpm/1200N and show a reasonable level of consistency between engagements. The sudden change in torque behaviour could indicate that this speed/load combination represents the power dissipation threshold required to produce type II morphology. As the initial rotational speed is higher, a greater level of total energy is dissipated and the cumulative effect of this may be enough to cause sufficient surface changes to trigger the formation of type II morphology. This will then lead to an increase in COF and in turn an increase in power dissipation level. Further type II morphology will then be formed and the effect will self-propagate.

The first engagement for the 1200N load case shows a torque output which is consistent with water desorption. The subsequent engagements exhibit high levels of torque output and as with the 7000rpm engagement tests, the increase in torque cannot be explained by the increase in clamp load alone. However, at 8000rpm, the torque does not decrease towards the end of the engagement. A possible explanation could be that due to the higher level of total energy dissipation, a greater amount of type II morphology is formed during the first morphology transition and the power dissipation levels are not great enough to convert a significant amount of type II morphology to type III morphology. As such, the type III morphology is not able to become dominant and the COF remains high.

Again, the results for the first engagement at 1400N is due to water desorption from the friction surface. The subsequent engagements have a higher peak torque as expected where the torque reduces towards the end of the engagement test. The power dissipation levels must therefore be high enough for type III morphology to form. As well as the torque instability during a single engagement, there is a large amount of inconsistency between engagements.

The results shown in Figures 4.5-4.10 agree well with previous dynamometer results [7] whereby at a low initial rotational speed and low clamp load combination, the torque output is both stable and consistent. As the initial speed and/or clamp load is increased, the torque output becomes less stable and less consistent. At the highest initial rotational speed and clamp load combination, the torque output is both unstable and highly inconsistent.

4.6 Thermal Imaging Results

Recording using the thermal imaging camera was triggered during the EM Clutch state of the engagement tests and switched off in the Pullback state. The videos were examined and the maximum friction surface temperatures during the engagements were noted along with the time at which they occurred. The times at which the maximum temperatures arose were inconsistent as the length of the engagement test varied due to the differing torque outputs. In general, the maximum temperatures occurred after the full clamp load was developed and before the peak torque occurred.

Figure 4.11 shows the friction surface temperature of the rotating clutch plate for Engagement4 at 7000rpm/1000N. The white circle has been superimposed on this image (and all subsequent images) to indicate where the circumference of the hole machined through the clutch basket, clutch-plate spacer and stationary clutch plate lies. Any temperatures indicated outside the white circle are the result of noise due the calibration range used (300-1500°C) being unsuitable for measuring room temperatures. The hole is centred upon the mean geometric radius of the clutch plate friction surface (40.5mm). The marker Sp1 identifies the innermost radial position viewed (34.5mm) and Sp2 identifies the outermost radial position observed (46.5mm). Sp3, and Sp4, mark the points where the maximum temperatures occur. A maximum temperature of ~550°C was observed just outside of the central radius. This temperature is approximately 75°C higher than the temperature at the innermost point of the viewed surface showing that the temperature across the friction surface is not uniform. However the differences in temperatures are not very large and therefore contact localisation is not extreme for this particular engagement test.

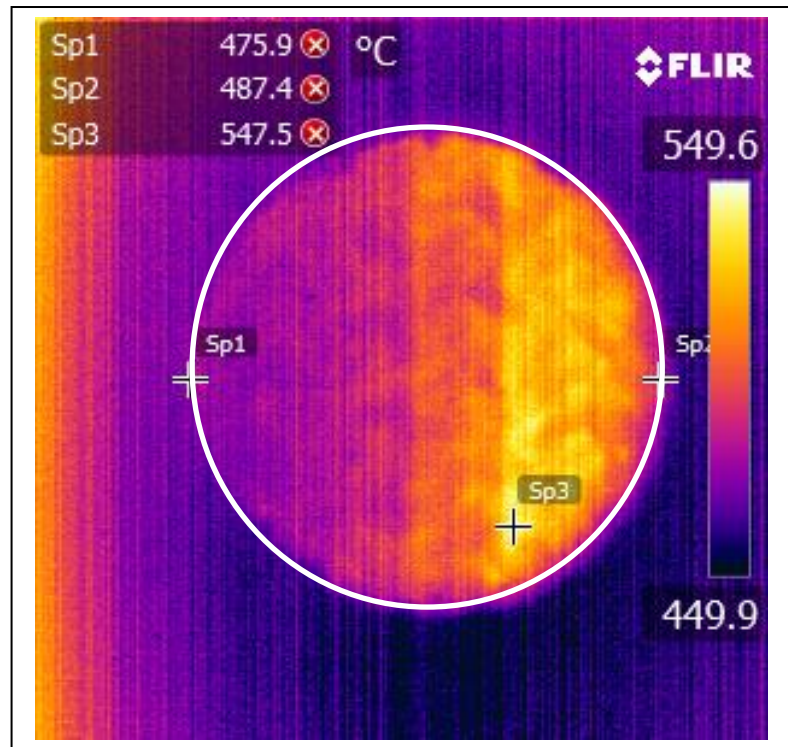


Figure 4.11 – Maximum Temperature Recorded During Engagement⁴ Occurring at 1.650s for 7000rpm/1000N Speed/Load Combination

Figure 4.12 shows the thermal imaging result from Engagement⁷ carried out at 7000rpm/1200N which shows a different kind of temperature profile to that of Figure 4.11. Two concurrent hot bands have been formed where the temperatures of the hot bands are 150-200°C higher than the temperature at the outermost radial position. This suggests that a greater degree of contact localisation has occurred than for the result shown in Figure 4.11. The bands are also inside the central radius as opposed to outside the central radius. For the engagement tests that showed this kind of thermal behaviour, the two bands existed concurrently but one band formed before the other and consequently faded first as well. The dark area across the radius is a cleaning groove in the rotating clutch plate that passed underneath the viewing hole when the frame was recorded.

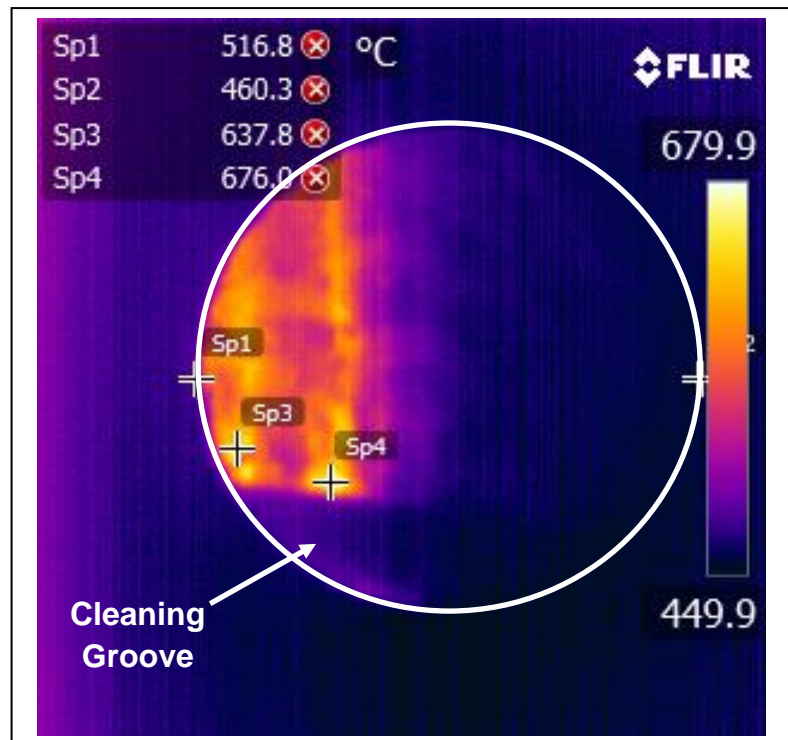


Figure 4.12 – Maximum Temperature Recorded During Engagement7 Occurring at 1.580s for 7000rpm/1200N Speed/Load Combination

The final type of temperature profile observed is shown in Figure 4.13 for Engagement5 at 8000rpm/1400N. It can clearly be seen that an extreme degree of contact localisation has occurred leading to a very high maximum temperature of over 1500°C. The hot band is approximately 2mm in width and the temperature outside this hot band is much lower.

For the 1000N load case, at both rotational speeds, the temperature profile shown in Figure 4.11 was observed most often. For the 1200N load case, one of the temperature profiles shown in Figures 4.12 and 4.13 was observed for each engagement test but which profile was established was inconsistent between engagements. For the 1400N load case, the temperature profile shown in Figure 4.13 occurred for all engagement tests showing the formation of distinct extreme hot bands on the friction surface.

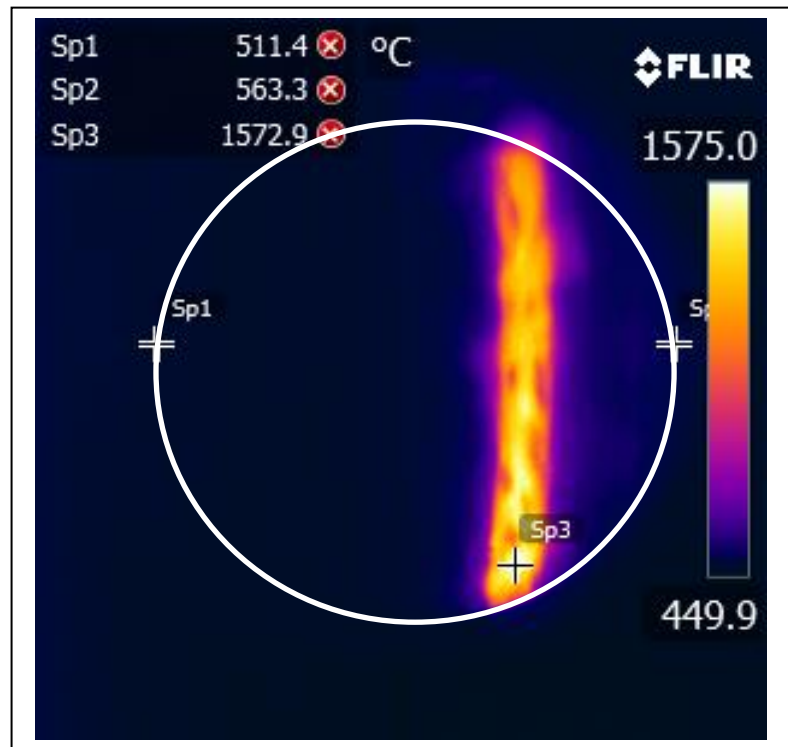


Figure 4.13 – Maximum Temperature Recorded During Engagement5 Occurring at 1.160s for 8000rpm/1400N Speed/Load Combination

In general, the first temperature profile shown in Figure 4.11 resulted in maximum temperatures of 550-700°C whereas the second profile shown in Figure 4.12 produced temperatures of 700-900°C. In the case of the third temperature profile where a distinct hot band was formed, such as in Figure 4.13, temperatures in excess of 1200°C were observed.

Figures 4.14-4.16 show the maximum temperatures recorded for the three different clamp loads investigated. Figure 4.14 shows that the maximum temperatures at 7000rpm remain stable for the 1000N load case which is a reflection of the torque output behaviour shown in Figure 4.5. Similarly the maximum temperature at 8000rpm reflects the torque output behaviour shown in Figure 4.8 whereby the torque becomes unstable and exhibits a degree of inconsistency after Engagement5.

Figure 4.15 shows the maximum temperatures for the 1200N load case which shows a high level of inconsistency between engagements. The torque outputs for this load case (Figures 4.6 and 4.9) show some inconsistency between engagements but not the same extent as the maximum temperatures. This suggests that the 1200N load

case represents a load case where both the torque output and thermal behaviour of the clutch plates are transitional and inconsistent.

Figure 4.16 shows the maximum temperatures for the 1400N load case. Figures 4.7 and 4.10 show that the torque outputs for this load case are both unstable and inconsistent but Figure 4.16 shows that the maximum temperatures reached are consistently high.

For all three load cases, greater maximum temperatures were recorded for the engagement tests carried out at the higher initial rotational speed. The theory of thermoelastic instabilities offers an explanation for this. With relation to Equation 4.1, the power dissipated at the friction interface will become greater as the clamp load is increased as well as the overall energy dissipation being greater as a result of the higher initial rotational speed. This results in the effect of TEI becoming stronger as the increase in power dissipation causes a greater amount of thermal expansion and localises contact even further resulting in higher maximum temperatures. This phenomenon was essentially observed as temperatures well above 1000°C existed in well-defined hot bands such as that shown in Figure 4.13.

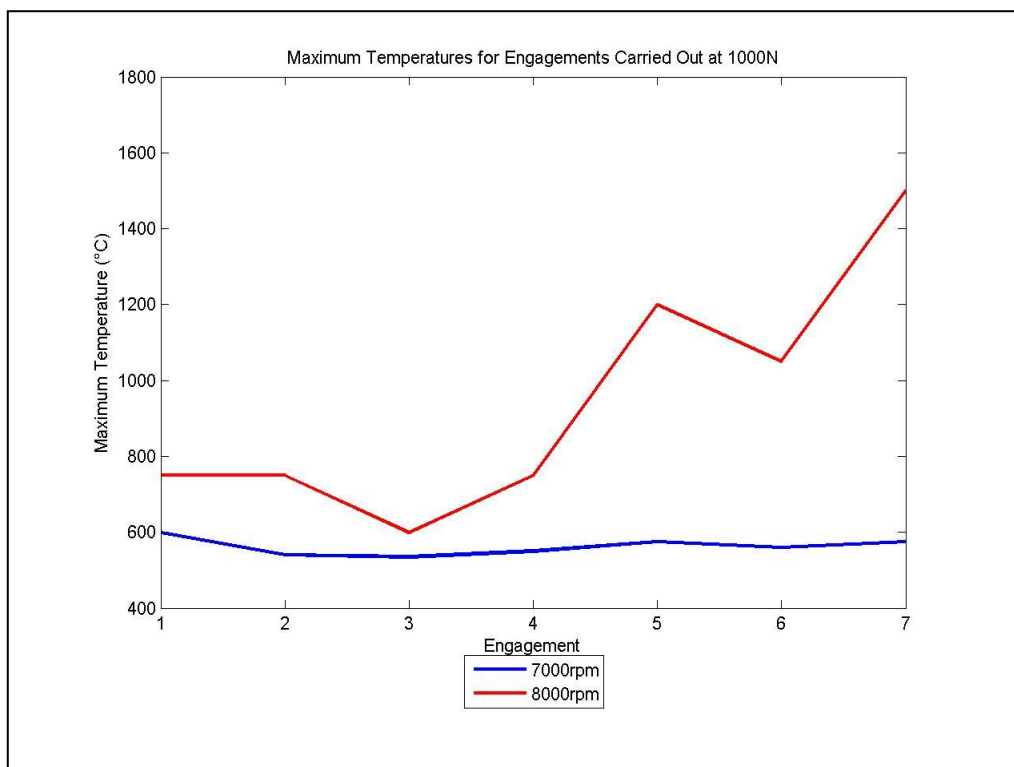


Figure 4.14 – Maximum Temperatures Recorded for 1000N Load Case

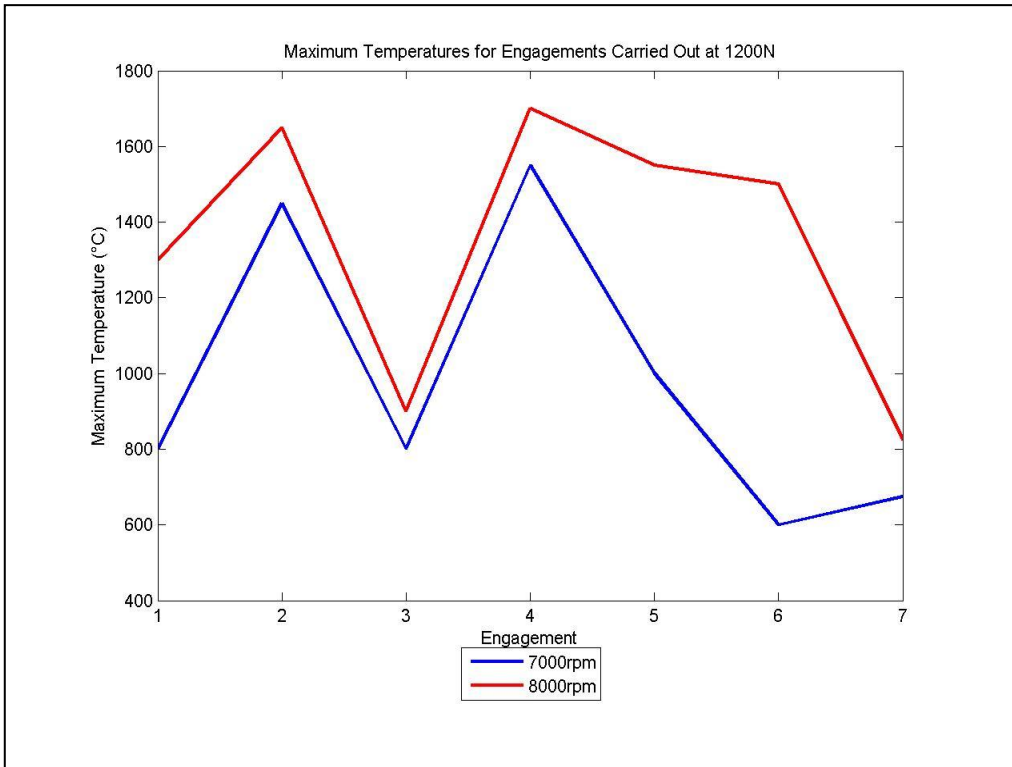


Figure 4.15 – Maximum Temperatures Recorded for 1200N Load Case

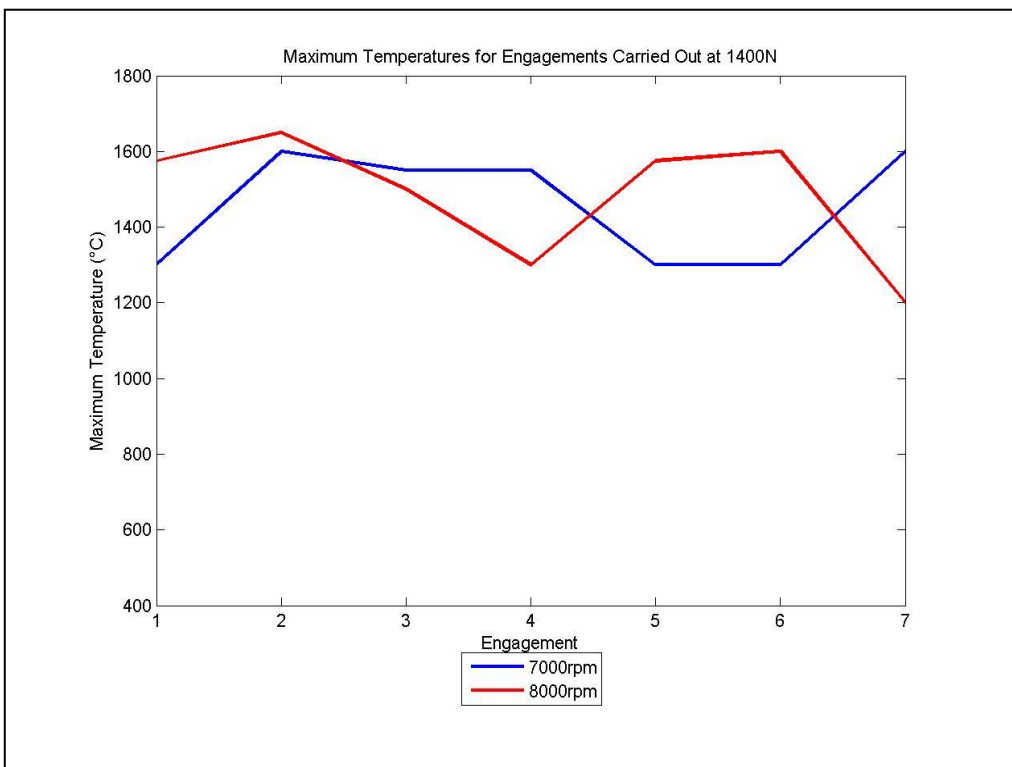


Figure 4.16 – Maximum Temperatures Recorded for 1400N Load Case

As the high temperatures observed during the 1400N clamp load test existed in well-defined hot bands, it can be assumed that contact is fully localised in the region of the hot band. This implies that most, if not all, of the frictional work is done in these hot bands and as such the hot band represents the effective friction radius (EFR). The torque output is related to the effective friction radius by Equation 4.2.

$$T = P\mu r_{eff} \quad (4.2)$$

Where; T – Torque (Nm)
 r_{eff} – Effective Friction Radius (m)

It can clearly be seen from Equation 4.2 that if the effective friction radius changes, the torque output will be affected even if all other factors remain constant. The COF is however known to change with the surface morphology but the clamp load remains fairly constant through the use of a PID controller operating the actuator.

Figure 4.17 shows the evolution of the hot band formed during Engagement5 at a speed/load combination of 8000rpm/1400N. It should be noted that the white circles indicating the position of the viewing hole vary slightly in size and position due to vibrations causes the IR mirror to move during the recording. The position of the viewing hole in relation to the camera therefore changes slightly in all three axes altering the size (due to zoom) and position of the recorded viewing hole.

At $t=0.80s$ the temperature of the friction surface is still low and no hot band can be seen. At $t=1.06s$ the hot band can be seen to be forming. At $t=1.16s$ the maximum temperature of the hot band is reached where the hot band is very narrow. By $t=1.29s$ the temperature of the hot band has reduced due a combination of heat being conducted away and the energy input level falling with the ever decreasing rotational speed of the rotating mass. Radial conduction causes the hot band to become wider along with a lower level of thermal expansion resulting from the lower temperature, increasing the real contact area. By $t=1.37s$ the hot band has approximately doubled in width and has a much lower temperature. The hot band is no longer visible after $t=1.57s$.

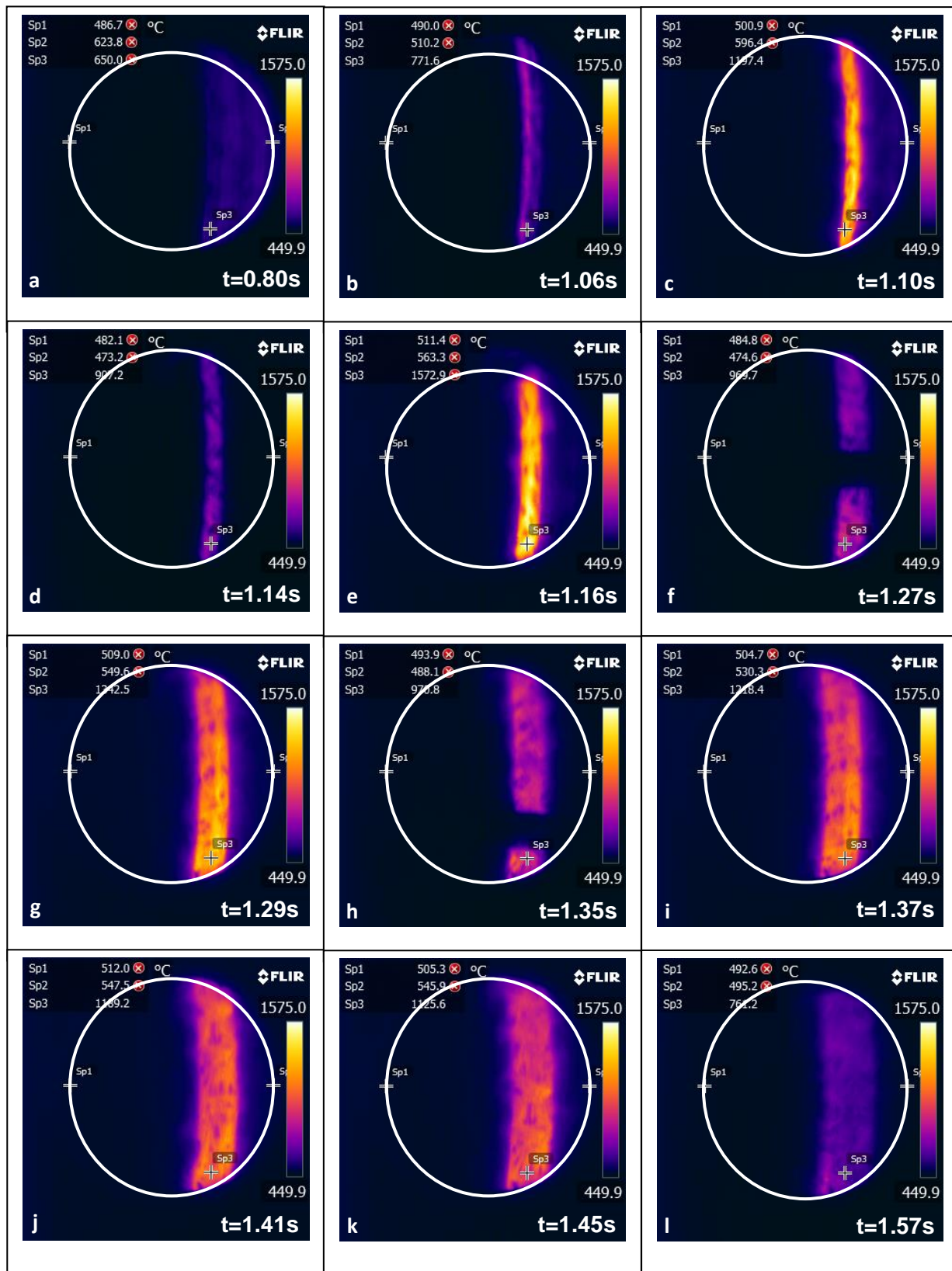


Figure 4.17 – Hot Band Evolution During Engagement5 for 8000rpm/1400N Speed/Load Combination

The evolution of the hot band temperature does not rise to a maximum and then fall in a completely consistent manner. It can be seen from Figure 4.17 that at $t=1.14s$ and $t=1.27s$ the temperature of the hot band is lower than expected. This type of behaviour was seen for all engagement tests that produced a distinct hot band. There are two likely contributory factors to this behaviour the first of which being small variations in the clamp load applied. The PID controller used to regulate the clamp load works on a load cell output which was seen to produce a large amount of noise. As such, the clamp load will not be perfectly constant and therefore a small amount of power dissipation fluctuation will occur, affecting the friction surface temperature. The influence of the clamp load variation will be very small compared to surface morphology effects. It is probable that the morphology is in a state of flux between type II and type III which in turn affects the COF. Again the power dissipation level will be affected causing changes in friction surface temperature.

Figure 4.17 also shows that once the hot band has formed it does not migrate to a different area of the friction surface. This was seen for all engagements tests that produced a distinct hot band. The effective friction radius therefore does not change during a single clutch-plate engagement.

Figure 4.18 shows images of the maximum recorded temperatures recorded for the 1400N load case. Based on the pixel location of Sp1 and Sp2 for the thermal camera images and how they relate to the geometry of the clutch plates, it was possible to calculate the radial position of the centre of the hot band and therefore the effective friction radius. This was done for the 1400N load case as all engagements resulted in definitive hot bands but the same was not true for the 1000N and 1200N load cases. Figure 4.19 shows the results of this analysis for the 1400N load case.

Figures 4.18 and 4.19 show the extent to which the effective friction radius was observed to migrate between engagement tests. For both the 7000rpm and 8000rpm engagement tests, the effective friction radius moved from close to the inner radius of the rotating clutch plate for Engagement1 to near the outside radius of the clutch plate for Engagement7. Without carrying out further engagement tests with new clutch-plate pairs, it is impossible to conclude whether the migration of the effective friction radius from inner to outer radius is a function of the load case or simply a function of those particular clutch-plate pairs and their surface finishes.

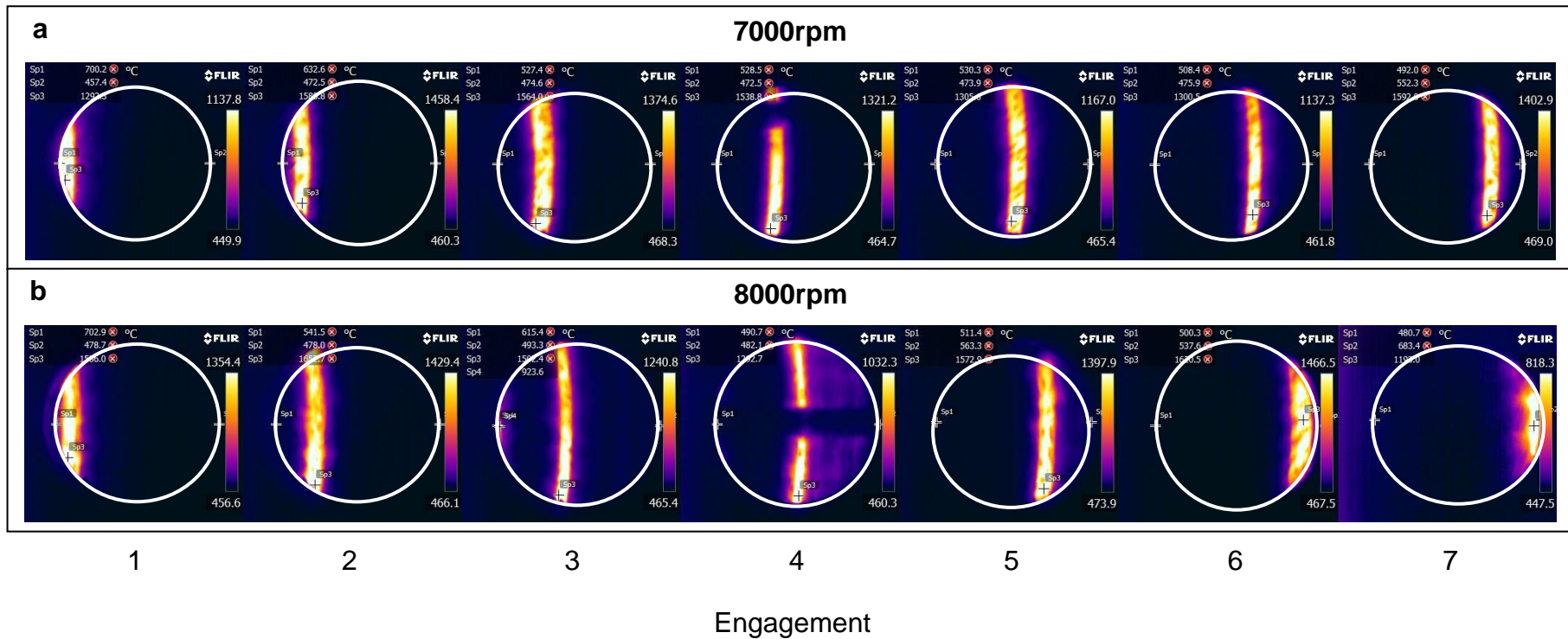


Figure 4.18 – Thermal Camera Images of Maximum Friction Surface Temperatures for 1400N Load Case at (a) 7000rpm and (b) 8000rpm

Note – Engagement3 for 8000rpm engagement test showed two hot bands but the central band is much hotter

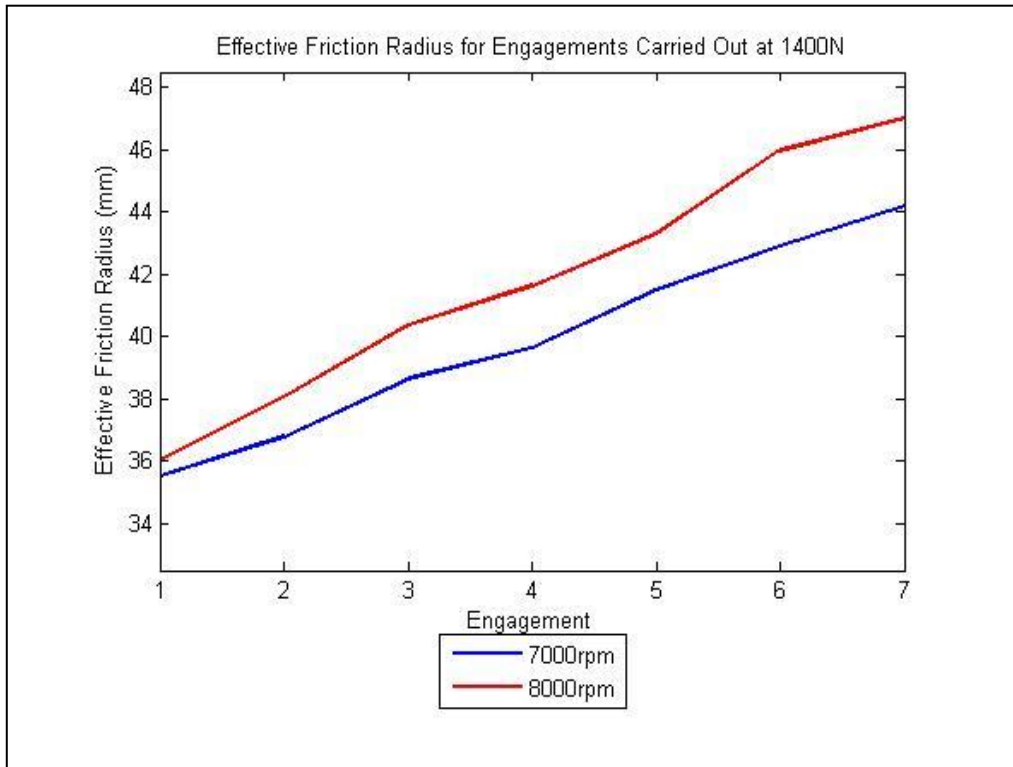


Figure 4.19 – Effective Friction Radius for 1400N Engagement Tests

What is clear however is that the effective friction radius migration could have a significant effect on the torque output of the clutch-plate pairs. Equation 4.2 is used, where the clamp load and COF have been set to constant values, to produce the values shown in Table 4.5 where the torque output at Engagement1 has been set to unity. The EFR values in red are estimates as the hot bands were partially covered as they lay partly outside the dimensions of the Ø12mm viewing hole.

	Engagement	1	2	3	4	5	6	7
7000rpm	EFR (mm)	35.52	36.80	38.65	39.65	41.50	42.92	44.20
	Torque	1.00	1.04	1.09	1.12	1.17	1.21	1.24
8000rpm	EFR (mm)	36.03	38.07	40.37	41.65	43.31	45.99	47.01
	Torque	1.00	1.06	1.12	1.16	1.20	1.28	1.30

Table 3.5 – Effect of Effective Friction Radius Migration on Torque Output
(Numbers in Red Indicate Estimated Values)

As no effective friction radius migration was observed during individual engagement tests, the torque instability during a single engagement is due to surface morphology changes alone. The inconsistency between engagement tests is most likely to be due to a combination of both effective friction radius migration and morphology effects. As the results presented in Table 4.5 illustrate, the migration of the effective friction radius between engagements can have a large effect on the torque output. Additionally, the effective friction radius may move to a region of the clutch-plate friction surface that has a different surface morphology to the previous region and therefore the evolution of the COF may be markedly different.

The hot bands will form due to surface asperities causing initial contact localisation and thermoelastic instabilities increasing the contact localisation. As the hot bands move between engagements, the surface asperity causing the previous hot band must have worn away for another surface asperity to become prevalent, where the next hot band forms. The wear could be due to either oxidation, abrasion or a combination of both. Given the temperatures of the hot bands, significant levels of oxidation would be expected but as the effective friction radius does not migrate during individual engagements, this appears to not be the case. However, it is possible that because the high temperatures have caused such high levels of thermal expansion, the hot band persists despite oxidation occurring. The significant thermal expansion would also greatly increase the normal load in the area of the hot band and hence could lead to abrasion of the friction surface. It is therefore possible that both oxidation and abrasion wear takes place simultaneously. It is however certain that at least one of these forms of wear must occur in order for the friction surface contact area to migrate between successive clutch-plate engagements.

The hot bands did not migrate during engagements due to the short time period being insufficient for wear to become dominant in comparison to thermal expansion. After the ten minute cooling period between engagements however, there will be no thermal expansion as the friction surfaces would have cooled to close to ambient temperature with a uniform temperature distribution resulting from thermal conduction (axial and radial). Wear during the previous engagement would have resulted in a friction surface recess at the previous contact point and in the absence of thermal expansion, contact is established elsewhere.

4.7 Summary

Clutch-plate friction pair engagement tests were carried out using the in-house SCID where six clutch-plate pairs were subjected to different speed and clamp load conditions. The results of the engagement tests show that the torque output is stable and consistent at low speed and clamp load combinations but becomes less stable and less consistent as the initial rotational speed and clamp load are increased.

Thermal imaging results have shown that increasing the initial rotational speed and clamp load combination leads to higher maximum surface temperatures. When the highest clamp load is applied, extreme hot bands are observed in excess of 1200°C. The temperature of the hot bands are much greater than the majority of the friction surface (~450°C) suggesting a large degree of contact localisation. It follows that all the frictional work is done in the region of the hot bands and therefore they indicate the location of the effective friction radius. The effective friction radius was not seen to migrate during individual clutch-plate engagements but did move between engagements. Wear of the friction surfaces must take place for the effective friction radius to migrate between engagements but the engagement time is too short for wear to cause effective friction radius migration during engagements.

The torque output instabilities observed during individual SCID engagement tests are most likely to be due to surface morphology changes alone as the effective friction radius does not migrate during single engagements. The inconsistencies in torque output observed between engagements are likely to be a product of both surface morphology changes and effective friction radius migration.

5. Clutch-Plate Friction Surface Characterisation

5.1 Introduction

Friction surface characterisation of new and used clutch plates was carried out using a combination of non-contact and contact techniques. White light interferometry and contact profilometry were used to examine the friction surface profile to assess factors such as roughness and waviness profiles. Scanning electron microscopy (SEM) was used to image the friction surface to permit examination of the surface structure and morphology whilst x-ray diffraction (XRD) was used to identify any compositional changes.

As an initial exercise, new and race-conditioned clutch plates (precise history unknown) were examined using white light interferometry and contact profilometry. The results of this work informed the surface profiles used in the thermomechanically coupled finite element analysis (Chapter 7).

Prior to SCID testing, new clutch plates were examined using contact profilometry, SEM and XRD. The same analyses were carried out on the clutch plates after SCID testing, allowing a direct comparison of the friction surfaces before and after the surfaces had been subjected to frictional work.

5.2 Characterisation Techniques

5.2.1 White Light Interferometry

Interferometry is the study of the interference between wavefronts of light beams that have originated from the same source. An interferometer is an optical device that divides a wave of light produced from a single source into two waves and recombines them to create an interference pattern. Figure 5.1 shows a schematic of the principle components of an interferometer [54]. The beamsplitter splits the light wave produced by the light source into two waves. The wave that travels along the reference arm is reflected by the reference mirror whilst the other wave is reflected by the sample. The beamsplitter then recombines the two waves and an interference pattern is produced.

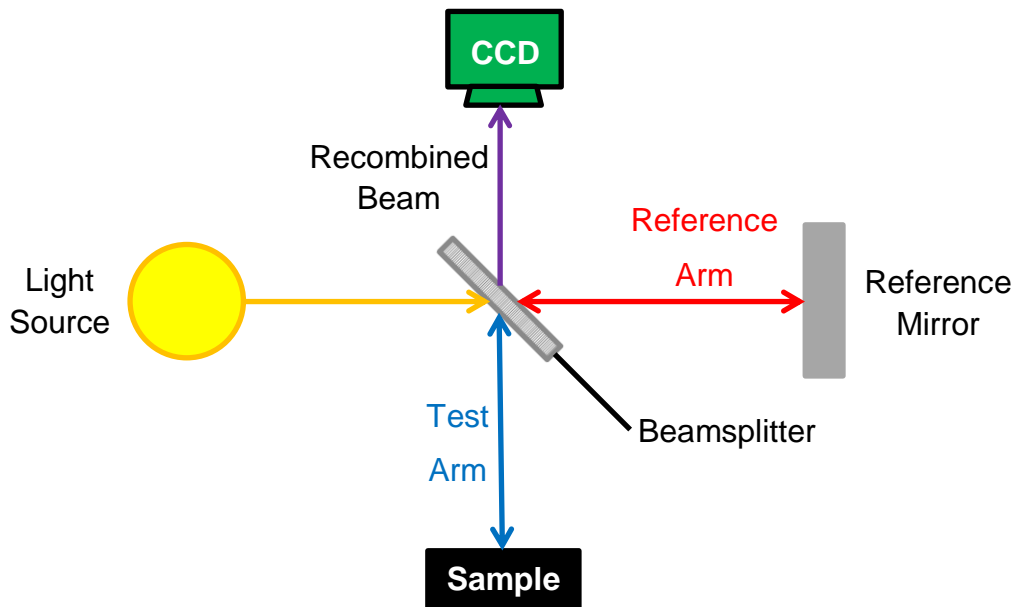


Figure 5.1 – Schematic of Key Interferometer Components [54]

The difference in optical path lengths that the beams travel in the reference and test arms is known as the optical path difference (OPD). Figure 5.2 shows the intensity of the recombined wave measured by the charge-coupled device (CCD) camera as a function of the OPD [55]. A 3D image of the sample surface can be obtained by vertically scanning the sample and by determining the vertical position at which the intensity is at its peak for each pixel, the height of the scanned surface at each pixel can be calculated. This is known as vertical scanning interferometry (VSI) or coherence-probe microscopy. Using a monochromatic light source has the drawback that a change in the optical path difference of one wavelength (eg. $0.5\mu\text{m}$ for green light) causes phase ambiguities in the interference pattern [55]. This leads to a limitation in the measurable depth variation of the sample. Using white light overcomes this issue.

A Veeco Wyko NT3300S interferometer was used to scan the clutch-plate friction surfaces. The clutch plates were placed underneath the white light beam such that the centre of the friction surface (radially) was scanned. Vision32 software was used to process the measured data. A magnification value closest to unity was used to allow a large area to be scanned using a vertical scan step size of $10\mu\text{m}$. Any effects due to tilt were removed and a median filter applied to obtain the surface roughness parameter values. The roughness parameters of interest are listed in Table 5.1.

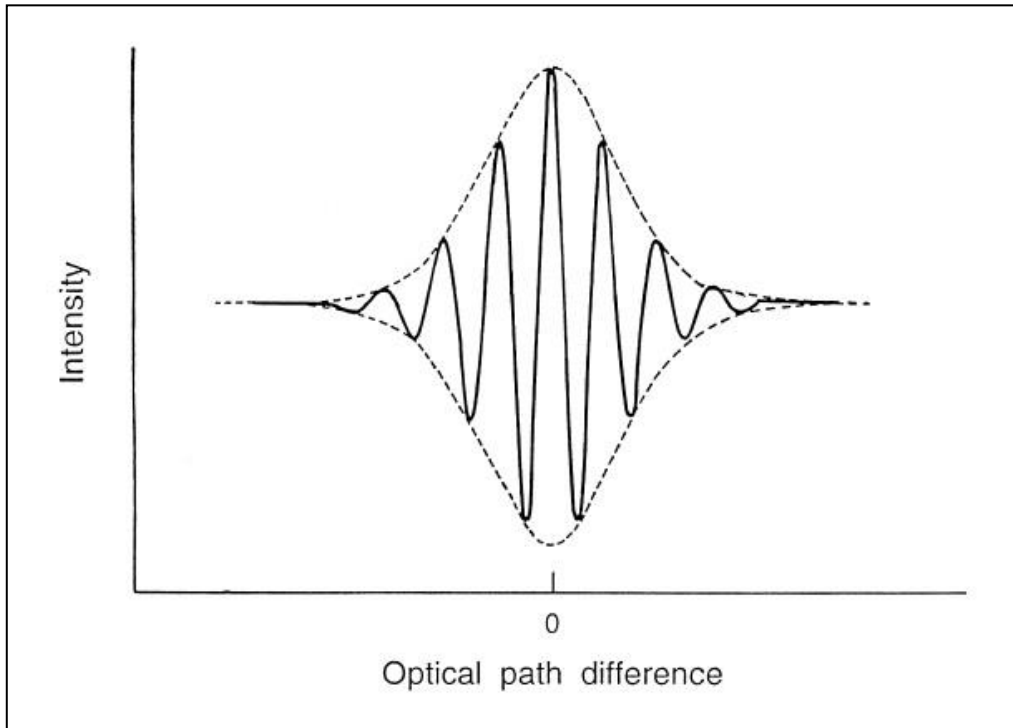


Figure 5.2 – Intensity of Recombined Light Wave as a Function of Optical Path Difference [55]

Parameter	Name	Definition
R_a	Average Roughness	The average surface deviation from the mean surface height. A value of 0 would indicate a perfectly flat surface.
R_p	Maximum Peak Height	The height of the largest surface peak above the average surface height.
R_v	Maximum Valley Depth	The depth of the largest surface valley/void below the average surface height.
R_t	Maximum Peak-to-Valley Distance	$R_t = R_p - R_v$
R_{sk}	Skewness	A measure of the surface asymmetry about the mean surface height. Negative skewness indicates a predominance of valleys and positive skewness indicates a spiky surface.

Table 5.1 – Surface Roughness Parameters

5.2.2 Contact Profilometry

Figure 5.3 shows a schematic of the contact profilometer used in this investigation [56]. The traverse unit contains the motor, gearboxes and control circuits required to move the gauge and stylus, and communicate data to the processor control unit. The gauge contains an inductance transducer and as the gauge (and therefore stylus) is moved horizontally, the vertical motion of the diamond-tipped stylus as it moves over the sample produces voltage changes in the transducer. The voltage changes are converted to height changes and because the gauge is moved at a constant horizontal speed, the surface profile of the sample can be determined.

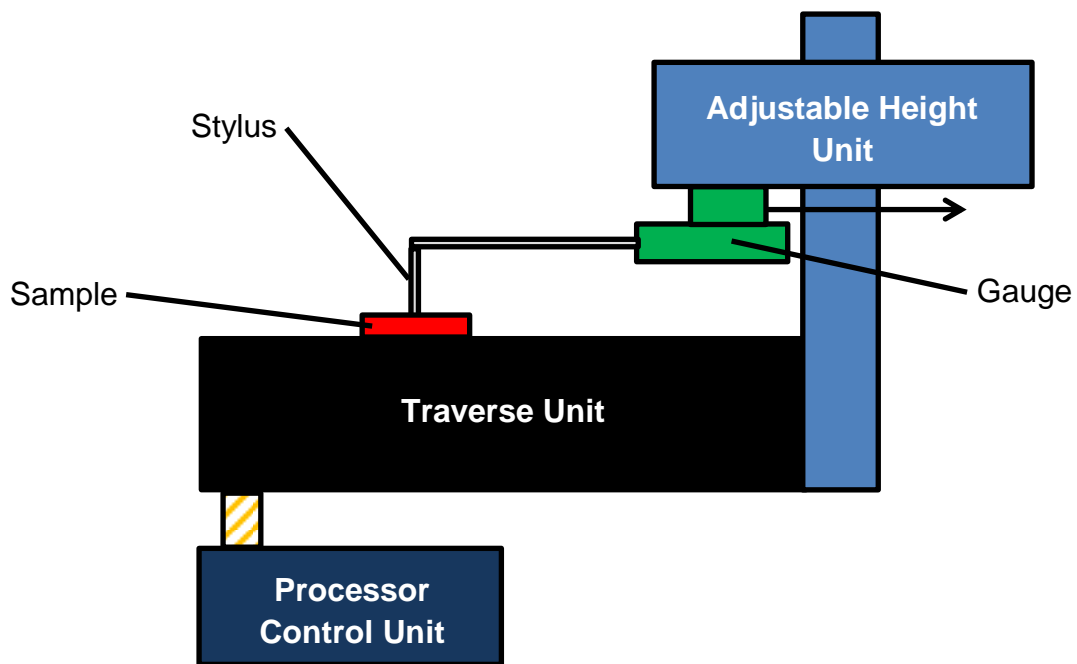


Figure 5.3 – Key Components of Contact Profilometer [56]

A Form Talysurf 120L Contact Profilometer was used to measure the clutch-plate friction surface profiles. The clutch plates were placed on the traverse unit and the stylus moved to contact the friction surface at the inner radius. A trace was then recorded from the inner to outer radius. Talymap Gold software was used to process the data. Any effects of tilt and noise were removed and a low-pass Robust Gaussian filter with a 0.8mm wavelength cut-off was applied to isolate any waviness profile from the short wavelength roughness profile. The waviness parameters of interest are listed in Table 5.2.

Parameter	Name	Definition
W_p	Maximum Peak Height	Height of the largest peak above the mean friction surface height
W_v	Maximum Valley Depth	Depth of the largest valley below the mean friction surface height
W_z	Maximum Peak-to-Valley Distance	$W_z = W_p - W_v$
W_{sm}	Waviness Profile Wavelength	Mean distance between waviness profile peaks. The number of peaks is therefore equal to $16/W_{sm}$ (friction surface is 16mm wide)

Table 5.2 – Surface Waviness Parameters

A Form Talysurf PGI 800 was used for the post-SCID surface measurements as the Form Talysurf 120L was undergoing repairs. The PGI 800 is an updated version of the 120L and the method for measuring the surface profile parameters was identical. The results were processed in the same way for both cases using Talymap Gold software.

5.2.3 Scanning Electron Microscopy

A scanning electron microscope uses a beam of electrons to produce a magnified image of the surface it is scanning. Figure 5.4 shows a schematic of the key elements of a scanning electron microscope [57]. Electrons are generated by the cathode and accelerated by the voltage difference with the anode. Scanning coils create a magnetic field which, through variation of the coil voltage, controls the direction of the beam upon the specimen. A small defined area can thus be scanned.

When the electrons interact with the specimen, two types of electron are emitted: secondary electrons (SE) and backscattered electrons (BSE). Secondary electrons are electrons that are excited within the atoms of the specimen surface and break free whilst backscattered electrons are the original electrons which are reflected by the specimen surface atoms. X-rays are also emitted but these are produced from below the specimen surface.

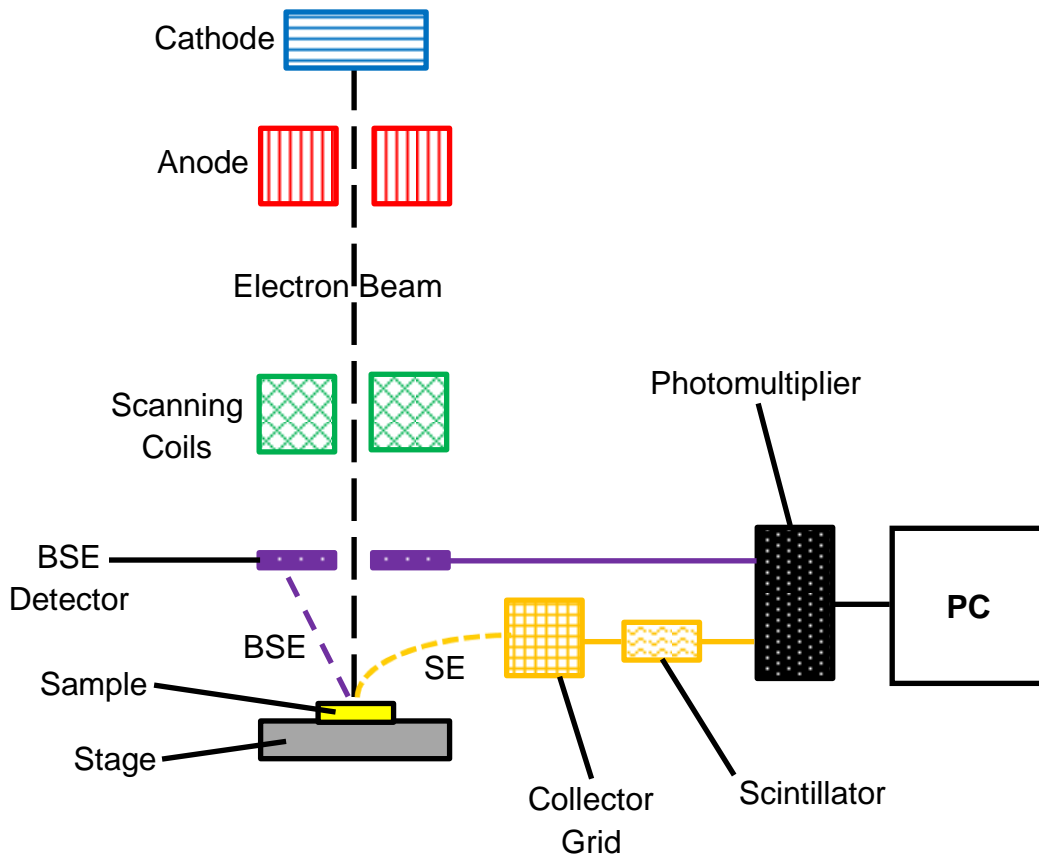


Figure 5.4 – Key Components of a Scanning Electron Microscope [57]

Secondary electrons have low energy and are accelerated by a positively-charged collector grid and the electrons then interact with a scintillator. This produces a current which is amplified by a photomultiplier. A black and white image of varying contrast is formed dependent on the number of electrons interacting with the scintillator producing a current. The backscattered electrons have a higher energy and are detected by a scintillator or semi-conductor.

A Carl Zeiss EVO MA15 SEM was used at a magnification value of 100. The clutch plates were placed on a stage in the measurement chamber and the chamber was then closed. The measurement chamber was evacuated of air as a vacuum is required. Due to the low energy of the electrons, any air molecules within the measurement chamber would interact with the electrons and affect their direction of motion and levels of kinetic energy. The electron beam is switched on once the pressure has fallen below 1.3×10^{-4} Pa (a complete vacuum cannot be practically achieved). The desired starting location was found using an optical camera within

the machine and the scan was performed over a defined area. SmartSEM was used to control the SEM. For each clutch-plate surface, 3.009x3.009mm sections of the surface were scanned in either 9x2 or 8x3 grids depending on the scan reference points on the clutch plate surfaces. These images were then stitched together (with some overlap) using SmartStitch to produce images showing the full radial width of the friction surface.

5.2.4 X-Ray Diffraction (XRD)

X-rays and their diffraction can be used to study the crystal structure and atomic spacing of a material through the application of Bragg's Law [58]:

$$2d_a \sin\theta = n_r \lambda \quad (5.1)$$

Where: d_a – Atomic Spacing (m)
 θ – Angle of Incidence Between X-Rays and Sample Surface (deg)
 n_r – Order of Reflection
 λ – Wavelength of X-Rays (m)

X-rays are diffracted by crystalline materials as their wavelengths are in the same order of magnitude as typical crystal atomic spacing. Constructive interference of the diffracted x-rays occurs when n is equal to an integer. By using a monochromatic x-ray source and rotating the sample (or x-ray source) through progressive angles (θ), the diffracted x-rays can be detected and information regarding the crystal structure of the material can be obtained based upon the detected intensity at different angles.

Figure 5.5 shows a schematic of how the PANalytical X'Pert MPD XRD machine used in this investigation works [59]. The sample was placed in a holder such that the friction surface was held parallel to the x-ray beam and detector at 0°. The beam scanned an area of 15x15mm centred as close as possible to the mean geometric radius of the friction surface. The beam could not be centred exactly on the mean geometric radius as the sample holder grips a small section of the friction surface and hence that section cannot be scanned. The x-ray source and x-ray detector

rotate around the stationary sample at the same rate and the intensity of the diffracted beams are measured. Data Collector software was used to operate the XRD machine and retrieve the data whilst HighScore Plus was used to export the data as an ASCII file. Matlab was then used to process and present the results.

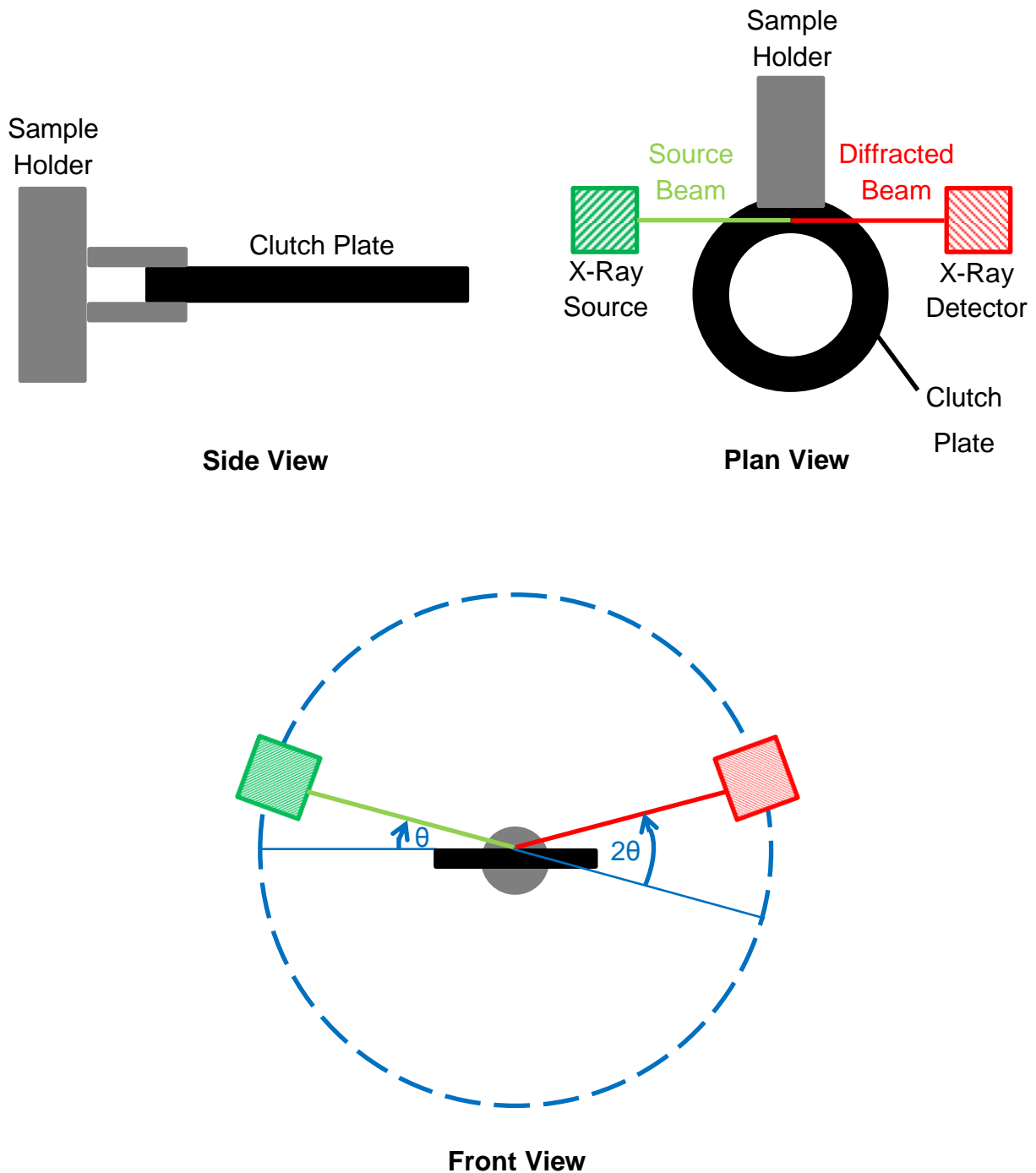


Figure 5.5 – Setup and Operation of XRD Machine [59]

5.3 New Clutch Plates – Initial Examination

As an initial exercise to inform the surface profiles used in the thermomechanically coupled finite element analysis (TCFEA) presented in Chapter 7, two new clutch plates (one driving plate and one driven plate) were examined using white light interferometry and contact profilometry. Interferometry scans were taken at five points equally spaced around the circumference of the friction surfaces (72° apart) centred at the mid-radius of the friction surfaces as shown in Figure 5.6. Profilometer traces were only taken at one circumferential position based on the white light interferometry results (discussed later in this section).

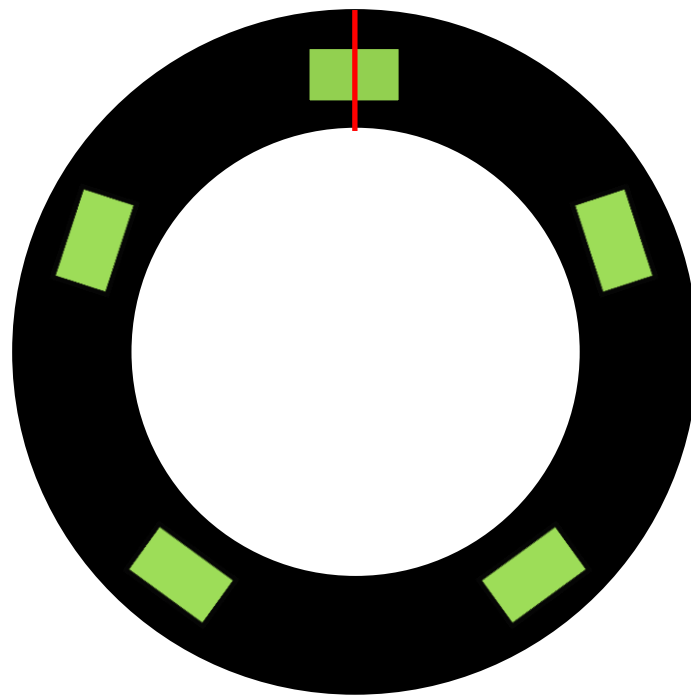


Figure 5.6 – Measurements Regions for White Light Interferometry (72° Apart) and Contact Profilometry

White Light Interferometer Scans:  Contact Profilometer Trace: 

The clutch plates are numbered within the clutch-plate pack such that the top driving plate nearest the Belleville spring (see Chapter 1.2) is Driving Plate 1. The next plate, which is the first driven plate, is Driven Plate 1 and so on.

The roughness parameter values obtained using white light interferometry are summarised in Table 5.3. The bottom surface of the driving plate and the top surface of the driven plate were examined.

Clutch Plate	Position	Reference	R _a (µm)	R _p (µm)	R _v (µm)	R _t (µm)	R _{sk}
Driving 1	1	NI-DR1-1R	9.12	12.90	-204.12	217.01	-4.95
	2	NI-DR1-2R	7.24	13.17	-203.38	216.55	-5.65
	3	NI-DR1-3R	9.72	13.28	-206.78	220.06	-4.33
	4	NI-DR1-4R	4.32	12.58	-171.70	184.27	-7.61
	5	NI-DR1-5R	0.32	8.99	-11.57	20.56	-4.48
Driven 1	1	NI-DN1-1R	0.56	10.38	-29.05	39.43	-8.44
	2	NI-DN1-2R	2.63	10.77	-83.13	93.90	-6.13
	3	NI-DN1-3R	5.52	13.78	-110.76	124.54	-4.62
	4	NI-DN1-4R	5.23	11.16	-141.29	152.44	-5.47
	5	NI-DN1-5R	5.09	8.61	-152.84	161.45	-5.60
Average			4.98	11.56	-131.46	143.02	-5.73

Table 5.3 – Roughness Parameter Values for New Clutch Plates (Initial Examination)

The results of the roughness analysis indicated a circumferential variability in all the roughness parameters with some areas having high roughness and deep voids with other areas showing the opposite. This suggests that even with processing and machining of the clutch plates, neither a perfectly flat nor smooth friction surface is achieved. Despite this variability, all the scans showed a similar trend to that shown in Figures 5.7 and 5.8 whereby there is no evidence of any initial bands or large surface perturbations and, regardless of the maximum void depths, the areas the voids occupy are relatively large.

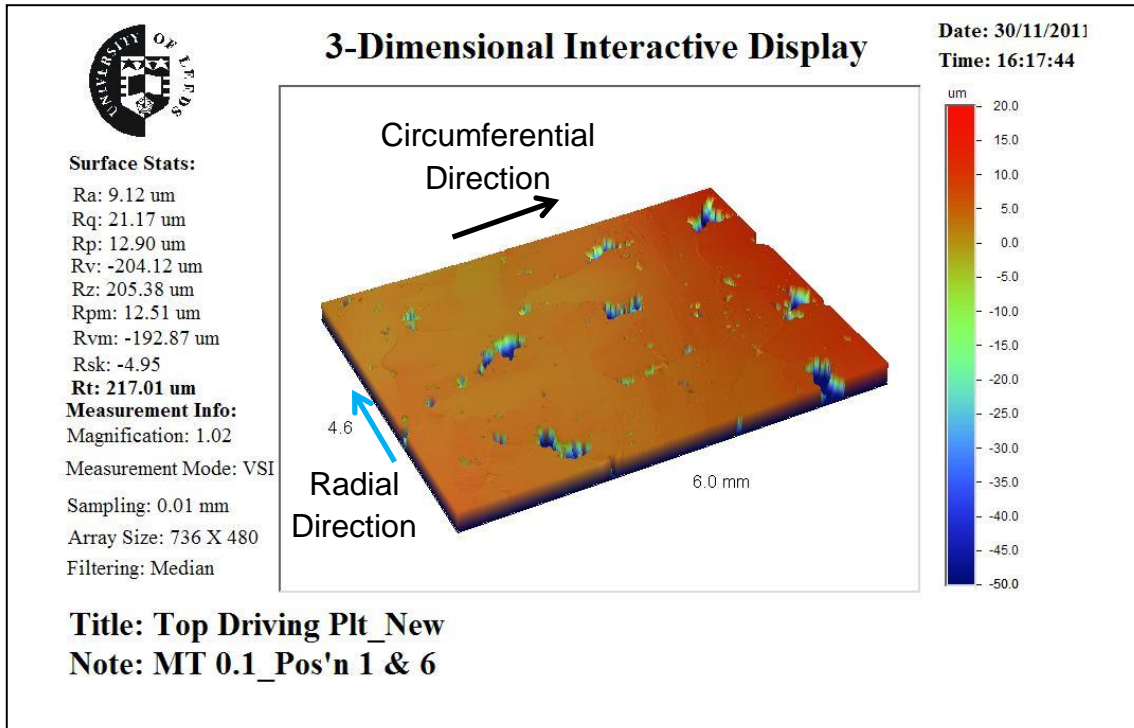


Figure 5.7 – Processed Image of Typical New Clutch-Plate Friction Surface (Initial Examination, Isometric View)

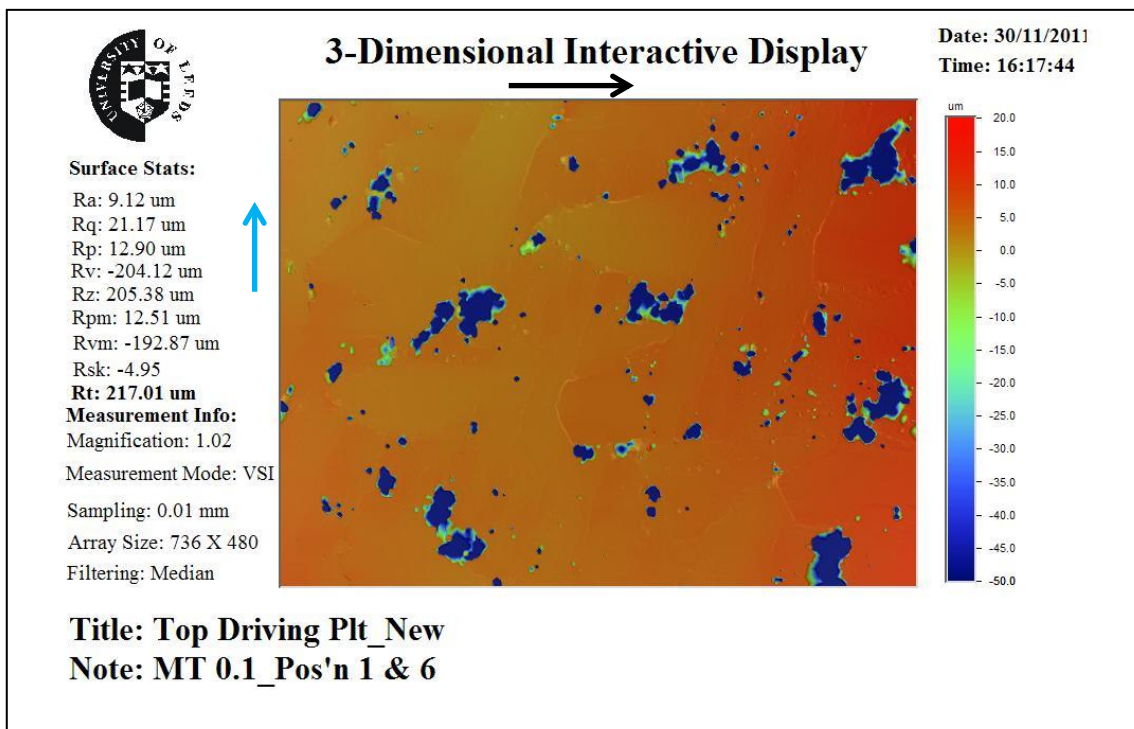


Figure 5.8 – Processed Image of Typical New Clutch-Plate Friction Surface (Initial Examination, Plan View)

As the previous analysis suggested that the new clutch-plate friction surfaces had no waviness profile, only one surface profile trace was carried out using contact profilometry at an arbitrary circumferential position. Table 5.4 shows the results of this analysis which also suggests the absence of any waviness profiles. A waviness profile wavelength (W_{sm}) could not be calculated for the driven plate showing that it did not have a waviness profile on its friction surface. The driving plate had such a large W_{sm} value and small peak height value (W_p) that it was unlikely that a genuine waviness profile was present on the friction surface. Figure 5.9 shows the profile trace for the driving clutch plate and it can clearly be seen that there is no distinct waviness profile: However, the trace shows a clear surface peak towards the outer radius which could lead to localised contact.

Clutch Plate	Reference	W_p (μm)	W_v (μm)	W_z (μm)	W_{sm} (mm)
Driving 1	NI-DR1-1W	0.155	-0.689	0.844	9.61
Driven 1	NI-DN1-1W	0.541	-0.160	0.701	N/A
Average		0.348	-0.425	0.773	9.61

Table 5.4 – Waviness Parameter Values for New Clutch Plates (Initial Examination)

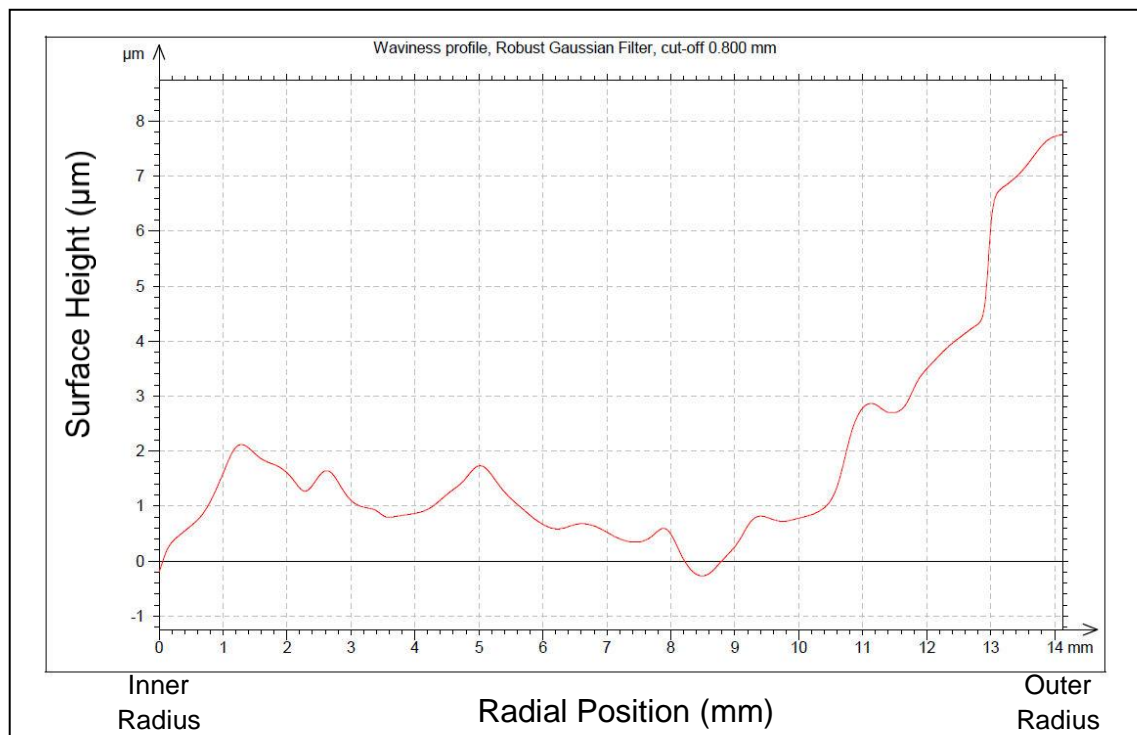


Figure 5.9 – Friction Surface Profile of Clutch Plate NI-DR1-1W (Initial Examination)

5.4 Used (Race-Conditioned) Clutch Plates – Initial Examination

Interferometry and contact profilometry were carried out on a set of used clutch plates to assess their roughness and waviness characteristics. The exact history of the used clutch plates was unknown except that the clutch-plate pack had been used for at least one full race weekend. Examination of these race-conditioned clutch-plate friction surfaces allowed a comparison to be made with the new clutch-plate surfaces that were discussed in Chapter 5.3, with the aim of gaining a preliminary understanding of how frictional work changes the characteristics of the friction surfaces. SEM and XRD were not used as the time and cost could not be justified for only a preliminary analysis.

The race-conditioned clutch-plate pack was from an older clutch design with only three driven and four driving plates. Using white light interferometry, five equally spaced interferometer scans were taken circumferentially for each friction surface centred at the mean geometric radius. No significant circumferential differences of the roughness parameters were observed so an average of the values was calculated for each clutch-plate friction surface. These results are shown in Table 5.5.

Clutch Plate	Surface	Reference	R_a (µm)	R_p (µm)	R_v (µm)	R_t (µm)	R_{sk}
Driving 1	Bottom	UI-DR1-BR	1.764	13.000	-131.886	144.888	-12.404
Driven 1	Top	UI-DN1-TR	1.616	9.872	-131.290	141.162	-12.700
	Bottom	UIDN1-BR	2.658	7.822	-163.928	171.248	-9.176
Driving 2	Top	UI-DR2-TR	1.478	4.438	-151.542	155.982	-12.638
	Bottom	UI-DR2-BR	2.072	6.520	-173.116	179.632	-10.636
Driven 2	Top	UI-DN2-TR	3.544	7.720	-187.898	195.618	-9.816
	Bottom	UI-DN2-BR	2.972	7.138	-179.944	187.122	-9.438
Driving 3	Top	UI-DR3-TR	3.040	9.668	-180.268	189.940	-9.382
	Bottom	UI-DR3-BR	3.474	9.962	-180.372	190.334	-8.734
Driven 3	Top	UI-DN3-TR	3.132	10.542	-204.316	214.838	-9.344
	Bottom	UI-DN3-BR	1.792	7.772	-190.658	198.432	-13.888
Driving 4	Top	UI-DR4-TR	2.786	8.952	-210.666	219.616	-10.298
Average			2.527	8.617	-173.842	182.443	-10.757

Table 5.5 – Roughness Parameter Values for Used (Race-Conditioned) Clutch Plates (Initial Examination)

In comparison to the new clutch plates, the average roughness value of the race-conditioned clutch plates is lower. Combined with the increase in negativity of the average skewness value (R_{sk}), this suggests that many of the original surface asperities have been worn away and the surface has become smoother as the result of frictional work. Both the average values of maximum void depth (R_v) and maximum peak height (R_p) are smaller in magnitude than for the new clutch plates and the size of their relative areas as a proportion of the total surface, are significantly smaller. This supports the idea that wear debris formed by wear of the surface asperities could be filling in the deep voids. This is further illustrated in Figures 5.10 and 5.11 which show typical scans of the used clutch plate friction surfaces.

Figures 5.10 and 5.11 also show that there appears to be a regular undulation of the friction surface in the radial direction that was not seen with the new clutch plates. This could have been caused by banding effects leading to localised contact and hence wear in a finite number of bands across the friction surface. Once these bands have worn away, contact would move to another band and eventually a regular wavy profile would be formed on the surface.

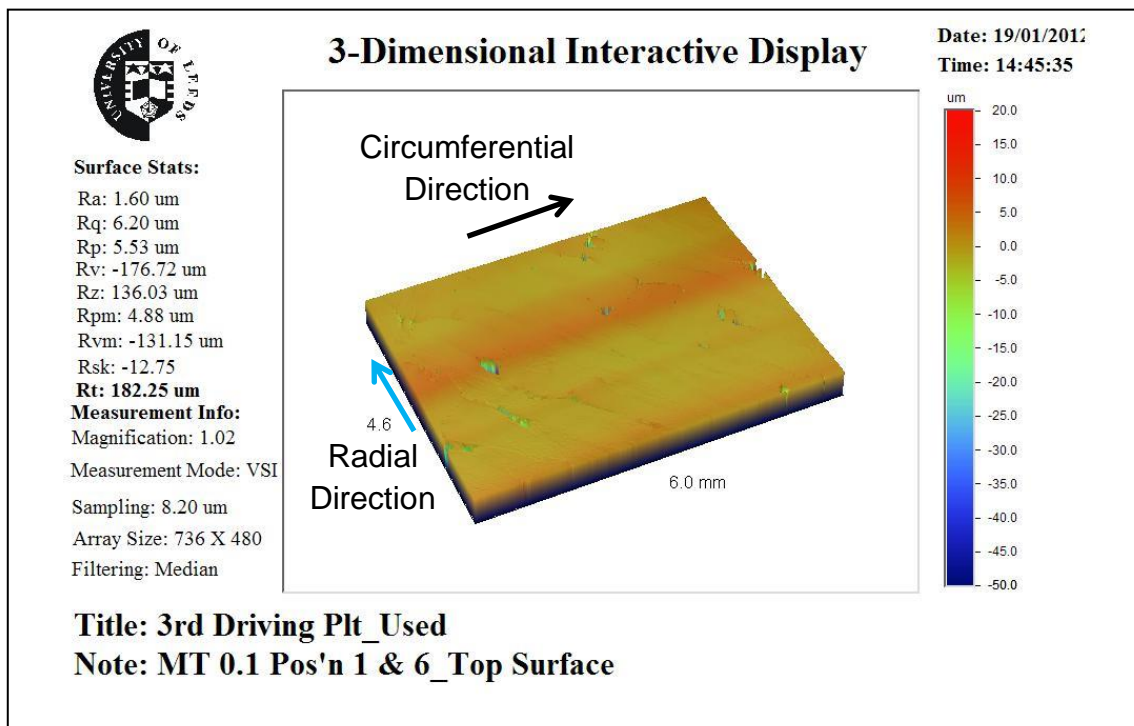


Figure 5.10 –Processed Image of a Typical Used (Race-Conditioned) Clutch-Plate Friction Surface (Initial Examination, Isometric View)

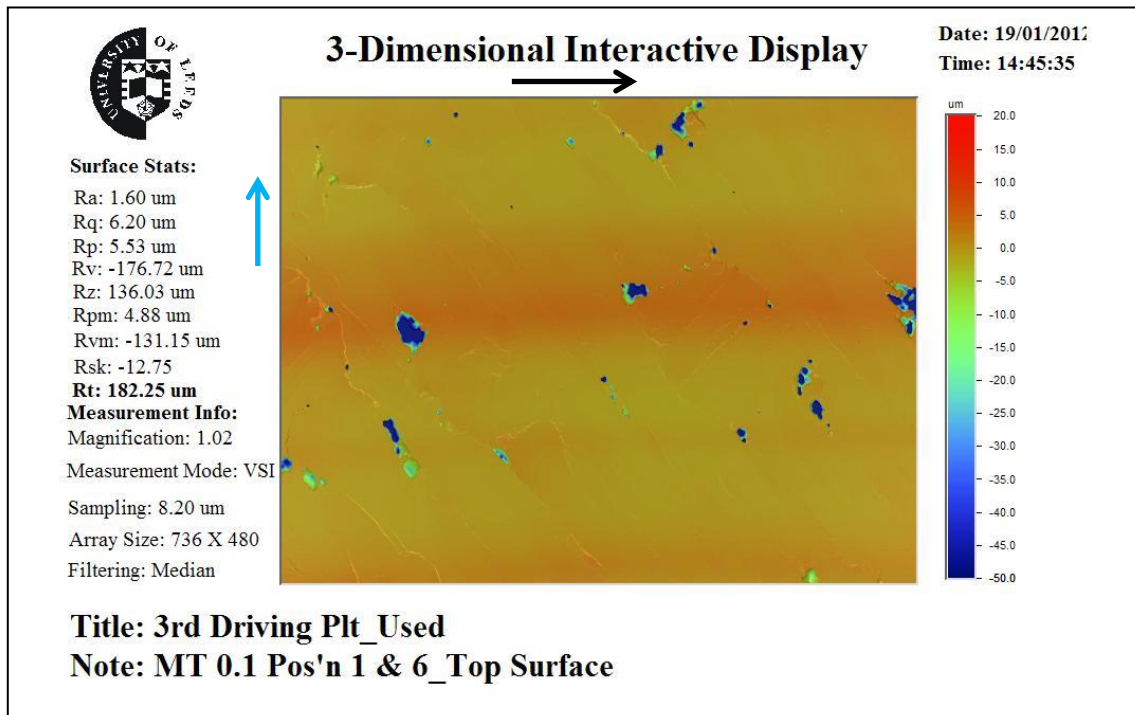


Figure 5.11 – Processed Image of a Typical Used (Race-Conditioned) Clutch-Plate Friction Surface (Initial Examination, Plan View)

Contact profilometry was also carried out on the race-conditioned clutch plate friction surfaces to measure any waviness parameter values and establish if there was any regularity between the clutch plates. As no significant circumferential differences were found in the roughness analysis, only a single profilometer trace was taken for each friction surface at an arbitrary circumferential position. The results of the profilometer tests are shown in Table 5.6.

In comparison to the new clutch plates, all used clutch plates showed a waviness profile that permitted a W_{sm} value to be calculated. Based on their W_{sm} values, the results highlighted in Table 5.6 were eliminated as statistical outliers. The other profiles showed that the average peak height and average valley depth of the waviness profiles were approximately $0.8\mu\text{m}$ and $0.7\mu\text{m}$ respectively with an average spacing between the peaks of 2.34mm equating to 6.84 wavelengths per friction surface. Figure 5.12 shows a typical trace for the used clutch plates showing a clear waviness profile. It can also be seen that the shape of the waviness profile is roughly sinusoidal. Based on these results, a sinusoidal waviness profile of $\pm 1\mu\text{m}$ amplitude and 7 peaks/ 6.5 wavelengths symmetrical about the mean geometric radius was used for the TCFEA models (see Chapter 7).

Clutch Plate	Surface	Reference	W_p (μm)	W_v (μm)	W_z (μm)	W_{sm} (mm)
Driving 1	Bottom	UI-DR1-BW	0.894	-0.839	1.733	2.39
Driven 1	Top	UI-DN1-TW	1.020	-0.494	1.514	1.91
	Bottom	UI-DN1-BW	0.620	-0.648	1.268	1.85
Driving 2	Top	UI-DR2-TW	0.553	-0.571	1.124	2.56
	Bottom	UIDR2-BW	0.552	-0.502	1.054	2.41
Driven 2	Top	UI-DN2-TW	0.677	-0.660	1.337	2.45
	Bottom	UI-DN2-BW	0.897	-1.240	2.137	5.01
Driving 3	Top	UI-DR3-TW	0.994	-0.867	1.861	2.16
	Bottom	UI-DR3-BW	1.160	-0.987	2.147	3.16
Driven 3	Top	UI-DN3-TW	1.040	-1.110	2.150	4.26
	Bottom	UI-DN3-BW	0.971	-0.986	1.957	6.85
Driving 4	Top	UI-DR4-TW	0.813	-0.826	1.639	2.67
Average			0.809	-0.710	1.520	2.34

Table 5.6 – Waviness Parameter Values for Used (Race-Conditioned) Clutch Plates (Initial Examination)

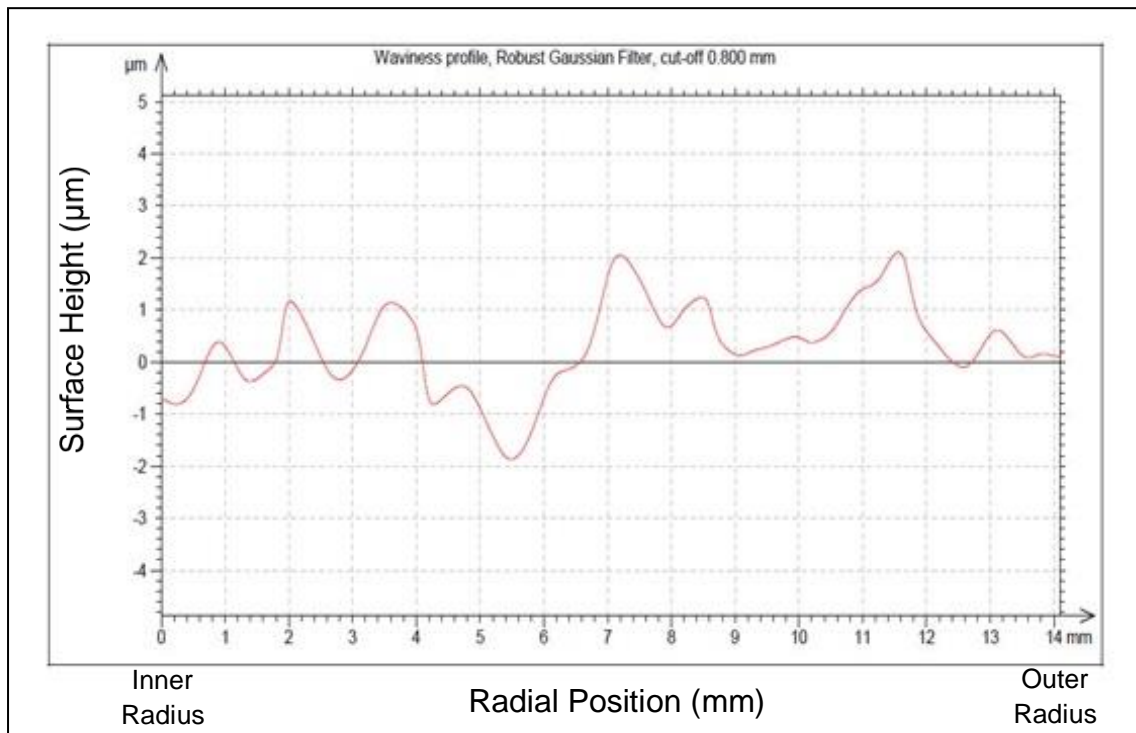


Figure 5.12 – Typical Friction Surface Profile of a Used (Race-Conditioned) Clutch Plate (Initial Examination)

5.5 New Clutch Plates – Prior to SCID Testing

Prior to SCID testing, a total of six new clutch-plate pairs were assigned for testing and only the friction surfaces that would be contacting each other were examined. See Chapter 4.2 for details regarding the clutch-plate pairs and their testing conditions. Digital photographs of the friction surfaces were taken before and after SCID testing to record the surface condition.

White light interferometry was not used on these new clutch plates as the same information regarding the roughness of the friction surfaces could be obtained using contact profilometry. As the latter also allowed the waviness parameters to be determined with the same measured data, the use of white light interferometry became unnecessary. A high-pass Gaussian filter with a 0.8mm wavelength cut-off was used to isolate the roughness profile from any long wavelength waviness profile.

The clutch plates were sufficiently small and thin that they were able to be mounted in both the SEM and XRD machine as whole plates. The only modification required was to cut off one of the external teeth on each driving plate to give the holder in the XRD machine a flat surface to grip onto. The friction surfaces did not require any special coatings to facilitate the scans. These two factors meant that the clutch plates could be examined without interfering with the friction surfaces, so a direct comparison of the surfaces before and after SCID tests was possible.

The clutch plates were marked to ensure that the same area of the friction surface was examined before and after SCID testing. For all surface examination techniques only one area of the friction surface was examined with respect to the circumference. With reference to Figure 5.6, the white light interferometry scan (top scan only) and contact profilometer positions are analogous to the XRD/SEM scans respectively.

5.5.1 Surface Condition

Figure 5.13 shows the clutch-plate pair B2 prior to SCID testing. As can be seen from the digital photographs, the friction surfaces appear to be smooth and uniform with no apparent surface deformities or asperities. This was the case for all the new clutch plates used for SCID testing. The profilometer traces and SEM/XRD scans were taken at the location of the missing external tooth on the driving plates and the location of the internal tooth marked with black ink for the driven plates.

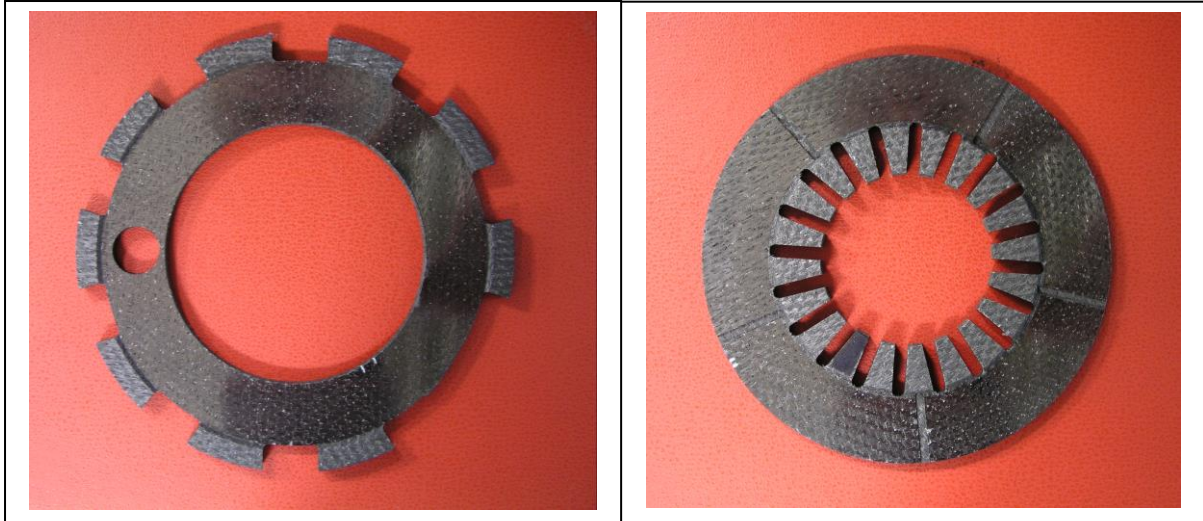


Figure 5.13 – Clutch-Plate Pair B2 Prior to SCID Testing

5.5.2 Roughness and Waviness Characteristics

Table 5.7 shows the results of the roughness analysis of the new clutch plates whilst Table 5.8 presents the results of the waviness analysis.

Clutch Plate	Clutch Pack	Reference	R_a (μm)	R_p (μm)	R_v (μm)	R_t (μm)	R_{sk}
Driving 2	A	A2-DR	1.93	3.19	-12.90	16.10	-10.20
Driven 2		A2-DN	3.96	8.14	-19.90	28.00	-7.53
Driving 3		A3-DR	1.96	3.47	-11.00	14.50	-7.10
Driven 3		A3-DN	3.38	7.06	-16.40	23.50	-7.39
Driving 4		A4-DR	3.77	6.87	-17.40	24.20	-9.93
Driven 4		A4-DN	3.68	7.79	-17.20	25.00	-4.81
Driving 2	B	B2-DR	2.77	5.10	-15.10	20.20	-6.71
Driven 2		B2-DN	4.24	9.41	-25.90	35.30	-17.90
Driving 3		B3-DR	2.07	3.46	-12.20	15.70	-13.70
Driven 3		B3-DN	3.00	6.76	-14.20	20.90	-13.20
Driving 4		B4-DR	3.85	6.50	-17.40	23.90	-5.75
Driven 4		B4-DN	3.57	8.15	-13.40	21.50	-8.54
Average			3.18	6.33	-16.08	22.32	-5.26

Table 5.7 – Roughness Parameter Values of Clutch Plates (Pre-SCID Testing)

Clutch Plate	Clutch Pack	Reference	W_p (μm)	W_v (μm)	W_z (μm)	W_{sm} (mm)
Driving 2	A	A2-DR	0.751	-0.554	1.310	N/A
Driven 2		A2-DN	0.309	-0.601	0.910	N/A
Driving 3		A3-DR	0.930	-0.497	1.430	N/A
Driven 3		A3-DN	1.660	-3.530	5.190	10.20
Driving 4		A4-DR	21.800	-19.200	41.000	8.63
Driven 4		A4-DN	1.430	-1.530	2.960	3.61
Driving 2	B	B2-DR	0.880	-0.494	1.370	N/A
Driven 2		B2-DN	0.858	-0.619	1.480	7.41
Driving 3		B3-DR	0.362	-0.377	0.738	N/A
Driven 3		B3-DN	0.403	-0.393	0.796	N/A
Driving 4		B4-DR	23.000	-36.400	59.400	8.18
Driven 4		B4-DN	0.389	-0.809	1.200	4.23
Average			8.190	-10.348	18.538	7.043

Table 5.8 – Waviness Parameter Values of Clutch Plates (Pre-SCID Testing)

From the roughness analysis, the peak depth values are much lower than those obtained using white light interferometry in the initial analysis. This is due to two factors related to the analysis technique. Firstly, in comparison to interferometry, the stylus used in the profilometer cannot detect large void depths if the void area is small as the stylus has a finite physical size. Secondly, the Talymap Gold software uses ISO 4287 to calculate the roughness parameter values whereby the average of the five largest peaks or depths is used to calculate the R_p and R_v values. Although this is a drawback of using profilometry rather than interferometry for the roughness analysis, the same technique is used for both pre-SCID and post SCID testing analysis and the results are therefore directly comparable. Also the SEM analysis can provide qualitative evidence of any voids being filled by wear debris.

No waviness profile could be calculated for half of the friction surfaces examined. The surfaces that did not have a W_{sm} value were excluded from the average value calculations. The other results however suggest that a waviness profile may exist on the friction surface of the new clutch plates although the wavelengths are relatively

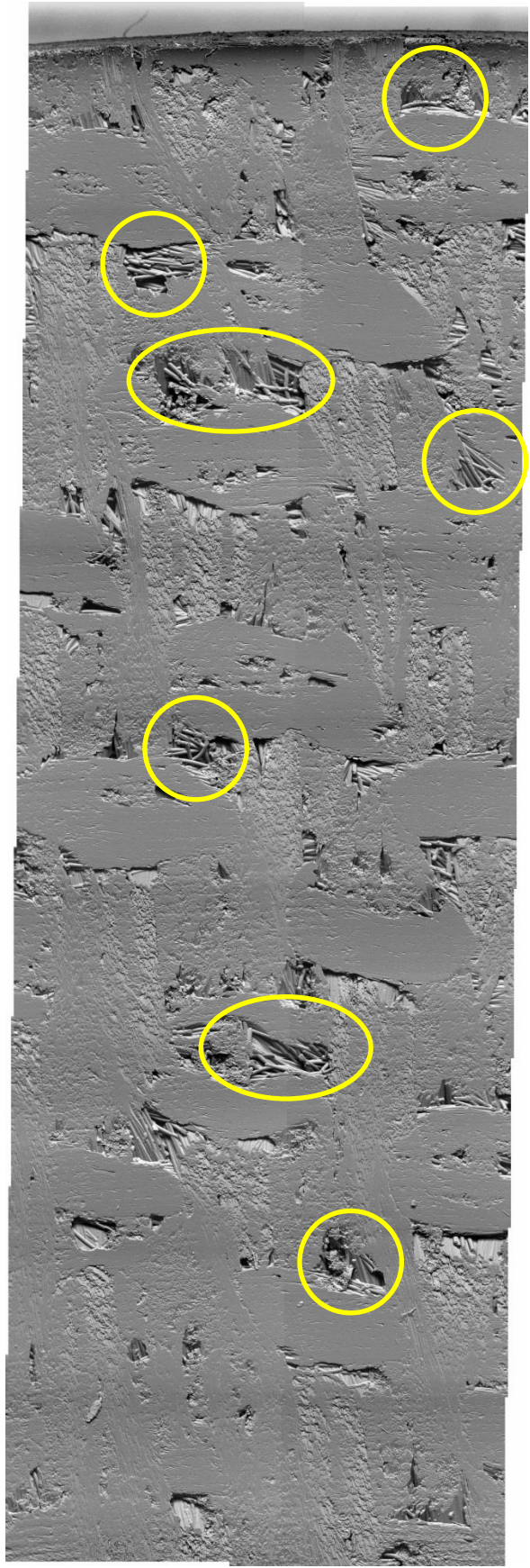
large in relation to the width of the friction surface. In comparison to the other measurements, the two results highlighted in Table 5.8 have very large W_p and W_v values and could be dismissed as outliers. The traces for these two measurements however did show an undulation of the friction surface with one large peak towards the centre suggesting that the clutch plates had not been well machined. The overall results of the waviness analysis therefore suggest a randomness of the surface finish which may or may not lead to localised contact.

5.5.3 Surface Structure & Morphology

The SEM images revealed the expected surface structure whereby the majority of the surface appears to be flat but there were numerous voids of varying areas. Within these voids, the SEM images show the sub-friction surface where the carbon fibres can clearly be seen due to insufficient matrix deposition in these areas. Figure 5.14 shows the BSE image for the friction surface of clutch plate A3-DN where the voids of largest areas have been highlighted.

The results of the XRD analysis are not discussed here as they do not offer any useful information on their own. Only by comparing the results of the XRD scans before and after SCID testing, can any useful conclusions be drawn. The results are therefore presented in Section 5.6.3.

Outer Radius



Inner Radius

Figure 5.14 – BSE SEM Image of Clutch Plate A3-DN (x100 Magnification)

5.6 Used Clutch Plates – After SCID Testing

The same examination procedures were carried out on the clutch-plate friction surfaces after SCID testing as were carried out prior to testing.

5.6.1 Surface Condition

Figure 5.15 shows the clutch-plate pair B2 after SCID testing. Wear dust was present on the surface of the driving plate but not the surface of the driven plate. This can be attributed to the cleaning grooves in the driven plates fulfilling their design purpose in removing wear dust from the friction interface. It is important to note however that similar amounts of wear dust were observed on all driving clutch plates after SCID testing and all driven plates were absent of wear dust on their friction surfaces. Given the greatly differing torque output characteristics of the clutch-plate pairs and that the radial location of the wear dust did not correlate with the locations of hot bands, the wear dust present after testing appears to have no effect on the friction behaviour of the clutch plates. The wear dust was very fine and easily removed suggesting that it was superfluous to the friction surface morphology. No wear tracks could be seen on this clutch-plate pair. Clutch-plate pairs A2 and A3 also showed no wear tracks on their friction surfaces.

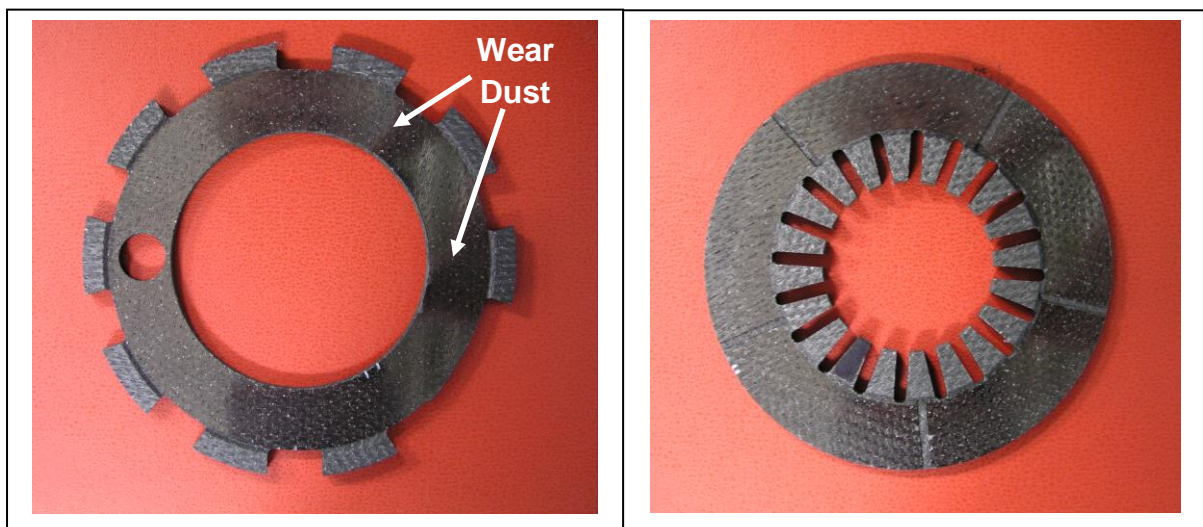


Figure 5.15 – Clutch-Plate Pair B2 After SCID Testing

The other clutch-plate pairs showed circumferential wear tracks on their friction surfaces. Figure 5.16 shows the clutch-plate pair A4 after SCID testing. This clutch-plate pair has a clear wear track towards the outer radius of both clutch plates where the radial position of the wear track is identical on each clutch plate friction surface. Clutch-plate pairs B3 and B4 showed similar wear tracks on their friction surfaces although the size and location of the wear tracks differed.

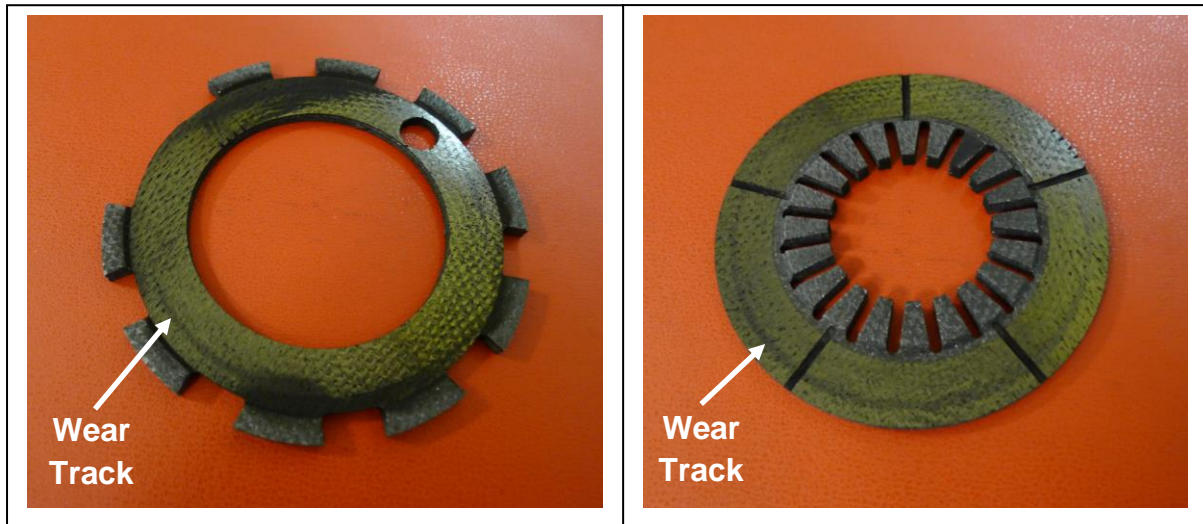


Figure 5.16 – Clutch-Plate Pair A4 After SCID Testing

To eliminate the possibility that the wear dust was produced from the hole machined through the driving clutch plates, a spare clutch-plate pair was subjected to SCID testing at 7000rpm/1400N (same conditions as A4). This clutch-plate pair (B1) had not been modified in any way. For the clutch-plate pair B1, similar amounts of wear dust were produced on the surface of the driving plate showing that the wear dust was not a consequence of any clutch-plate modifications but was purely a characteristic of the clutch plates.

Table 5.9 summarises the surface conditions of the clutch-plate pairs after SCID testing, the conditions under which they were tested and details of the hot bands observed. See Chapter 4.6 for further details regarding the locations of hot bands observed on clutch-plate pairs A4 and B4 and the maximum temperatures observed for all clutch-plate pairs.

Clutch-Plate Pair	Test Condition	Hot Band Temperatures (°C)	Hot Band Location	Wear Track Width	Wear Track Location
A2	7000rpm/1000N	~600°C	Variable	N/A	N/A
A3	7000rpm/1200N	~600°C-1500°C	Variable	N/A	N/A
A4	7000rpm/1400N	~1300°C-1600°C	R _i to R _o	Wide	R _o
B2	8000rpm/1000N	~750°C-1500°C	Variable	N/A	N/A
B3	8000rpm/1200N	~800°C-1700°C	R _i	Narrow	R _i
B4	8000rpm/1400N	~1200°C-1650°C	R _i to R _o	Wide	R _o

Table 5.9 – Summary of Wear Tracks for All Clutch-Plate Pairs

R_i – Inner Radius, R_o – Outer Radius

A clear relationship between maximum surface temperature and the formation of a wear track was seen. The clutch-plate pairs subjected to a 1000N clamp load did not produce a wear track but also did not experience consistently high maximum surface temperatures. For the clutch-plate pairs subjected to a 1400N clamp load that produced consistently high maximum surface temperatures, distinct wear tracks were observed. The wear tracks were formed towards the outer radius where the final hot band was seen. The fact that the wear tracks only appear with high temperature suggests that oxidation is responsible for the wear. However no wear track was observed for the 1200N load case at 7000rpm but was observed for the same load case at 8000rpm and if the difference in initial rotational speeds is the cause in the difference in wear, it would suggest that abrasion wear has occurred.

Clutch-plate pair B1, which was subjected to the same speed and clamp load combination as clutch-plate pair A4, showed a similarly sized wear track at its mid-radius as opposed to towards the outer radius as for clutch-plate pair A4. Obviously no temperature data could be recorded for this clutch-plate pair but the different wear track location suggests that the locations of the wear tracks produced are not a function of the speed/load combination.

The differences in observed wear tracks do not however clarify which wear mechanism is occurring, if not both. The high temperatures of the hot bands imply that oxidation will occur but the high temperature will also cause thermal expansion

thereby increasing the normal loads in the regions of the hot bands. As such, abrasion wear would also occur if the normal load was increased sufficiently. It is clear that the speed/load combination influences the extent of thermoelastic instabilities which in turn will affect temperature and thermal expansion levels which could lead to abrasion wear, oxidation or a combination of both.

5.6.2 Roughness & Waviness Characteristics

Table 5.10 lists the roughness analysis results for the clutch plates after SCID testing. Comparing these values to those presented in Table 5.7 for the clutch plates prior to SCID testing, on average the maximum peak height shows a small increase, the maximum valley depth shows a small decrease whilst the skewness value is almost identical. As discussed, the maximum peak height and maximum valley depth values are calculated according to ISO 4287 whereby the average of the five largest peaks/valleys is taken to obtain the R_p and R_v values. As such the values may not be representative of the friction surface as a whole whereas the roughness values are. On average, the friction surface roughness was reduced which would be consistent with frictional work wearing away surface asperities. The large quantities of wear dust produced strongly suggest that this occurred.

Clutch Plate	Clutch Pack	Reference	R_a (μm)	R_p (μm)	R_v (μm)	R_t (μm)	R_{sk}
Driving 2	A	A2-DR	0.94	1.81	-5.53	7.34	-8.76
Driven 2		A2-DN	1.57	4.26	-9.62	13.90	-7.90
Driving 3		A3-DR	2.60	6.27	-12.70	19.00	-6.32
Driven 3		A3-DN	4.08	14.00	-20.10	34.10	-2.82
Driving 4		A4-DR	2.82	7.12	-17.70	24.90	-5.95
Driven 4		A4-DN	2.14	5.45	-10.90	16.40	-2.60
Driving 2	B	B2-DR	1.94	4.50	-10.50	15.00	-4.92
Driven 2		B2-DN	3.34	10.50	-19.60	30.10	-6.98
Driving 3		B3-DR	3.27	11.20	-15.10	26.20	-2.45
Driven 3		B3-DN	2.60	5.68	-12.20	18.90	-10.80
Driving 4		B4-DR	3.95	11.30	-18.20	29.50	-1.97
Driven 4		B4-DN	4.22	12.00	-16.20	28.10	-1.22
Average			2.79	7.84	14.03	21.95	-5.22

Table 5.10 – Roughness Parameter Values of Clutch Plates (Post-SCID Testing)

Figure 5.17 shows the direct comparison of the roughness values of the clutch-plates before and after SCID testing. It can be seen that for most clutch plates, the roughness is lower after SCID testing but there are also instances where the roughness has increased. There appears to be no correlation between the roughness values and the loading conditions the clutch-plates were subjected to suggesting that the loading conditions do not dictate changes in the surface roughness.

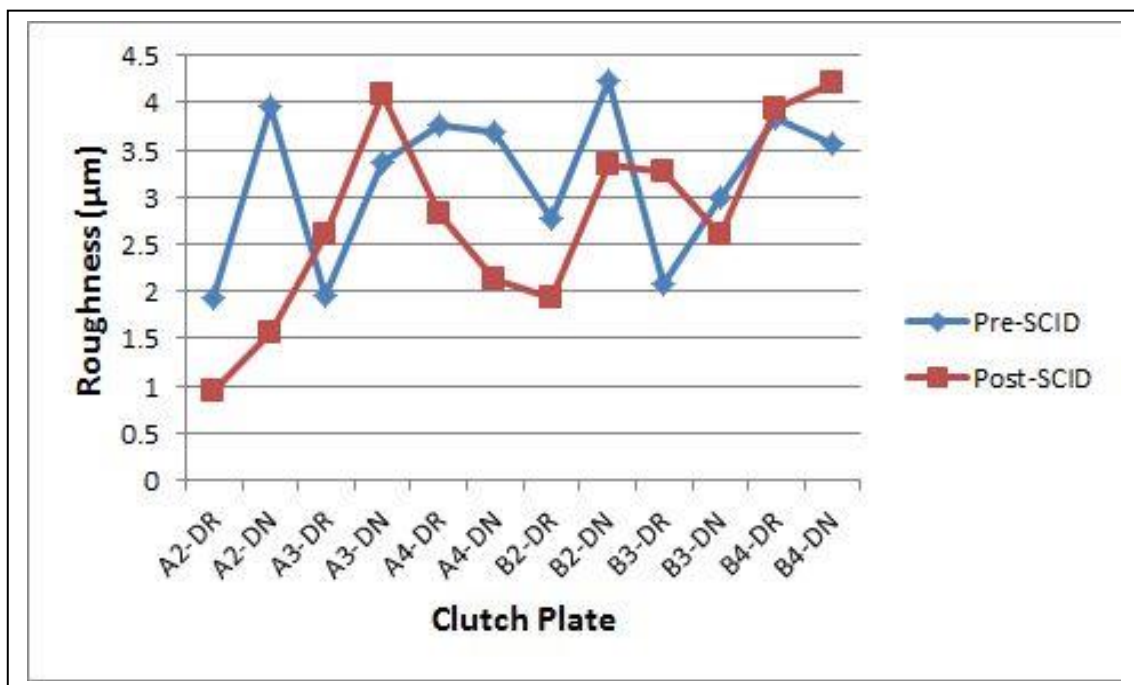


Figure 5.17 – Clutch-Plate Roughness Values Before and After SCID Testing

Table 5.11 lists the waviness analysis results for the clutch plates after SCID testing. Comparing these values to those in Table 5.8 for the clutch plates prior to SCID testing, on average the maximum waviness peak height and maximum waviness valley depth have reduced after SCID testing. The peak spacing value has also reduced but most importantly, a W_{sm} value could be calculated for most of the clutch plates after SCID testing as opposed to only half the clutch plates prior to SCID testing. The W_p and W_v values for the clutch plates highlighted in Table 5.11 are much higher than the other clutch plates but this is consistent with the results of the pre-SCID waviness analysis, supporting the conclusion that those particular clutch plates have been poorly machined.

Clutch Plate	Clutch Pack	Reference	W_p (μm)	W_v (μm)	W_z (μm)	W_{sm} (mm)
Driving 2	A	A2-DR	0.202	-0.154	0.356	3.47
Driven 2		A2-DN	0.152	-0.303	0.454	11.30
Driving 3		A3-DR	0.534	-0.314	0.849	6.16
Driven 3		A3-DN	0.653	-0.365	1.020	10.60
Driving 4		A4-DR	8.94	-8.460	17.400	N/A
Driven 4		A4-DN	0.606	-0.658	1.260	4.63
Driving 2	B	B2-DR	0.385	-0.734	1.120	5.41
Driven 2		B2-DN	3.190	-3.100	6.290	8.71
Driving 3		B3-DR	3.620	-0.811	4.430	7.66
Driven 3		B3-DN	0.651	-0.597	1.250	N/A
Driving 4		B4-DR	10.000	-8.560	18.600	5.65
Driven 4		B4-DN	0.722	-0.956	1.680	6.06
Average			2.006	1.596	3.606	6.97

Table 5.11 – Waviness Parameter Values of Clutch Plates (Post-SCID Testing)

The results of the waviness analysis suggest that frictional work leads to the formation of a waviness profile on the friction surfaces of the clutch plates. The waviness parameter values are however much less consistent for the clutch plates after SCID testing than for the race-conditioned clutch plates that were examined as an initial exercise, the results of which have been used in the thermomechanically couple finite element analysis (see Chapter 7). The precise history of the race-conditioned clutch plates was unknown but it is safe to assume that they were subjected to a greater amount of frictional work than the clutch plates used in the SCID tests. As such, a regular waviness profile may have formed over many engagements and, as frictional work during the SCID tests has been shown to encourage more waviness profiles to form, if more SCID engagements were carried out, a regular waviness profile may also be established on the clutch plates used for SCID testing.

5.6.3 Surface Structure & Morphology

The same areas of the clutch-plate friction surfaces were scanned using SEM after SCID testing as were scanned prior to SCID testing. The wear dust present on the surface of the driving clutch plates was inconsistent in location and abundance and presented difficulties in making direct comparisons of the friction surfaces before and after SCID testing. The SEM scans of the driven plates have hence been used for friction surface comparison.

However, some additional scans were taken where a large amount of wear dust was present on the friction surface. Figure 5.18 shows a digital photograph of clutch plate B4-DR after SCID testing with wear debris clearly visible on its friction surface. The highlighted area, 72° clockwise to the reference point, was scanned using SEM and a section of the resultant image is shown in Figure 5.19. Figure 5.18 shows that the wear dust is not uniform across the selected area but is biased to the right-hand side. This is reiterated in the SEM image where the wear dust can be seen as a very fine powder on the friction surface.

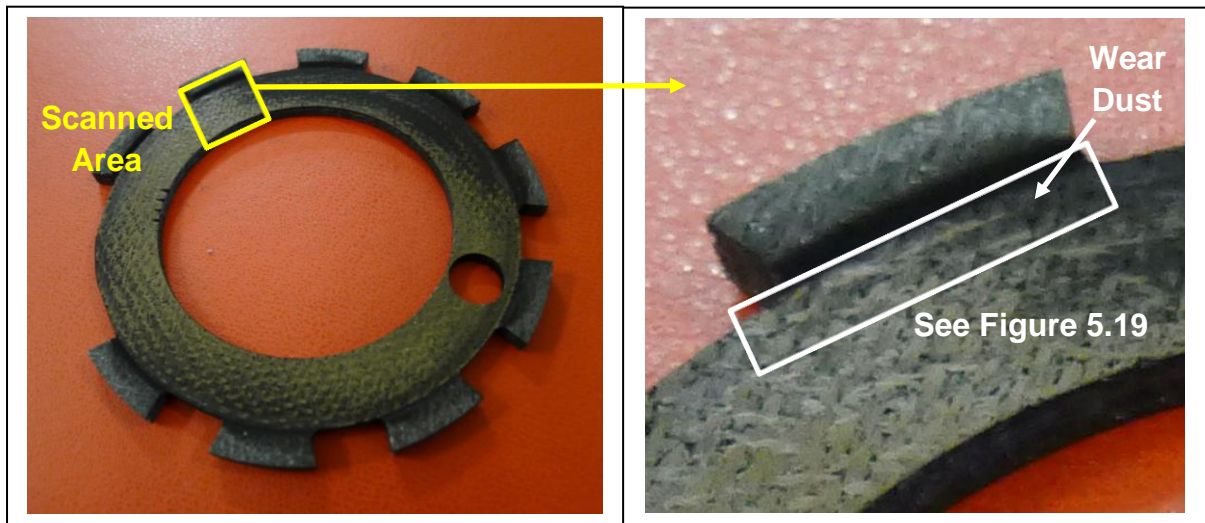


Figure 5.18 – Clutch Plate B4-DR After SCID Testing

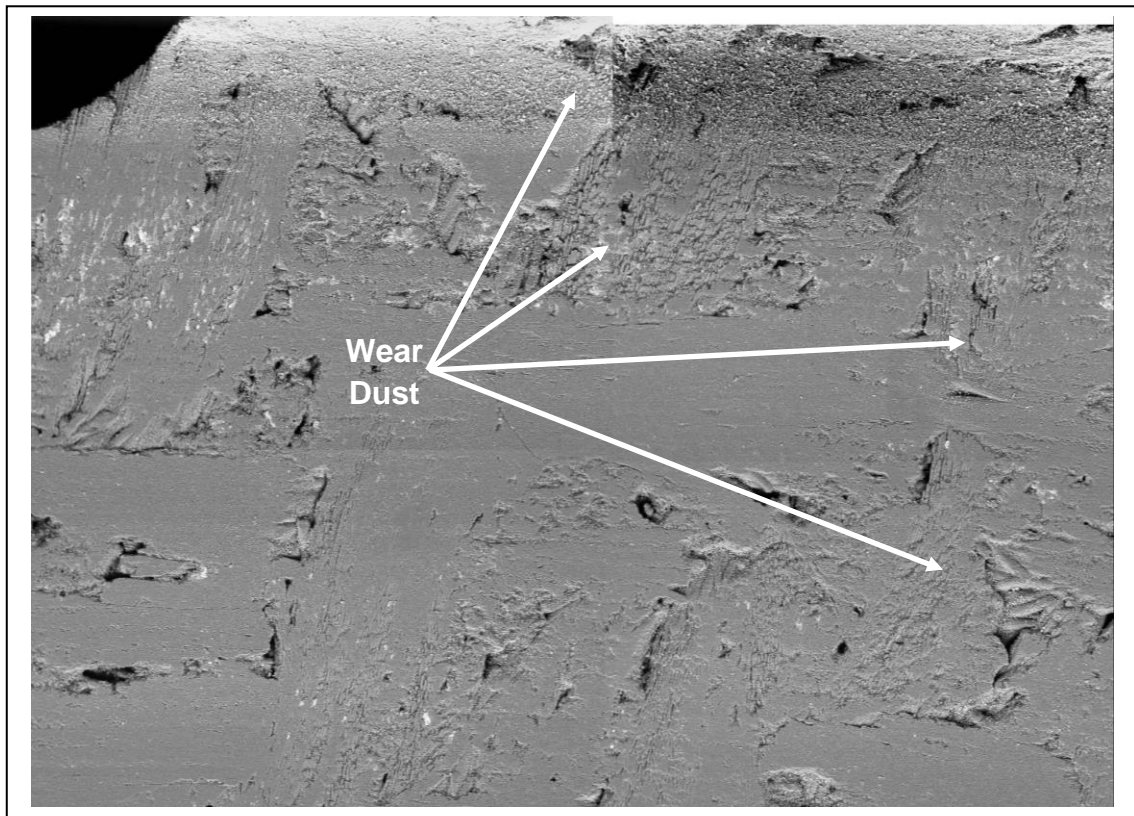


Figure 5.19 – Section of SEM Image of Clutch-Plate B4-DR After SCID Testing
(72° Clockwise to Reference Point, x100 Magnification)

Figures 5.20 and 5.21 show full SEM images for clutch plates A2-DN and A3-DN before and after SCID testing. Areas where the changes are most notable have been highlighted. Clutch plates B2-DN, B3-DN and B4-DN showed similar results to their respective counterparts so are not shown here. It can be seen from these figures that the appearance of the friction surfaces has been changed as the result of frictional work. For clutch plate A2-DN, the friction surface appears to be covered in a thin, smooth film which has partially filled some of the voids that were clearly visible prior to friction testing. Clutch plate A3-DN appears to be covered in a thicker, smooth film where there has been more extensive filling in of the voids.

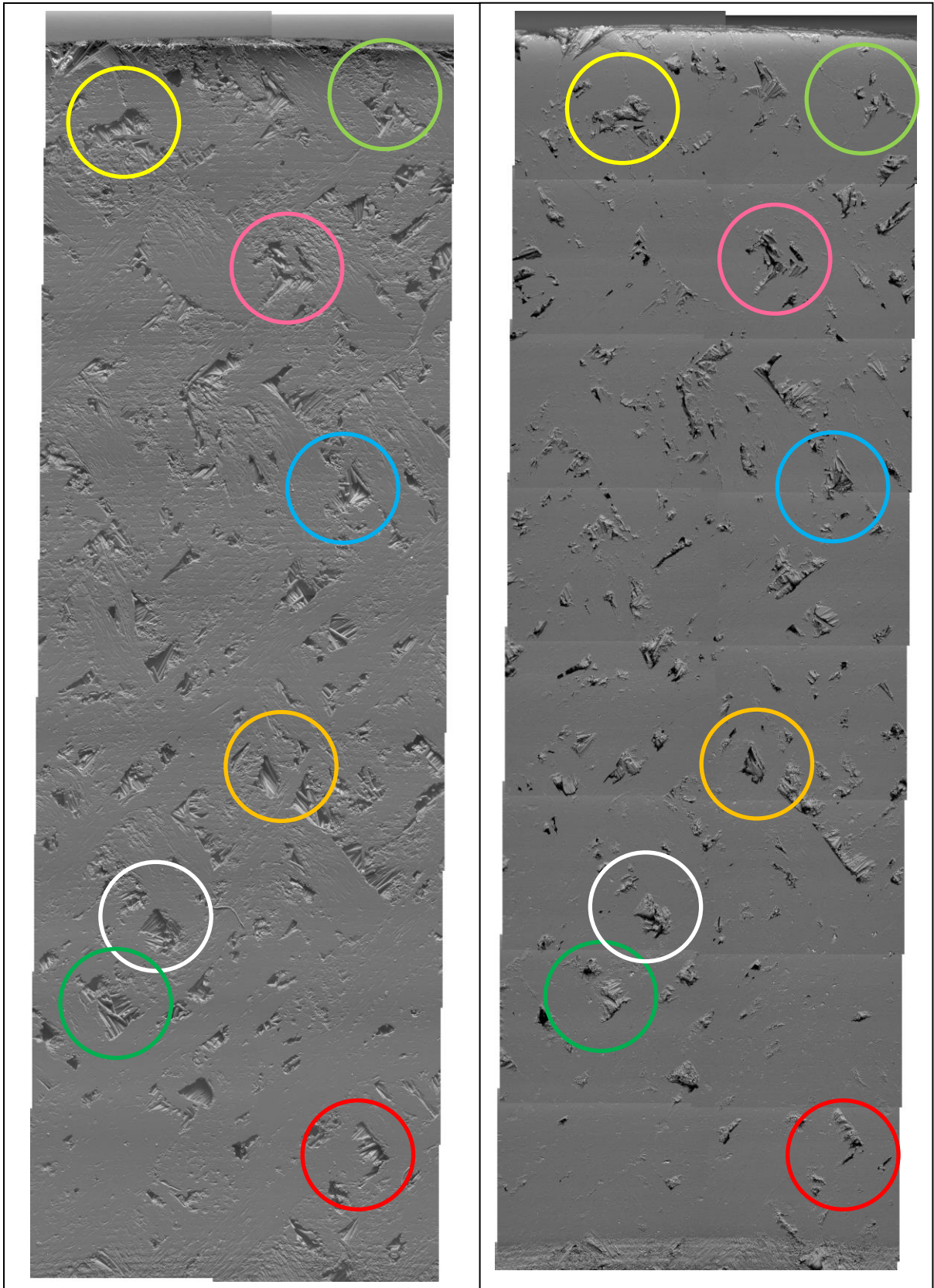


Figure 5.20 – SEM Images of Clutch Plate A2-DN Before (Left) and After (Right) SCID Testing (x100 Magnification)

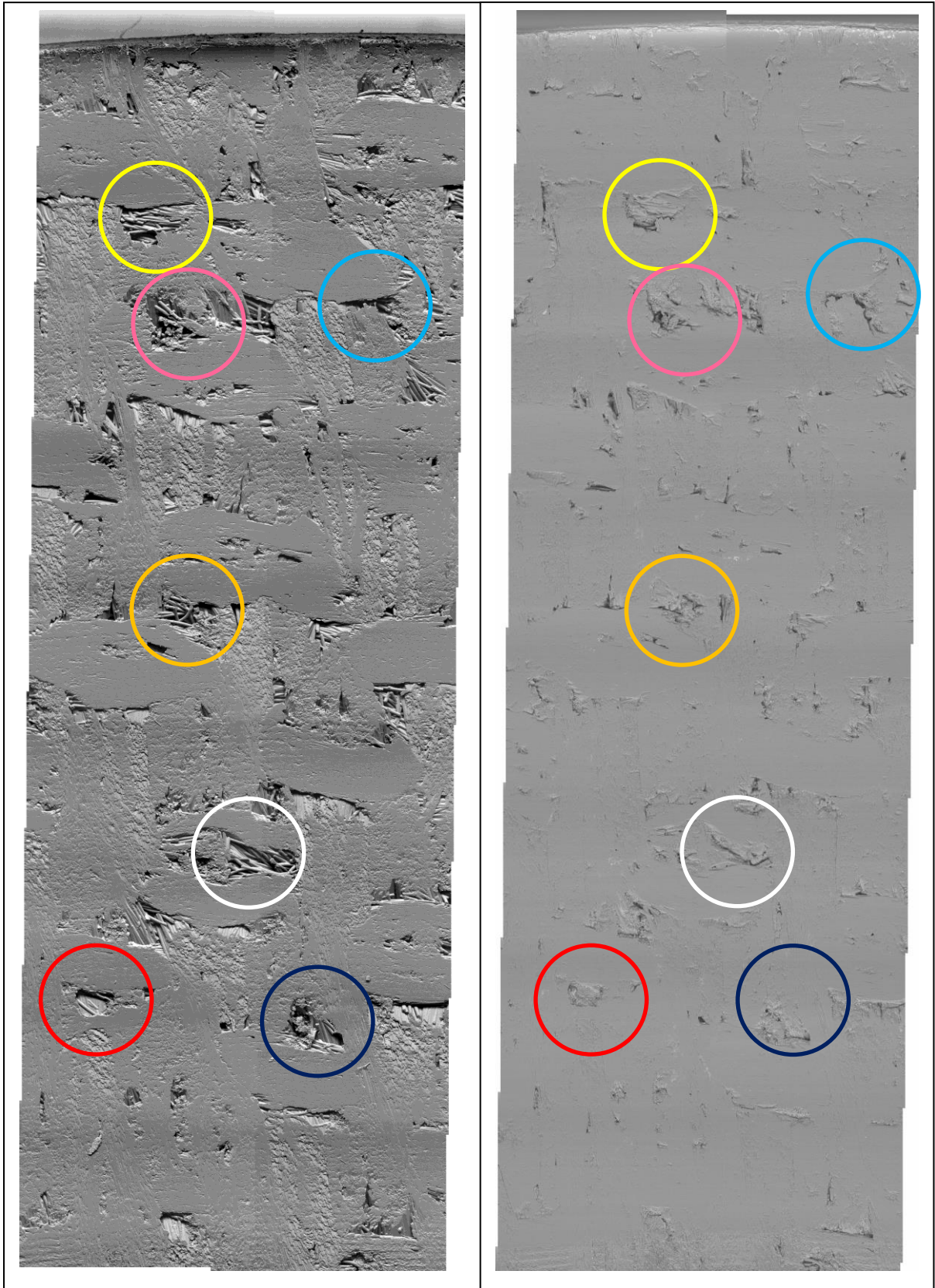


Figure 5.21 – SEM Images of Clutch Plate A3-DN Before (Left) and After (Right) SCID Testing (x100 Magnification)

Clutch plate A4-DN had similar characteristics to that of A3-DN except in the area of the wear track. A scan was taken at 144° anti-clockwise to the reference point where the observed wear track is clearly visible. No direct comparison with the original surface is possible as no SEM scan was taken in this area. Figure 5.22 is a section of a scan where the wear track was seen. In this area the carbon fibres appear to be distorted in comparison to the fibres prior to SCID testing (and on the clutch plates subjected to lower loads) in that they originally appeared to be cylindrical but in Figure 5.22 the fibres appear much flatter. It is unclear whether this is the result of damage where the sections of the fibres near the friction surface have been sheared away or whether it is simply wear debris filling voids and covering the fibres.

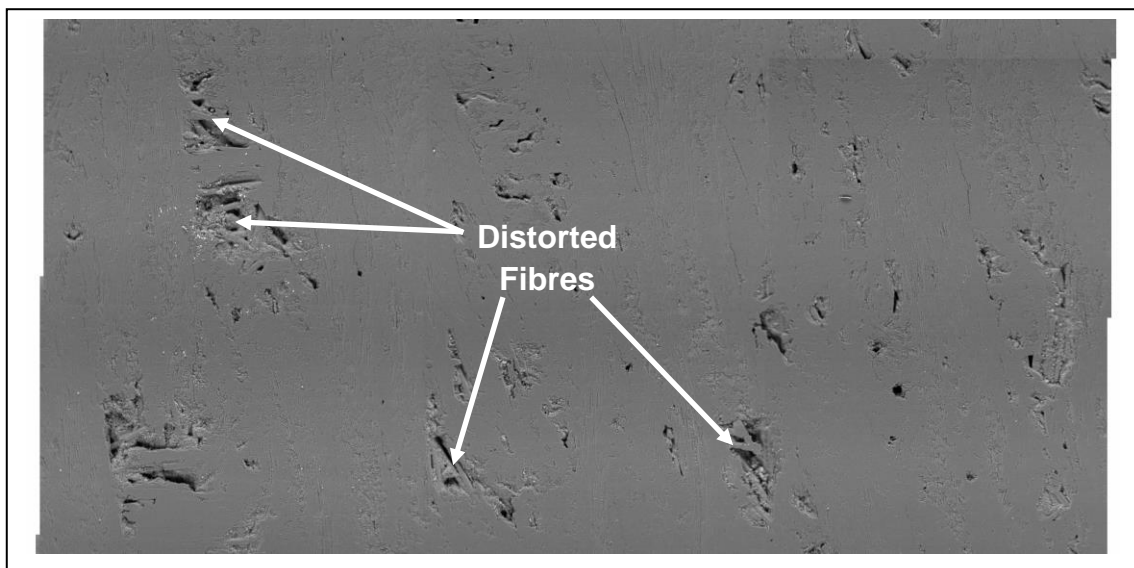


Figure 5.22 – SEM Image of Wear Track on Friction Surface of Clutch Plate A4-DN After SCID Testing (x100 Magnification)

The SEM images of the clutch plates before and after SCID testing show several friction surface changes which appear to be related to the clamp load and potentially the initial rotational speed at which the clutch-plate engagements were carried out. It appears that increasing the clamp load results in a thicker friction film being formed on the friction surface which also leads to more extensive void filling. The 1400N load case may have been sufficient to cause fibre damage. However, if the fibres were indeed damaged, it could not be determined whether this damage was caused by abrasion or oxidation. High temperatures, which could cause oxidation, were observed where the wear tracks formed but the preferential thermal expansion would also increase the normal loads in the hot band region leading to increased abrasion.

Figure 5.23 shows the comparison between the XRD results obtained for clutch plate B4-DN before and after SCID testing. The intensity depends upon the amount of material that is scanned by the x-ray beam. As the sample holder used to hold the clutch plates had to grip on to the clutch plate friction surface itself and the x-ray beam was 15x15mm, part of the x-ray beam misses the clutch-plate material as the width of the clutch-plate friction surface is only 16mm. Hence, even small inconsistencies in how the clutch plates were gripped by the holder could cause large differences in the counts. As such, the intensity values themselves do not provide any useful information. In order to directly compare the curve profiles, which do reveal useful information, a scale factor (SF) has been calculated in order to set the maximum intensity value of the post-SCID XRD curve to the same value as that of the pre-SCID XRD curve for the particular clutch-plate being compared.

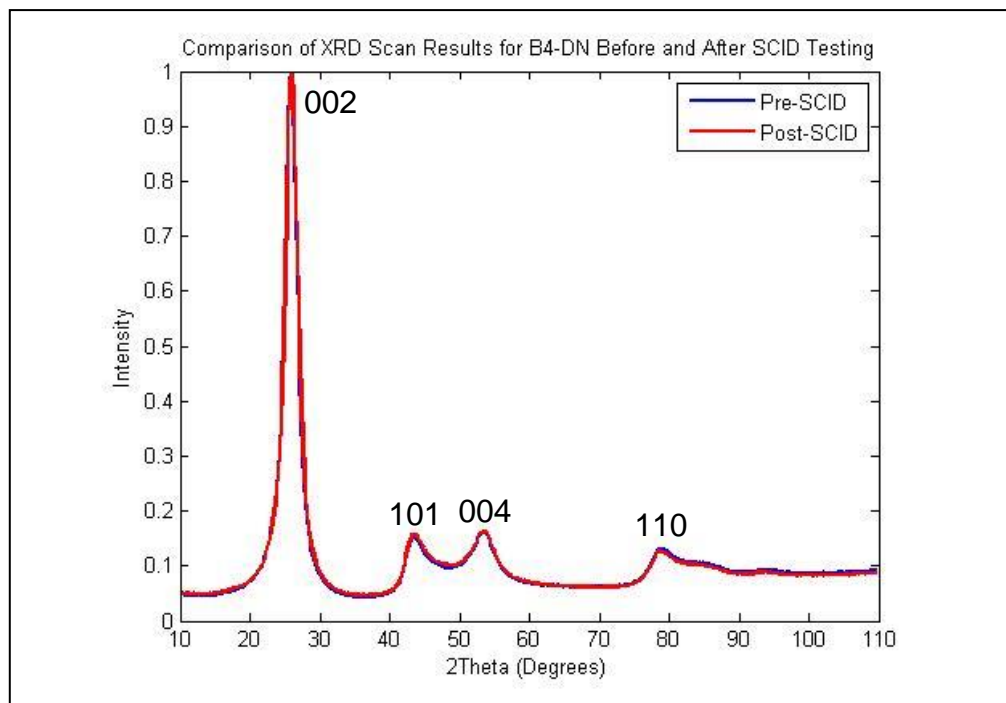


Figure 5.23 – XRD Curves for Clutch-Plate B4-DN Before and After SCID Testing

The peaks represent graphite structures with different interlayer dimensions and hence results in the differences in the scanning angle at which their maximum intensities occur. Table 5.12 summarises the interlayer spacing (Angstroms, 10^{-10} m) represented by the four peaks shown in Figure 5.23 with reference to a standard graphite 2H crystal structure.

Peak Number	Interlayer Spacing (Å)
001 (Standard)	6.6900
002	3.3450
101	2.0262
004	1.5725
110	1.2275

Table 5.12 – Interlayer Spacing of Graphite Crystal Structures

Ideally the peaks would be very sharp if only the specific interlayer spacings listed in Table 5.12 were present. However, the peaks are broad which shows a large amount of residual stress in the material leading to strain of the crystal structures. The left side of the peaks represent interlayer spacings that are slightly larger due to tensile stress and strain and the right side of the peaks represent interlayer spacings that are slightly smaller due to compressive stress and strain. The asymmetry of the peaks simply indicates the bias of tensile and compressive stress and strain for that particular crystal structure.

As can be seen in Figure 5.23, there was very little difference between the results of the XRD scans for clutch plate B4-DN before and after SCID testing. Numerical analysis confirmed this lack of difference where the intensity values were subtracted from one another. There was however a small shift to the left for the peaks suggesting a possible reduction in compressive residual stress and strain. This was also true for all other clutch plates regardless of the presence of wear debris or a wear track. However, the lack of difference between pre-SCID and post-SCID results is most likely due to the scan depth of the x-ray beams. For the first crystal structure (002), the scan depth was 671 μ m increasing to 2mm for the fourth peak (110). This means that, along with the friction surface, a large amount of bulk material will also have been scanned. As such, it is impossible to isolate any information regarding changes in the thin friction surface layers from the information relating to the bulk material which is unlikely to have been significantly affected. No conclusions regarding any friction surface changes can therefore be drawn from this analysis.

5.7 Summary

Initial surface characterisation of new and race-conditioned clutch plates using white light interferometry and contact profilometry suggested that roughness and waviness parameters are affected by frictional work. The roughness of the friction surfaces was reduced by frictional work whilst distinct waviness profiles were formed most likely due to the wear of surface asperities and thermoelastic instability effects. Roughness and waviness analyses as well as SEM and XRD scans were carried out on new clutch plates prior to SCID testing. These results were compared with the clutch-plate friction surfaces after SCID testing. The results of the roughness and waviness analyses showed a reduction in average roughness and an increase in the presence of a waviness profile as the result of frictional work. The waviness profiles did not however show as much agreement with each other as the race-conditioned clutch plates did, suggesting that a regular waviness profile may be produced as more frictional work is done by the friction surfaces.

SEM images clearly showed the effect that the applied clamp load has on the friction surface whereby a thicker friction film is formed by increasing the clamp load. At the highest clamp load, distortion of the carbon fibres was observed but whether the cause was due to wear debris filling the void and covering the fibres or damage to the fibres due to a wear mechanism was unclear.

Due to the scan depth of the x-ray beams used in the XRD analysis, it was not possible to identify any friction surface layer changes as a result of frictional work using this analysis technique.

6. 1D Heat Transfer Model

6.1 Introduction

A one-dimensional (1D) heat transfer model was constructed using Matlab to provide a quick and simple technique of predicting clutch plate temperatures expected during engagement tests using the in-house Single Clutch-plate Interface Dynamometer (SCID). The main purpose of the 1D heat transfer model was to enable a Taguchi Design of Experiment analysis to be carried out to determine which factors of the clutch plate engagement system and material properties have the greatest influence upon the maximum friction surface temperature reached.

6.2 Finite Difference Method

The 1D model uses a finite difference numerical method as discussed by Incropera et al. [60]. The medium of interest is divided into a number of small regions with a reference point being placed in the centre of each region or at the boundaries between regions. The reference points are referred to as nodes and together form a nodal network. Figure 6.1 shows how the clutch plate is modelled in this way.

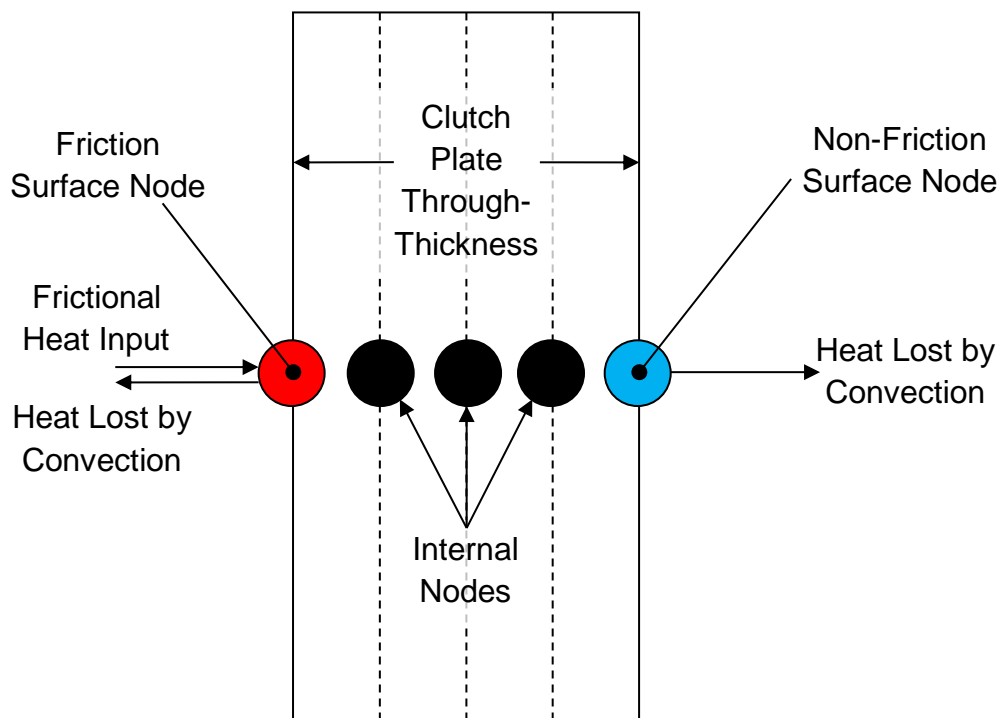


Figure 6.1 – Single Clutch-Plate Nodal Network [60]

Limpert [61] discusses how this method works. The clutch plate is an unsteady-state system where the initial temperature distribution is known but the variation with time must be determined. The temperature is analysed as a function of distance and time. Application of the first law of thermodynamics (energy balance) is applied to each node to produce a set of algebraic equations whose solutions yield the individual nodal temperatures at every finite time interval. Essentially, the temperature distribution at any time is determined from the temperature distribution at an earlier time starting with the known initial temperature distribution.

6.3 Finite Difference Equations

Limpert [61] presents the finite difference equations for calculating the temperature of the surface nodes.

$$T_0' = \left(1 - \left(\frac{2N + 2}{M}\right)\right)T_0 + \frac{2NT_\infty}{M} + \frac{2T_1}{M} + \frac{\Delta x q''}{kM} \quad (6.1)$$

$$M = \frac{(\Delta x)^2}{\alpha \Delta t} \quad (6.2)$$

$$N = \frac{h_c \Delta x}{k_c} \quad (6.3)$$

$$\alpha = \frac{k}{\rho c} \quad (6.4)$$

Where:

- T_0' – Surface Node Temperature at Current Time Step (K)
- T_0 – Surface Node Temperature at Previous Time Step (K)
- T_∞ - Ambient Temperature (K)
- T_1 – Adjacent Internal Node Temperature at Previous Time Step (K)
- Δx – Distance Between Nodes (m)
- Δt – Time Step (s)
- q'' – Heat Flux Input (Wm^{-2})
- k_c – Through-Thickness Thermal Conductivity ($\text{Wm}^{-1}\text{K}^{-1}$)

h_c – Convective Heat Transfer Coefficient ($\text{Wm}^{-2}\text{K}^{-1}$)

α - Thermal Diffusivity (m^2/s)

ρ – Material Density (kgm^{-3})

c – Specific Heat Capacity ($\text{Jkg}^{-1}\text{K}^{-1}$)

The stability condition must be considered in order to prevent the solution from becoming unstable. The node spacing and time step are therefore linked in that a small node spacing requires a small time step in order to solve the finite difference equations.

$$M \geq 2N + 2 \quad (6.5)$$

For the single clutch plate there is no heat flux input to the non-friction surface node so the heat flux term in Equation 6.1 can be eliminated when calculating the temperature of the non-friction surface. The temperatures of the internal nodes are calculated using Equation 6.6 [61].

$$T_n' = \frac{(T_{n+1} + T_{n-1})}{M} + \left(1 - \frac{2}{M}\right)T_n \quad (6.6)$$

Where: T_n' – Current Temperature at Internal Node (K)

T_n – Previous Temperature at Internal Node (K)

T_{n+1}/T_{n-1} – Previous Temperature at Adjacent Internal Node (K)

6.4 Model Assumptions

It is important to note that for the clutch plate application several assumptions have been made which simplify the 1D heat transfer model equations. The assumptions that were made are as follows:

- The clutch plates are identical in material and geometry

- Each clutch plate receives an equal proportion of the energy dissipated at the clutch plate interface
- The clutch plate friction surfaces are perfectly flat
- Convective heat losses are negligible
- Material properties remain constant at all temperatures

The first two assumptions simplify the model in that only one clutch plate needs to be modelled. In reality, the clutch plates are not identical as the driven and driving clutch plates have differing features for assembly purposes. There is also a small thickness difference between the driven and driving clutch plates. However, the friction surface geometry is identical and the model's main purpose is to enable a Taguchi Design of Experiment analysis (presented in Section 6.9) as opposed to the accurate prediction of clutch plate temperatures during SCID tests. Therefore an average thickness has been used in the model in order to justify the assumptions and simplify the model.

Assuming that the clutch-plate surfaces are perfectly flat means that the energy dissipated at the clutch plate interface can be assumed to be uniformly dissipated over the entire friction surface. The method discussed in Section 6.3 is therefore valid for this application (discussed further in Section 6.6).

It is reasonable to assume that convective heat losses are negligible for two reasons. Firstly the clutch plates are mounted in a system in which very little air can circulate. Secondly, assuming that the clutch plate surfaces are perfectly flat, no convective losses can occur at the clutch plate interface or back faces of the plates due to full area contact. This assumption allows all parts of Equation 6.1 that contain the convective heat transfer coefficient to be eliminated ($N = 0$).

Finally, assuming that the material properties are constant with temperature, even though they are known to change with temperature, is a necessary assumption as the main purpose of the 1D heat transfer model is to facilitate a Taguchi analysis which requires the properties to be set at discrete levels.

6.5 Model Structure

The overall structure of the model is shown in Figure 6.2. Initially, all nodes are at room temperature and the clutch plate is spinning at 8000rpm. The surface coefficient of friction (COF) determines the clutch torque generated which in turn determines the deceleration of the rotating mass. The change in rotational speed during the time step can be used to calculate the loss in kinetic energy of the rotating mass. This kinetic energy is assumed to be dissipated entirely at the clutch-plate interface. The amount of energy dissipated determines the temperature rise of the friction surfaces node and hence the other nodes. This new temperature distribution then forms the initial temperature distribution for the next time step.

Two different models can be used to calculate the torque generated by the clutch. These are the uniform pressure model and the uniform wear model [3] (see Chapter 1.2).

$$\begin{array}{l} \text{Uniform} \\ \text{Pressure} \end{array} \quad T_p = \frac{2\mu P_p (R_o^3 - R_i^3)}{3(R_o^2 - R_i^2)} \quad (6.7)$$

$$\begin{array}{l} \text{Uniform} \\ \text{Wear} \end{array} \quad T_w = \frac{\mu P_w (R_o + R_i)}{2} \quad (6.8)$$

Where: T_p, T_w – Torque (Nm)
 μ – Surface Coefficient of Friction
 P_p, P_w – Clamp Load (N)
 R_i – Clutch Plate Inner Radius (m)
 R_o – Clutch Plate Outer Radius (m)

The instantaneous angular deceleration of the flywheel can be calculated using Equation 6.9.

$$T = I_f \dot{\omega} \quad (6.9)$$

Where: I_f – Flywheel Inertia (kgm^2)
 $\dot{\omega}$ – Angular Deceleration (rads^{-2})

The new angular velocity and loss in kinetic energy (KE) of the flywheel can then be calculated.

$$\omega_2 = \omega_1 - \dot{\omega}\Delta t \quad (6.10)$$

$$\Delta KE = \frac{I_f(\omega_1^2 - \omega_2^2)}{2} \quad (6.11)$$

As the COF is assumed to be constant throughout the clutch plate engagement, the torque will also be constant resulting in a constant angular deceleration. It follows that the change in angular velocity is also constant as the time step used does not change during the simulation. Expanding Equation 6.11 and simplifying gives:

$$\Delta KE = \frac{I_f(\omega_1 - \omega_2)(\omega_1 + \omega_2)}{2} \quad (6.12)$$

$$\Delta KE = I_f\Delta\omega \frac{(\omega_1 + \omega_2)}{2} \quad (6.13)$$

As the COF is set at a constant value, $\Delta\omega$ is also constant and ω_1 and ω_2 will decrease linearly. The kinetic energy lost by the flywheel during a single time step, and therefore the heat flux input, will also decrease linearly over the engagement period. The heat flux will thus be highest at the beginning of the simulated clutch-plate engagement when the flywheel speed is at its greatest. The heat flux input is calculated using Equation 6.14.

$$q'' = \frac{\Delta KE}{A\Delta t} = \frac{\Delta KE}{\pi(R_o^2 - R_i^2)\Delta t} \quad (6.14)$$

Where: q'' – Heat Flux Input (Wm^{-2})

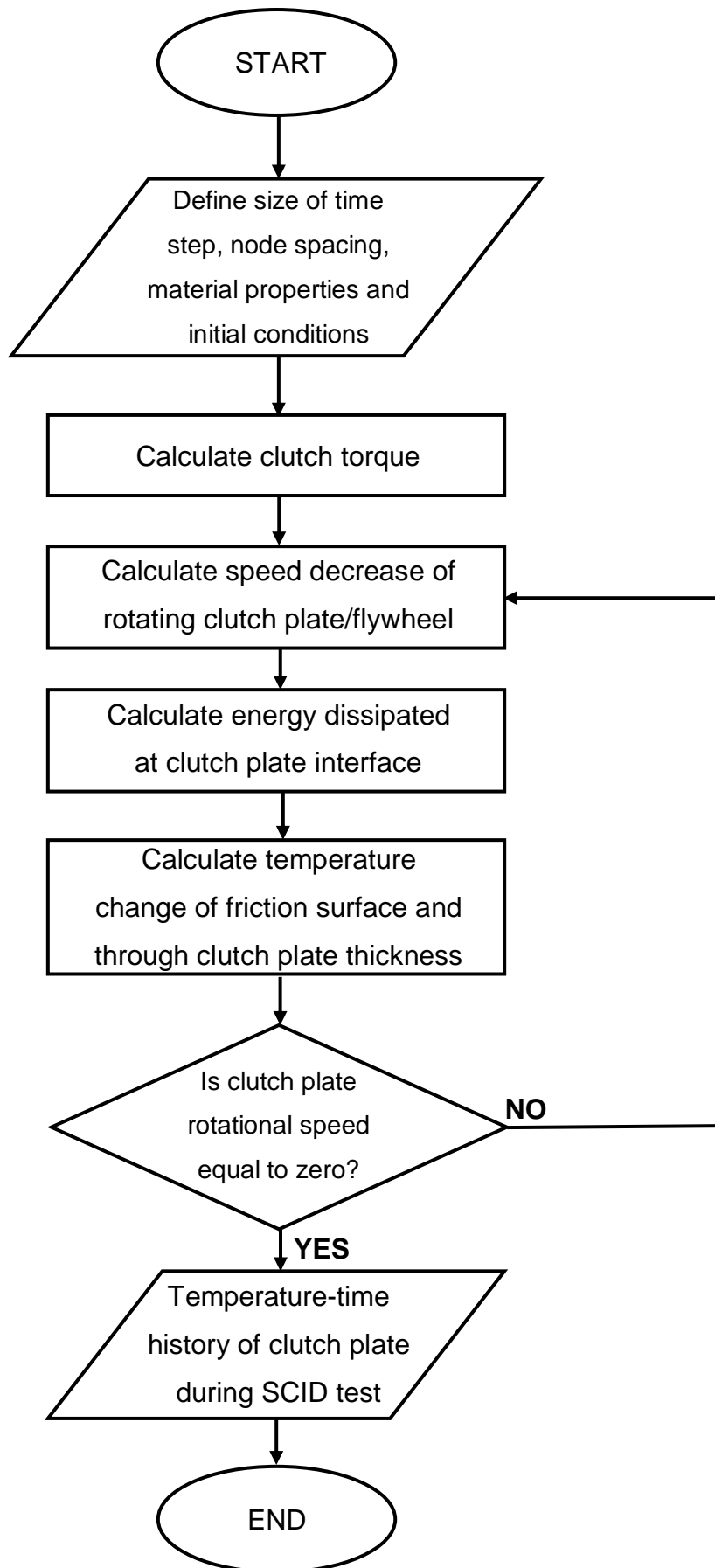


Figure 6.2 – Overall 1D Heat Transfer Model Structure

6.6 Heat Flux Input

The heat flux input is calculated by dividing the kinetic energy lost in the flywheel during a time step by the product of the friction surface area and time step size. This method assumes a uniform heat flux input over the clutch plate surface such that if the clutch plate is divided into a series of annular rings with equal radial widths, the heat flux input to each annulus would be equal. The amount of energy dissipated however, would increase due to the increase in annular area with increasing radius.

It can be shown that the heat flux remains constant with respect to radius by first considering the power dissipation with respect to the radial position of the point under consideration. The power dissipated at a given radius (r_i) is calculated using Equation 6.15:

$$Power_i = Fu_i \quad (6.15)$$

Where: F – In-plane Friction Force (N)
 u_i – Sliding Velocity (ms^{-1})

$$F = P\mu \quad (6.16)$$

$$Power_i = P\mu u_i \quad (6.17)$$

$$Power_i = P\mu\omega r_i \quad (6.18)$$

Equation 6.18 shows that the power dissipated is proportional to the clutch plate radius for a fixed clamp load, COF and rotational speed. A greater amount of power will be dissipated at the outer radius and hence a greater amount of energy will be dissipated there. The heat flux is simply the power dissipated per unit area. If the clutch plate is divided into a number of annular areas, each of equal width, the heat flux per annulus can be shown to be constant. For an annulus between two arbitrary radii r_1 and r_2 as shown in Figure 6.3, the heat flux would be given by Equation 6.19. As the sliding speed is directly proportional to the radius, the average sliding velocity is calculated at the mean of the two radii defining the annulus.

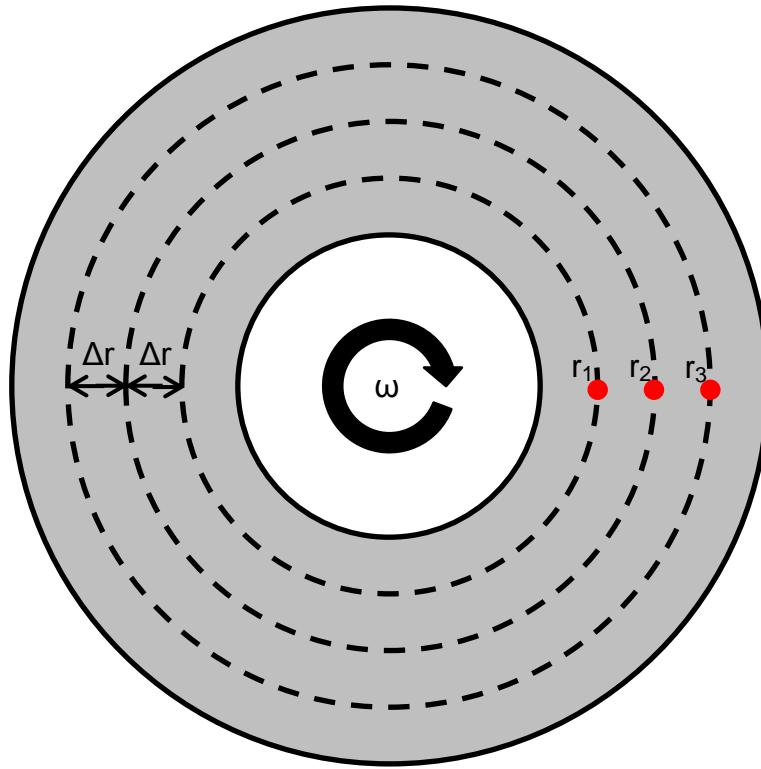


Figure 6.3 – Clutch Plate Divided Into Annuli of Equal Width

$$q_{1,2}'' = \frac{P\mu\omega(r_1 + r_2)}{2\pi(r_2^2 - r_1^2)} \quad (6.19)$$

The heat flux over the adjacent annulus would then be:

$$q_{2,3}'' = \frac{P\mu\omega(r_2 + r_3)}{2\pi(r_3^2 - r_2^2)} \quad (6.20)$$

Hence the difference in heat flux between the two annuli would be:

$$q_{2,3}'' - q_{1,2}'' = \frac{P\mu\omega(r_2 + r_3)}{2\pi(r_3^2 - r_2^2)} - \frac{P\mu\omega(r_1 + r_2)}{2\pi(r_2^2 - r_1^2)} \quad (6.21)$$

Noting that:

$$r_2^2 - r_1^2 = (r_2 - r_1)(r_2 + r_1) \quad (6.22)$$

$$r_3^2 - r_2^2 = (r_3 - r_2)(r_3 + r_2) \quad (6.23)$$

Allows Equation 6.21 to be expressed as:

$$q_{2,3}'' - q_{1,2}'' = \Delta q'' = \frac{P\mu\omega}{2\pi(r_3 - r_2)} - \frac{P\mu\omega}{2\pi(r_2 - r_1)} \quad (6.24)$$

Also, noting that:

$$r_3 - r_2 = r_2 - r_1 = \Delta r \quad (6.25)$$

Equation 1.24 becomes:

$$\Delta q'' = \frac{P\mu\omega}{2\pi\Delta r} - \frac{P\mu\omega}{2\pi\Delta r} \quad (6.26)$$

From which it is evident that:

$$\Delta q'' = 0 \quad (6.27)$$

This shows that the heat flux does not vary radially and, assuming there is no heat flux variation in the circumferential direction (always assumed in this application), it is therefore uniform over the entire clutch plate surface. This means that the through-thickness temperature distribution predicted by the 1D heat transfer model is the same throughout the entire clutch plate.

This differs from the approach of several authors discussed in the literature review. Zagrodzki [12], Zhao et al. [13, 14] and Abdullah et al. [16, 17, 18] assumed that the heat flux was proportional to radius but as has been shown in the above analysis, this is not the case. Either the terminology used by the authors discussed is incorrect and they are actually referring to an overall heat input which is proportional to radius or, they have wrongly assumed that the heat flux is proportional to the radius.

6.7 Sensitivity Analysis

Before using the 1D model to perform a Taguchi analysis, a sensitivity analysis was carried out to determine the number of nodes and time step size required to give reliable results.

In reality, the clutch engagement process is a transient event and the heat transfer through the clutch plate occurs continuously. The finite difference method however requires that the event be divided into a series of discrete time steps and the clutch

plate be divided into a series of discrete regions. Therefore, reality is best approximated by using the smallest possible time step and smallest possible node spacing. However, this would greatly increase computing and processing time and would also result in needlessly excessive amounts of data.

As the clutch plates are very thin (3-3.5mm), the node spacing will also be very small and hence there is no need for a large number of nodes in order to gain an understanding of the temperature distribution through the clutch plate. However, a minimum number of three nodes are required as there must be two surface nodes and at least one internal node for the finite difference method to work. The entire clutch plate engagement takes less than two seconds so a time step of 0.1seconds would be the largest practical time step that could be used to model the transient thermal behaviour of the clutch plate. Anything larger could result in peaks of temperature not being predicted depending on how quickly heat is conducted away from the friction surface.

The outputs considered in the sensitivity analysis were the maximum temperatures reached at the friction surface and non-friction surface nodes. The internal nodes were not considered as their positions within the clutch plate change depending on the number of nodes used whereas the position of the friction surface and non-friction surface nodes do not change. Table 6.1 shows the results of the sensitivity analysis.

	Maximum Friction Surface Temperature (K)					Maximum Non-Friction Surface Temperature (K)				
	3	5	7	9	11	3	5	7	9	11
Number of Nodes										
Time Step (s)										
0.1	578.5	Error	Error	Error	Error	526.3	Error	Error	Error	Error
0.05	581.1	Error	Error	Error	Error	524.6	Error	Error	Error	Error
0.01	583.0	581.0	580.5	580.4	Error	523.3	526.6	527.1	527.3	Error
0.005	583.3	581.3	580.8	580.7	580.6	522.8	526.1	526.6	526.8	526.9
0.001	583.4	581.5	581.0	580.9	580.8	522.6	525.9	526.5	526.6	526.7
0.0005	583.5	581.5	581.1	580.9	580.8	522.5	525.8	526.4	526.6	526.7

Table 6.1 –Sensitivity Analysis Results for 1D Heat Transfer Model

As can be seen from Table 6.1, errors occurred in several runs of the 1D model due to the time step being too large and causing instability (see Equation 6.5). The results of the time step sensitivity analysis are shown in Figure 6.4 where 3 nodes are used in each run.

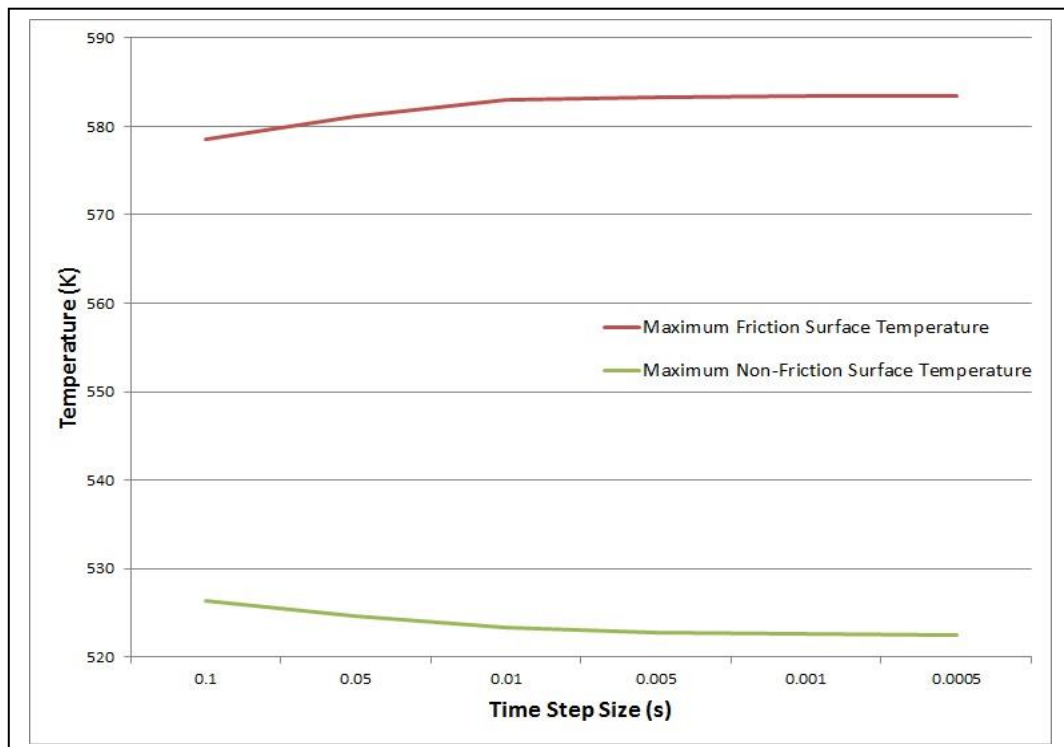


Figure 6.4 – Time Step Size Sensitivity Analysis Results for 1D Heat Transfer Model

Over the range of time step sizes investigated, the differences in predicted temperatures were small ($\leq 5K$). As can be seen from Figure 6.4, at time steps of 0.01seconds and larger, the difference in predicted temperatures becomes less than 0.5K showing that a time step size of 0.01 is the best compromise between accuracy and computing time. This was the time step used in all subsequent runs of the 1D model. Using this time step size, the sensitivity of the number of nodes was investigated. These results are shown in Figure 6.5.

As with the time step results, there is only a small difference between the predicted temperatures over the range of number of nodes investigated ($\leq 4K$). At 5 nodes and above the temperature difference becomes less than 1K showing that 5 nodes are sufficient. This was the number of nodes used in all subsequent runs of the 1D model.

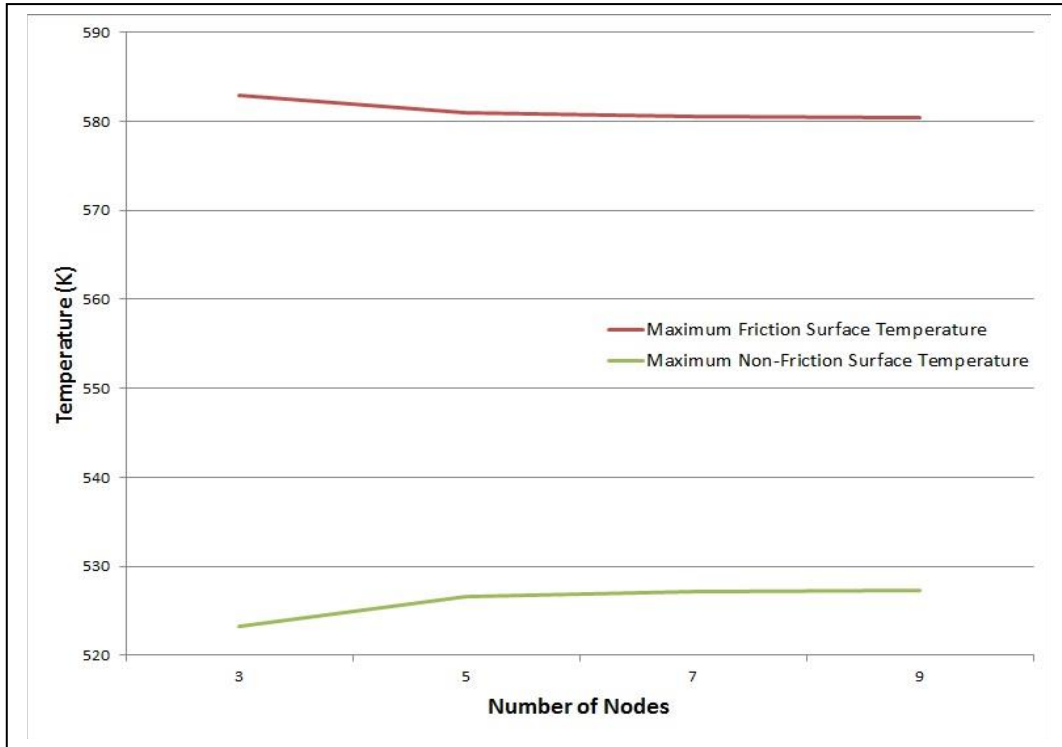


Figure 6.5 – Mesh Density Sensitivity Analysis Results for 1D Heat Transfer Model

6.8 Validation of Method Used in 1D Model

In order to confirm that the finite difference method used was correct, a 1D model was constructed using the finite element package Abaqus and the results compared.

Table 6.2 shows the inputs and material properties used in both models.

Property	Value
Clamp Load	1400N*
Rotational Speed	8000rpm*
Inertia	0.0344kgm ² *
COF	0.35*
Density	1850kgm ⁻³ *
Thermal Conductivity	13Wm ⁻¹ K ⁻¹ *
Specific Heat Capacity	1000Jkg ⁻¹ K ⁻¹ *
Time Step	0.01s
Number of Nodes	5
Clutch Plate Thickness	3.25mm

Table 6.2 – Inputs and Material Properties Used in 1D Models

*Values obtained from confidential technical report [7]

The heat flux was calculated in Matlab using the method discussed in Section 6.5 and this heat flux was used for both the Matlab and Abaqus 1D models. It is not possible to simply construct a 1D model in Abaqus so an axisymmetric model was constructed using heat transfer elements only. The heat flux was applied to one surface only with the entire clutch plate having the same initial temperature of 298K. As the heat flux is uniform over the entire friction surface, there will be no temperature gradient in the radial direction. Therefore the heat can only be conducted in one direction through the clutch plate essentially forming a 1D model. Figure 6.6 shows the mesh used (5 nodes in trough thickness direction) in the Abaqus 1D model and Figure 6.7 shows how the heat flux was applied.

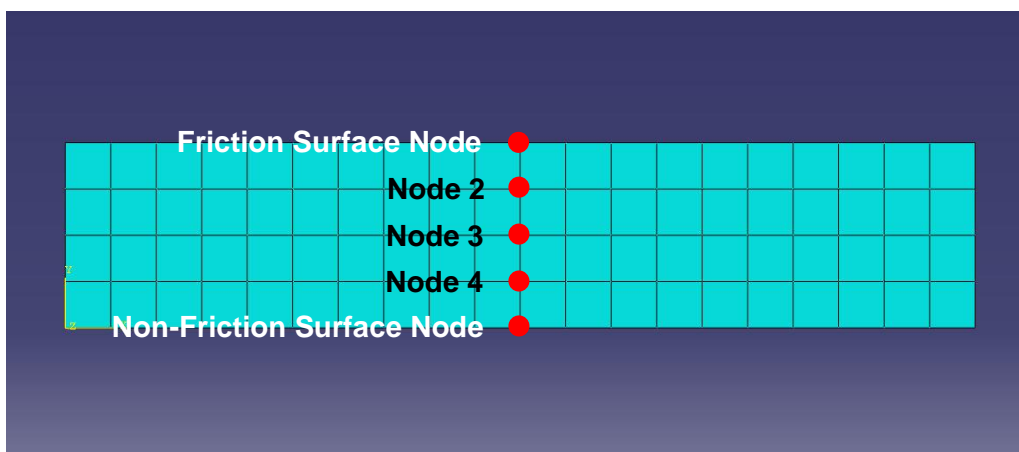


Figure 6.6 – Mesh Used in 1D Abaqus Model

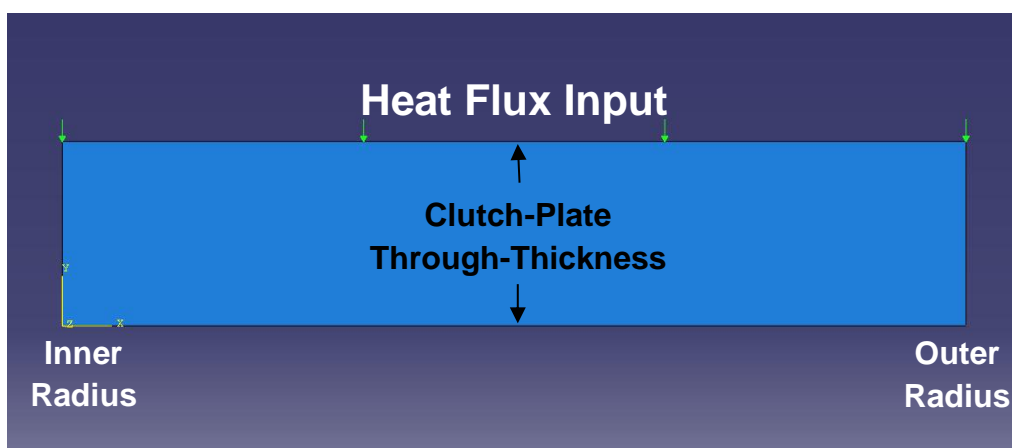


Figure 6.7 – Application of Heat Flux in 1D Abaqus Model

Only the uniform pressure model was run using both Matlab and Abaqus (discussed further in Section 6.9). Figure 6.8 shows the temperatures predicted by the Matlab and Abaqus models and Figure 6.9 shows the comparison between these results.

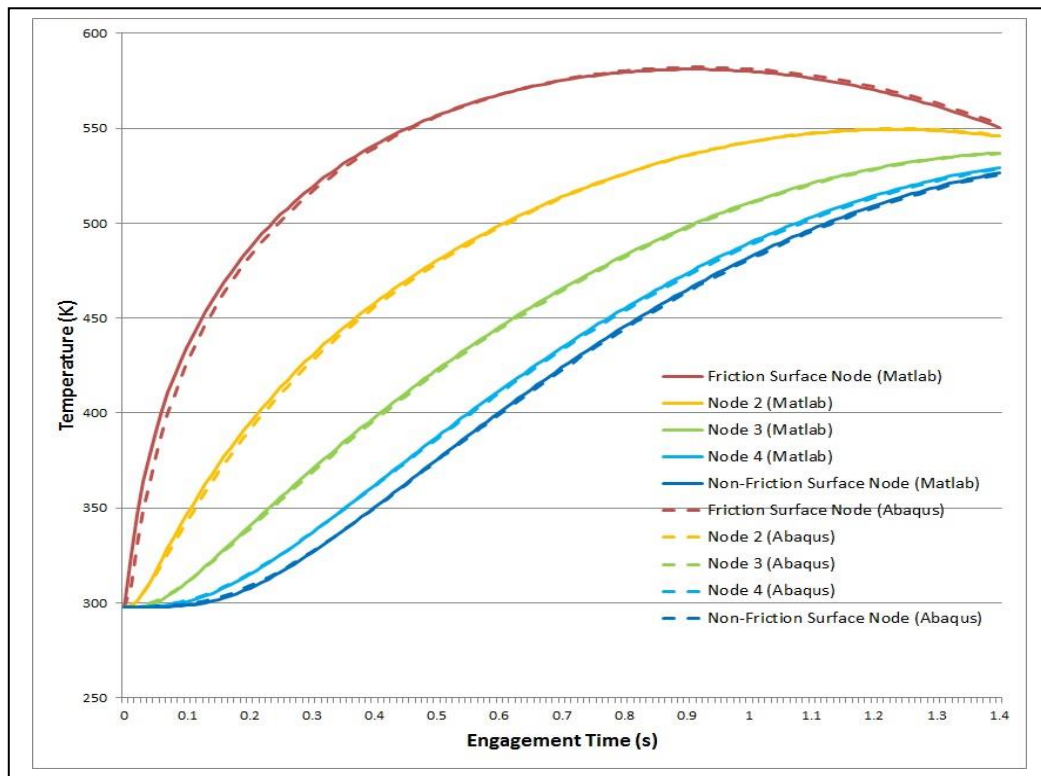


Figure 6.8 – Clutch-Plate Temperatures Predicted by Matlab and Abaqus 1D Models

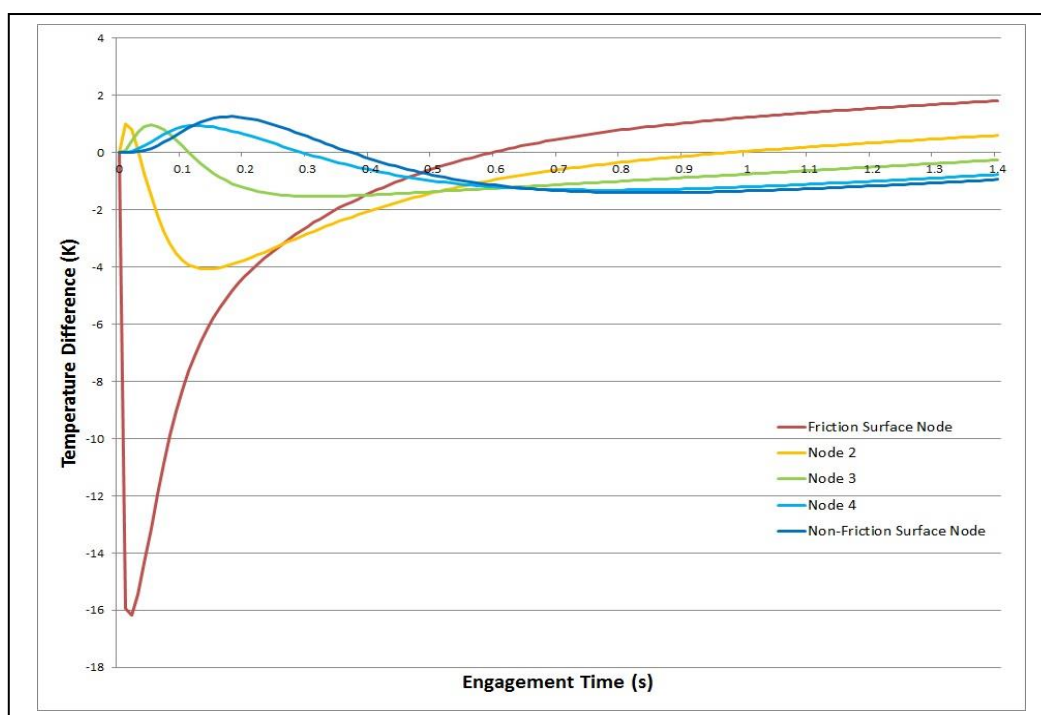


Figure 6.9 – Temperature Differences Between Matlab and Abaqus 1D Models

Figure 6.8 shows that the maximum friction surface temperature predicted by both models is approximately 580K and the total engagement time was 1.4 seconds. This is the time taken for the rotating clutch plate to become stationary (analogous to the driving and driven clutch plates reaching the same relative speed during a race start) and so the program exited as per Figure 6.2.

The heat flux input was applied throughout the engagement but as the engagement process continues, the heat flux decreases due to the lower rotational speeds and hence the kinetic energy lost during a single time step reduces. This was shown to be a linear decrease in Section 6.4. The maximum friction surface temperature occurs before the end of the engagement and then falls due to the heat flux input becoming less than the amount of heat being conducted away from the friction surface, through the clutch plate, due to the temperature gradients.

Figure 6.9 shows that there is a large initial temperature difference between the two models at the friction surface but as the engagement continues this temperature difference falls rapidly. For the majority of the engagement, the differences are small ($\pm 2\text{K}$) showing that the finite difference method used in the 1D Matlab model is valid.

6.9 Uniform Pressure Model vs Uniform Wear Model

As mentioned in Section 6.8, only the uniform pressure model was considered for validation. The uniform pressure model assumes that the clutch plates are perfectly flat and also accurately aligned [3] resulting in the pressure and clamp load being uniform over the entire surface.

The uniform wear model assumes that the mating surfaces of the clutch plates are rigid and hence wear is uniform across the surface [3]. This is only valid if the amount of energy dissipated is uniform over the surface. Equation 6.17 showed that the rate of energy dissipation (power), and hence the level of energy dissipation, is proportional to the product of clamp load and sliding velocity. The surface pressure is related to clamp load according to Equation 6.28.

$$p = \frac{P}{A} \quad (6.28)$$

Where: p – Contact Pressure (Pa)

Rearranging Equation 6.28 and substituting into Equation 6.17 gives:

$$Power = pA\mu u \quad (6.29)$$

Since the sliding velocity increases with radius, the pressure must decrease in relation to the radius for the energy dissipation to remain constant as required by the wear model.

These two models are two extreme cases but as not enough is known about the wear of the clutch plates and it was believed that the pressure is reasonably uniform across the clutch plate surfaces in the full clutch system, the uniform pressure model is the most appropriate. Also, as discussed in Section 6.6, the 1D model assumes a greater level of power dissipation with increasing radius. This is contradictory to the assumptions of the uniform wear model and hence the uniform wear model is inappropriate for the 1D model at this stage of its development.

6.10 Taguchi Design of Experiment

Taguchi [62] defines a Design of Experiment approach as ‘the system by which one can efficiently and reliably evaluate all possible methods being considered for use in reaching a particular objective’. This technique is often used in manufacturing and production processes in order to improve quality by finding the optimum combination of factors which give the highest quality product where the quality is measured by defining certain objectives. In turn, this also gives an indication of which factors, when changed, have the greatest influence on the quality of the product. It is this feature of design of experiments which has been used to determine which factors of the clutch plate engagement system and material properties are most influential on friction surface temperature.

The first step is to decide how many factors are to be investigated and how many finite levels these factors can be set at. A standard orthogonal array can then be chosen which outlines the experiments to be carried out. For seven factors that can be set at two discrete levels, an L_8 orthogonal array can be used. Table 6.3 shows the L_8 orthogonal array as presented by Taguchi [62].

	Column	1	2	3	4	5	6	7
Experiment Number (EN)								
1		1	1	1	1	1	1	1
2		1	1	1	2	2	2	2
3		1	2	2	1	1	2	2
4		1	2	2	2	2	1	1
5		2	1	2	1	2	1	2
6		2	1	2	2	1	2	1
7		2	2	1	1	2	2	1
8		2	2	1	2	1	1	2

Table 6.3 – L₈ Orthogonal Array

Each column contains the same number of 1's and 2's (four each). Taking any two columns, there are four combinations of the two numerals and each appears the same number of times. This is the definition of an orthogonal array.

If each column is considered to represent an experimental factor which can be set at either level 1 or 2, this orthogonal array presents eight experiments where each experiment is run with the seven factors at eight different combinations of levels. By doing this, the critical output can be measured for each experiment and statistical analysis can then be carried out to assess which factor has the largest influence on the critical output.

For the clutch plates, Table 6.4 shows the factors considered with the maximum friction surface temperature being the critical output. Table 6.5 shows the level 1 (minimum) and level 2 (maximum) values used. Some of these factors are physical values that can be controlled when carrying out SCID tests. The COF and material property values have been obtained from literature sources [7, 13, 27, 28, 29, 40, 63] where the properties of the carbon/carbon material being investigated have been listed. The values shown in Table 6.5 are simply the minimum and maximum values of these properties that have been documented in the referenced literature sources.

	Factor	Clamp Load (N)	Initial Rotational Speed (rpm)	Inertia (kgm ²)	COF	Thermal Conductivity (Wm ⁻¹ K ⁻¹)	Specific Heat Capacity (Jkg ⁻¹ K ⁻¹)	Density (kgm ⁻³)
EN								
1		1	1	1	1	1	1	1
2		1	1	1	2	2	2	2
3		1	2	2	1	1	2	2
4		1	2	2	2	2	1	1
5		2	1	2	1	2	1	2
6		2	1	2	2	1	2	1
7		2	2	1	1	2	2	1
8		2	2	1	2	1	1	2

Table 6.4 – Factors Investigated in Design of Experiment Analysis

Factor	Level	
	1	2
Clamp Load (N)*	1000	2000
Initial Rotational Speed (rpm)*	8000	10000
Inertia (kgm ²)*	0.025077 (SCID)	0.033436 [7]
COF**	0.2	0.5
Thermal Conductivity (Wm ⁻¹ K ⁻¹)**	10	60
Specific Heat Capacity (Jkg ⁻¹ K ⁻¹)**	700	1900
Density (kgm ⁻³)**	1600	1900

Table 6.5 – Factor Values Used in Design of Experiment Analysis

*Factor values can be set in SCID experiments or via design changes

**Factor values obtained from literature [7, 13, 27, 28, 29, 40, 63]

6.11 The Signal-to-Noise Ratio

The Signal-to-Noise (S/N) ratio is used to optimise the robustness of a product or process. Fowlkes et al. [64] discuss the four properties of the ideal S/N ratio:

1. The S/N ratio reflects the variability in the response of a system caused by noise factors.
2. The S/N ratio is independent of the adjustment of the mean.
3. The S/N ratio measures relative quality because it is to be used for comparative purposes.
4. The S/N ratio does not induce unnecessary complications, such as control factor interactions, when the influences of many factors on product quality are analysed.

It is properties 3 and 4 that make the S/N ratio particularly useful for the clutch plate application. The S/N ratio will allow the influence of each factor to be compared independently. The S/N ratio can be calculated from the mean square deviation (MSD) using Equation 6.30.

$$S/N = -10\log(MSD) \quad (6.30)$$

The mean square deviation can be calculated using Equation 6.31:

$$MSD = \frac{S^2}{\bar{y}^2} = \frac{Noise}{Signal} \quad (6.31)$$

Where: S^2 – Variance
 \bar{y} – Mean

The variance is calculated using Equation 6.32:

$$S^2 = \frac{1}{n-1} \sum_{i=1}^n (y_i - \bar{y})^2 \quad (6.32)$$

Where: n – Number of Data Points
 y_i – Value of Data Point i

The output that is most important in this investigation is the maximum friction surface temperature and hence it is this output that was used as the signal. To determine which factor has the biggest influence on the signal, the following procedure was carried out using the Matlab 1D heat transfer model:

1. Run all 8 simulations (experiments) shown in Table 6.4 and record the maximum predicted friction surface temperature.
2. For the first factor, take the four simulations with that factor set at level 1 and calculate the mean and variance of the maximum friction surface temperature.
3. Calculate the S/N ratio using these values.
4. Repeat steps 2 and 3 for that factor at level 2.
5. Calculate the difference between the S/N ratio at level 1 and level 2 to give the 'Main Effect' of that factor.
6. Repeat steps 2-5 for the other factors.

The results of this procedure are given in Table 6.6 and shown in Figure 6.10.

	Factor	Clamp Load (N)	Initial Rotational Speed (rpm)	Inertia (kgm ²)	COF	Thermal Conductivity (Wm ⁻¹ K ⁻¹)	Specific Heat Capacity (Jkg ⁻¹ K ⁻¹)	Density (kgm ⁻³)
Level 1 S/N Ratio		20.011	31.983	19.177	39.949	26.976	29.893	25.051
Level 2 S/N Ratio		25.623	21.130	27.333	20.896	19.234	32.583	20.323
Main Effect		5.612	10.852	8.156	19.053	7.742	2.689	4.278

Table 6.6 – S/N Ratio and Main Effect Results

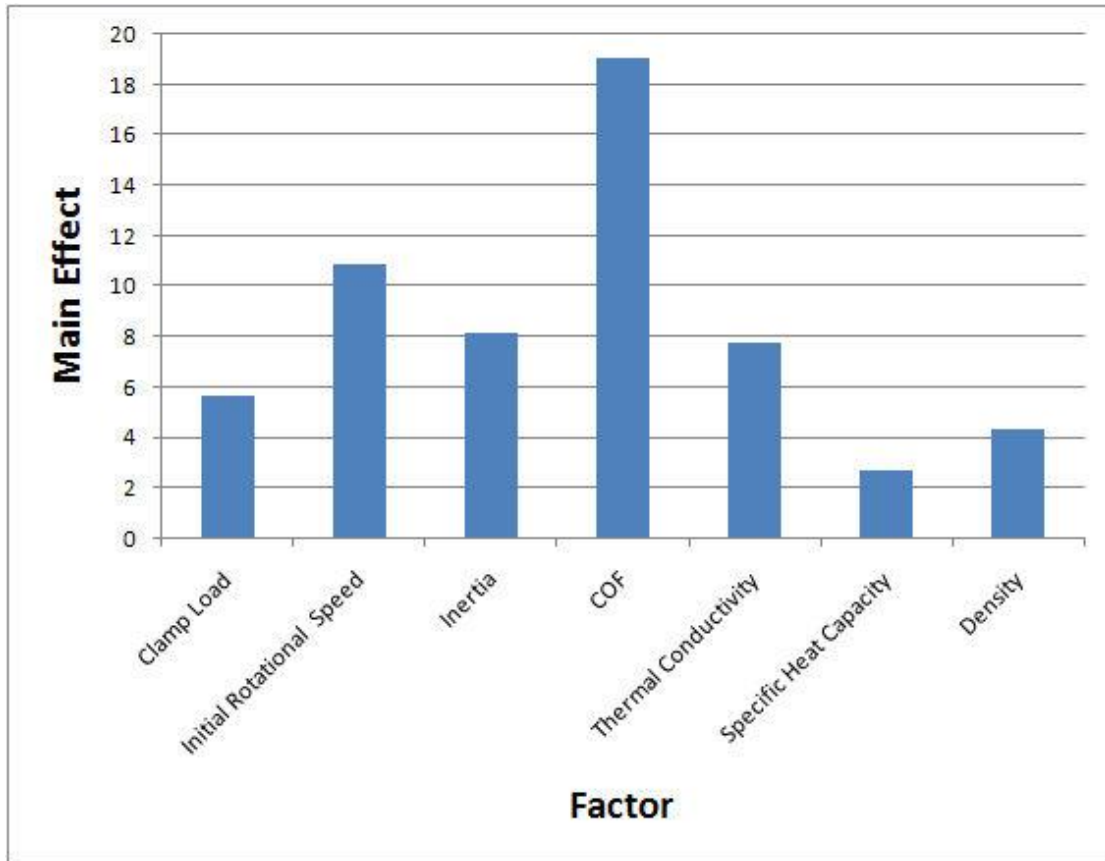


Figure 6.10 – Main Effect Results

The limitations of this analysis are that the level 1 and 2 values used are two extreme values representing the minimum and maximum possible values that factor could have. The clamp load, initial rotational speed and inertia are all factors that can be carefully controlled during engagement tests using the SCID and the level 1 and level 2 values are the realistic limits of those values. Hence the main effects shown for these factors are representative of the actual system and show that, of these three factors, changing the initial rotational speed would have the largest effect on the maximum friction surface temperature.

The material properties are much more difficult to change as this would require a different type of material to be ordered from the clutch plate manufacturer. This would involve a process change which would be very costly and the production time of carbon/carbon materials can be up to six months so a material property change is not something that can be implemented in a short timescale. It is also very unlikely that the three material properties discussed here can be at level 1 or level 2 independently of the other material properties as assumed in this analysis. The

implication of this would be that the properties could not independently be at their extreme values thereby reducing the main effects predicted in this analysis. Even so, the only material property that has a larger main effect than any of the system properties is the thermal conductivity.

As can be seen from Figure 6.10, this analysis has shown that the coefficient of friction is the factor that has the largest influence on the maximum friction surface temperature. The values used in this analysis for level 1 and level 2 are extreme values but have been taken from previous dynamometer data [7] which showed that the coefficient of friction can vary between the level 1 and level 2 values during a single clutch engagement. These friction characteristics were discussed in the literature review. Based on these sources, this result was expected and confirms that the coefficient of friction, which is a function of surface temperature and morphology, is the critical factor that requires careful control.

It must be noted though that this result assumes full area contact between two perfectly flat clutch-plate friction surfaces. The thermal imaging results from the SCID tests indicated that hot banding does occur, leading to contact localisation and hence less than full area contact. This contact localisation will also have a large effect on the maximum friction surface temperature and thus the 1D model is insufficient for accurately predicting clutch-plate temperatures. This is demonstrated by Figure 6.8 which showed that the 1D heat transfer model predicts a maximum friction surface temperature of well below those recorded during SCID testing. It can clearly be seen from Figure 6.8 that despite the inertia value used in the 1D model being ~35% greater than the inertia used in the SCID, the maximum friction surface temperature predicted by the model is approximately 1000K less than the lowest maximum temperature recorded during SCID engagement tests for that speed/load combination.

The results of the 1D model do however suggest that the surface morphology-COF-temperature relationship shown in Figure 1.11 in Chapter 1.2 does exist. Hence by understanding which factors have the largest influence on friction surface temperature, it may be possible to control the friction surface morphology and COF.

6.12 Summary

A 1D heat transfer model has been constructed using Matlab. This model was validated against a 1D finite element model constructed in Abaqus in order to ensure that the finite difference method used was correct. The 1D Matlab model was then used to carry out a Taguchi design of experiment in order to determine which of the factors of the clutch-plate engagement process (both system factors and material properties) have the greatest influence upon maximum friction surface temperature. This analysis showed that the surface coefficient of friction is the most influential factor upon friction surface temperature when full area contact is assumed. However, the 1D model is insufficient for accurately predicting clutch-plate temperatures during clutch-plate engagements.

7. Thermomechanically Coupled Finite Element Analysis (TCFEA)

7.1 Introduction

A thermomechanically coupled finite element analysis was carried out by coupling Matlab and Abaqus in order to accurately predict clutch-plate friction surface temperatures during SCID engagement tests. The use of a finite element model allowed material deformation and surface profile variations due to thermal expansion to be taken into account leading to predictions of contact pressure localisation and by extension, hot banding.

Introduction of worn surface profiles allowed analyses to be carried out to understand how the initial surface profile of the clutch plates affects their behaviour. A wear model was then introduced which allowed hot band migration to be modelled and its effect on torque behaviour to be predicted.

Finally, the results of the TCFEA were then compared to SCID engagement test results to assess how well the TCFEA models simulate real clutch-plate friction performance and thermal behaviour.

7.2 Abaqus Thermomechanical Model

The initial stage in the TCFEA process was to create a finite element model of the clutch plates in Abaqus. Table 7.1 lists the key parameters of the Abaqus model and Table 7.2 lists the material properties used. A representation of the Abaqus model is shown in Figure 7.1. The clamp load, initial rotational speed, inertia and time step values used in the TCFEA simulations are the same as those listed in Table 6.2.

Model Type	Axisymmetric
Analysis Type	Coupled Temperature-Displacement
Element Type	Coupled Temperature-Displacement CAX4T (Quad)
Mesh	21 x 41-221 (discussed in section 7.4)
Bias Ratio	2.0

Table 7.1 – Key Parameters in Abaqus Thermomechanical Model

Property	Temp (K)	Parallel to Friction Surface (Radial)	Perpendicular to Friction Surface (Axial)
Density (kgm^{-3})	All	1850	
Young's Modulus (Nm^{-2})	All	17.5×10^9	
Thermal Conductivity ($\text{Wm}^{-1}\text{K}^{-1}$)	298	16.3	10.5
	573	22.4	14.3
	873	23.8	14.9
Specific Heat Capacity ($\text{Jkg}^{-1}\text{K}^{-1}$)	298	708	
	573	1350	
	773	1730	
	873	1720	
Expansion coefficient	All	3.9×10^{-6}	1.6×10^{-6}

Table 7.2 – Material Properties Used in Abaqus Thermomechanical Model [7]

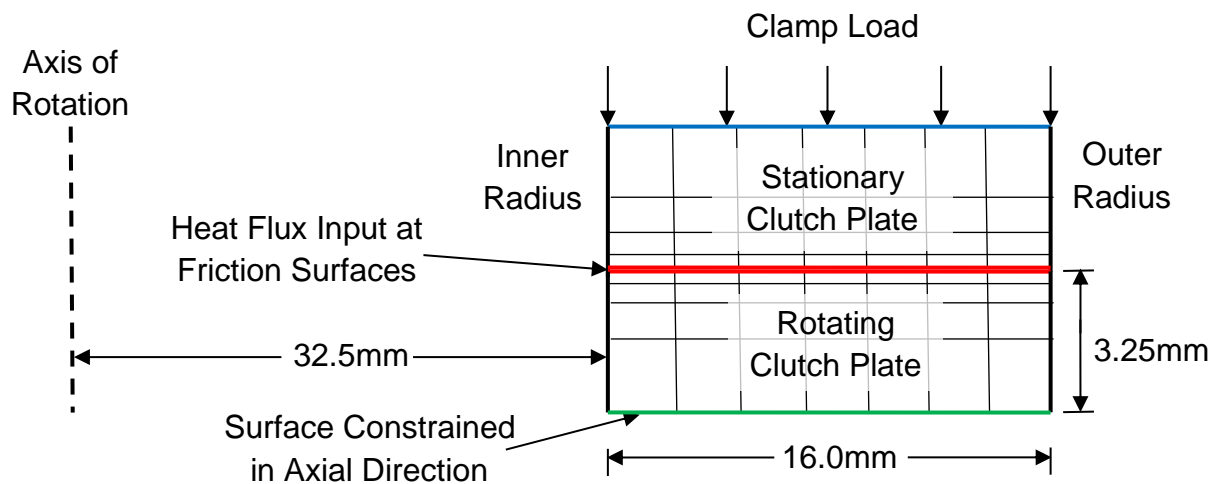


Figure 7.1 – Abaqus Axisymmetric Finite Element Model of Clutch Plates
(Through-thickness=3.25mm for both clutch plates)

For the temperature dependent properties shown in Table 7.2, Abaqus uses linear interpolation to calculate the property values [65]. If any temperatures higher than those referenced are predicted, Abaqus uses the property value of the highest given reference temperature as opposed to extrapolating a value.

An axisymmetric model differs from a planar 2D model in that the former model is referenced to an axis of rotation which in this case is the clutch plate centre. Figure 7.1 shows how this is modelled in Abaqus where only one internal face of each clutch plate is modelled. In axisymmetric theory, this cross-section would be extruded through 360° about the axis of rotation to form the full three-dimensional clutch plates. This type of model is only valid therefore if circumferential variations are negligible, which is believed to be true for this application. This negates the need for a 3D model which would increase complexity and computing time. It is important to note that in Figure 7.1, one clutch plate has been defined as stationary and one as rotating as this represents the setup in the SCID which the TCFEA is simulating. In the model however, it is not necessary for either clutch plate to be able to rotate. They are however referred to as stationary or rotating in the remainder of this chapter as per Figure 7.1.

The analysis and element type used are both Coupled Temperature-Displacement as the thermal expansion at the surface is a critical consideration. A heat transfer analysis alone would be insufficient as thermal expansion would not be simulated.

The 1D heat transfer model showed that 5 nodes were sufficient to model the heat transfer through the thickness of the clutch plates due to the clutch plates being very thin. In the axisymmetric model, the thermal expansion also needs to be modelled and hence 5 nodes would likely be insufficient. A preliminary model with 21 nodes (20 elements) in the through-thickness direction was used with a bias ratio of 2.0 towards the friction surfaces. The mesh is therefore twice as dense at the friction surfaces as it is at the non-friction surfaces. This was done to allow the behaviour of the friction surface to be simulated more accurately. This preliminary model was used to determine the number of nodes required along the friction surface through a mesh sensitivity analysis. A separate mesh sensitivity analysis was then carried out to determine the number of nodes required in the through-thickness direction to provide reliable results (see Section 7.4).

Only one boundary condition was applied to the model at its bottom edge. This edge is constrained in the axial direction only, leaving the edge free to expand radially. This was considered to be the most realistic boundary condition based on the how the clutch plates are mounted within the SCID. Firstly, no radial constraints were applied as the clutch basket and splined hub upon which the clutch plates are mounted, are designed and manufactured with a small clearance (~0.5mm) to allow for radial thermal expansion. The bottom edge was constrained in the axial direction as this edge of the rotating clutch plate is flat against a rigid surface and therefore the surface cannot move in the axial direction. Although some thermal expansion may take place in reality, the temperature across this edge is likely to be relatively uniform during the clutch plate engagement, unlike the non-uniform distribution at the friction surface, due to the time delay in the heat being conducted through the clutch plate. No other axial constraints were applied to the model. The friction surfaces must be free from boundary conditions in order to fully predict thermal expansion effects. The top edge where the clamp load is applied is free to move in the axial direction which is necessary in order for any friction surface contact pressure to be generated. If it was constrained in the axial direction, the clamp load applied to the top edge would simply be reacted by the top edge.

An interaction was imposed on the friction surfaces to define contact. Surface-to-Surface Contact was used with the normal behaviour defined as “hard” contact. “Hard” contact means that no penetration of the materials can occur and contact pressure can only arise if there is contact. Thermal conductivity was introduced to allow the transfer of heat between the clutch plates provided that they are touching. The friction surfaces were allowed to separate after initial contact. Hard contact dictates that no contact pressure can arise where the surfaces have separated.

The clamp load was modelled as a pressure applied to the top edge of the model. This is the back face of the stationary clutch plate in the SCID and as this face is against a machined flat surface, it is reasonable to assume a uniform pressure along this edge. Every element along both friction surfaces were defined as individual surfaces (see Section 7.3.1) such that a different value of heat flux could be applied to each surface to establish a non-uniform heat flux distribution.

7.3 Matlab-Abaqus Coupling

The axisymmetric model constructed in Abaqus can be used to predict temperature variations in the radial and axial directions of the clutch plates. It can also predict material deformations which will affect how the heat flux is applied to the friction surface and therefore affect the temperature distribution.

Matlab is particularly effective at carrying out user-defined tasks which can operate in a continuous loop until another user-defined condition is met. The programming interface and language are easy to learn and data is simple to save and present.

These features of Abaqus and Matlab were utilised by coupling the two programs such that after construction of the initial axisymmetric finite element model in Abaqus, the TCFEA was carried out entirely using a Matlab script. This allowed the Abaqus model to be run in a continuous loop where the inputs are calculated in Matlab and the output data also processed in Matlab. The output data was then saved to file which can be read and presented using Matlab as well as constructing an output database which can be opened via the Abaqus graphical user interface (GUI).

Figure 7.2 shows how the TCFEA works by coupling Matlab and Abaqus. The construction of the Matlab scripts that make this possible are discussed in the subsequent sections.

Key: ——— Matlab
 ——— Abaqus

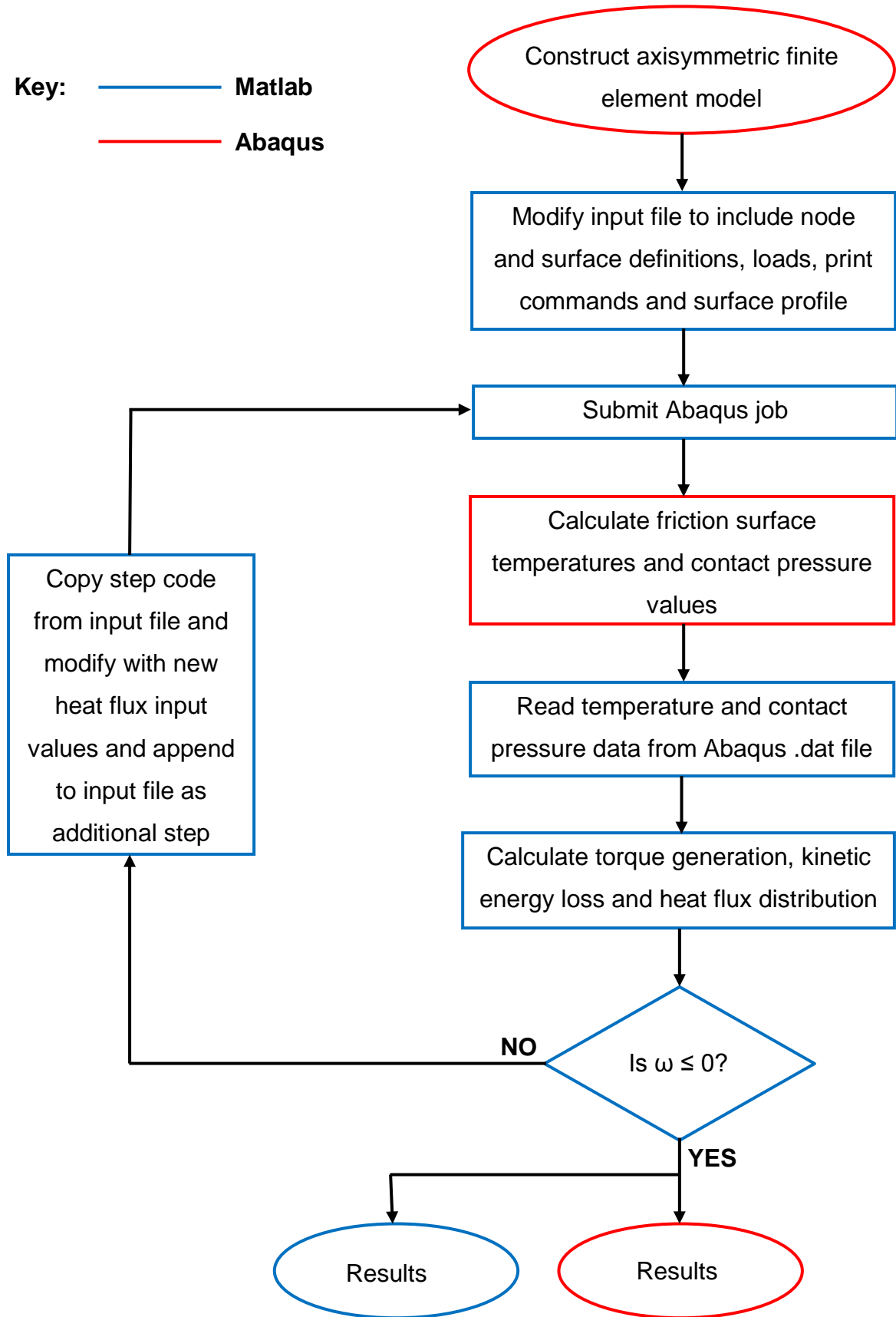


Figure 7.2 – Matlab-Abaqus Coupling for TCFEA

7.3.1 Input File Setup

In order for the data calculated in Abaqus to be output to the .dat file from which Matlab can read the values, the relevant nodes must first be defined as specific sets in the Abaqus finite element model before print commands can be added. The same applies for the loads in that surfaces must first be defined to which the loads are applied. For a small model that has 21 nodes along the friction surfaces, 21 nodes (only need to be defined on the slave surface as contact pressure and temperature will be identical on both surfaces) and 40 surfaces (both plates, 20 elements each) would need to be defined manually using the Abaqus GUI. This would be time consuming for one model let alone a series of models. Matlab has therefore been used to automate this process.

First, an axisymmetric model was created in Abaqus defining the geometry, analysis and element type, boundary conditions, interactions and mesh construction. The job for the model was then submitted using the Abaqus GUI which creates the input file (.inp) for that model. The job source was then changed from 'Model' to 'Input File' meaning that only the script contained in the input file is used for the analysis. Any changes made to the model using the GUI are ignored but any changes made to the input file affect the analysis.

Initially, a single node, surface and load were defined manually and the input file examined to understand where the scripts for these functions are inserted into the input file. The print commands were found in the Abaqus Keywords Manual [65]. Once it was understood how the input file is structured, Matlab was used to insert lines of script into the original input file to define nodes, surfaces, loads, print data and friction surface profiles. Figure 7.3 shows how this process works. The process is repeated to first insert the lines of script defining node sets and then the lines of script defining the surfaces and so on.

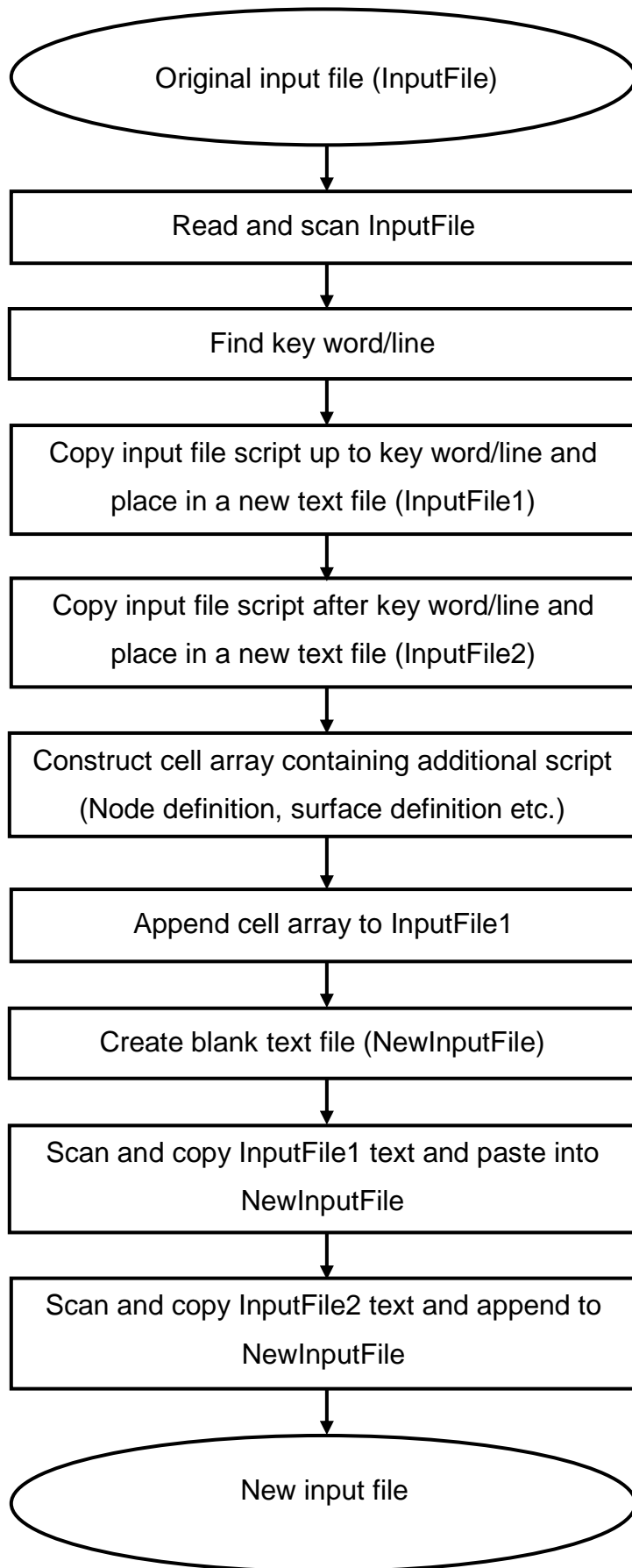


Figure 7.3 – Process for Modifying Input Files

Before this process could be carried out however, it needed to be understood how Abaqus numbers the nodes and elements in the model in order to then define node sets, surfaces etc. Using the global (default) coordinate system, Abaqus numbers the surfaces of a single element as shown in Figure 7.4 and numbers the nodes and elements within a mesh as shown in Figure 7.5. Understanding how Abaqus does this allowed user-defined surfaces and node set definitions to be added to the input files using Matlab as opposed to a manual approach.

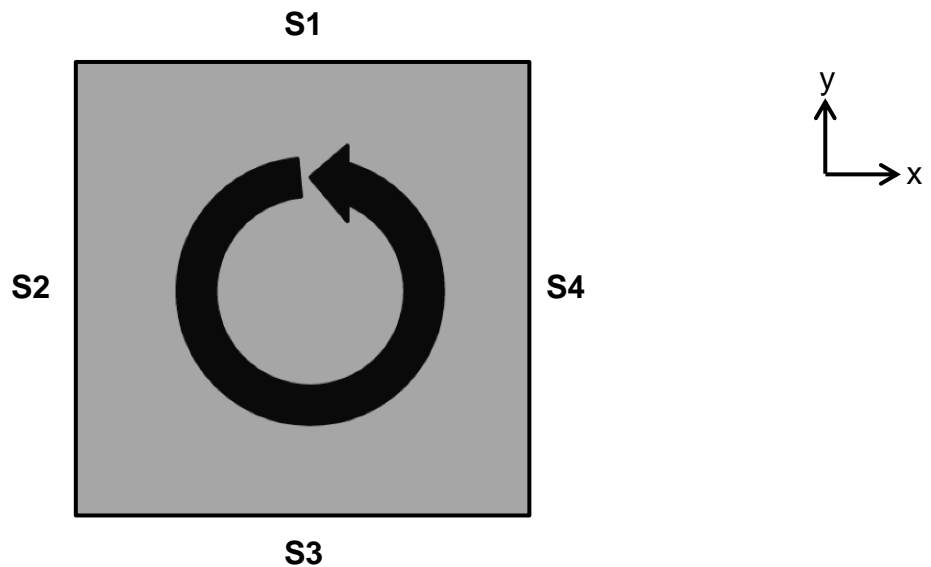


Figure 7.4 – Default Surface Numbering of Elements in Abaqus

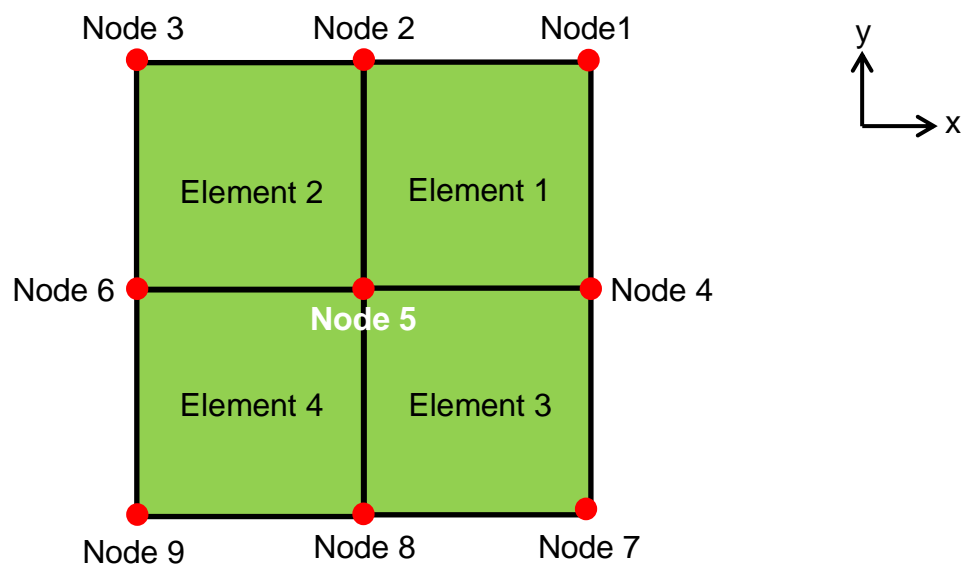


Figure 7.5 – Default Node and Element Numbering in Abaqus

The coordinates that represent the position of each node in the model are written near the beginning of the input file. Changing the surface profile simply involves cutting the lines of script that define the friction surface nodes and inserting new lines of script with new coordinates. For example, a simple sine-wave profile was introduced to model the waviness of a used clutch plate using Equation 7.1. The original friction surface y-coordinates (uniform as surface is constructed as flat) and the inner radius of the clutch plate were defined as the origin from which the sine wave was produced where the height of the sine wave, and hence friction surface, is calculate using Equation 7.1:

$$y = A_s \sin(B_s x - C_s) \quad (7.1)$$

Where: y – Height of Surface Above Origin (m)

x – Radial Position (m)

A_s – Amplitude (m)

B_s – 1/Wavelength (m^{-1})

C_s – Phase Shift (rad)

The amplitude of the sine wave profile is simply the mean peak height found from the race-conditioned clutch-plate surface waviness investigation (see Chapter 5.4). A phase shift was only used to create profiles for the simulations of the contact of two used clutch plates where the phase shift was applied to one of the surfaces only. Peak-to peak contact is achieved using a phase shift of zero, $\pi/2$ for peak-to-trough contact and $\pi/4$ for the intermediate case. B_s is a constant related to the length of a single complete wave of the sine wave profile and hence dictates the number of peaks and troughs along the friction surface. This value must be set such that the value inside the brackets in Equation 7.1 is equal to 2π after one full wavelength where the value of x would equal the radial position at which the first full wavelength is complete if the inner radius of the clutch plate is defined as the origin.

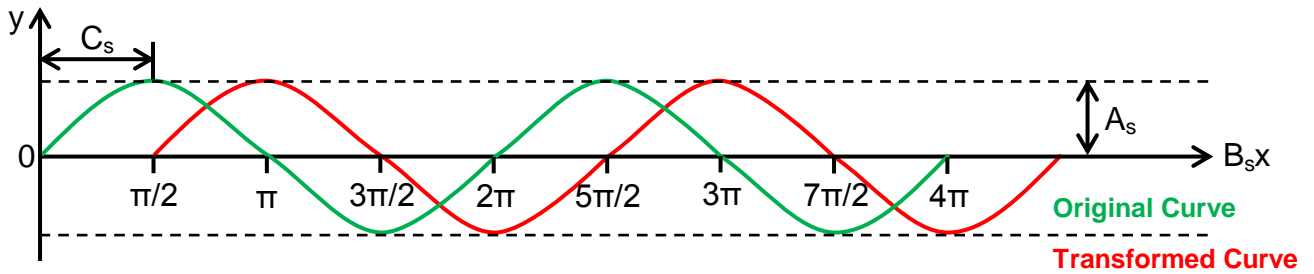


Figure 7.6 – Sine Wave Profile Parameters

Nodes were defined for the slave friction surface (friction surface of stationary plate) according to the Abaqus numbering system (Figure 7.5). Therefore Node1 corresponds to the node at the outer radius of the friction surface and NodeN corresponds to the node at the inner radius of the friction surface. If N is the number of nodes along the friction surface and Y is the number of nodes in the through-thickness direction of the clutch plate, the default node numbers assigned by Abaqus would be equal to:

$$N \times Y - (N - 1) : N \times Y \quad (7.2)$$

For instance, for a 6x3 mesh, the slave friction surface nodes would be node 13 to node 18 where Node1 would be assigned to node 13, Node2 to node 14 and so on. This would result in the node set definitions shown in Figure 7.7:

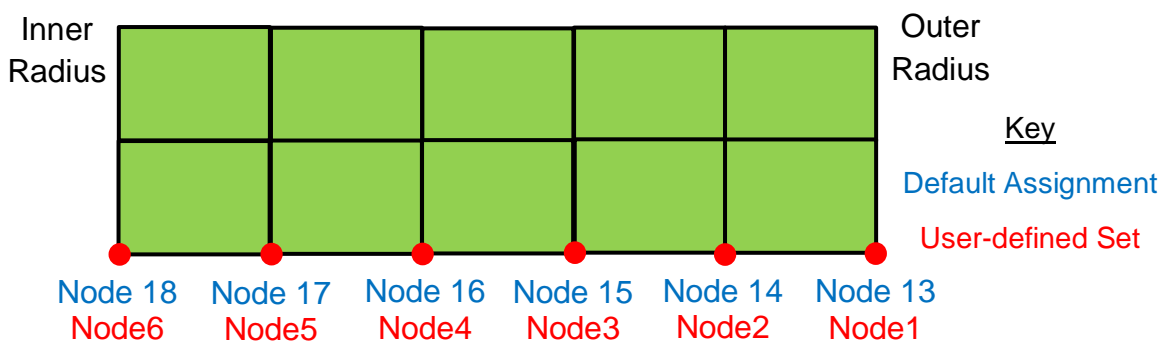


Figure 7.7 – Node Set Definitions for Slave Friction Surface

The user-defined surface sets are defined in a very similar way to the nodes except they are defined in relation to elements and edges of those elements. The surfaces were defined such that the element surfaces of the stationary plate were assigned

odd numbers and the surfaces of the rotating plate were assigned even numbers. For the stationary plate, user-defined surfaces were assigned to the S3 surface of the friction surface elements (see Figure 7.4) whilst user-defined surfaces were assigned to the S1 surface of the friction surface elements of the rotating plate. The element numbers were calculated according to Equation 7.3 and 7.4 as per the system shown in Figure 7.5:

$$\text{Instance 1 (Rotating):} \quad 1 : N - 1 \quad (7.3)$$

$$\text{Instance 2 (Stationary):} \quad (N - 1) \times (Y - 1) - (N - 2) : (N - 1) \times (Y - 1) \quad (7.4)$$

The heat flux inputs are simply implemented by defining a heat flux to the user-defined surfaces. A non-uniform heat flux distribution can therefore be established by applying different values of heat flux to each surface.

Finally, print commands are added towards the end of the input file so that the contact pressure and temperature values at each node set at the end of the time step are written to the Abaqus .dat file.

7.3.2 Full Analysis

After the input file is modified, the full analysis can be carried out according to Figure 7.2. The first stage in this process involves scanning the input file and copying the lines of script that define the initial step into a cell array which is stored within Matlab during the analysis. This saves computing time in that rather than writing the entire step script for the new step that will be appended to the input file, only the lines of script that will be different have to be modified and can be done so entirely within Matlab by editing lines within the cell array.

The Abaqus job is submitted from the Matlab code by use of the '!' character which submits the job using the CPU negating the use of the Abaqus GUI resulting in no direct user input being required to submit the job beyond running the Matlab script.

Once the job is complete, the Matlab program opens and scans the Abaqus .dat file using the 'textscan' function and then uses the 'strcmp' function to find a user-defined line of script. The line of script that Matlab searches for is related to the line

in the .dat file that precedes the printed results for a particular node. This is done in a loop such that the contact pressure result for a single node is read and stored in a matrix within Matlab. This process is then repeated by Matlab for the other nodes and repeats the whole process again for temperature results.

A simple relationship between temperature and coefficient of friction was used in the analysis to model COF variation. These values have been taken from previous dynamometer test results [7]. Table 7.3 shows the values used in the full analysis. The spline function within Matlab was used to linearly interpolate the COF value from Table 7.3 based on the surface node temperature. If the node temperature is above 1473K, the COF value is linearly extrapolated.

Temperature (K)	COF
298	0.20
473	0.25
673	0.30
873	0.35
1073	0.40
1273	0.45
1473	0.50

Table 7.3 –Temperature-COF Reference Values Used in TCFEA [7]

The COF values are used to calculate the torque produced at the friction interface. The overall value of torque produced is calculated by summing the torque produced at each element along the friction interface according to Equation 7.5:

$$T = \sum T_{element} \quad (7.5)$$

The torque at each element is calculated using Equation 7.6:

$$T_{Element} = C_{Press_{Element}} \times A_{Element} \times COF_{Element} \times r_{Element} \quad (7.6)$$

Where: T – Torque (Nm)
 $CPress$ – Contact Pressure (Pa)
 A – Annular Area (m²)
 COF – Coefficient of Friction
 r – Radius (m)

The contact pressure is calculated only at the surface nodes so the contact pressure for the element was calculated by taking the average of the contact pressure values at each element's surface nodes. The same method applied to calculating the radius at which the torque was produced. The COF value was taken as the average of the COF values calculated for the two surface nodes based upon their temperatures. It can be seen from Equation 7.6 that torque can only be produced if there is contact pressure meaning that no torque can be generated where the friction surfaces have separated.

The effective friction radius (EFR) is calculated separately from the torque using Equation 7.7:

$$EFR = \frac{\sum(r_{Node} \times CPress_{Node})}{\sum CPress_{Node}} \quad (7.7)$$

The total torque produced at the friction interface is then used to calculate the decrease in rotational speed of the rotating clutch plate and associated inertia and therefore the energy dissipated at the friction interface during the next time step, equal to the reduction in kinetic energy of the rotating mass. This value is divided by the clutch plate area to obtain an overall heat flux just as in the 1D model (Equation 6.14). However, the heat flux is then partitioned according to the contact pressure distribution across the friction interface which reflects the fact that no torque can be produced without contact and therefore no energy will be dissipated at those points. The first stage in calculating the distribution of heat flux involves calculating a contact pressure ratio for each element using Equations 7.8 and 7.9:

$$CPress_{Average} = \frac{\sum CPress_{Node}}{N} \quad (7.8)$$

$$CPressRatio_{Element} = \frac{CPress_{Element}}{CPress_{Average}} \quad (7.9)$$

The heat flux input to each element's friction surface is then calculated:

$$HeatFlux_{Element} = HeatFlux \times CPressRatio_{Element} \quad (7.10)$$

The torque generated at each element's friction surface is proportional to the contact pressure across that element and the contact pressure ratio is proportional to the contact pressure across that element. The heat flux applied at each element is therefore proportional to the torque generated at that element. This means that no heat flux is applied at elements that do not generate any torque and hence do no work and large proportions of heat flux are applied to elements that generate torque reflecting the fact that more work is done at those parts of the friction interface.

Once the heat flux distribution has been calculated, the cell array containing the lines of script that define the step is modified to include the new step name and new values of heat flux. All other parts of the step remain the same. This modified cell array is then appended to the input file.

There are now two sets of print commands in the input file; those in the first step and those in the appended step. This means that contact pressure and temperature results will be printed for each node for both steps. As more and more steps are added to the analysis, the amount of text that Matlab has to scan will become larger and increase the computing time. As only the results at the end of the latest step are of interest (the previous results have been stored in a matrix within Matlab), the input file is modified to include print data for only the final step in the analysis. This is achieved by dividing the input file into three sections with the first containing the input file script up to the first set of print commands, the second part containing the first set of print commands and the third part containing the remaining script. The second part is discarded and the third part is appended to the first part to form the new input file which contains only one set of print commands for the final step in the analysis.

The process described in this section is repeated using a for loop until the rotating clutch plate has become stationary at which point a break command forces Matlab to exit the for loop. The results of the analysis are saved to text files which can then be read by Matlab using scripts that have been written specifically to present the results.

7.4 Mesh Sensitivity Analysis

A mesh sensitivity analysis was carried out in order to determine the number of nodes required along the friction surfaces to give accurate results. All models had 21 nodes in the clutch plate through-thickness direction and the friction surfaces were modelled as being initially perfectly flat. The outputs of interest were the maximum contact pressure and maximum friction surface temperature predicted. Figure 7.8 shows the mesh sensitivity analysis results. All the maxima occur at approximately the same time during the engagement (0.4-0.5s) and at approximately the same radius of the friction surface (~37mm). This result is discussed further in Section 7.5.

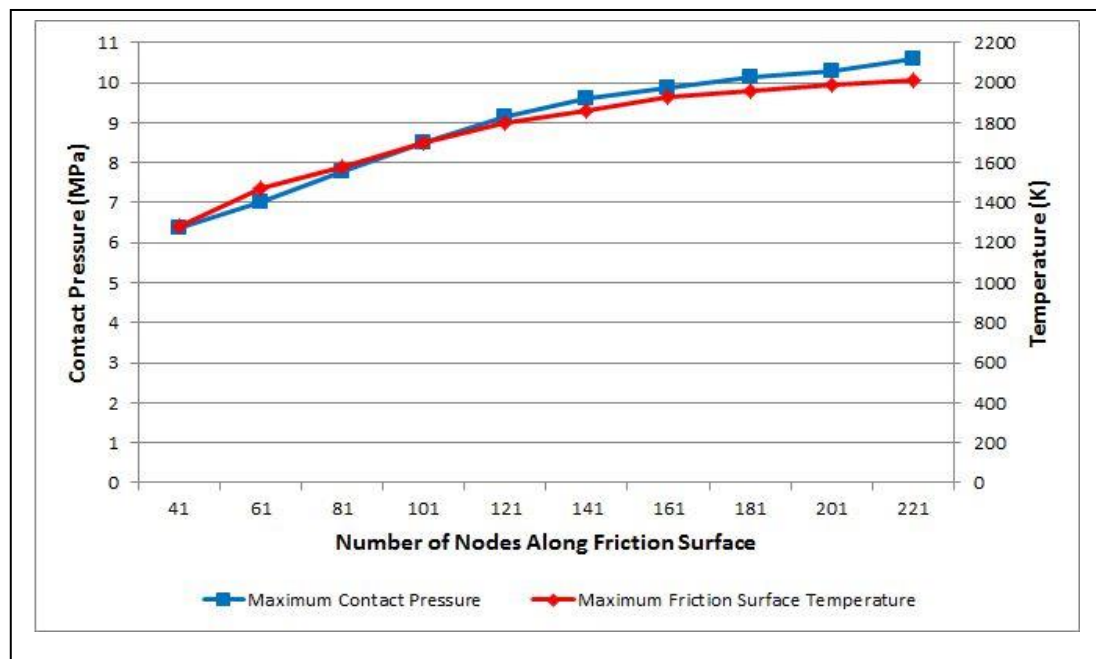


Figure 7.8 – Friction Surface Mesh Sensitivity Analysis Results

As can be seen from Figure 7.8, the difference between 41 nodes and 61 nodes is very large. It is around 200K for the maximum friction surface temperature and 0.7MPa for the maximum contact pressure which equates to approximately 16.67%

and 10% of the maximum temperature and pressure respectively. As expected, as more nodes are included on the friction surfaces, the difference between the simulations becomes less and less. Comparing the result at 181 nodes to the result at 201 nodes and the result at 201 nodes to the result at 221 nodes, the difference in maximum temperature and pressure falls to around 30K (~1.5%) and 0.2MPa (~2%). These differences could be reduced by further increasing the number of nodes along the friction surfaces but it was decided that these small differences were acceptable especially when the computing times were taken into account (see Figure 7.9). The computing time increases approximately linearly with the number of nodes such that gains in accuracy for each extra hour of computing time become smaller and the extra computing time becomes unjustifiable. A compromise of 201 nodes along the friction surfaces was therefore chosen for subsequent simulations.

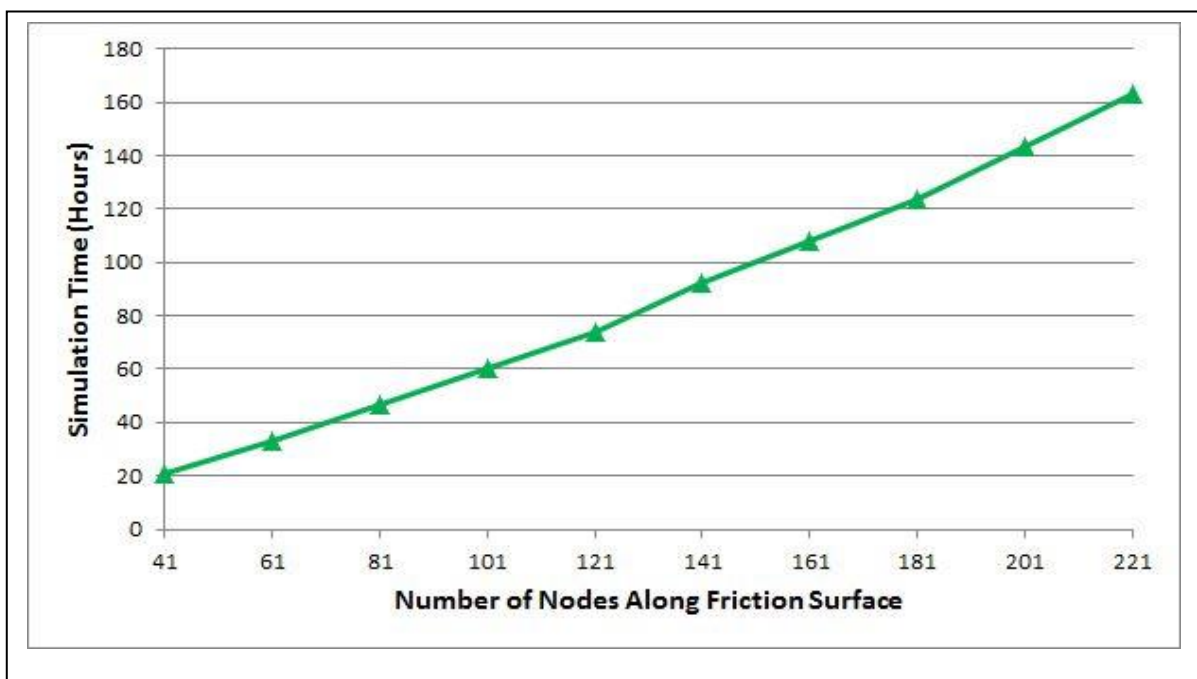


Figure 7.9 – Computing Time for Friction Surface Mesh Sensitivity Analysis

A further mesh sensitivity analysis was carried out for the through-thickness direction. Figure 7.10 shows the results of this analysis. The difference between the results for 11 and 21 nodes is around 120K (~6%) and 0.75MPa (~7.3%) for the maximum friction surface temperature and contact pressure. The difference between 21 nodes and 31 nodes however is much smaller at around 40K (~2%) and 0.4MPa (~3.7%). Although these differences are larger than those deemed acceptable for the

number of nodes along the friction surface, it was decided that 21 nodes in the through-thickness direction is sufficient when the computing time is taken into account. Figure 7.11 shows that the computing time increases considerably as more nodes are used due to the finite element model becoming larger and therefore more computing time is required to complete the analysis within Abaqus.

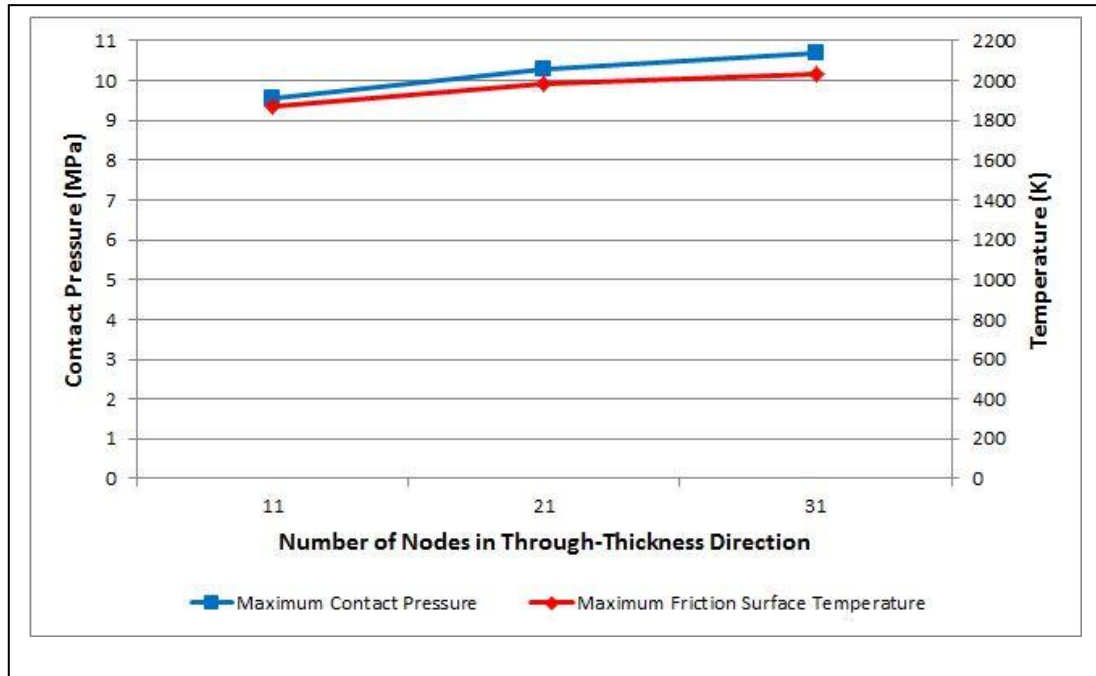


Figure 7.10 – Through-Thickness Mesh Sensitivity Analysis Results

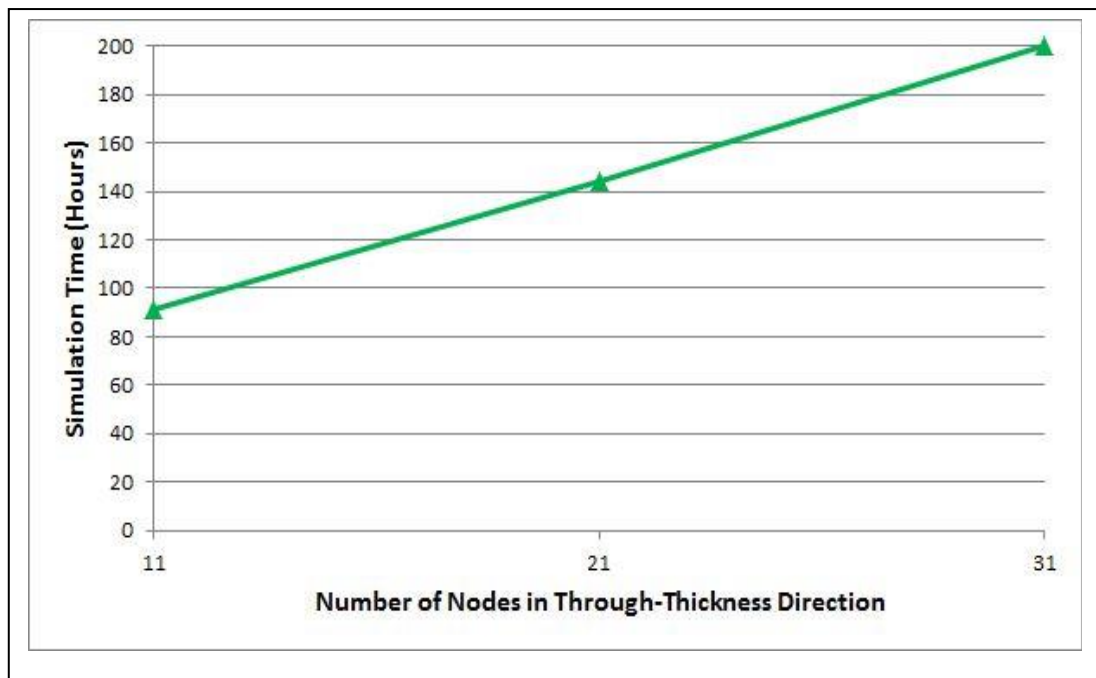


Figure 7.11 – Computing Time for Through-Thickness Mesh Sensitivity Analysis

7.5 Initially Flat Surface Results (Non-Wear Model)

The TCFEA was first carried out simulating clutch plates with initially perfectly flat friction surfaces (ie. no wear profile). The full length of the friction surfaces are therefore in contact leading to a uniform contact pressure distribution at the beginning of the clutch plate engagement. In reality, it is very rare that this situation would arise as even machined surfaces are not perfectly flat and will have some surface asperities which will lead to localised contact and hence a non-uniform contact pressure distribution. However, the flat-to-flat surface analysis was carried out in order to understand how the contact pressure and temperature fields may evolve during the course of a clutch plate engagement without initial surface profiles being an influencing factor.

Figure 7.12 shows the initial contact pressure and friction surface temperature profiles predicted by the analysis. The contact pressure distribution is uniform due to the friction surfaces being modelled as perfectly flat and the initial temperature profile is also uniform across the friction surface. These figures show the results after 0.01 seconds of the simulation as one time step must be completed to obtain contact pressure values from Abaqus. In reality, this represents the moment of clutch-plate engagement.

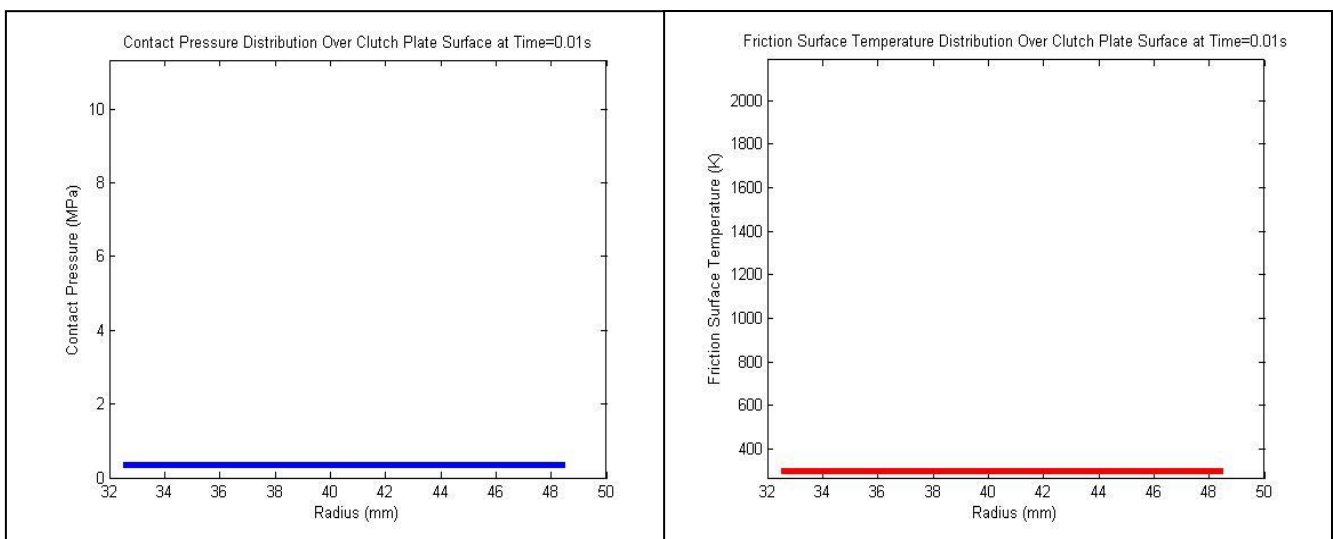


Figure 7.12 – Contact Pressure and Friction Surface Temperature Profiles at $t=0.01s$

Figure 7.13 shows the contact pressure and friction surface temperature profiles after a further time step ($t_{step}=0.01s$) and it is important to note how the contact pressure distribution has changed. It can clearly be seen that the contact pressure at the inner and outer radius has fallen to zero. This is due to a loss of contact between the friction surfaces as a result of expansion of the clutch plates in the radial direction. The surface temperature profile is not affected at this point as very little heat input has taken place.

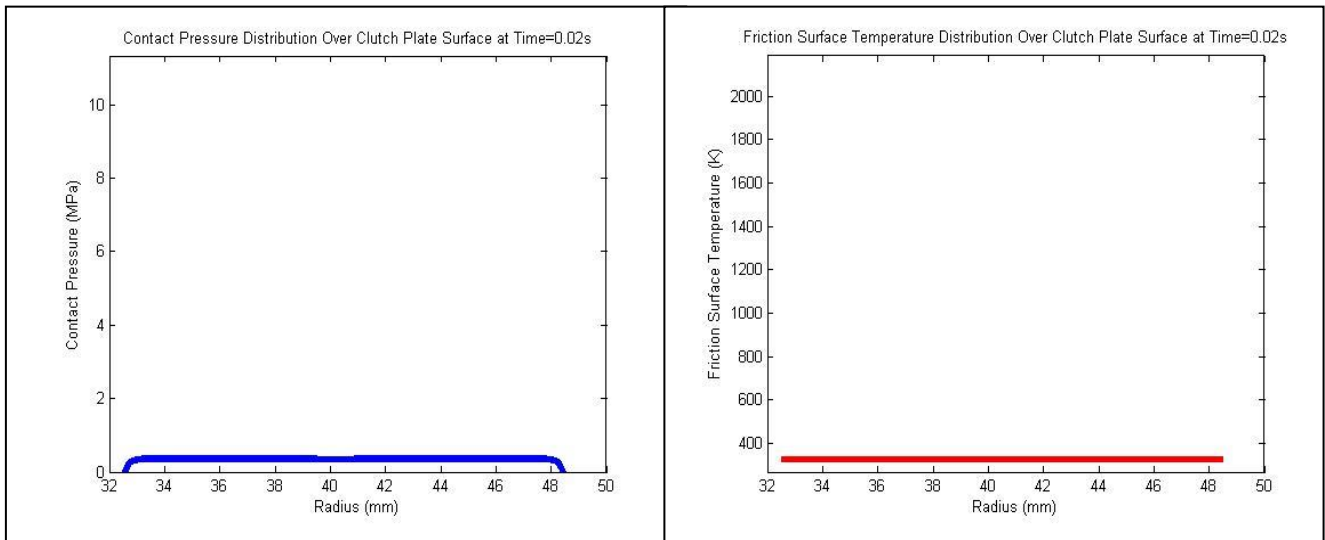


Figure 7.13 – Contact Pressure and Friction Surface Temperature Profiles at $t=0.02s$

Figure 7.14 shows that as the simulation progresses, further loss of contact at the inner and outer radii occurs leading to a rise in contact pressure towards the inside of the clutch-plate friction surface and two small peaks of higher contact pressure are established. Due to the results shown in Figure 7.13, no heat flux has been applied to the inner and outer radius and the effect this has on the temperature profile is apparent. A similar trend to that of the contact pressure is followed whereby two small peaks of higher temperatures have arisen, coinciding with the peaks of contact pressure. This is due to the heat flux becoming concentrated in the areas of higher contact pressure as a greater amount of energy is dissipated in these areas as a result of the higher normal force. The coefficient of friction is also greater as a result of the higher temperatures (Table 7.3).

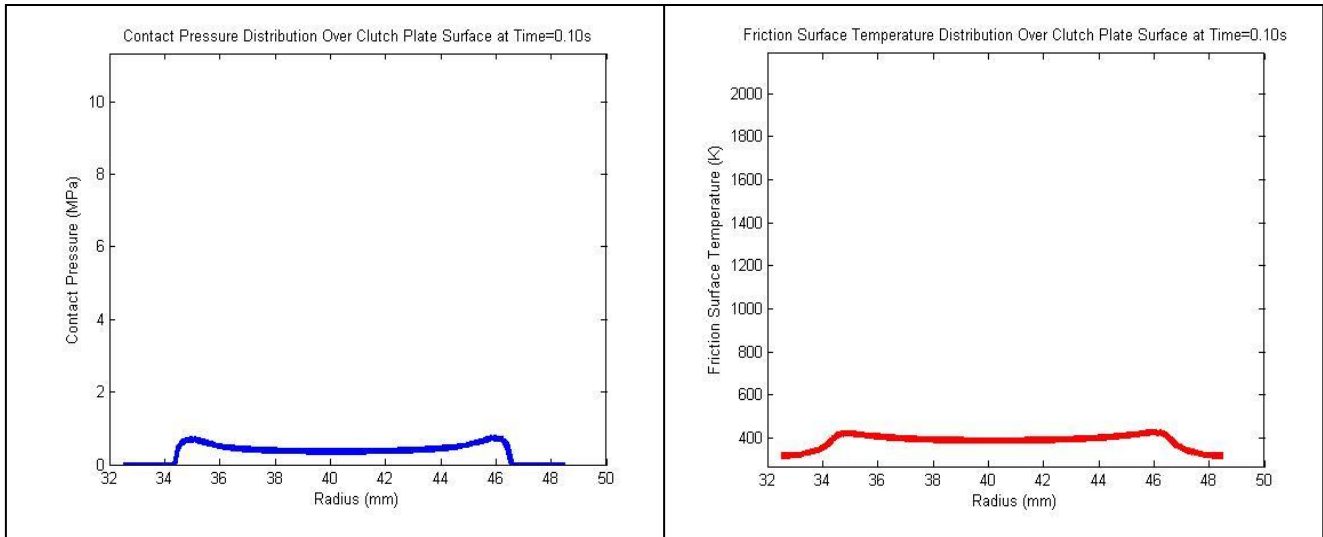


Figure 7.14 – Contact Pressure and Friction Surface Temperature Profiles at t=0.10s

The consequence of the heat flux concentration causing peaks of temperature is that greater amounts of thermal expansion occur at these points leading to further separation of the friction surfaces as they are effectively pushed apart. The effect of this can be seen in Figure 7.15 where the profiles seen after 0.10s have become more extreme after a further 0.10s and two distinct peaks of contact pressure and temperature have formed. The thermal expansion at these points has resulted in contact pressure being reduced at the centre of the clutch plate as well as a further loss of contact near the inner and outer radii. This in turn will cause the heat flux to become more concentrated towards the areas of high contact pressure.

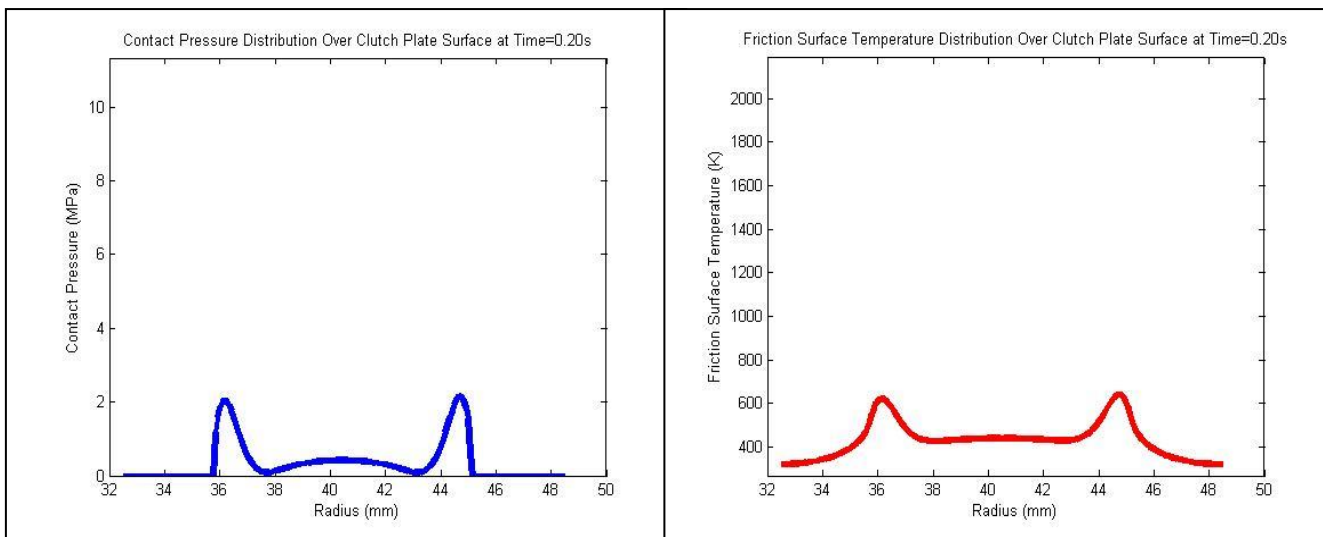


Figure 7.15 – Contact Pressure and Friction Surface Temperature Profiles at t=0.20s

Figure 7.16 shows the contact pressure and surface temperature profiles at the time at which the maximum contact pressure and maximum surface temperature occurs. At these points, it can clearly be seen that contact is isolated to two discrete bands and large friction surface temperatures have resulted in these bands. The maximum contact pressure is approximately 10.3MPa which is almost thirty times greater than the initial contact pressure of approximately 0.35MPa. The maximum surface temperature is almost 2000K compared to that at the centre of the friction surface and the inner and outer radii which are at around 350K. Figure 7.17 shows a temperature contour plot for the clutch plates at $t=0.45s$ showing that the friction surface temperature is much higher than that of the rest of the clutch plate. There has been insufficient time for heat to be conducted away from the friction surface such that large temperature gradients exist in the through-thickness direction as well as along the friction surface. The non-friction surfaces are at around 320K compared to 2000K at the friction surfaces, a difference which is comparable to the temperature gradients predicted across the friction surface.

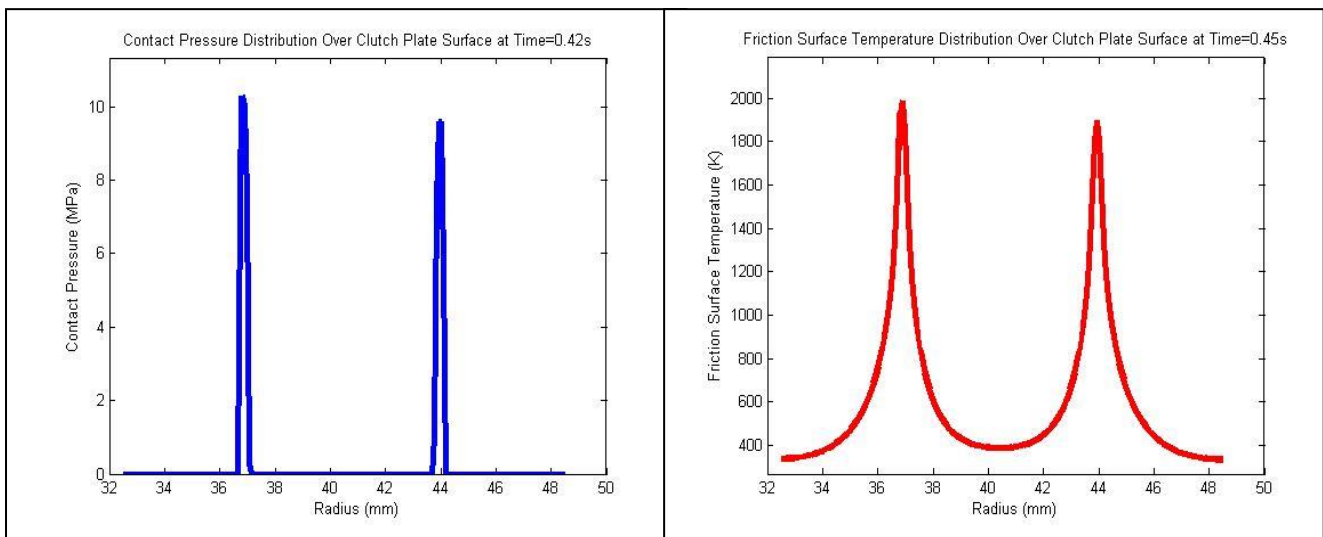


Figure 7.16 – Maximum Contact Pressure and Friction Surface Temperature Profiles at $t=0.42s$ (Contact Pressure) and $t=0.45s$ (Temperature)

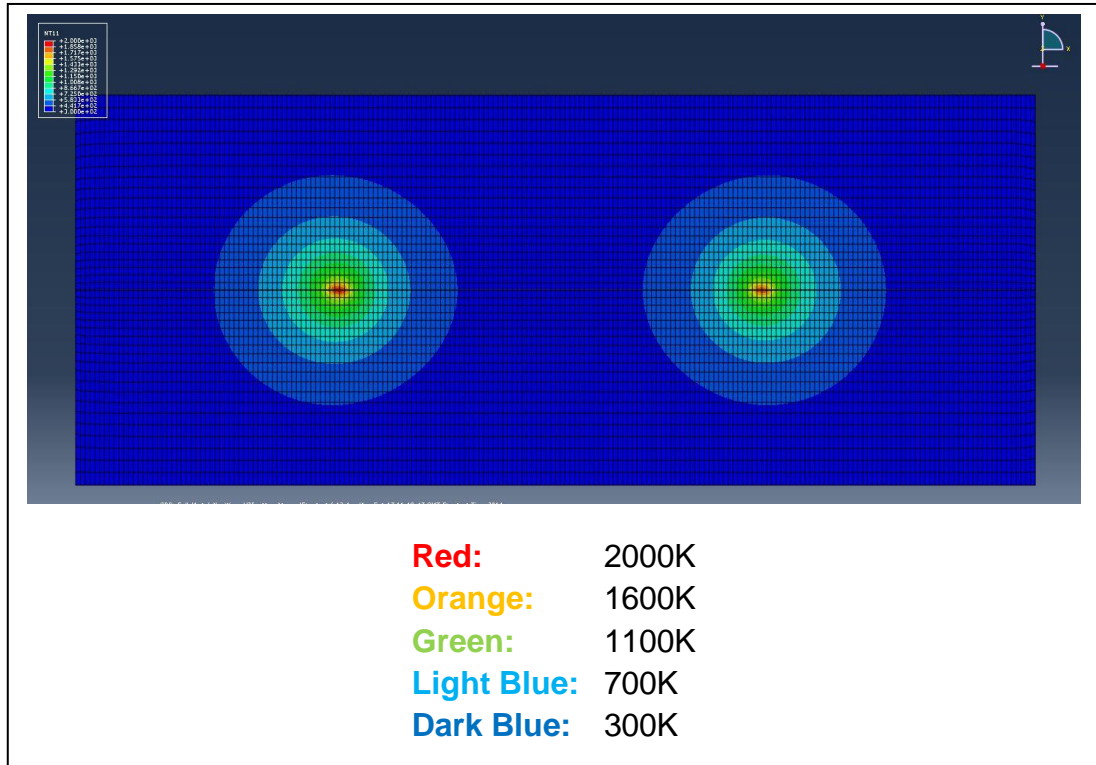


Figure 7.17 – Temperature Contour Plot of Clutch Plates at t=0.45s

Figure 7.16 clearly shows hot banding behaviour due to contact localisation. The effect of this is extreme in this application due to a large amount of energy being dissipated in a very short period of time. The TCFEA has predicted this behaviour even though the friction surfaces were initially flat according to the mechanisms that have been discussed in this section.

The concentration of the heat flux is a self-propagating effect as a greater amount of heat flux over a small region leads to a greater energy input which leads to a greater temperature rise. This then leads to greater thermal expansion in these regions and a greater contact pressure results. A greater amount of energy is then dissipated in these regions (also due to the higher COF) as the heat flux input increases. Figure 7.18 is an extension of Figure 1.11 presented in Chapter 1.2 which incorporates this new understanding.

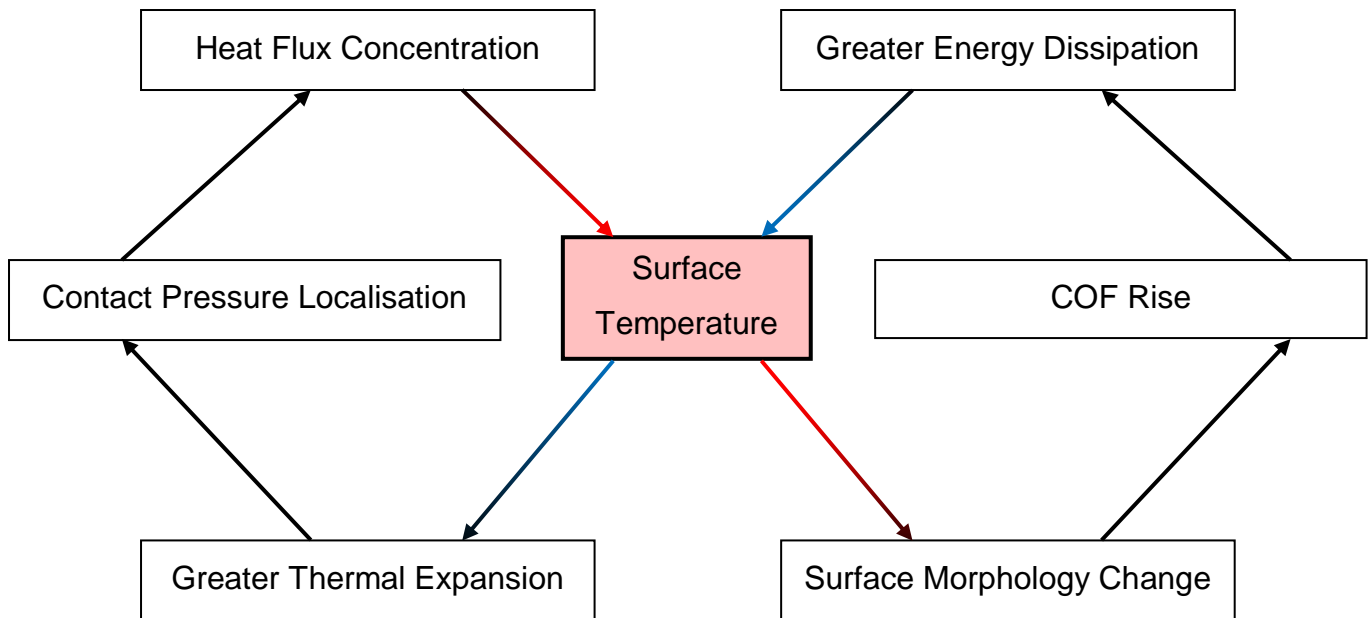


Figure 7.18 – Hot Banding Mechanism

As the simulation progresses, the peak contact pressure and temperature falls as the amount of energy being dissipated at the friction surfaces becomes less than the amount of energy being conducted away from the friction surface and through the clutch-plate thickness. Figure 7.19 shows the contact pressure and surface temperature profiles at $t=1.00s$. The peak temperature falls as heat is conducted away from the hot band in both the radial and axial directions. The thermal expansion at the hot bands falls and as the temperature gradients along the friction surfaces reduce, contact is re-established either side of the hot bands, reducing the peak contact pressures.

Figure 7.20 shows the temperature contour plot at $t=1.00s$ which shows that the temperature gradients have reduced through the thickness of the clutch plate as well as along the friction surface.

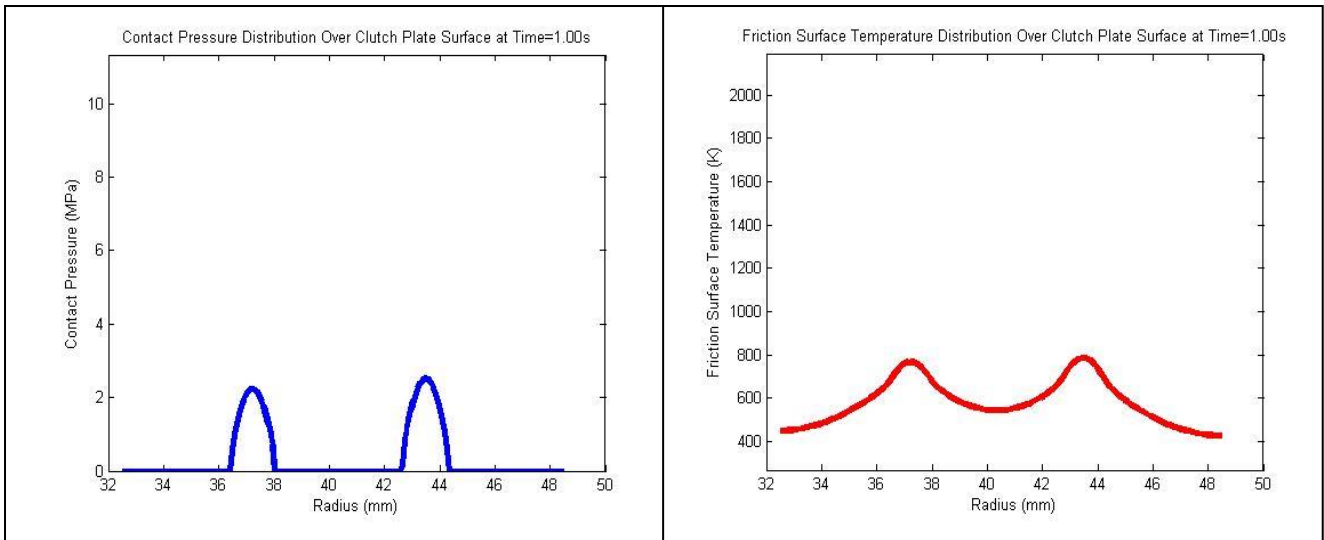


Figure 7.19 – Contact Pressure and Friction Surface Temperature Profiles at t=1.00s



Figure 7.20 – Temperature Contour Plot of Clutch Plate at t=1.00s

Figures 7.21 and 7.22 show that by the end of the simulation, when the clutch plates have become fully coupled, contact has been re-established over much of the friction interface. Contact has even been re-established at the inner and outer radii. The temperature gradients along the friction surfaces and through the thickness of the clutch plates have greatly reduced.

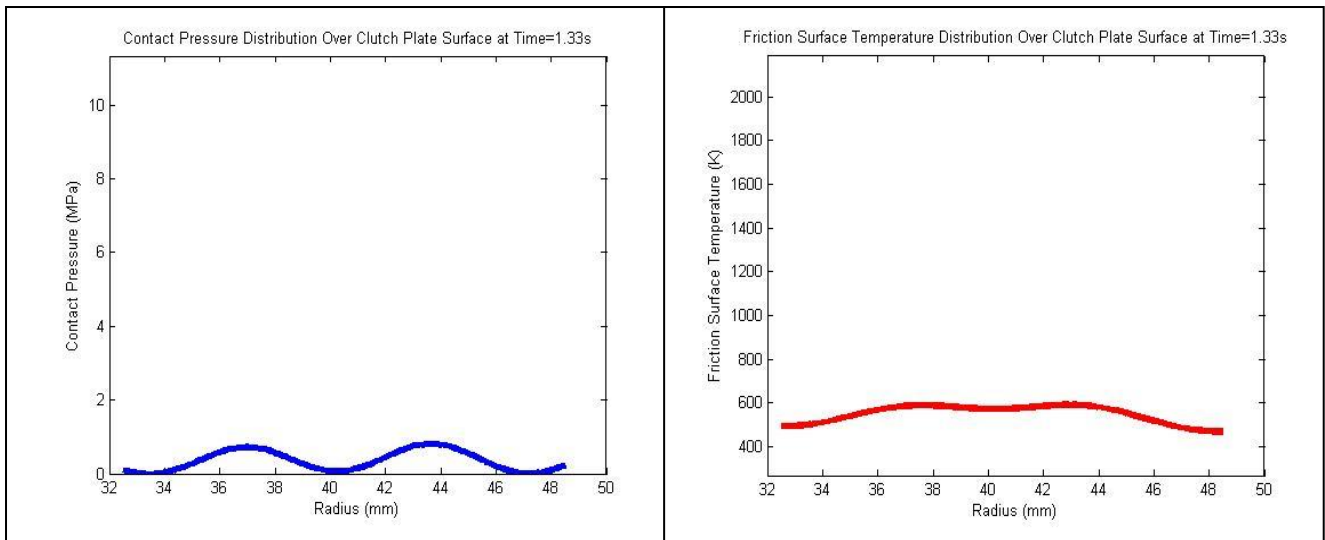


Figure 7.21 – Contact Pressure and Friction Surface Temperature Profiles at t=1.33s



Figure 7.22 – Temperature Contour Plot of Clutch Plates at t=1.33s

Finally, Figures 7.23 and 7.24 show the torque output and the effective friction radius predicted by the simulation. Figure 7.23 clearly shows that the torque output increases rapidly and reaches a peak before reducing. This behaviour is associated with the rapid temperature rise of the friction surfaces causing an increase in COF leading to an increased torque output. As the clutch cools down, the COF (and hence the torque) reduces. The COF values used are those presented in Table 7.3 which are only an estimate of the relationship between COF and temperature based on previous dynamometer results [7]. Figure 7.24 shows that there is no significant effective friction radius migration and hence the torque output behaviour shown in Figure 7.23 is due to the COF of the friction surface changing with temperature rather than as a result of effective friction radius migration.

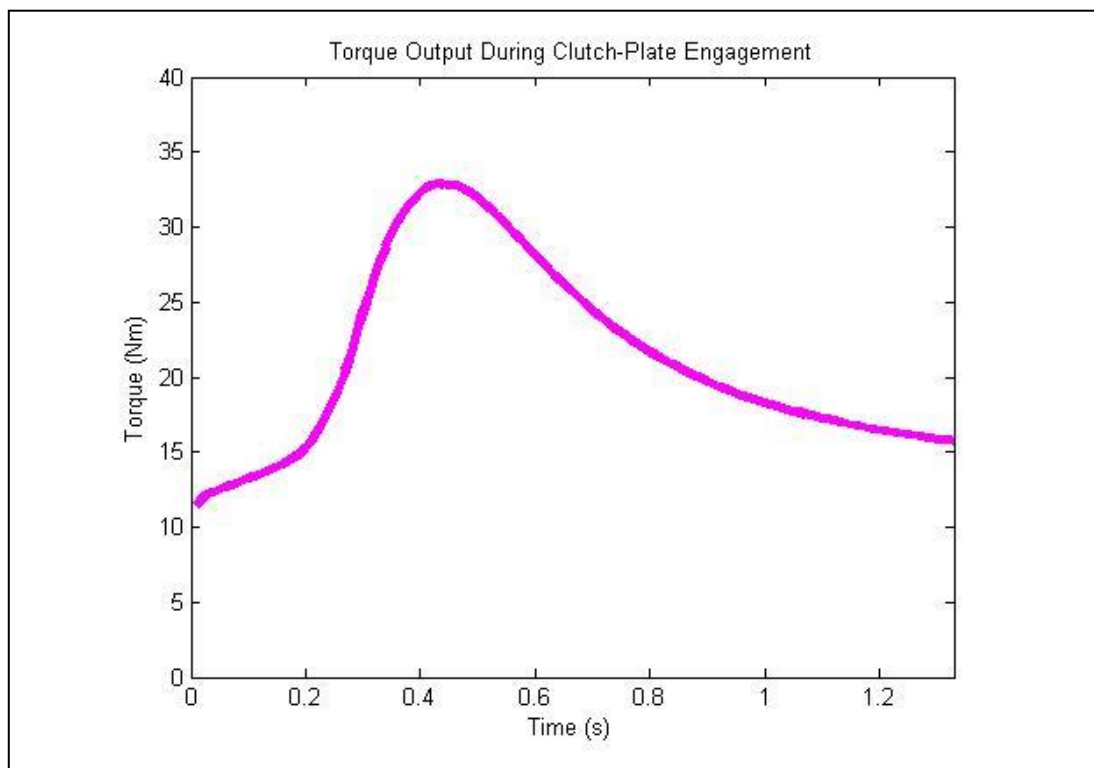


Figure 7.23 –Torque Output Predicted During Clutch-Plate Engagement (Non-Wear Model)

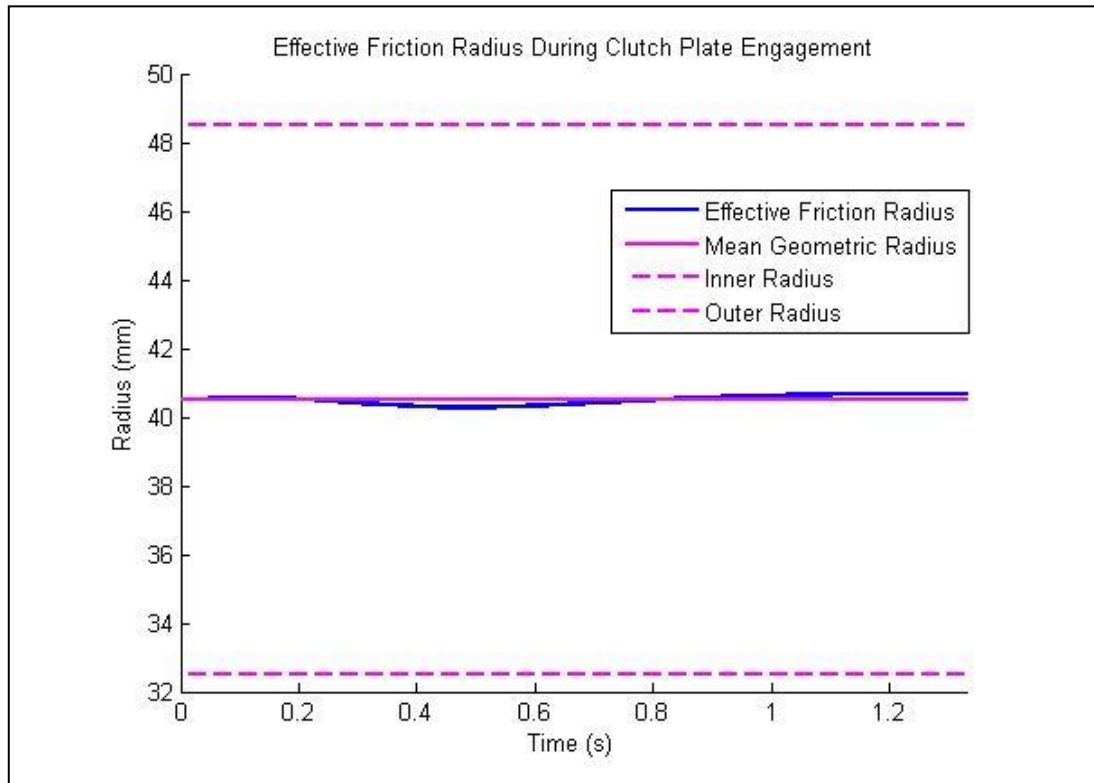


Figure 7.24 – Effective Friction Radius Predicted During Clutch Plate Engagement (Non-Wear Model)

7.6 Initially Non-Flat Surface Results (Non-Wear Model)

The simulation carried out using initially flat surfaces showed that hot banding would still occur even in the absence of surface asperities. However, it is almost impossible that the clutch plate surfaces would be initially perfectly flat. As shown in Chapter 5, the new clutch plates show no signs of waviness profiles but did have surface asperities which would localise contact. To investigate the effect of initially non-flat friction surfaces, simulations were carried out where the initial profiles of the friction surfaces were altered based on the results presented in Chapter 5 and implemented into the TCFEA using the methods discussed in Section 7.3.1. Table 7.4 shows the amplitudes, wavelength and phase angles modelled. For the amplitude and wavelength analyses, the surface profile was modelled on one clutch plate only with the other clutch plate being modelled as initially flat. Profile 0 is that of two completely flat surfaces as discussed in Section 7.5 and has been included for reference.

Profile	Type	Number of Peaks	Amplitude	Phase Angle
0	Flat-to-Flat	N/A	N/A	N/A
1	Flat-to-Sine	7	0.5 μm	N/A
2	Flat-to-Sine	7	1.0 μm	N/A
3	Flat-to-Sine	7	2.0 μm	N/A
4	Flat-to-Sine	5	1.0 μm	N/A
5	Flat-to-Sine	4	1.0 μm	N/A
6	Flat-to-Sine	3	1.0 μm	N/A
7	Sine-to-Sine	7	1.0 μm	180° (peak-to-trough)
8	Sine-to-Sine	7	1.0 μm	90°
9	Sine-to-Sine	7	1.0 μm	0° (peak-to-peak)

Table 7.4 – Surface Profiles Used in TCFEA

Figure 7.12 showed that the initial contact pressure distribution for the flat-to-flat case (Profile 0) was uniform across the friction interface. For Profiles 1-9 however, the initial contact pressure distribution is non-uniform due to the surface profiles that have been introduced. Figure 7.25 shows the initial contact pressure profiles for Profiles 1-3 where only the amplitude of the surface profile peaks vary. It can clearly be seen that contact pressure is immediately localised due to the surface profiles limiting the points of contact. Figure 7.25 also shows that the local contact pressure at the points of contact increases with the amplitude of the surface profile peaks. This is due to the fact that as the amplitude increases, the friction surface becomes more 'spiky' as the gradients of the sine wave either side of the peak become steeper.

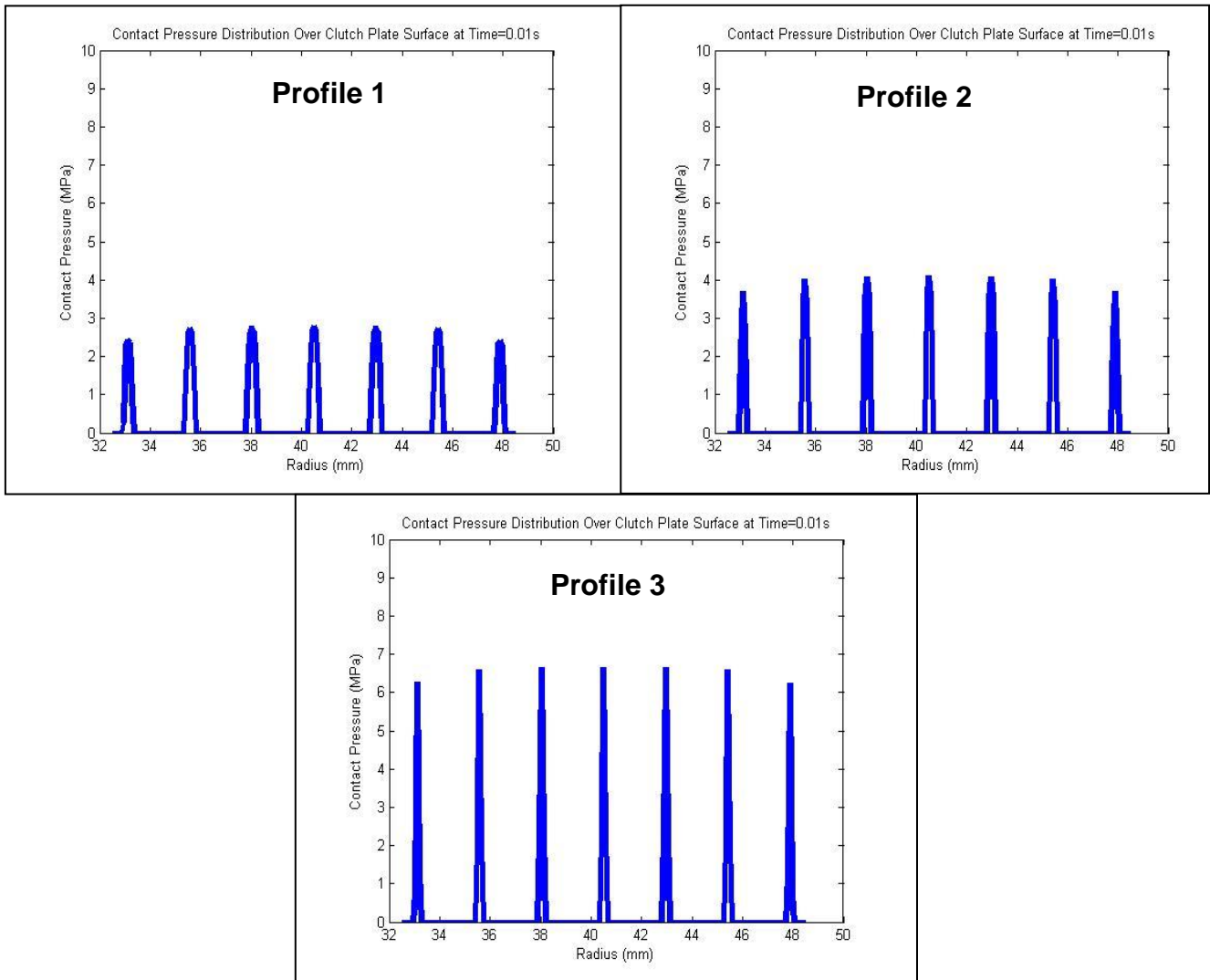


Figure 7.25 – Initial Contact Pressure Distributions for Profiles 1-3

Figure 7.26 shows the initial contact pressure distributions for Profile 2 and Profiles 4-6 where only the numbers of peaks have been changed by altering the wavelength of the sine wave profile. Figure 7.26 shows that the local contact pressure at the points of contact decreases as the number of peaks reduces (wavelength increases). The reduction in contact pressure with decreasing number of peaks is due to the friction surface becoming less 'spiky' as the gradients either side of the sine wave peak become shallower.

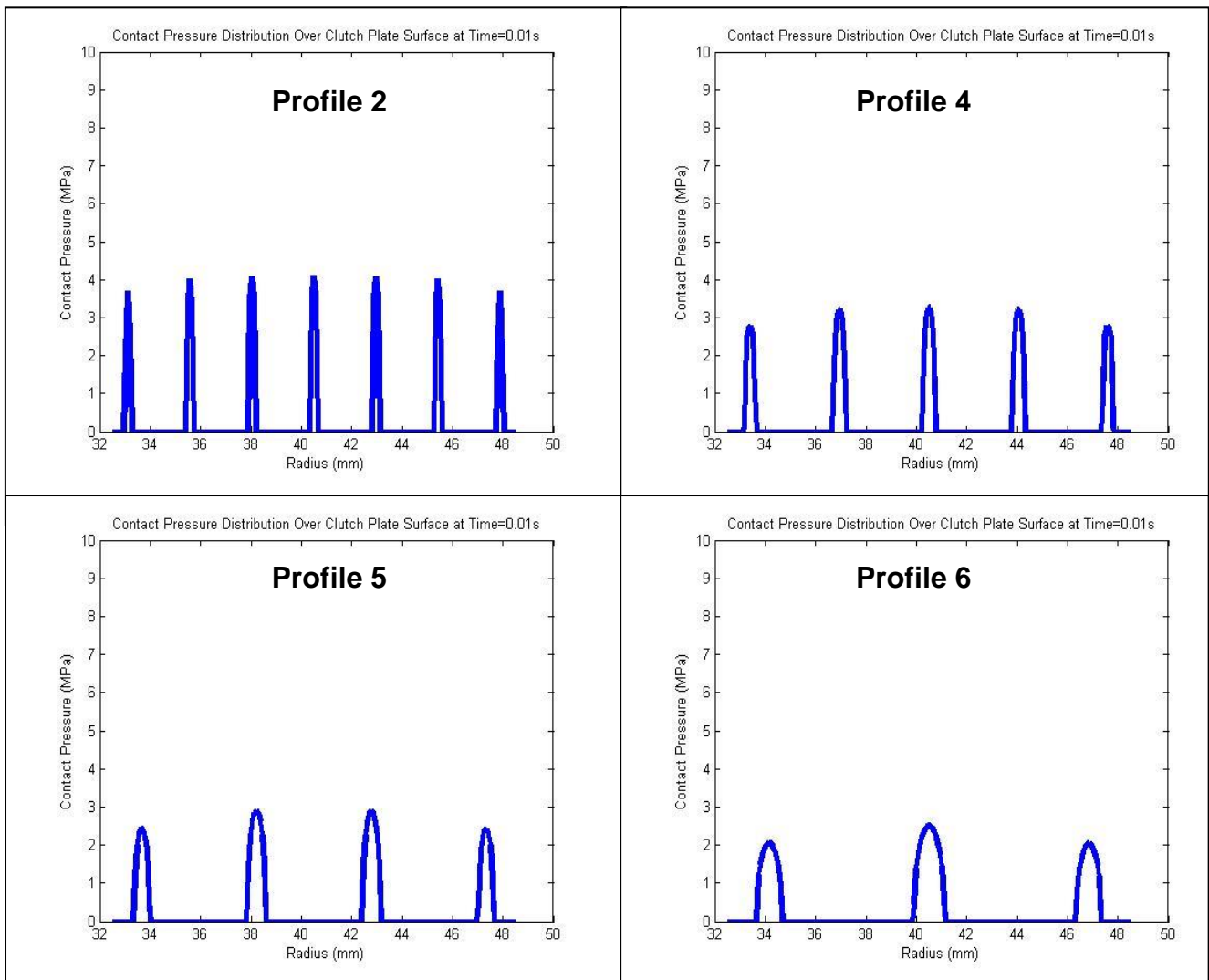


Figure 7.26 – Initial Contact Pressure Distribution for Profile 2 & Profiles 4-6

Figure 7.27 shows the initial contact pressure distributions for Profiles 7-9 where the phase angle between the two friction surfaces has been changed where sine wave profiles have been introduced on both friction surfaces. The contact pressure distribution for Profile 7 is uniform due to the 180° phase angle resulting in full contact across the entire friction interface just as with Profile 0 (flat-to-flat). This is because the 180° phase angle results in the two clutch plates contacting like a jigsaw puzzle. The opposite scenario of 0° phase angle (Profile 9) results in high contact pressure at the peak-to-peak contact points, with Profile 8 producing a similar contact pressure distribution but with lower contact pressures.

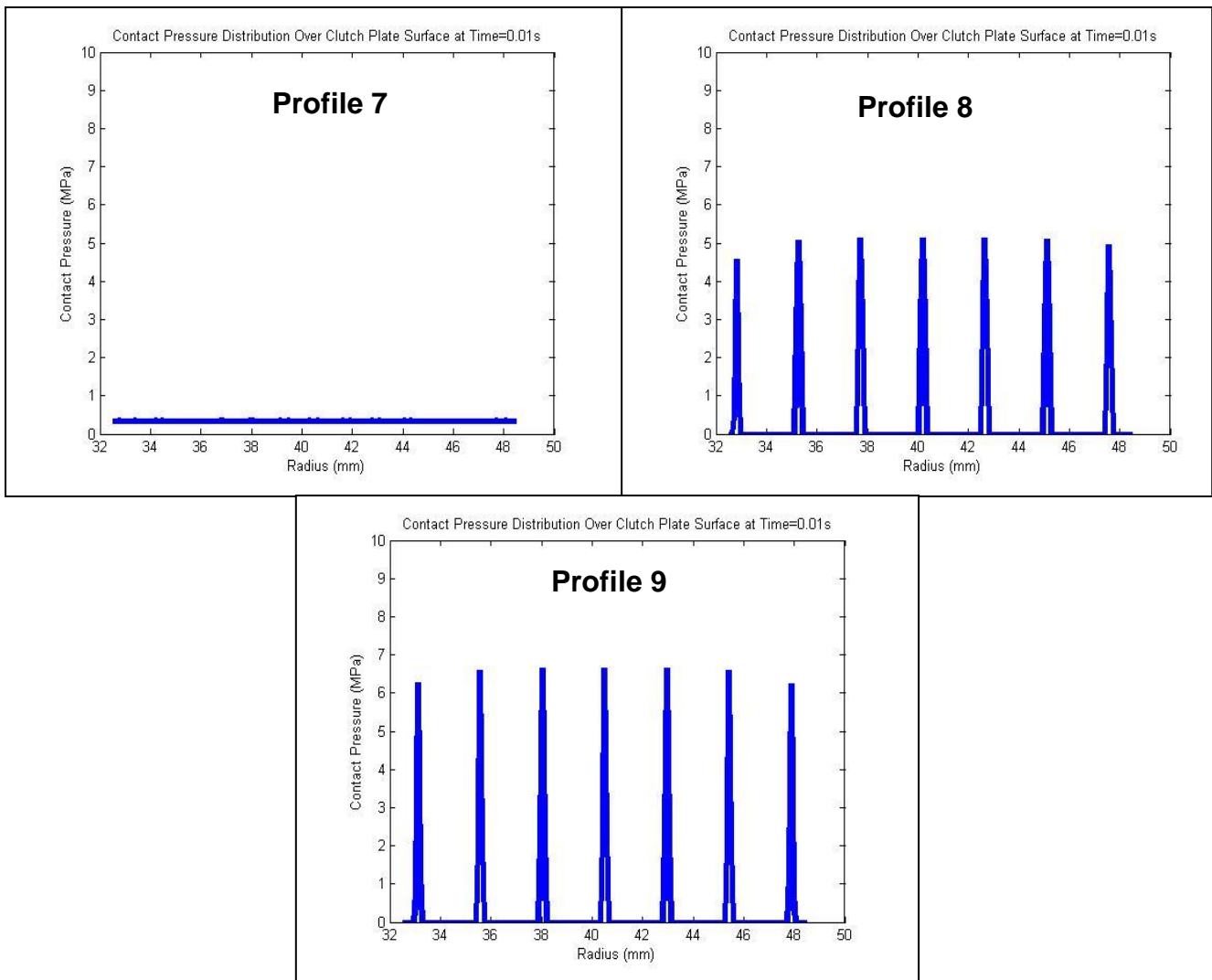


Figure 7.27 – Initial Contact Pressure Distribution for Profiles 7-9

Figures 7.28-7.30 show the results from the simulations run using the surface profiles listed in Table 7.4. All the simulations followed a similar trend to the flat-to-flat model whereby two hot bands are formed either side of the mean geometric radius of the clutch plates with the exception of Profile 6 which forms a single hot band at the centre of the clutch plate. All the simulations followed the same mechanism as that discussed in Section 7.5 except for Profile 6. As Profile 6 only has 3 contact points to begin with, when contact is first lost at the outermost contact points, the two points of contact either side of the central contact point are lost leaving only a single point of contact. This does not occur with the other profiles as when contact is lost at the outermost contact points, at least two points of contact remain.

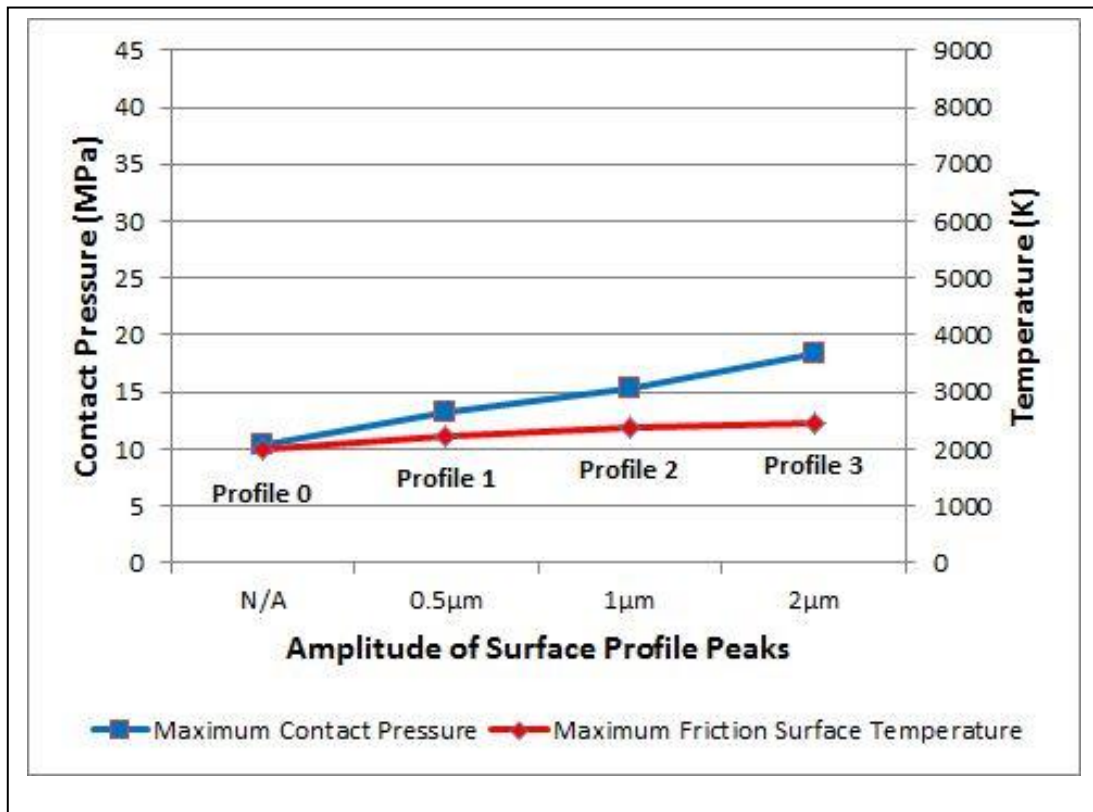


Figure 7.28 – Results of Varying Peak Amplitude on Maximum Contact Pressure and Maximum Friction Surface Temperature

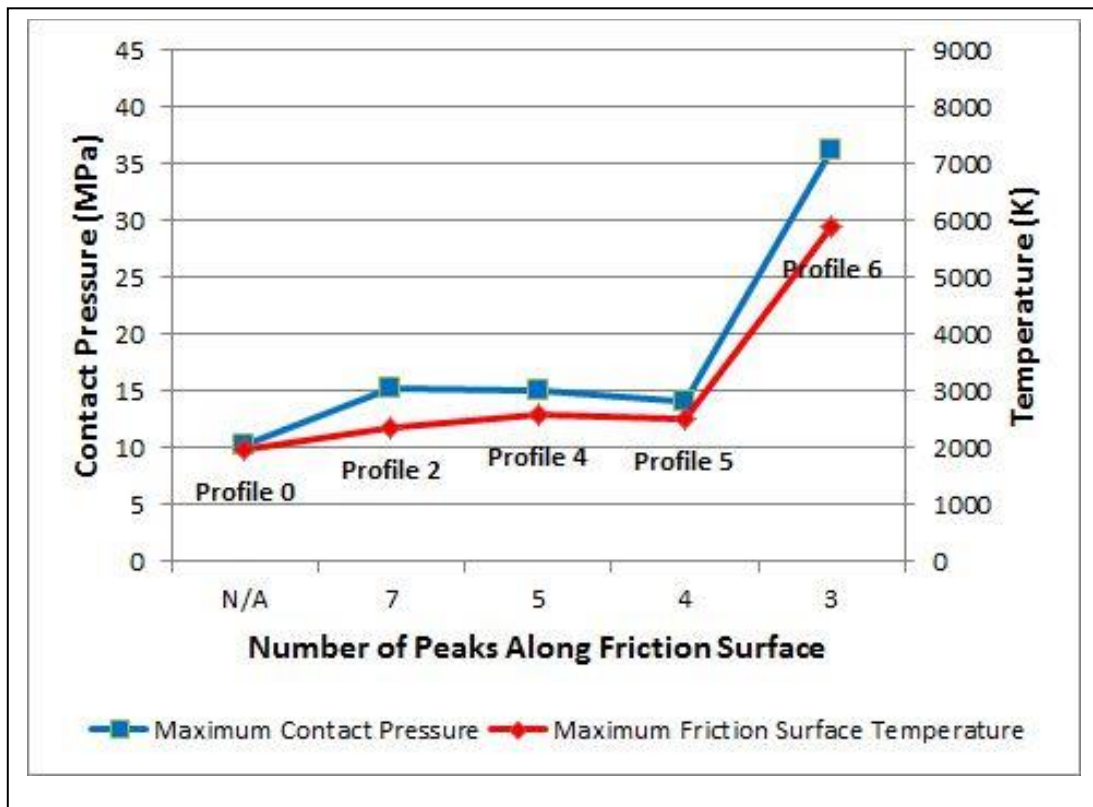


Figure 7.29 – Results of Varying Number of Peaks (Wavelength) on Maximum Contact Pressure and Maximum Friction Surface Temperature

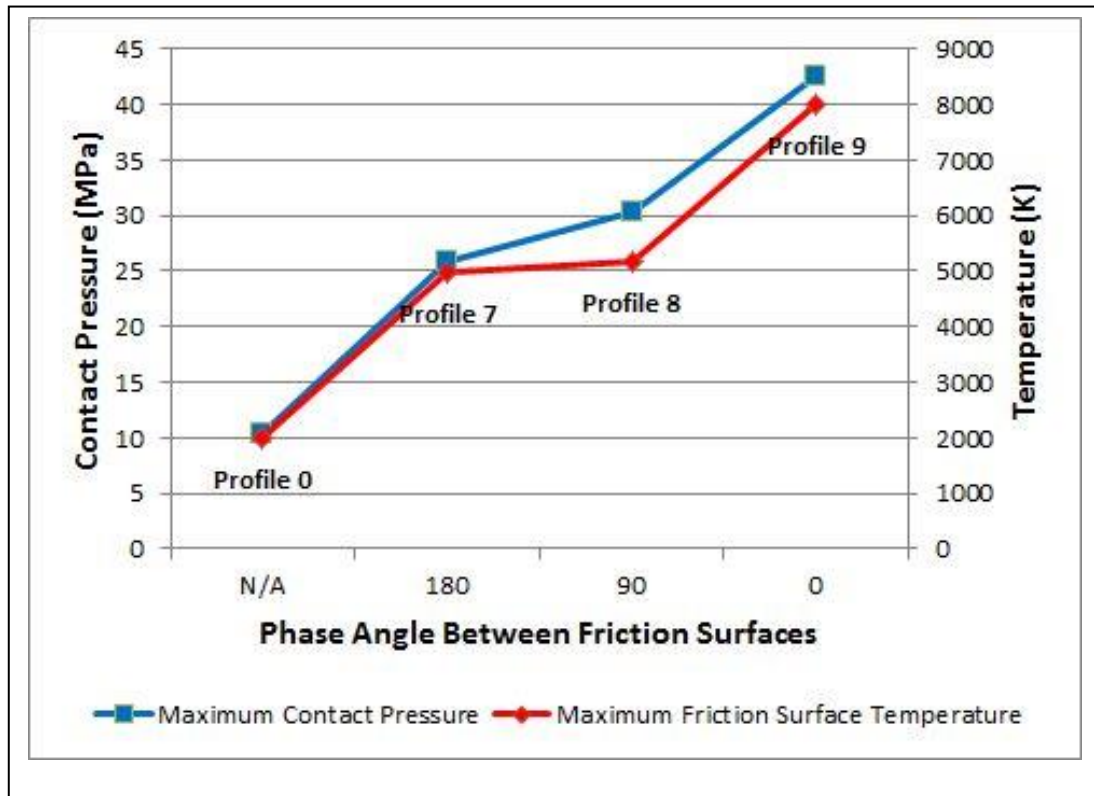


Figure 7.30 – Results of Varying Phase Angle on Maximum Contact Pressure and Maximum Friction Surface Temperature

Figures 7.28-7.30 clearly show that the initial surface profile can have a large influence upon the maximum contact pressures and maximum friction surface temperatures during a clutch plate engagement. Figure 7.28 shows that increasing the amplitude of the surface profile peaks increases the maximum contact pressure and maximum friction surface temperature which can be explained with reference to Figure 7.25. The increase in peak amplitude causes stronger localisation of contact and hence higher contact pressures, resulting in higher proportions of heat flux being input at the contact points, leading to higher temperatures. The mechanism presented in Figure 7.18 then leads to a higher maximum contact pressure and higher maximum friction surface temperature.

Figure 7.29 shows that reducing the number of peaks (increasing wavelength) increases the maximum contact pressure and maximum friction surface temperature. Profiles 2, 4 and 5 show this relationship to be gradual but Profile 6 produced an extreme result. As discussed, Profiles 2, 4 and 5 follow a similar trend to Profile 0 and each other whereby twin-bands of high contact pressure and temperature are

formed. However this regime is reached more quickly with a reduced number of surface profile peaks. The loss of contact at the outermost contact points is more significant for Profile 5 than Profile 2 as this loss of contact for Profile 5 leads immediately to the twin-band regime. This is not the case for Profile 2 as further contact must be lost before the twin-band regime is established. A reduction in the number of peaks therefore produces a higher maximum contact pressure and higher maximum friction surface temperature as the twin-band regime occurs earlier in the engagement when the energy dissipation is greater and hence the heat flux inputs are larger at the points of contact. Profile 6 differs from the others in that only one band is formed leading to heat flux concentration over a single small area resulting in an extremely high maximum friction surface temperature.

Figure 7.30 shows that decreasing the phase angle between two clutch plates with identical surface profiles, increases the maximum contact pressure and maximum friction surface temperature. The reason for this is apparent from Figure 7.27 which shows that decreasing the phase angle results in increased localisation of contact and hence higher initial contact pressures. Although Profile 7 produces an initially uniform contact pressure it does not follow the same progression as that of Profile 0 and quickly evolves to a contact pressure profile similar to that of Profiles 8 and 9 but with lower values of contact pressures.

Profiles 6-9 predict unrealistically high maximum friction surfaces due to the method of calculating the COF from the friction surface node temperatures. For any temperatures above 1473K (Table 7.3), the COF value is linearly extrapolated. The result of this is that for Profiles 6-9, the COF is greatly overestimated and as such so is the torque and heat flux input leading to the unrealistic high temperatures. Nevertheless, this analysis has shown that the initial surface profile of the clutch plates can have a large influence on the maximum contact pressure and maximum friction surface temperature during a clutch plate engagement.

7.7 Wear Model

The non-wear models predicted contact localisation where the contact points, and hence hot bands, persisted as thermal expansion was completely dominant in the absence of wear. As a result no contact point migration was predicted which could cause migration of the effective friction radius. A wear model was therefore required.

In order to model wear using Abaqus, the 'Adaptive Meshing' function was used in order to affect the location of friction surface nodes based on the calculation of a wear rate. Abaqus features two methods of adaptive meshing: displacement control and velocity control. For each step in the simulation, a different value for the adaptive mesh can be applied to any node in the mesh. Displacement control involves defining the position of that node within the Abaqus global coordinate system such that Abaqus attempts to move that node to the specified position over the course of the time step. This option however ignores any expansion that may occur in order to move the node to the specified position. The velocity control option defines a velocity for the node during a step with relation to the Abaqus global coordinate system. Unlike displacement control, velocity control takes expansion into account such that if applied to a friction surface node, the node can be moving in one direction due to wear but still move in the opposite direction due to thermal expansion and the aggregate effect is calculated. Velocity control was therefore used in order to model wear within Abaqus. The adaptive mesh commands were added to the Abaqus input file using the same method as that for the heat flux inputs discussed in Section 7.3.1.

The wear model used in the simulations was that discussed by Zhao et al. [14] which is based on Archard's wear law [66]. The equation presented by Zhao et al [14] relates the amount of wear to contact pressure, sliding velocity and time:

$$\Delta h = kp_c u \Delta t \quad (7.11)$$

Where:

- h – Incremental Wear (m)
- k – Wear Constant (m^2N^{-1})
- p_c – Contact Pressure (Pa)
- u – Sliding Velocity (ms^{-1})
- Δt – Time Step (s)

Equation 7.11 does not take into account any wear due to temperature effects such as oxidation or increased abrasion which, at the elevated temperatures predicted in the non-wear simulations, is likely to be significant. Equation 7.11 was therefore modified to incorporate the effects of temperature. An exponential term has been included as, for carbon/carbon composites, wear is likely to be negligible at low temperatures but increase rapidly at higher temperature [5, 6, 7, 41].

$$\Delta h_w = k p_c u \Delta t e^{(Z/Z_o)} \quad (7.12)$$

Where: Z – Temperature (K)
 Z_o – Reference Temperature (K)

The use of a reference temperature is necessary for two reasons. Firstly, the exponential term must be dimensionless. The individual elements inside the brackets may have units but the overall term in the brackets must be dimensionless. Secondly, if the term in the brackets becomes too large, the exponential value may become too large to compute. The inclusion of the reference temperature scales down the bracketed term in order to avoid this potential issue. Room temperature of 298K was chosen as the reference temperature as this is the minimum temperature at which the clutch would realistically ever be operated.

In order to calculate the value of the wear constant, a value of wear was defined at a specific contact pressure, sliding velocity and temperature. From the results of the flat-to-flat surface simulations, the maximum amount of wear was defined at the time and location where the maximum temperature occurred. These values are presented in Table 7.5.

Contact Pressure (MPa)	Radius (mm)	RPM	Sliding Velocity (ms⁻¹)	Maximum Temperature (K)
10.258	36.90	5375	20.770	1987

Table 7.5 – Values Used to Calculate Wear Constant

No experimental data regarding wear was available and as such the potential amount of wear that might occur was estimated using race-conditioned clutch-plate surface profile waviness results discussed in Chapter 5. These results showed the average peak-to-trough depth of the surface profile was approximately 2µm. Assuming that this amount of wear occurs during a single clutch engagement, it was postulated that this amount of wear would occur when and where the peak temperature arose. From the results of the flat-to-flat surface simulation, the peak temperature persists for around 0.2s of the clutch-plate engagement. Therefore if 2µm of wear occurs over this period, 0.1µm of wear will occur during one time step. Substituting this value of wear and the values presented in Table 7.5 into Equation 7.12 allowed the wear constant to be calculated. 1973K was chosen as the peak temperature rather than 1987K to simplify the relationship presented in Figure 7.31.

$$1 \times 10^{-7} = k \times 1025800 \times 20.770 \times 0.01 \times e^{(1973/298)}$$

$$1 \times 10^{-7} = 1.599 \times 10^9 k$$

$$k = 6.2535 \times 10^{-17} \text{ m}^2/\text{N}$$

The wear rate is then simply calculated using Equation 7.13:

$$w = \frac{\Delta h}{\Delta t} \tag{7.13}$$

Where: w – Dimensional Wear Rate (m/s)

The wear rate at every friction surface node is calculated using equations 7.12 and 7.13 and this wear rate is applied as an adaptive mesh velocity within Abaqus in order to simulate wear. Figure 7.31 shows how the wear rate varies with temperature according to Equations 7.12 and 7.13 at the values of pressure and sliding velocity presented in Table 7.5. Figure 7.31 shows that the wear model used in the wear simulations results in greatly increased amounts of wear at elevated temperatures.

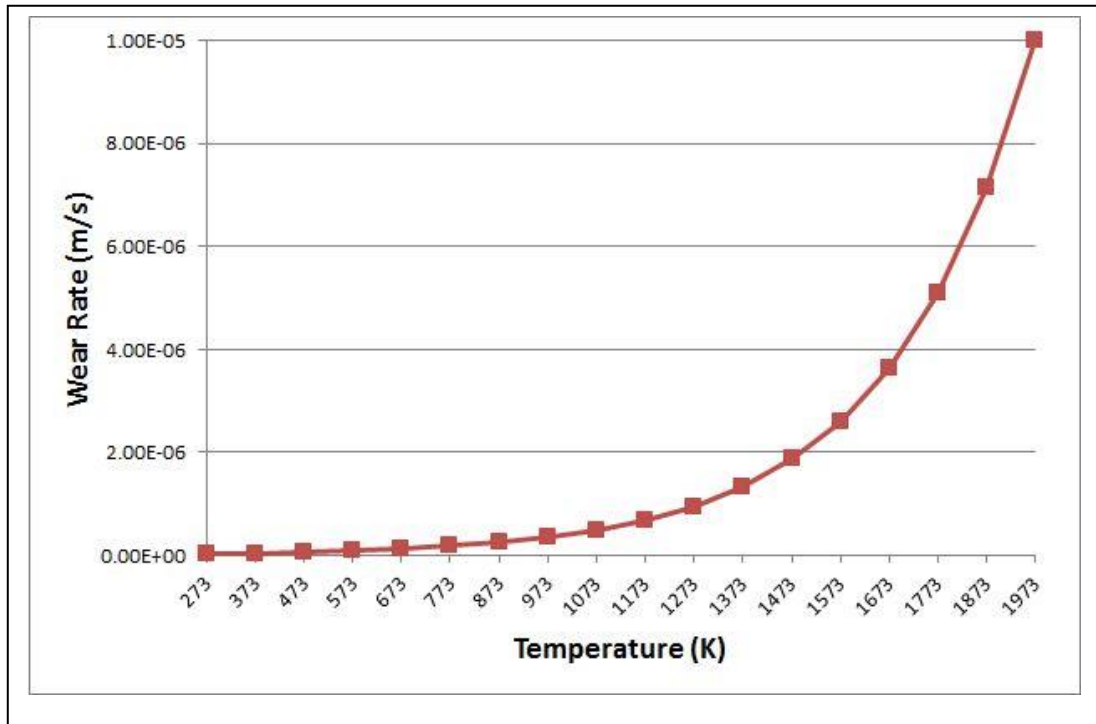


Figure 7.31 – Wear Rate as a Function of Temperature at Pressure and Sliding Velocity Values Presented in Table 7.5

7.7.1 Initially Flat Surface Results

A simulation was carried out using Profile 0 (flat-to-flat) with the addition of the wear model. Initially, the evolution of the contact pressure and friction surface temperature is similar for both the non-wear model and the wear model. However, as the friction surface temperature increases during the engagement, wear becomes significant and influences the contact pressure distribution and hence the surface temperature profile. Figure 7.32 shows the contact pressure distribution and friction surface temperature profile at $t=0.20s$ allowing a direct comparison with the results shown in Figure 7.15 for the non-wear model. Figure 7.32 shows that the addition of wear has actually caused acceleration of the rate of contact localisation with the two bands of contact located close to the geometric centre of the clutch plate. The higher contact pressure has led to a more extreme temperature profile with two distinct regions of high temperature.

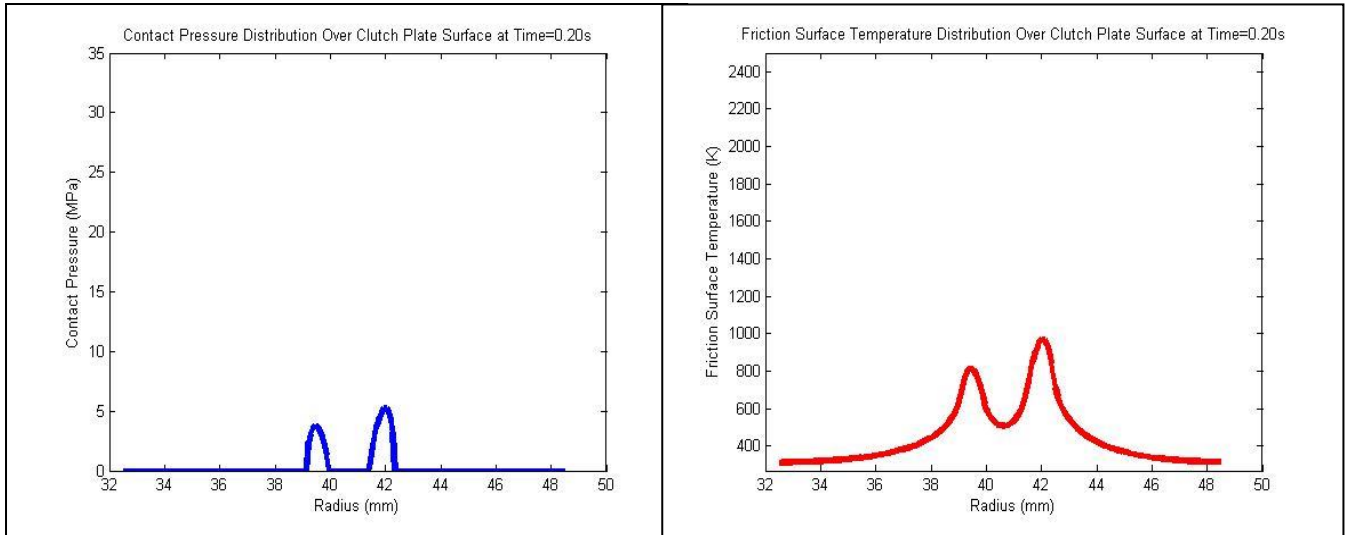


Figure 7.32 – Contact Pressure and Friction Surface Temperature Profiles at $t=0.20s$

Figure 7.33 shows how the contact pressure distribution and surface temperature profiles have evolved by $t=0.34s$ which is the time at which the maximum friction surface temperature occurs. At this point contact has become localised to a narrow band at the centre of the clutch plate leading to a concentration of heat input resulting in a very high friction surface temperature. This result seems counter-intuitive as it would be expected that any contact points where high temperatures arise would be worn away and hence limit the contact pressure. However, the wear model predicts a higher peak contact pressure and higher peak surface temperature than for the non-wear model.

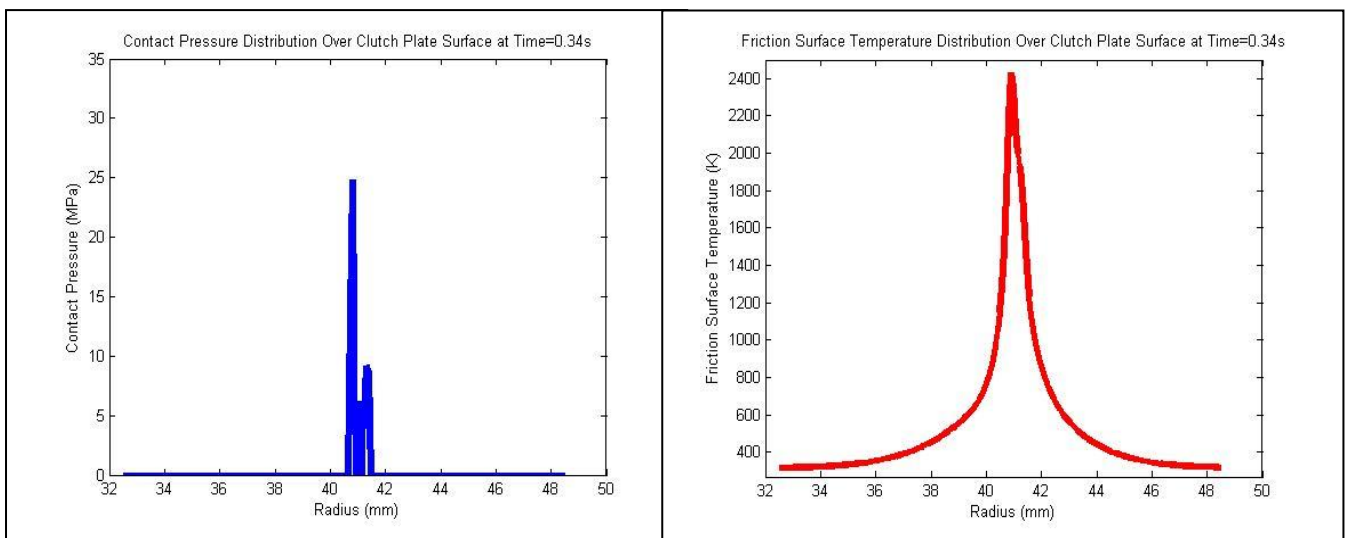


Figure 7.33 – Contact Pressure and Friction Surface Temperature Profiles at $t=0.34s$

Figure 7.34 shows the contact pressure distribution and surface temperature profile at the time at which the peak contact pressure occurs. Figure 7.34 clearly shows the extent to which the contact is localised and the high peak contact pressure that results; which is approximately 350% greater than that predicted in the non-wear model.

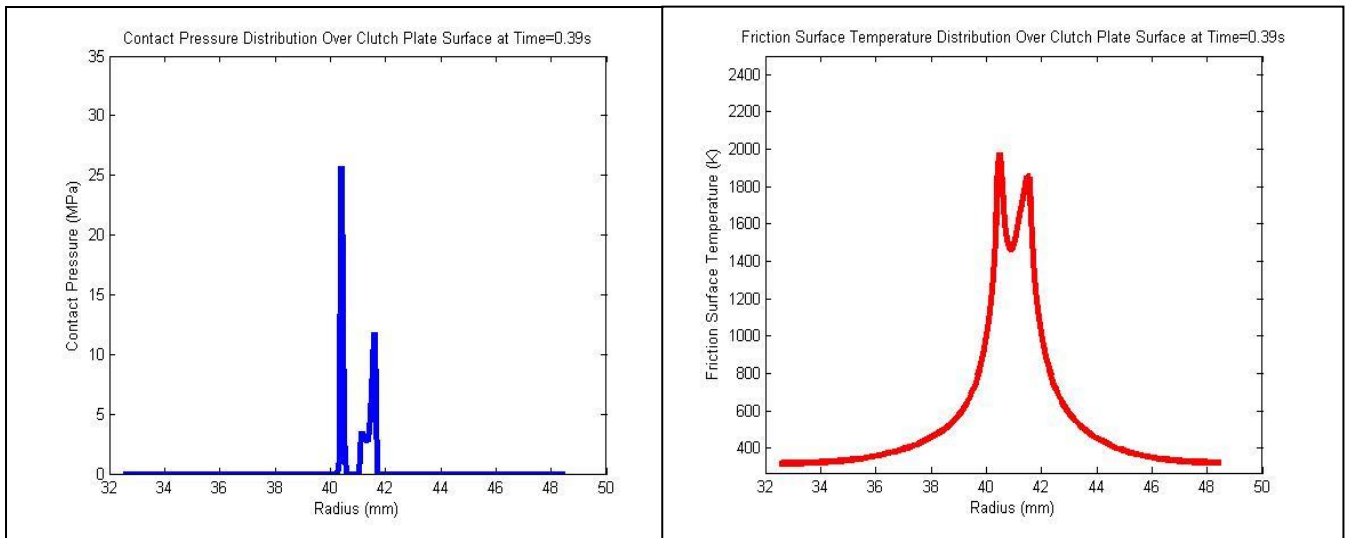


Figure 7.34 – Contact Pressure and Friction Surface Temperature Profiles at $t=0.39s$

Finally, Figure 7.35 shows that as the temperatures and contact pressure reduce as the engagement progresses, the contact pressure distribution returns to the twin-band regime as predicted by the non-wear model.

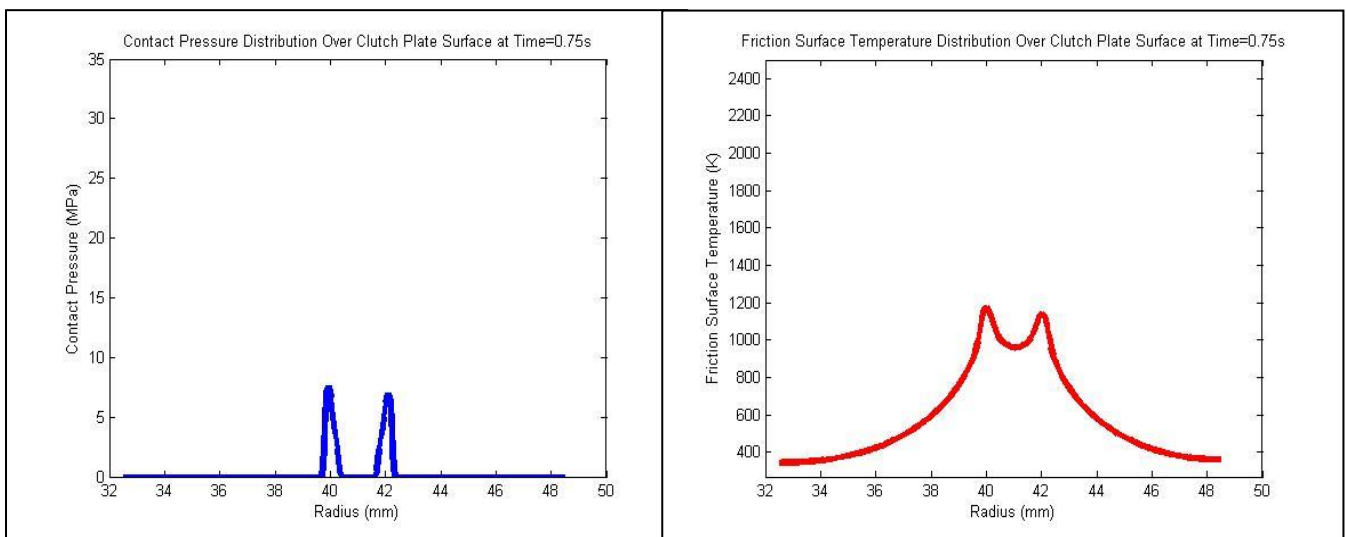


Figure 7.35 – Contact Pressure and Friction Surface Temperature Profiles at $t=0.75s$

It was expected that the introduction of wear would reduce the effects of contact localisation and hence reduce the peak contact pressure and peak friction surface temperature. The opposite has in fact been predicted. It must be stressed however that, as stated previously, initially perfectly flat surfaces are extremely unlikely to occur in reality. Another analysis was therefore carried out with an initially non-flat surface profile.

7.7.2 Initially Non-Flat Surface Results

Profile 2 listed in Table 7.4 was used as the initial surface profile as this is the surface profile that was experimentally measured (Chapter 5). The initial contact pressure distribution produced using Profile 2 has been presented in Figure 7.25. As discussed in Section 7.6, the initial evolution of the contact pressure distribution is similar to that of Profile 0 whereby two bands of contact are formed. Figure 7.36 shows the contact pressure distribution and surface temperature profile at the times at which the maximum values occur. Comparing these results to those shown in Figure 7.28, it can be seen that both the peak contact pressure and friction surface temperature are lower in the wear model than in the non-wear model. This is the expected result as wear acts as a limiting factor for the contact pressure and friction surface temperature.

The effect of wear becomes clear as the engagement progresses. Figure 7.37 shows the contact pressure distribution for both the wear model and non-wear model at $t=0.75s$. Wear at the two hot bands has resulted in contact being regained at the centre of the clutch plates whilst the non-wear model still has only two points of contact. The omission of wear means the contact pressure can only reduce by virtue of thermal contraction as the hot bands cool. Wear has accelerated the process as both thermal contraction and wear reduces the contact pressure. Mostly due to the high temperature of the hot bands resulting in a large amount of wear, the contact points cannot persist as in the non-wear model.

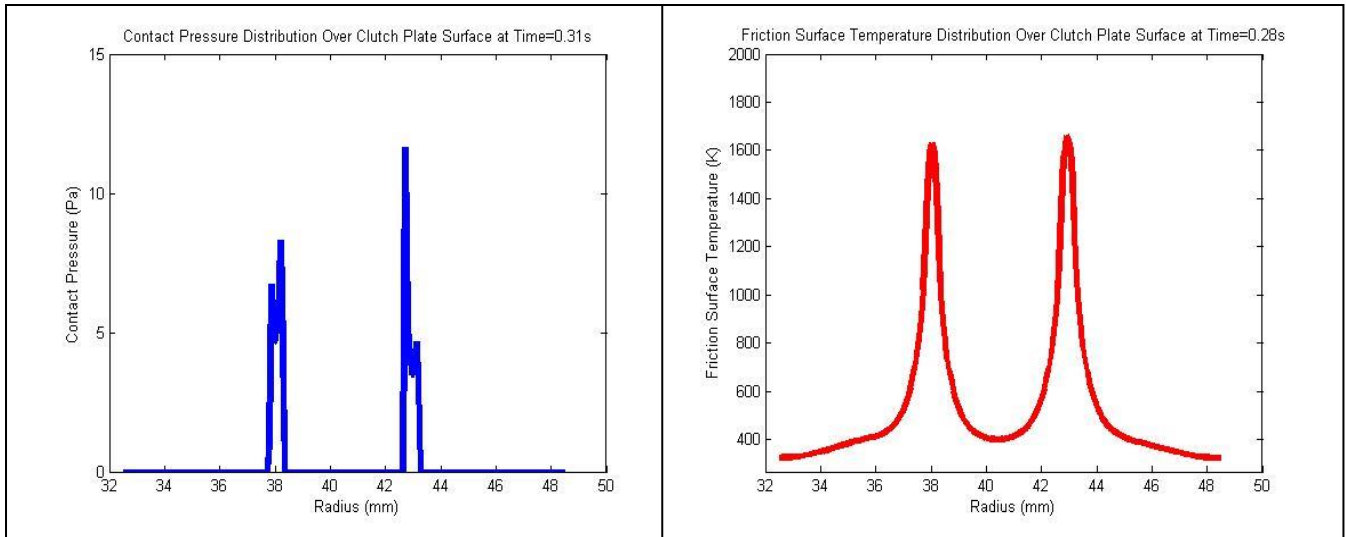


Figure 7.36 – Maximum Contact Pressure and Friction Surface Temperature Profiles at $t=0.31s$ (Contact Pressure) and $t=0.28s$ (Surface Temperature)

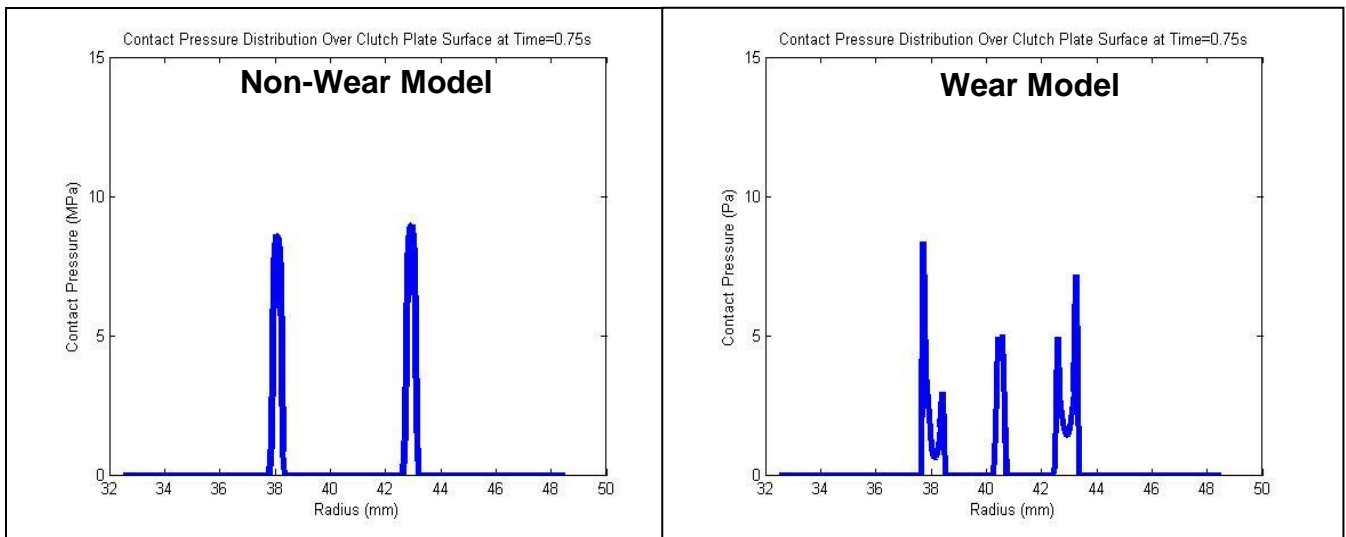


Figure 7.37 – Contact Pressure Distribution at $t=0.75s$ (Non-Wear and Wear Models)

Figure 7.38 shows that at $t=1.00s$, contact has now been regained at the centre of the clutch plate in the non-wear model such that three points of contact exist. For the wear model however, wear has resulted in the two outer bands being lost and contact being isolated entirely to the centre of the clutch plate. However, this has very little impact on the friction surface temperature as the effect of the heat flux concentration is minimal due to the overall heat flux input being low as the engagement nears completion.

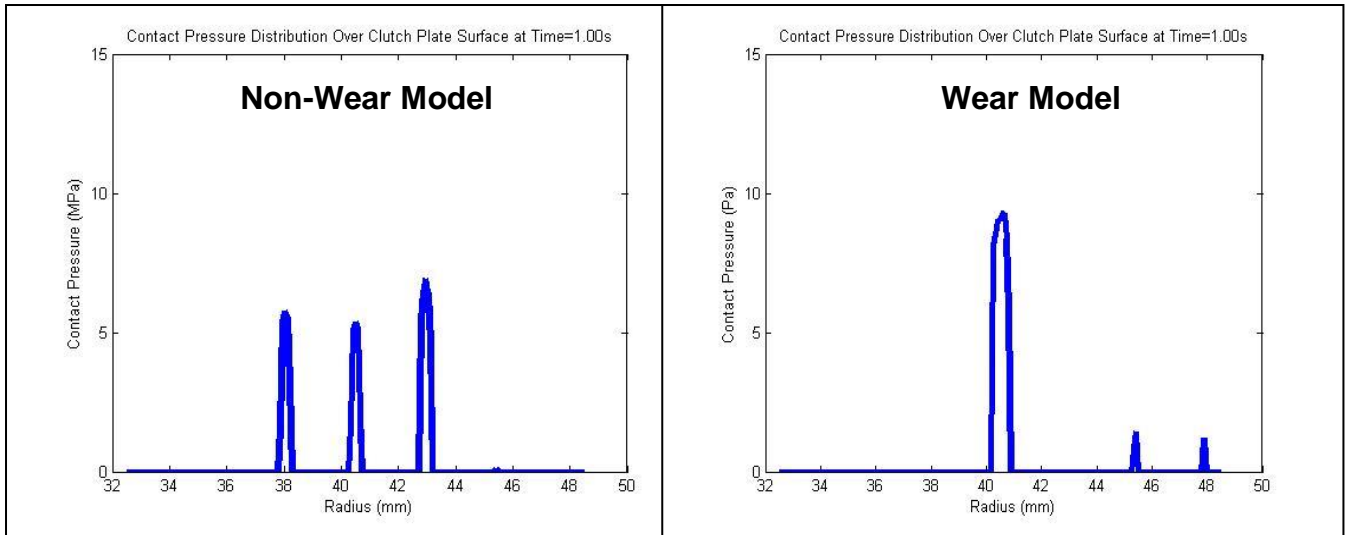


Figure 7.38 – Contact Pressure Distribution at t=1.00s (Non-Wear and Wear Models)

The effect that the contact point migration has on the effective friction radius is minimal as the initial profile of the friction surfaces is assumed to be symmetrical about the mean geometric radius of the clutch plates. The effective friction radius therefore only migrates by a maximum of ± 1 mm about the mean geometric radius which would cause a $\pm 2.5\%$ torque output variation (Equation 4.2). Any predicted torque variation during the clutch plate engagement is therefore due mainly to the increase in COF with temperature as presented in Table 7.3.

Figure 7.39 shows the predicted torque output for the non-wear model using Profile 2 (see Table 7.4) and Figure 7.40 shows the predicted torque output for the equivalent wear model. The introduction of wear to the TCFEA has clearly had an effect on the torque output of the clutch plates. Figure 7.38 showed that a central band of contact is predicted by the wear model as the engagement approaches t=1.00s. Figure 7.40 illustrates that the effect of this is to cause a sudden increase in torque towards the end of the engagement as the temperature, and hence COF, suddenly increase when the central hot band forms

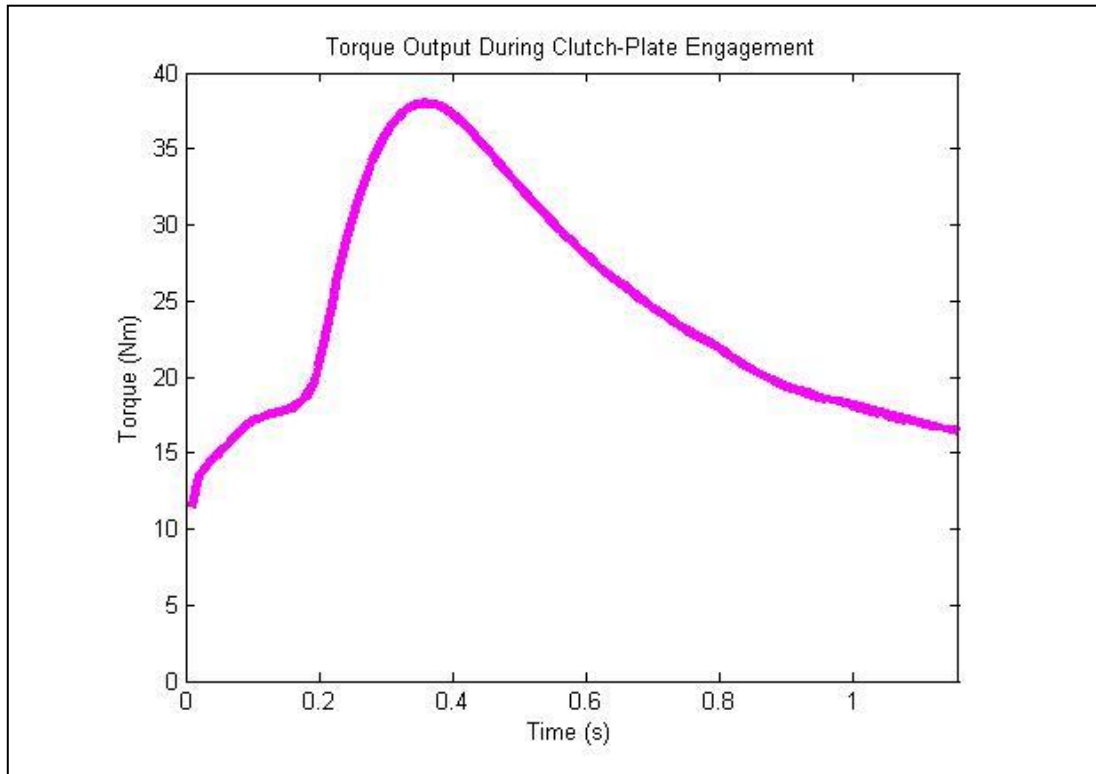


Figure 7.39 – Torque Predicted by Non-Wear Model Using Profile 2

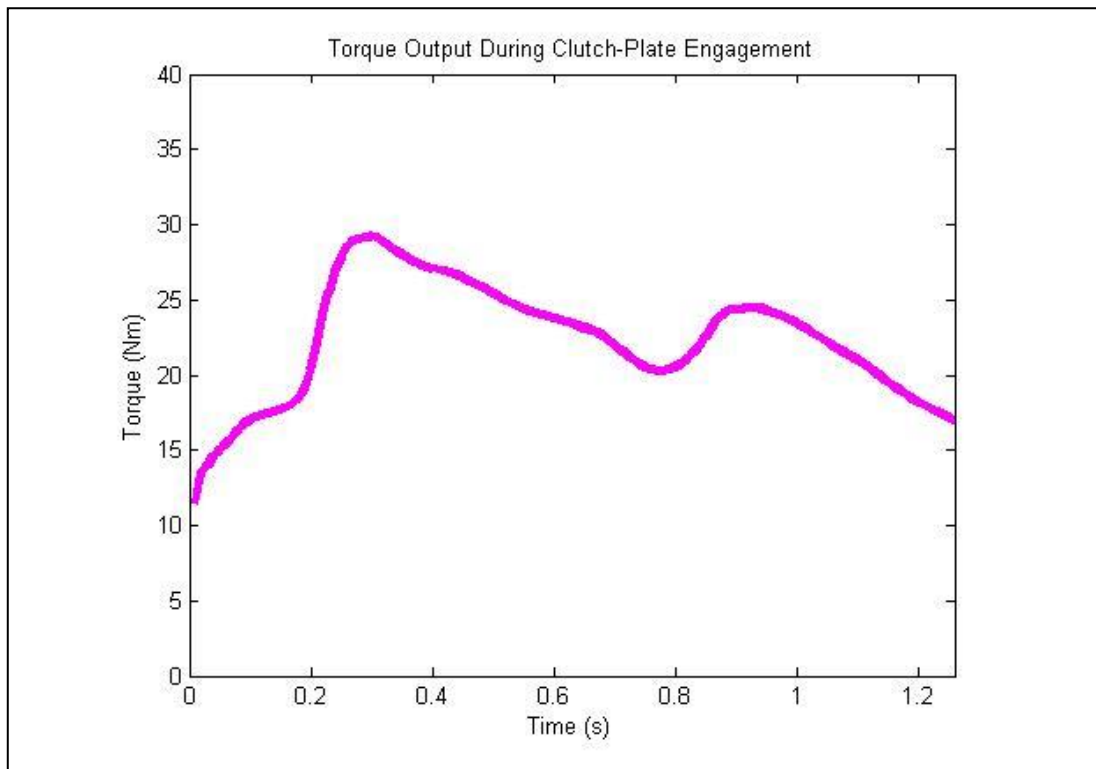


Figure 7.40 – Torque Output Predicted by Wear Model Using Profile 2

7.7.3 Wear Constant Sensitivity Analysis

The results of the initial wear models discussed have shown that for initially perfectly flat surfaces, the introduction of wear to the model increases the peak contact pressure and peak friction surface temperature compared to the non-wear model. For initially non-flat surfaces however, the introduction of wear reduces the peak contact pressure and peak friction surface temperature which is the expected result if wear limits the persistence of hot bands via loss of material due to increased wear at elevated temperatures.

As no experimental data regarding wear was available to inform the wear model represented by Equation 7.12, it is difficult to know whether the wear model used is correct. A sensitivity analysis was therefore carried out to understand how sensitive the TCFEA is to the degree of wear introduced. This was done by carrying out a sensitivity analysis, varying the order of magnitude of the wear constant used. Figures 7.41 and 7.42 show the results of this sensitivity analysis for both the flat-to-flat surface analysis (Profile 0) and flat-to-sine surface analysis (Profile 2).

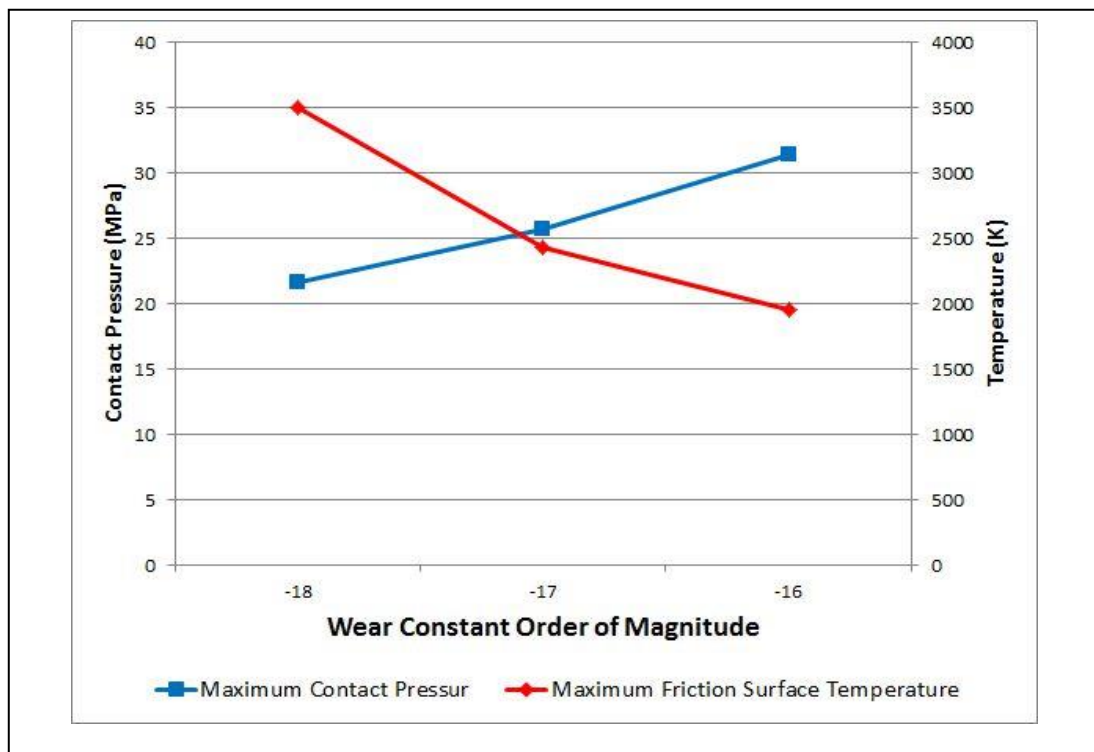


Figure 7.41 – Wear Constant Sensitivity Analysis for Flat-to-Flat Surfaces (Profile 0)

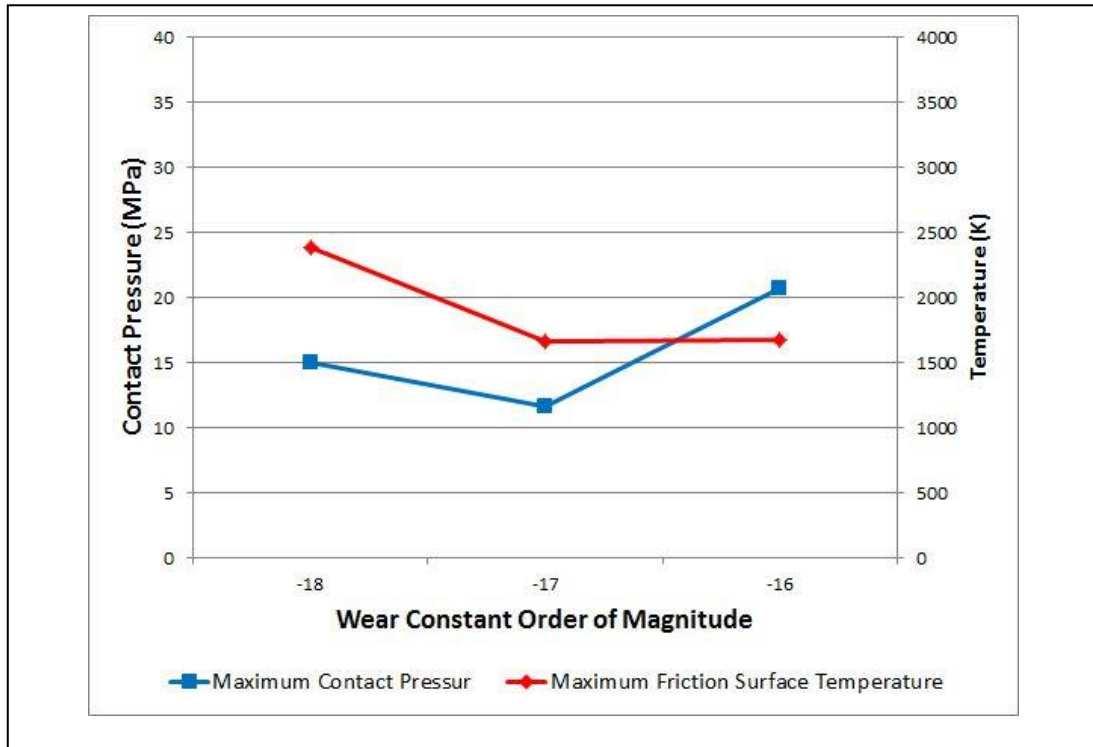


Figure 7.42 – Wear Constant Sensitivity Analysis for Flat-to-Sine Surfaces (Profile 2)

The results of the wear constant sensitivity analysis show that as the magnitude of the wear constant is increased, the maximum contact pressure increases but the maximum friction surface temperature decreases. Initially this result seems implausible as according to the mechanism illustrated by Figure 7.18, the maximum friction surface temperature would follow the same trend as the maximum contact pressure due to heat flux concentration.

Upon closer examination of the results however, it became apparent that the maximum contact pressure values occur over a very small time period and as such do not have a significant effect on friction surface temperature. Wear of the surfaces at the points of high contact pressure cause the contact points to migrate and thus, although heat flux concentration occurs, it occurs over a greater area of the friction surfaces and the maximum friction surface temperature is minimised. An increase in the order of magnitude of the wear constant reduces the maximum friction surface temperature by preventing persistence of the high pressure contact points and therefore limiting heat flux concentration despite the peak contact pressures increasing.

If, as originally postulated, the key to achieving a consistent torque output lies in having a consistent COF which can be achieved through control of the friction surface temperature, increasing the rate of wear of the clutch plates would appear to be a potential solution. Wear would limit the maximum friction surface temperature and therefore reduce the variation of COF during the engagement and consequently the surface morphology which dictates the initial COF for the following engagement. It can be seen however that the introduction of wear reduces the maximum peak torque output of the clutch plates (Figure 7.39 and 7.40) which has an effect on the overall engagement time as show in Figure 7.43. It is important to have a consistent torque output to achieve an optimum race start (discussed in Chapter 1.2) but it may conflict with the need to complete the engagement in the shortest possible time. Increasing the wear may also be an impractical solution in that the clutch plates may not last a full race distance.

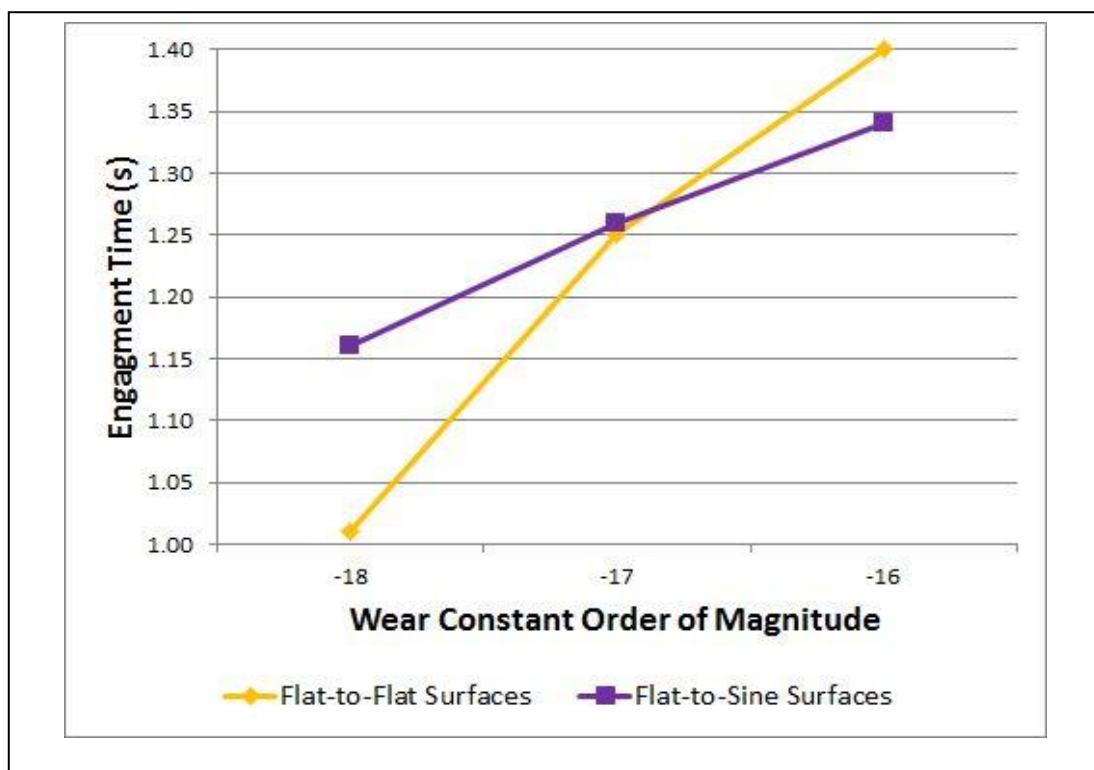


Figure 7.43 – Clutch-Plate Engagement Times as a Function of Wear Constant Order of Magnitude

7.7.4 Asymmetric Surface Profiles

The results discussed in this chapter are based on models where the initial surface profiles have all been symmetric about the geometric centre of the clutch-plate friction surfaces. The analyses carried out have predicted no significant effective friction radius migration and hence the torque behaviour predicted is due mainly to COF variation. It is possible however that this result is due to the symmetry of the initial surface profile and an asymmetry of the initial surface profiles may produce significant effective friction radius migration.

In order to establish the influence of the symmetry of the initial surface profile, two further simulations (including wear) were carried out modelling one clutch plate friction surface as initially perfectly flat with the other clutch plate having an initially non-flat, asymmetric friction surface profile. The two surface profiles used (Profile 10 and Profile 11) were based on Profile 2 listed in Table 7.4 and modified such that Profile 10 only has a single peak (peak 6 of 7) near the outer radius of the clutch plate where the rest of the friction surface is flat. Profile 11 conversely only has a single peak (peak 2 of 7) near the inner radius of the clutch plate. Figure 7.44 shows the initial contact pressure distribution produced by these two surface profiles. Contact is not completely isolated to the surface peaks but the contact pressure is much higher at the surface peaks. Contact is maintained on the opposite side of the clutch plate surfaces but at a much lower value. There is no contact at either side of the surface peaks.

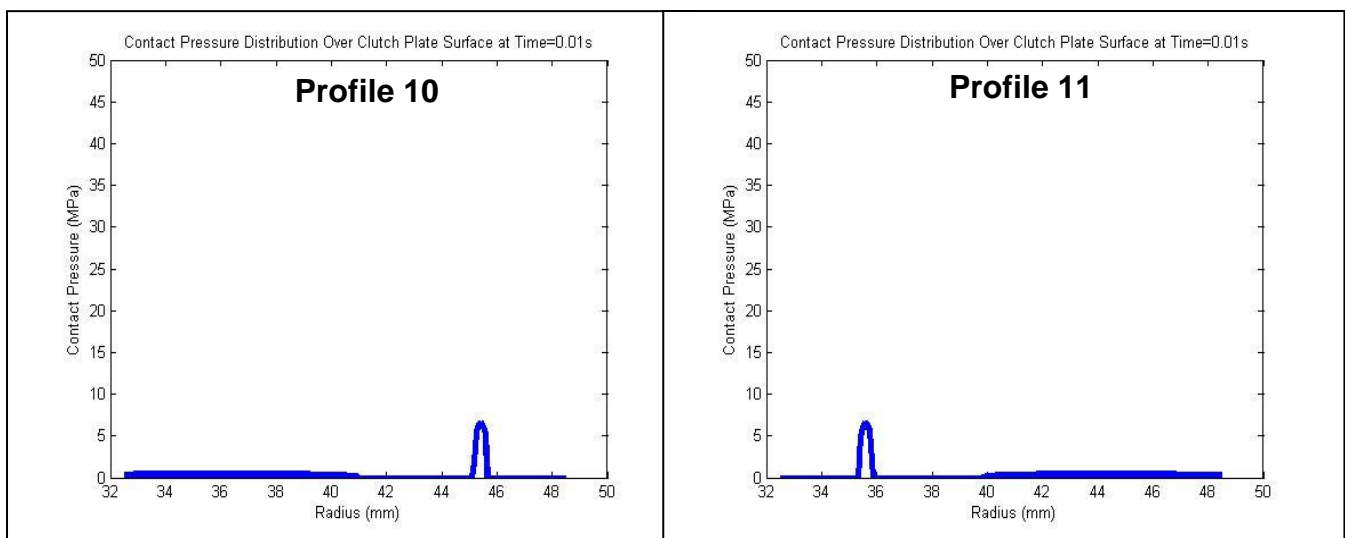


Figure 7.44 – Initial Contact Pressure Distribution for Profiles 10 and 11

As with all previous simulations, contact is quickly lost at the outer edges and a secondary contact pressure peak is formed resulting in the familiar twin-peak contact pressure profile.

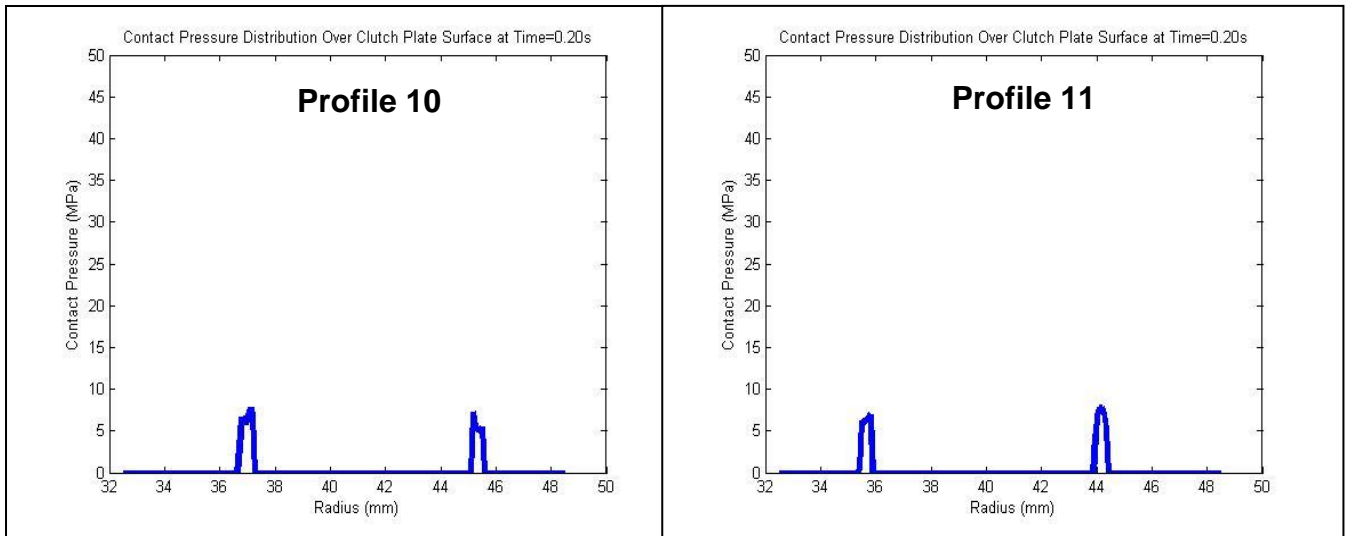


Figure 7.45 – Contact Pressure Distribution at t=0.20s (Profiles 10 and 11)

The original surface peak then wears away whilst the secondary contact pressure peak migrates towards the centre of the clutch plate friction surface.

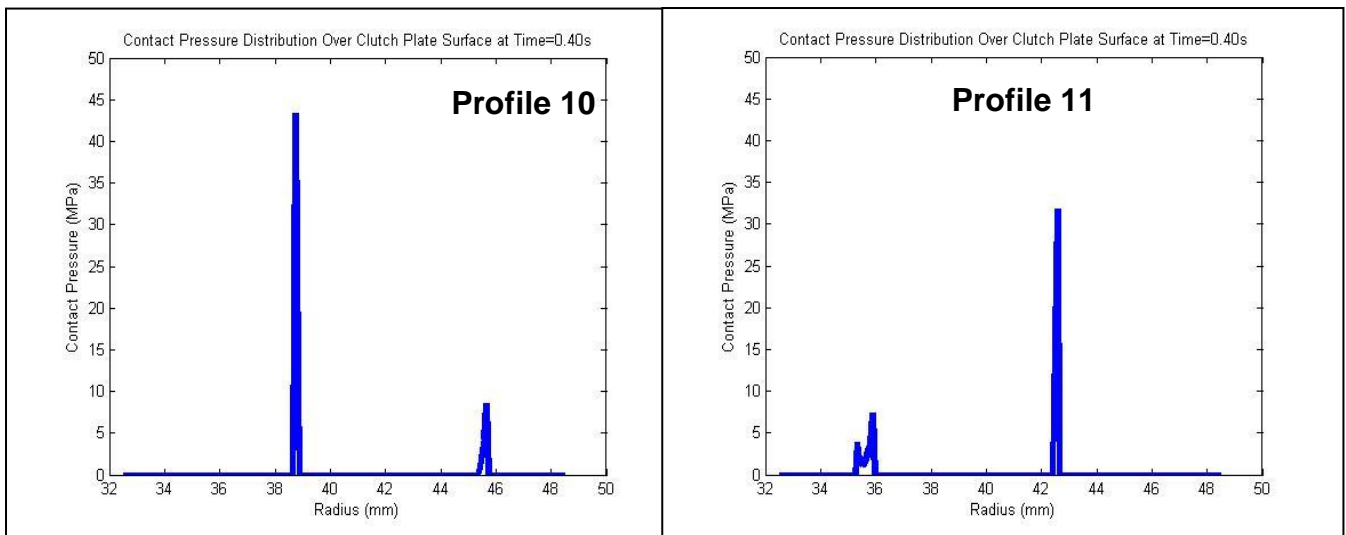


Figure 7.46 – Contact Pressure Distribution at t=0.40s (Profiles 10 and 11)

Further wear of the original surface peak and migration of the secondary contact point results in contact becoming isolated to the centre of the clutch plates leading to a single band of high contact pressure.

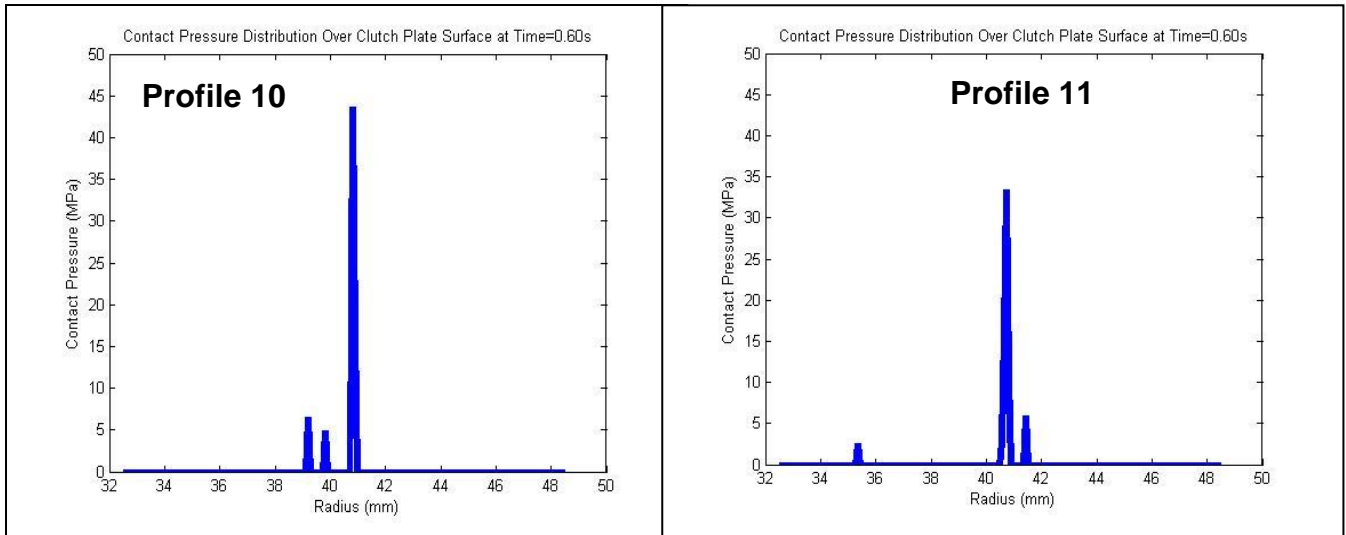


Figure 7.47 – Contact Pressure Distribution at $t=0.60s$ (Profiles 10 and 11)

As the clutch plate engagement progresses, the central band of contact pressure reduces due to wear and a reduced level of thermal expansion as a result of heat conduction through the clutch plate combined with a reduced heat flux input. As the engagement reaches completion, contact is re-established at the original surface peak and the secondary contact peak as shown in Figure 7.48.

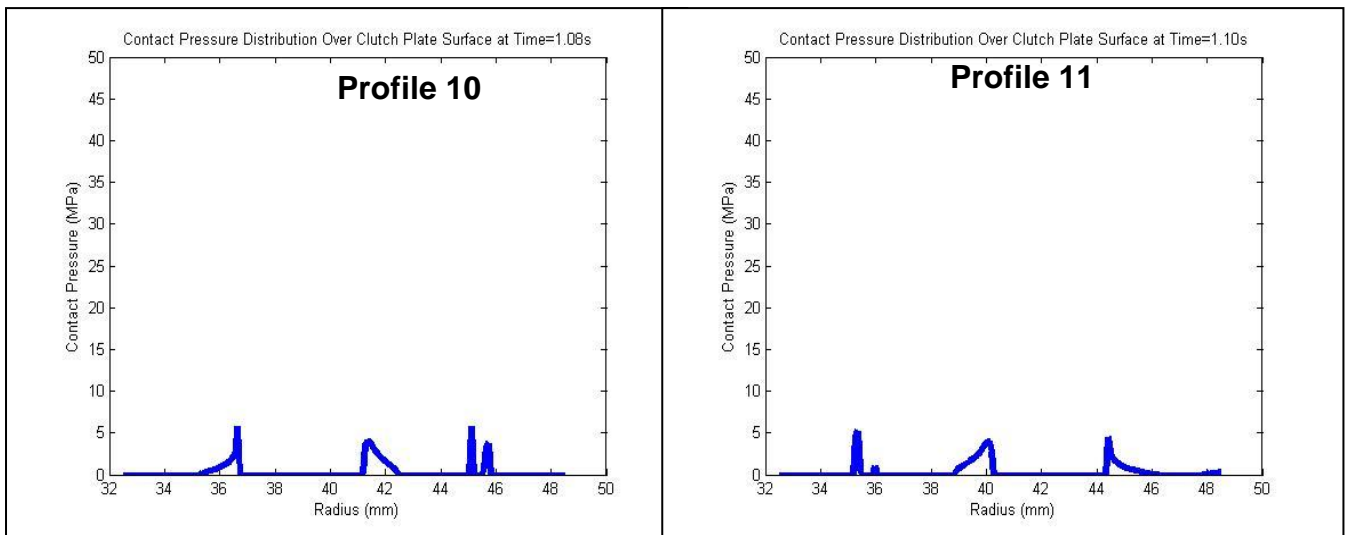


Figure 7.48 – Contact Pressure Distribution at Completion of Clutch-Plate Engagement ($t=1.08s$ for Profile 10, $t=1.10s$ for Profile 11)

Despite the contact point migration shown in Figures 7.44-7.48, the effect on the effective friction radius is minimal. As can be seen in Figures 7.49 and 7.50, there is some migration of the effective friction radius about the geometric centre of the

clutch plates but with a maximum deviation of approximately $\pm 0.3\text{mm}$. This would equate to a maximum influence upon the torque generation of the clutch plates of less than $\pm 1\%$. This analysis has shown therefore that, regardless of the symmetry of the initial surface profile about the geometric centre of the clutch plates, the effective friction radius tends towards the geometric clutch-plate centre with only minor deviation. Hence, the torque behaviour simulated must be due to mainly to the effects of the temperature-dependent variation of the friction surface COF.

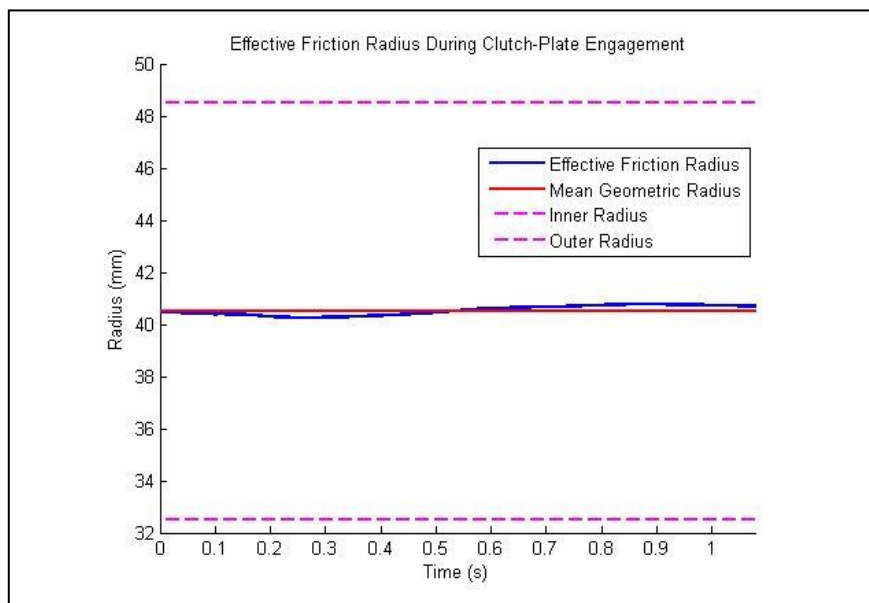


Figure 7.49 – Effective Friction Radius History for Profile 10

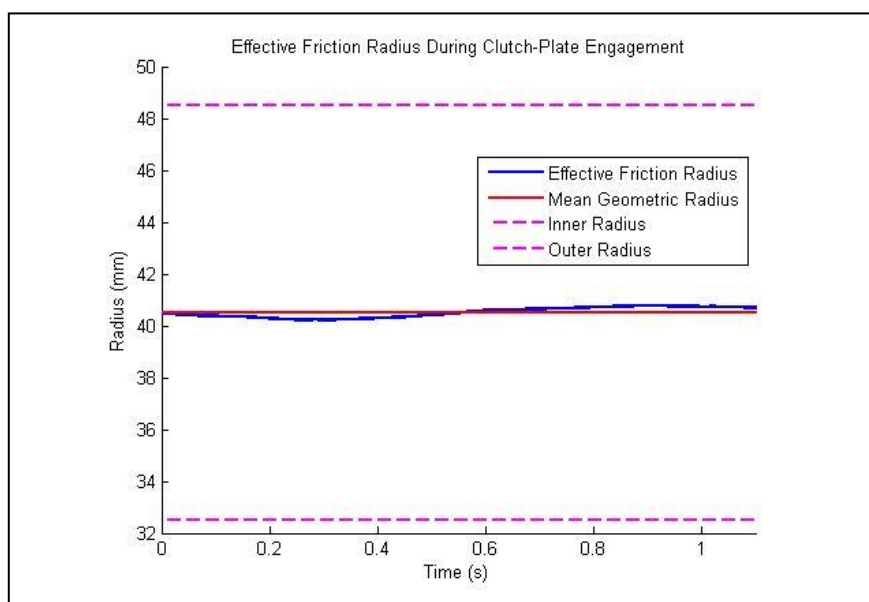


Figure 7.50 – Effective Friction Radius History for Profile 11

7.7.5 Consecutive Clutch-Plate Engagements

The simulations discussed in this chapter have not taken into account the history of the clutch plates and how the effects of wear from previous engagements might affect the performance of the next engagement. Knowledge of this could be critical in leading to an understanding of the clutch torque variability seen between consecutive clutch-plate engagements (Chapters 1.2 and 4).

Ten consecutive clutch-plate engagement simulations were carried out where the Matlab scripts used to introduce surface profiles (see Section 7.3.1) were modified so that the initial surface profiles for an individual engagement reflected the wear that occurred during previous engagements. The change in initial position of the friction surface nodes was equal to the cumulative wear at each node. For the first engagement, the surface profile was flat-to-flat (Profile 0).

The results of the first clutch-plate engagement are identical to that discussed in Section 7.7.1 whereby a central band of contact pressure is formed resulting in a very high maximum surface temperature. The consequence of this is that the centre of the clutch plate is worn away by the high localised temperature and contact, at the centre of the clutch plates, does not occur in subsequent engagements. A typical twin-band regime is established during engagements 2-10 during which wear of the contact points shifts the location of the bands towards the centre of the clutch plates. During later engagements (5-10), these bands disappear as the engagement progresses and are re-established towards the outer edges of the clutch plates before again, migrating towards the centre of the clutch plates.

The effect of the contact point migration however, has very little effect upon the effective friction radius which fluctuates only slightly about the mean geometric radius of the clutch plates. The torque output and effective friction radius results for all 10 clutch-plate engagements simulated with typical race start (RS) inputs are shown in Figures 7.51 and 7.52. Engagement 1 (RS1) produces a higher peak torque than the other engagements due to the high friction surface temperature, and hence COF, resulting from the single central contact band. Figure 7.52 clearly shows that very little effective friction radius migration occurs during single engagements and the torque output instability shown in Figure 7.51 must therefore, as with all other simulations, be due mostly to COF variation.

The effective friction radius reduces from the first engagement to the last which is mirrored by the torque outputs. This suggests that the inconsistency of torque output between engagements is entirely due to differences in effective friction radius. The simulations do not however model the initial surface morphology, and hence the initial friction surface COF, based on previous engagements. The COF varies with temperature and because all clutch-plate engagements are modelled with the clutch plates initially at room temperature, the initial COF is uniform across the friction surface for all ten engagements. In reality, this is highly unlikely to be the case. The surface morphology and COF would be non-uniform across the friction surface as the work done at the friction surface during the previous clutch-plate engagement would be non-uniform. Parts of the friction surface could therefore have an initial COF higher than 0.2 as modelled (Table 7.3). The results shown in Figures 7.51 and 7.52 therefore do not model surface morphology effects affecting the consistency of torque output.

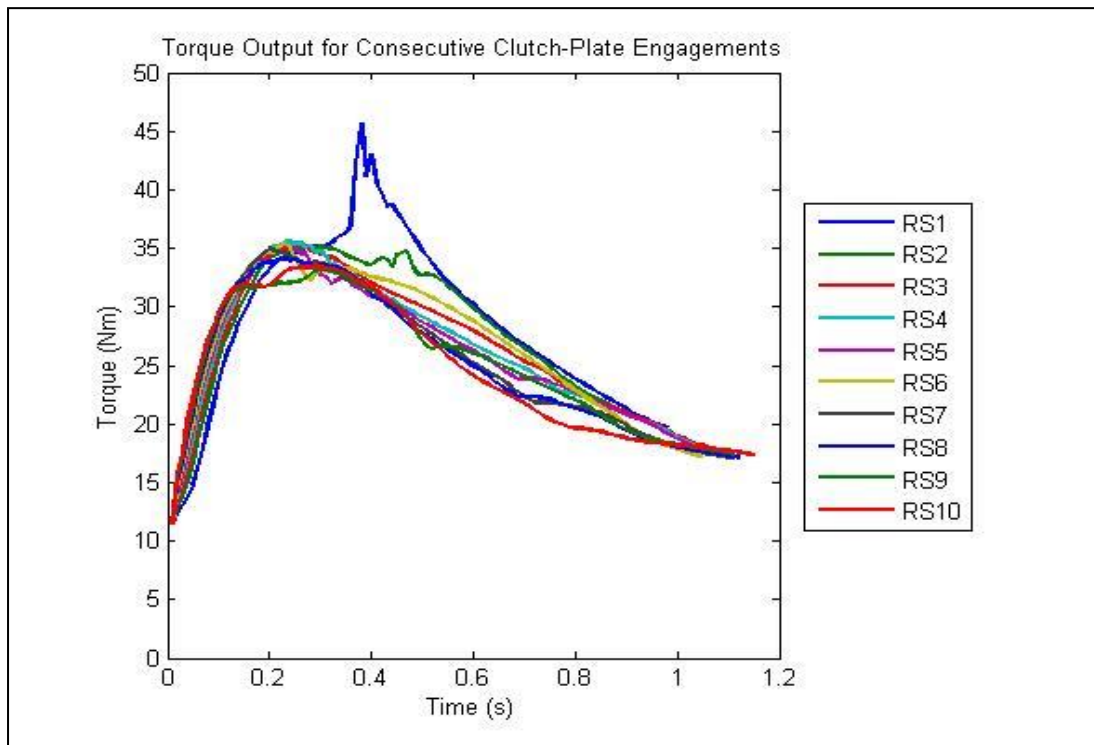


Figure 7.51 – Torque Output History for Ten Consecutive Clutch-Plate Engagements (RS)

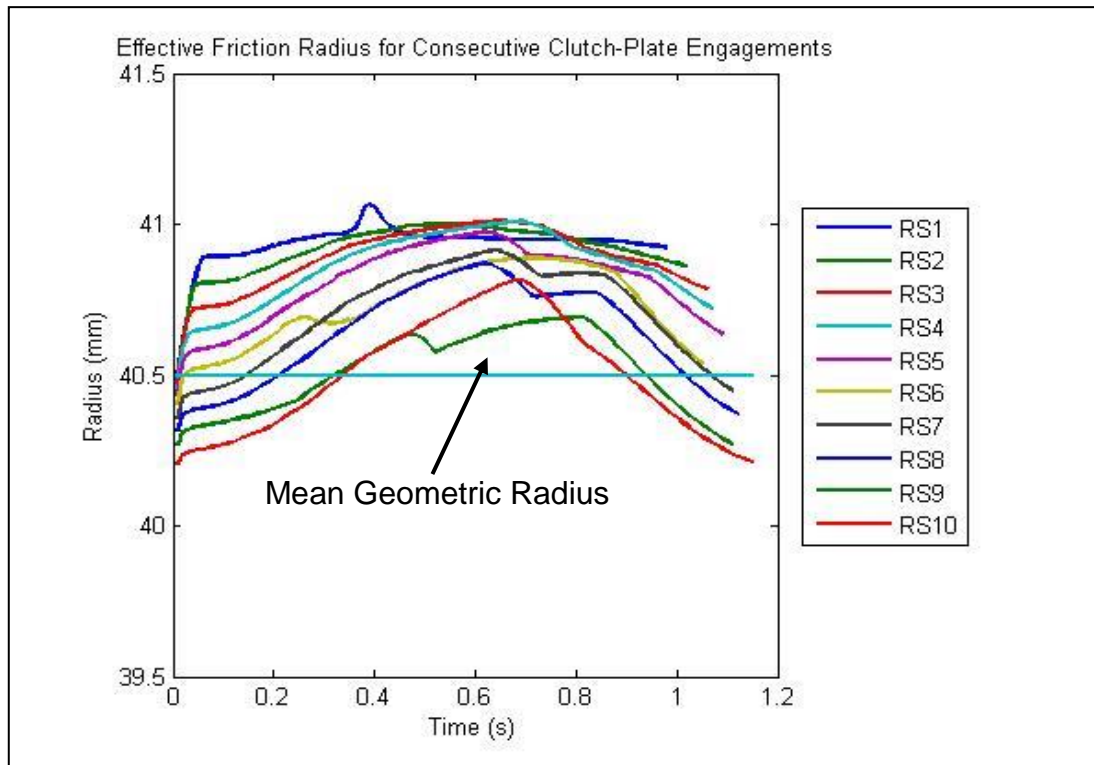


Figure 7.52 – Effective Friction Radius History for Ten Consecutive Clutch-Plate Engagements (RS)

7.8 Modifications Made to TCFEA Based on SCID Results

The simulations that have been discussed in this chapter were used to simulate clutch-plate behaviour during SCID engagements tests. However, the simulations were carried out before the SCID had been commissioned. Several aspects of the TCFEA were subsequently modified based on the results of SCID testing.

Firstly, as discussed in Chapter 4, the clamp load for the 1400N load case took approximately 1.0s to build up to the full clamp load doing so in a linear manner. The TCFEA was constructed with an instantaneous clamp load and therefore does not reflect the true behaviour of the SCID. The clamp load was modified to build up linearly from 0N to 1400N during the first second of the simulation and remain constant thereafter until the engagement is complete.

Secondly, the TCFEA used the spline function to calculate the COF at each friction surface node based on its temperature. Temperatures above 1473K were extrapolated from the reference values (Table.7.3). From the torque results of the SCID engagement tests, an estimate of the COF was calculated based on both the

mean geometric radius and effective friction radius. No COF values greater than 0.5 were calculated from this analysis. The TCFEA was therefore modified so that above 1473K, the COF was set at the maximum value of 0.5.

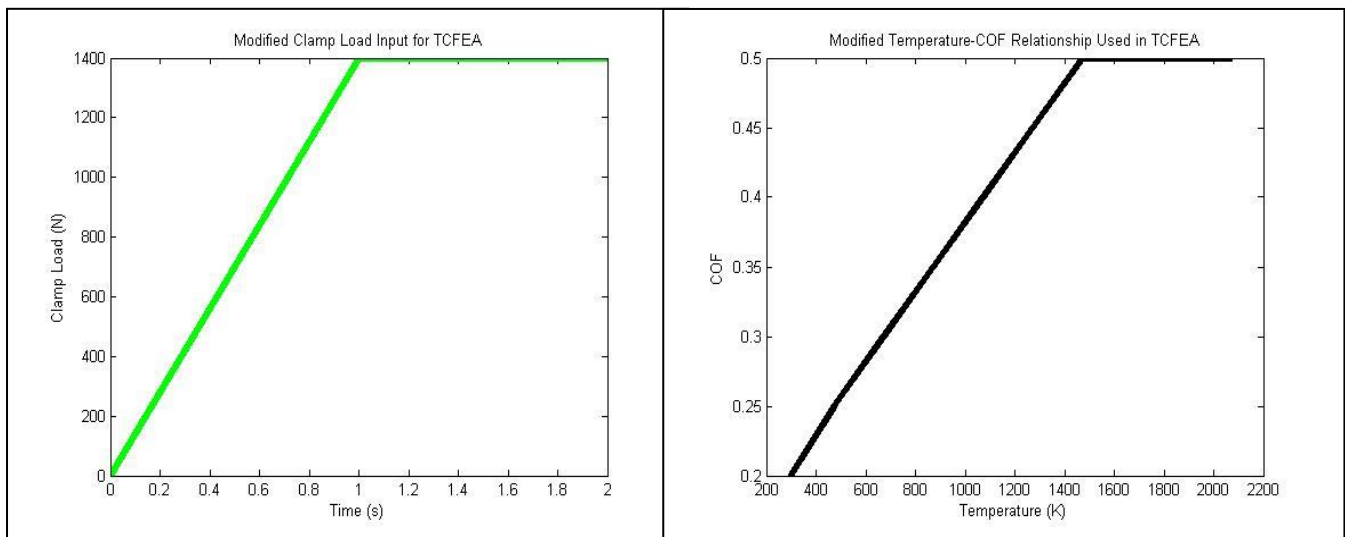


Figure 7.53 – Modified Time-Clamp Load and Temperature-COF Relationships

The wear model used in the TCFEA was based on the assumption that the high friction surface temperatures would lead to oxidation wear or the greatly increased normal loads due to the high contact pressure would lead to abrasion wear (or possibly both). It was assumed that the wear rate would follow an exponential relationship with temperature. The SCID and surface characterisation results showed that wear does occur. Narrow wear tracks were formed in areas of high temperature but wider and more distinct wear tracks formed in areas where extreme hot bands occurred suggesting that greater amounts of wear occur at elevated temperatures as assumed when the wear model was established. Whether the relationship is linear or exponential cannot be determined from these results nor could the amount of wear (in terms of depth) be accurately determined. In view of the lack of any more accurate data, the wear model used in the TCFEA was not modified.

The inertia value was also reduced from 0.0344kgm^2 (Table 6.2) to 0.0251kgm^2 (Table 3.1) to reflect the final SCID design.

Both the non-wear and wear models were rerun for the initially flat friction surface case. Table 7.6 shows a comparison of the results of the original simulations and the modified simulations.

Model Version	Type	Engagement Time (s)	Maximum Contact Pressure (MPa)	Maximum Friction Surface Temperature (K)	Time (s)	Radius (mm)
Original	Non-Wear	1.33	10.301	1987	0.42/0.45	36.82/36.90
	Wear	1.25	25.731	2430	0.39/0.34	40.42/40.90
Modified	Non-Wear	1.50	9.297	1814	0.81/0.78	36.82/36.82
	Wear	1.38	12.114	1808	0.77/0.73	40.66/40.98

Table 7.6 – Results of TCFEA Simulations (Original and Modified)

The evolution of the contact pressure and friction surface temperature for the modified models follow the same trends as the original models presented in Sections 7.5 and 7.7.1. The maximum contact pressures and friction surface temperatures are lower for both modified versions which is due to the change in torque output behaviour as a result of the gradual clamp load build-up and limited COF as well as the reduced level of overall energy input associated with the smaller inertia value. Figure 7.54 shows the torque outputs predicted by the models listed in Table 7.6.

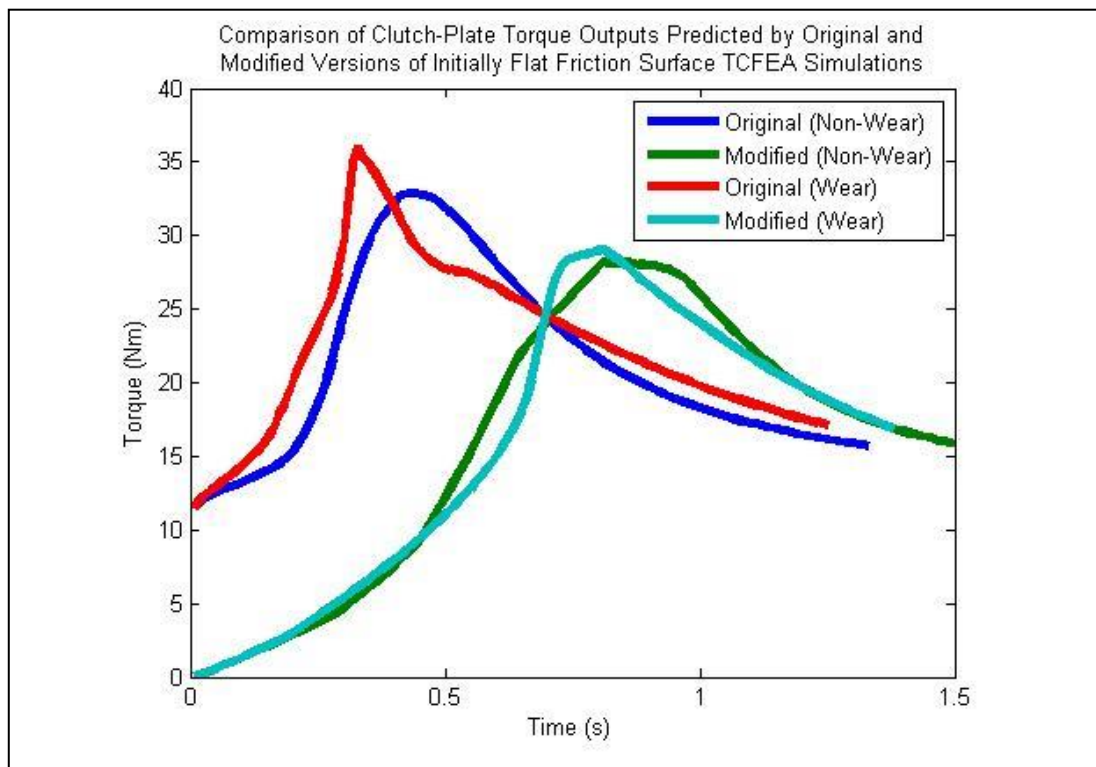


Figure 7.54 – Torque Outputs Predicted by TCFEA Simulations Listed in Table 7.6

As the original models were based on an instantaneous clamp load, a torque output is generated from the start of the engagement. The heat flux input will therefore also start from the beginning of the engagement causing immediate temperature rises which will lead to COF increases. As a result the maximum contact pressure and friction surface temperature occur much earlier in the engagement than for the modified models. The peak torque output value therefore also occurs earlier in the engagement. For the modified models, the lower maximum contact pressure and friction surface temperature is due to the fact that by the time the full clamp load is built up in the modified model, energy will have been lost from the rotating mass at a low power dissipation level and its rotational speed will be lower than at the beginning of the engagement. As the kinetic energy loss follows a square law relationship with rotational speed, there is a much lower level of overall energy input after the point at which the full clamp load has built up (also due to the smaller inertia value). The effect of this is that the phenomenon of TEI is less extreme leading to a lower degree of contact localisation and a lower maximum friction surface temperature. The peak torque output being generated later in the engagement is simply a function of the clamp load build-up delay.

The higher torque outputs predicted by the original models are due to the COF being able to rise above a value of 0.5 and as such the COF values in the original model rose to ~ 0.625 and ~ 0.75 for the non-wear and wear models respectively. Limiting the COF to a maximum value of 0.5 limits the maximum torque output predicted by the modified models. The limited COF also reduced the levels of heat flux input resulting in lower maximum contact pressures (due to less thermal expansion) and lower maximum friction surface temperatures.

For both the non-wear and wear models, lower maximum friction surface temperatures were predicted in the modified versions. However, the difference for the wear model ($\sim 600\text{K}$) is much greater than the difference for the non-wear model ($\sim 150\text{K}$). This is due to the way that the contact localisation occurs. In the non-wear model, two contact bands are formed where high temperatures arise. These localised points of contact are established early in the engagement and in the absence of wear, persist for much of the engagement, particularly when the highest torque and hence highest power dissipation occurs. Modification of the non-wear model does not have a large effect on the maximum friction surface as the energy is

dissipated at these contact points in both the original and modified model but it is the limited COF and hence limited torque and heat flux input that result in a lower maximum friction surface temperature.

In the wear model, the two localised contact points are worn away and a single contact point is established at the mean geometric radius of the clutch plate leading to a single, centralised hot band. In the modified version of the wear model, this occurs later in the engagement when a greater amount of energy of the rotating mass has already been lost during the clamp load build-up but before contact localisation has occurred. As such, a lower amount of overall energy is input to the centralised band of contact and a lower maximum friction surface temperature is reached.

7.9 Alternative TCFEA Models

7.9.1 Alternative Temperature-COF Relationship

The temperature-COF relationship shown in Table 7.3 was used as an estimate based on previous findings [7] but no experimental validation could be provided. To verify the validity of the assumed relationship an alternative temperature-COF was investigated where the values in Table 7.3 have essentially been reversed to give the values shown in Table 7.7. As with the modified TCFEA models, the COF values were linearly interpolated between the reference temperature values and at temperatures above 1473K, the COF remains at a constant value of 0.2.

Temperature (K)	COF
298	0.50
473	0.45
673	0.40
873	0.35
1073	0.30
1273	0.25
1473	0.20

Table 7.7 – Alternative Temperature-COF Relationship Used in TCFEA

Both the modified non-wear and wear simulations discussed in section 7.8 were rerun for the flat-to flat surface condition.

Figure 7.55 shows the contact pressure distribution and friction surface temperature profile for the non-wear model after 0.20s. In comparison to the results of the original non-wear model shown in Figure 7.15 (modified model very similar as discussed in section 7.8) it can be seen that the contact pressure distribution has a similar profile whereby contact has been isolated to a few regions leading to two contact pressure peaks either side of a central contact area with a lower contact pressure. However, due to the COF being higher at lower temperatures, a greater amount of energy dissipation occurs in the early stages of the engagement compared to the modified non-wear model. This leads to more rapid contact localisation resulting in the two contact points either side of the centre becoming smaller leading to narrower contact pressure peaks. The friction surface temperature follows a similar profile.

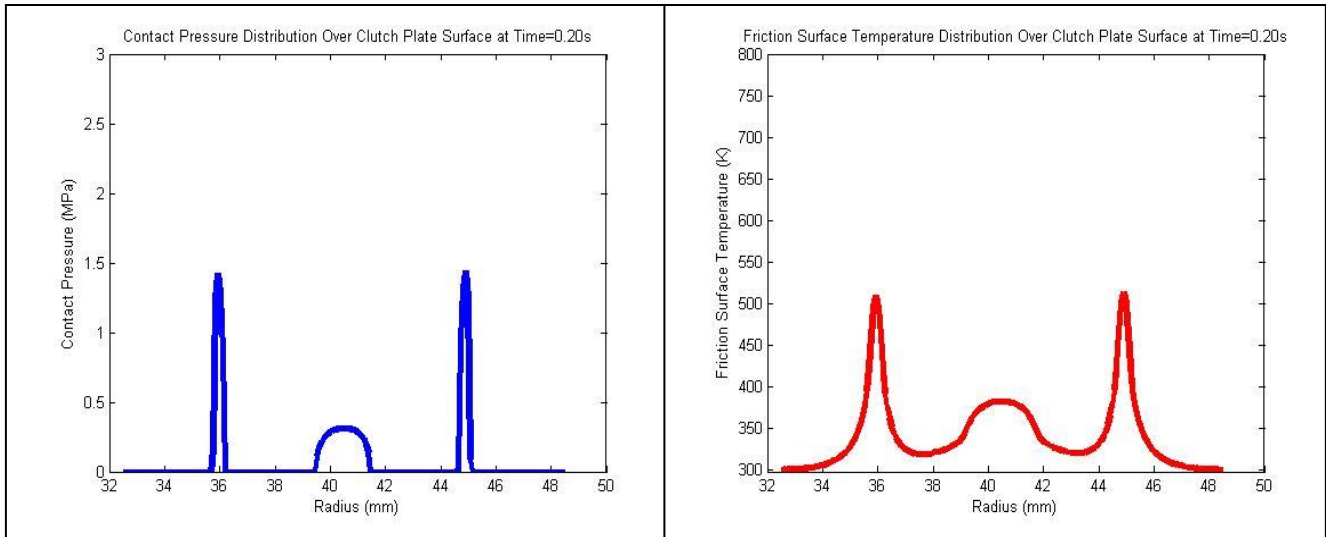


Figure 7.55 – Contact Pressure and Friction Surface Temperature Profiles at $t=0.20s$
(Non-Wear Model, Alternative Temperature-COF Relationship)

The result of the two narrower contact regions is that the overall heat input to the two small contact areas is less than the heat input to the central region despite the lower contact pressure at the friction surface centre. As such thermal expansion in the central contact region becomes greater than at the two contact points on either side and contact is isolated to the central contact region. Figure 7.56 shows the contact pressure and friction surface temperature profiles after 0.25s where it can be seen that the contact pressure at the central region has become greater than at the two regions either side. The friction surface temperature follows a similar profile.

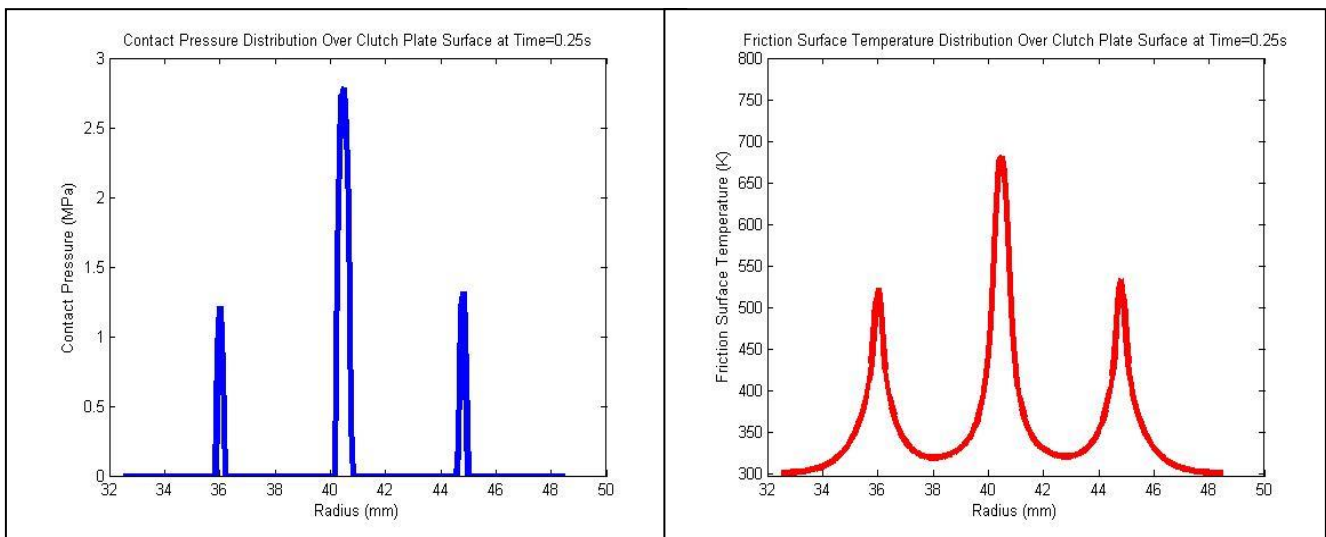


Figure 7.56 – Contact Pressure and Friction Surface Temperature Profiles at $t=0.25s$
(Non-Wear Model, Alternative Temperature-COF Relationship)

At 0.33s into the engagement, contact is completely isolated to the central contact region and a single hot band regime is established for much of the remainder of the engagement. Contact is re-established at other regions of the friction interface towards the end of the engagement as with the other models. In this respect, the non-wear model with the alternative temperature-COF relationship shows similar behaviour to the simulations including wear rather than either the original or modified non-wear models. A maximum friction surface temperature of 1600K was predicted at 0.84s into the engagement which is less than the 1814K predicted by the modified non-wear model (see Table 7.6).

Figure 7.57 shows the torque outputs predicted by the modified non-wear model and the non-wear model with the alternative temperature-COF relationship. Due to the higher COF values at low temperatures, the torque output for the model with the alternative temperature-COF relationship is initially higher leading to greater initial energy dissipation resulting in the more rapid level of contact localisation discussed. As the surface temperatures increase, the COF rises for the modified model but falls for the model with the alternative temperature-COF relationship resulting in the torque output being much higher for the modified model. As a consequence, the overall engagement time for the model with the alternative temperature-COF relationship takes longer. The lower torque, and hence lower rate of energy dissipation, thus allows more time for heat to be conducted away from the location of the hot band both radially and axially and therefore results in the model with the alternative temperature-COF relationship predicting a lower maximum friction surface temperature than the modified non-wear model.

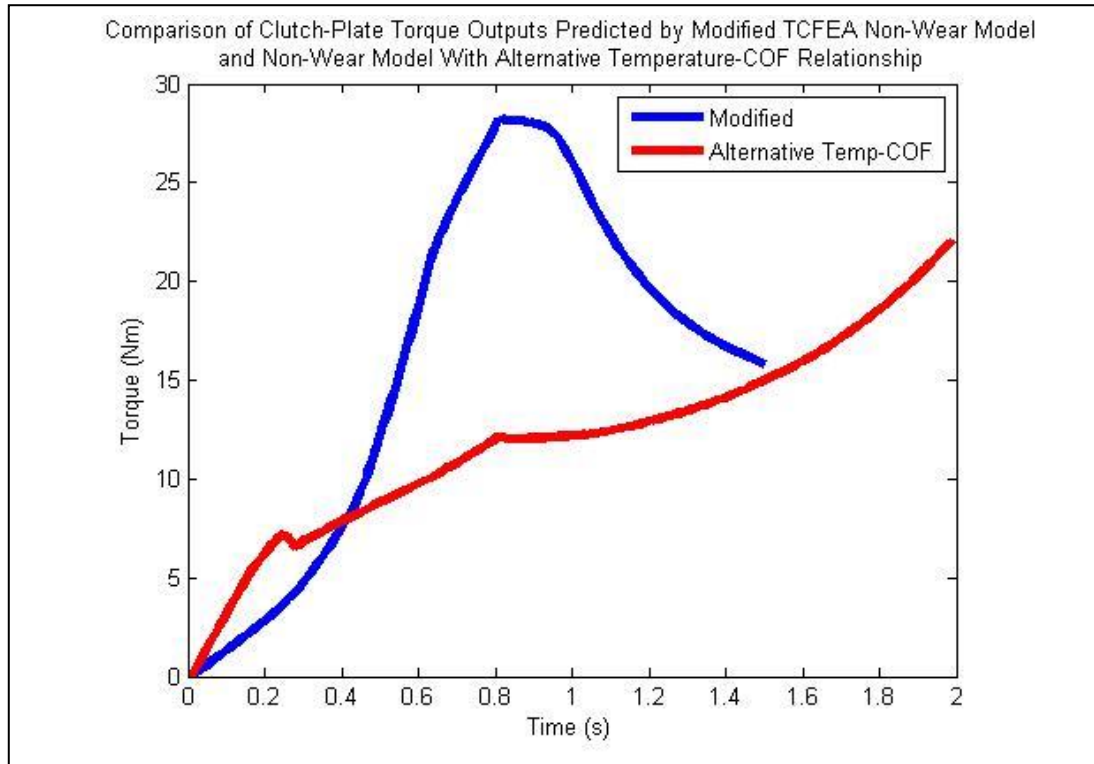


Figure 7.57 – Torque Outputs Predicted by Modified TCFEA Non-Wear Model and Non-Wear Model With Alternative Temperature-COF Relationship

The wear model with the alternative temperature-COF relationship follows a similar contact pressure and friction surface profile evolution to that of the original wear model shown in Figures 7.32-7.35 (modified model very similar as discussed in section 7.8). However, the central hot band formed has a much lower maximum temperature of 1165K compared to 1808K for the modified wear model (see Table 7.6). As with the non-wear model, this is due to the alternative temperature-COF relationship affecting the torque output which in turn influences the rate of energy dissipation. Figure 7.58 shows the torque outputs predicted by the modified wear model and the wear model with the alternative temperature-COF relationship. As with the non-wear model, the alternative temperature-COF relationship results in a higher initial torque output but as the surface temperature increases and the COF falls as opposed to rising, the torque output is much less than for the modified model. The lower torque and lower rate of energy dissipation in the single central hot band results in a lower maximum friction surface temperature.

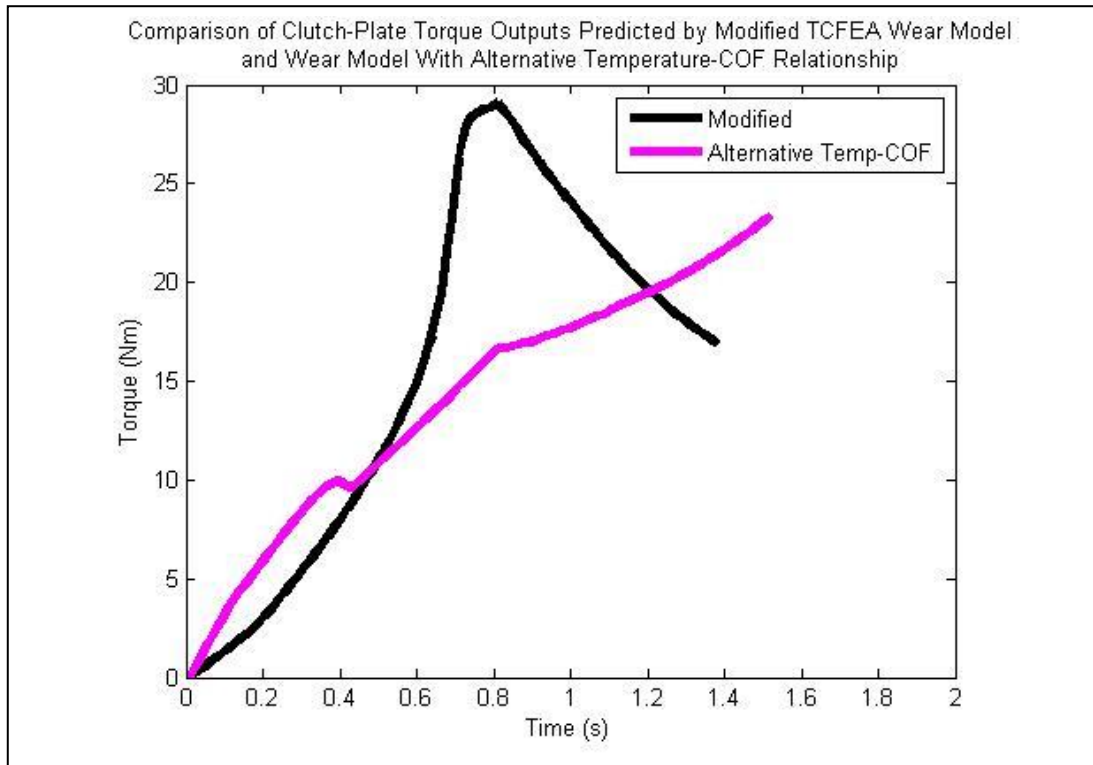


Figure 7.58 – Torque Outputs Predicted by Modified TCFEA Wear Model and Wear Model With Alternative Temperature-COF Relationship

Clearly the alternative temperature-COF relationship affected the results of the TCFEA simulations particularly in the case of the non-wear model. The wear model followed the same single hot band regime as the modified wear model but the non-wear model also predicted a single hot band regime whereas the modified non-wear model predicted a twin-band regime. In both cases, the alternative temperature-COF relationship led to initially higher torque output values compared to the modified models but which were subsequently lower due to the reduced COF values at high temperatures. This led to increased engagement times and hence a reduction in the rate of energy dissipation which had the consequence of lower maximum friction surface temperatures being predicted.

7.9.2 Alternative Wear Equation

As with the temperature-COF relationship used, an assumption was made with regards to wear in that the wear rate would increase exponentially with temperature (Equation 7.12). To verify the validity of this assumption, an alternative wear model was investigated using Equation 7.11 with no temperature dependency. For the wear model based on Equation 7.12, it was assumed that $2\mu\text{m}$ of wear occurred during the time ($\sim 0.2\text{s}$) at which the maximum contact pressure and maximum surface temperature arose. The same assumption was made for the alternative wear model based on Equation 7.11 using the values listed in Table 7.5. This gave a wear constant value of $4.6936 \times 10^{-14} \text{ m}^2/\text{N}$. Figure 7.59 shows how the wear rate varies linearly with the product of contact pressure and sliding velocity. The product of the contact pressure and sliding velocity in Table 7.5 was set to a $p_c u$ ratio value of 1.

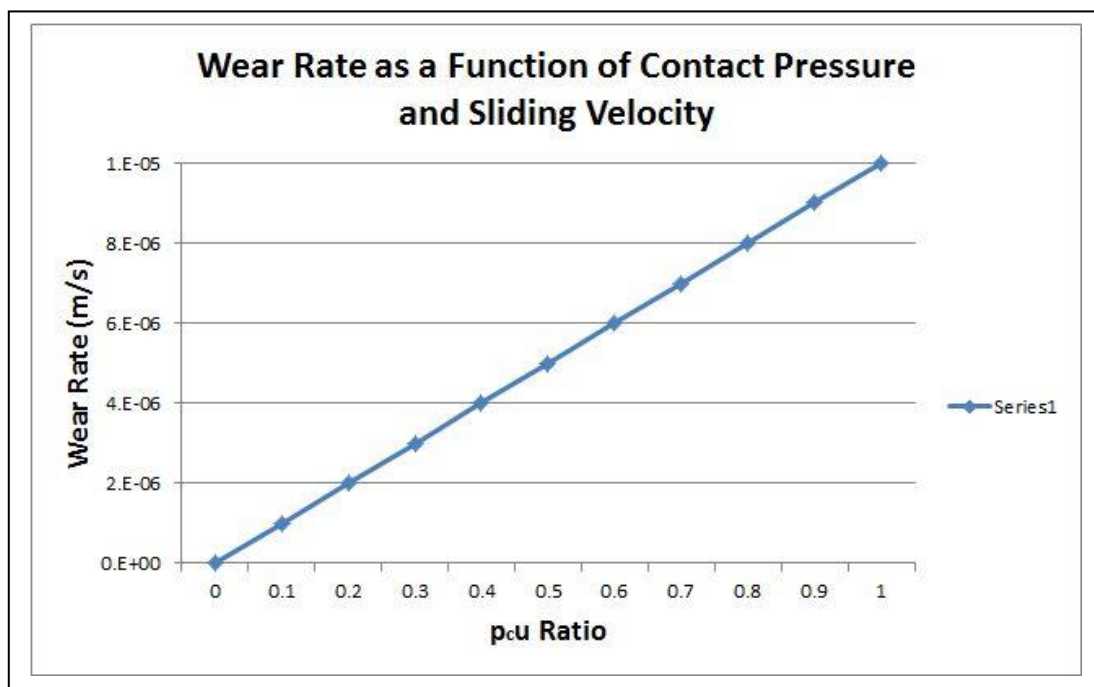


Figure 7.59 – Alternative Wear Rate as a Function of Contact Pressure and Sliding Velocity

The modified TCFEA simulations were rerun using the alternative wear equation for both the original and alternative temperature-COF relationship for the flat-to-flat surface condition.

Figures 7.60-7.64 show the contact pressure and friction surface temperature profiles at several stages during the engagement simulated by the alternative wear model with the original temperature-COF relationship.

As shown in Figure 7.60, at 0.20s into the engagement, the contact pressure distribution is similar to the modified wear model and the original wear model with the alternative temperature-COF relationship in that two localised contact regions have been established either side of the friction surface centre. The peak profiles however are not as smooth as a greater amount of wear has taken place early in the engagement for the alternative wear model in comparison to the original wear model where high rates of wear only occurred at elevated temperatures. The surface temperatures, which are still low, follow a similar profile to the contact pressure distribution.

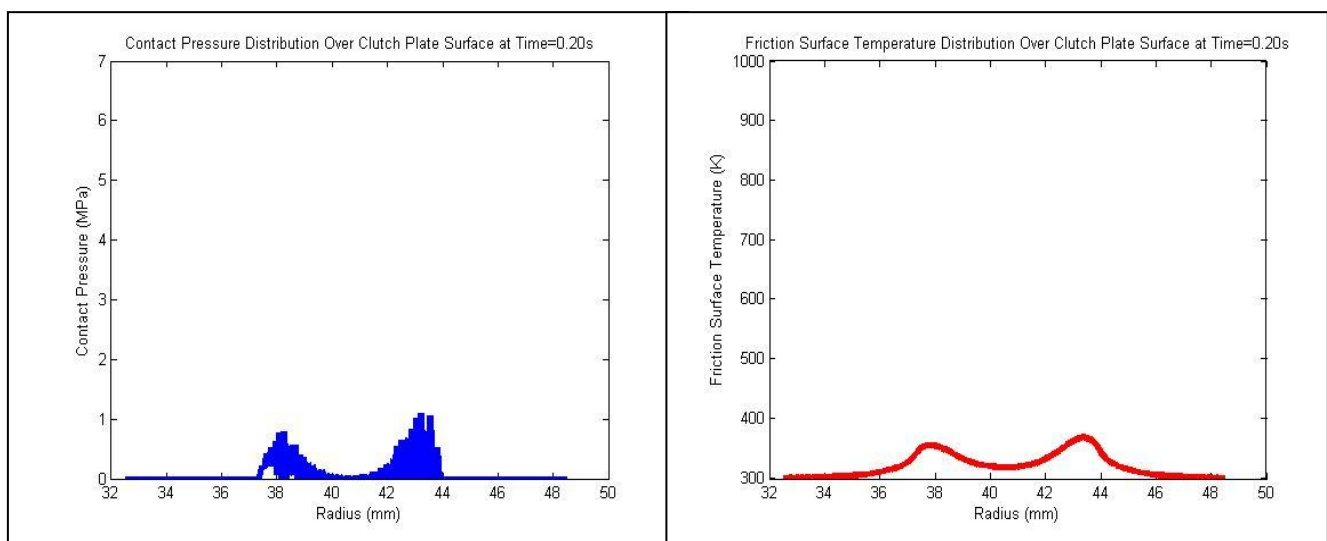


Figure 7.60 – Contact Pressure and Friction Surface Temperature Profiles at $t=0.20s$ (Alternative Wear Model, Original Temperature-COF Relationship)

As with the previous models, the two contact regions are then worn away and contact becomes localised at the friction surface centre as shown in Figure 7.61. The effect this has on the friction surface temperature profile is to lead to the formation of a single central hot band. The temperature of the hot band is fairly low ($\sim 650K$) at this point as the overall amount of heat input to the central contact region up to this point is still low as the contact region has only just been established.

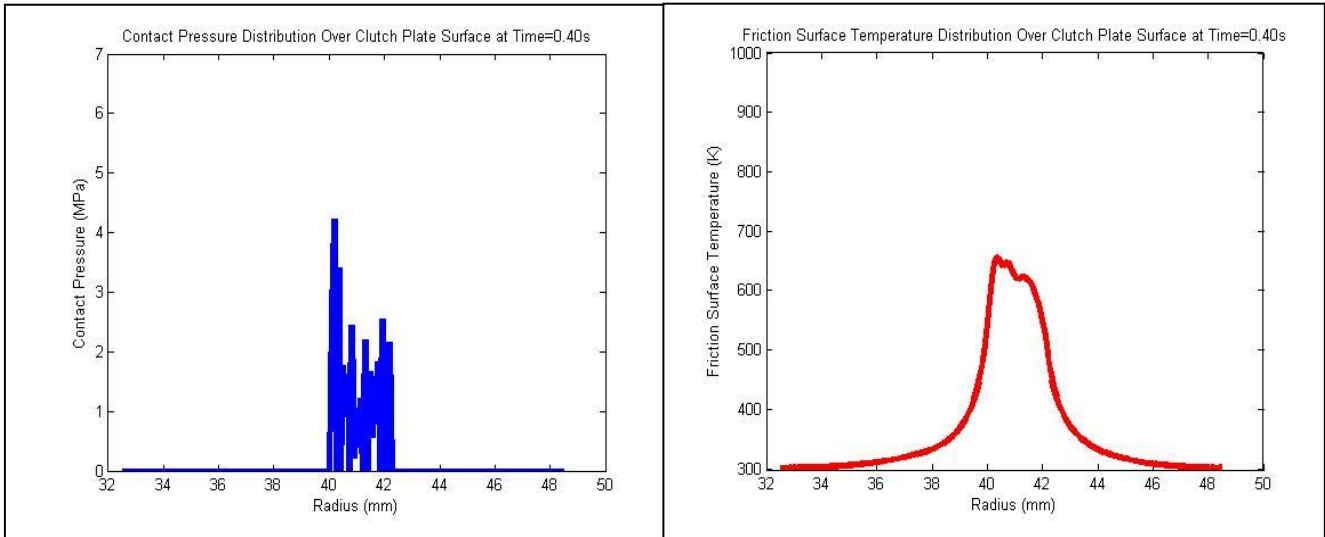


Figure 7.61 – Contact Pressure and Friction Surface Temperature Profiles at $t=0.40s$
(Alternative Wear Model, Original Temperature-COF Relationship)

In contrast to the original wear models, the alternative wear model results in a high enough rate of wear to quickly eliminate the central contact region and contact is re-established at the two contact regions on either side as shown in Figure 7.62. This then results in the formation of a twin peak hot band of around 700K/800K.

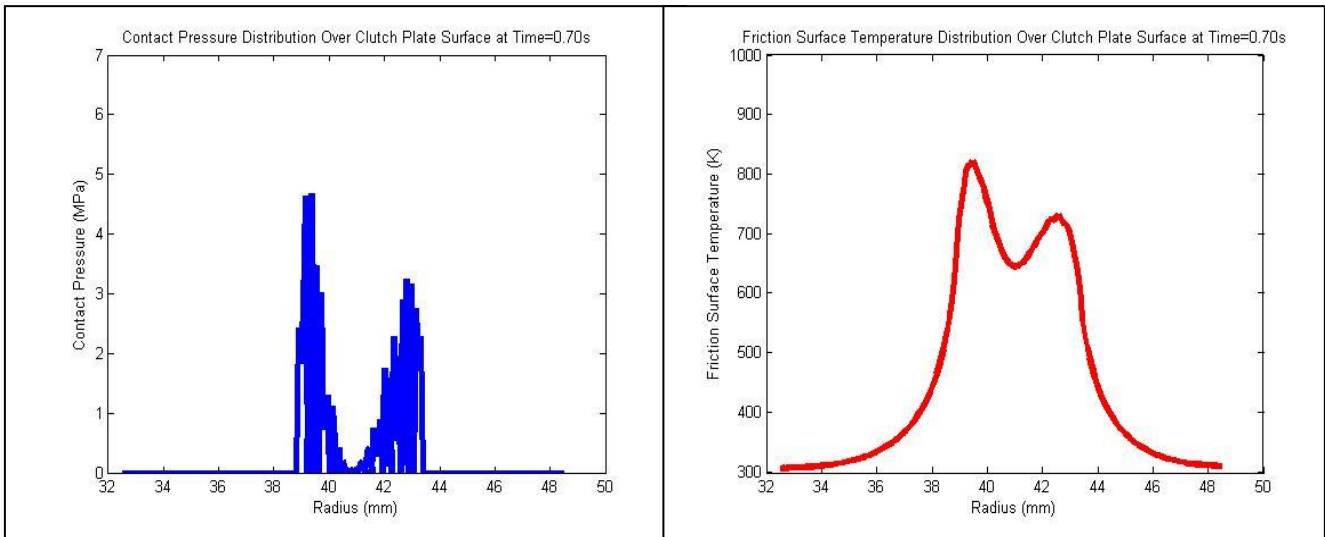


Figure 7.62 – Contact Pressure and Friction Surface Temperature Profiles at $t=0.70s$
(Alternative Wear Model, Original Temperature-COF Relationship)

The two contact regions are then again worn away and the central contact region is re-established leading to a single central hot band, as shown in Figure 7.63, with a maximum temperature of just below 1000K (much less than the modified wear model and the original wear model with the alternative temperature-COF relationship).

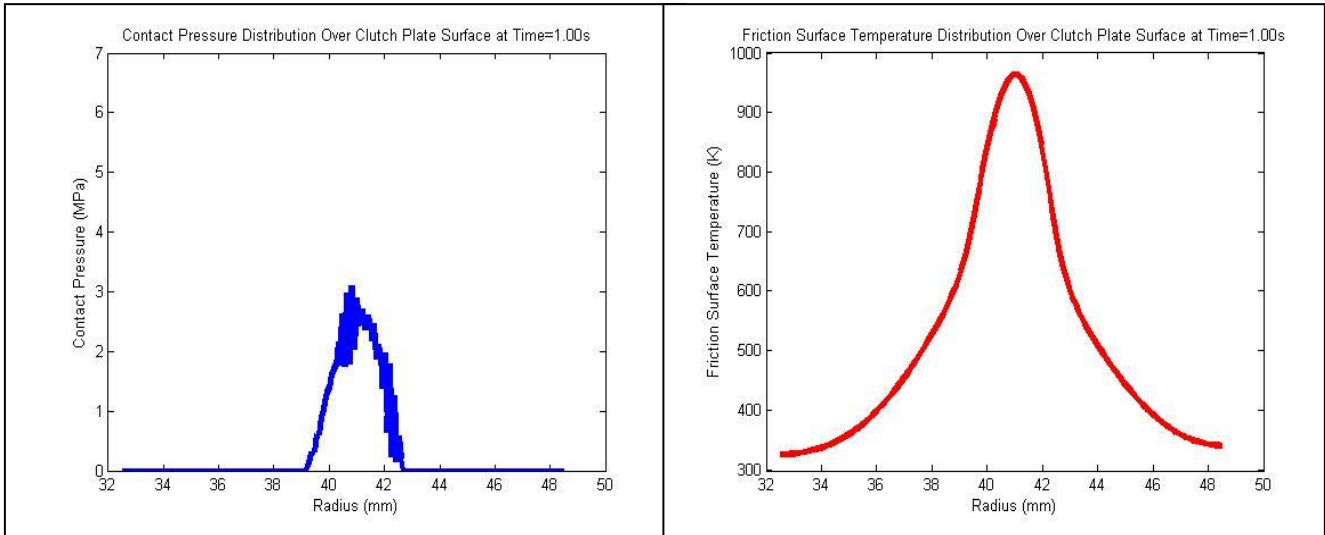


Figure 7.63 – Contact Pressure and Friction Surface Temperature Profiles at $t=1.00s$
(Alternative Wear Model, Original Temperature-COF Relationship)

The central contact region is then again worn away and the twin contact points either side are re-established. As a consequence of the energy being dissipated over a greater area and the heat flux input becoming less than the amount of heat conducted away from the region of the hot band, the hot band temperature falls and increases greatly in width as shown in Figure 7.64.

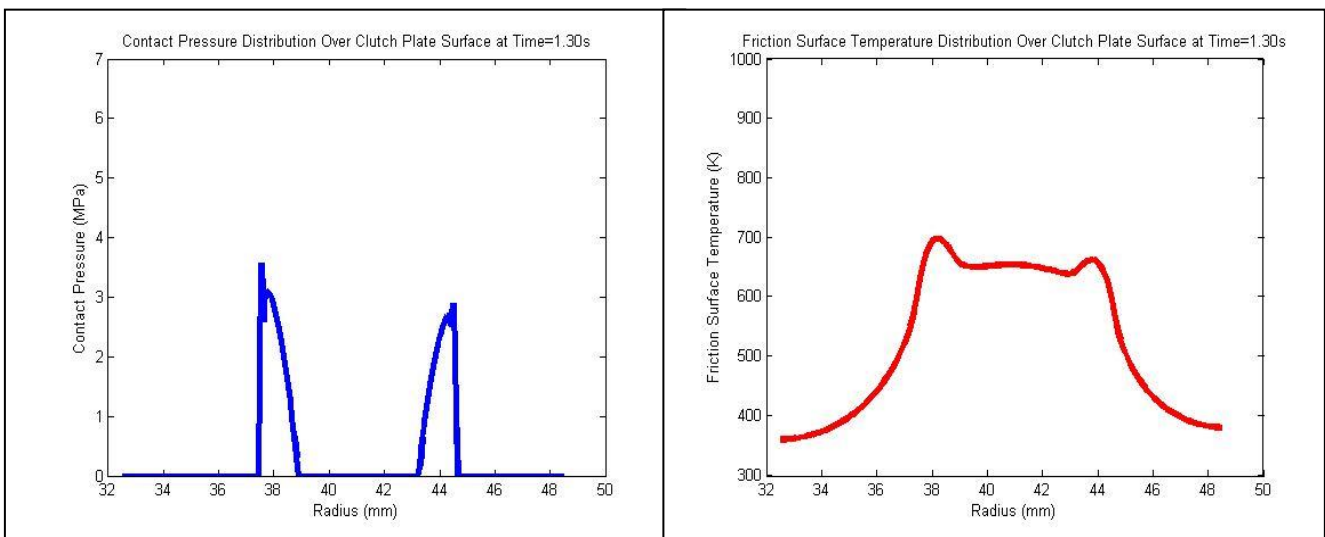


Figure 7.64 – Contact Pressure and Friction Surface Temperature Profiles at $t=1.30s$
(Alternative Wear Model, Original Temperature-COF Relationship)

The alternative wear model with the alternative temperature-COF relationship predicts very similar behaviour to that shown in Figures 7.60-7.64. However the alternative wear model with the alternative temperature-COF relationship predicts a higher maximum friction surface temperature (~1100K) and a shorter engagement time of 1.38s as opposed to 1.64s. The lower maximum friction surface temperatures predicted by the alternative wear equation are due to the increased movement of the contact regions leading to energy being dissipated over a larger area as opposed to mostly at the centre of the friction surface. The torque outputs predicted by all four wear models investigated are shown in Figure 7.65.

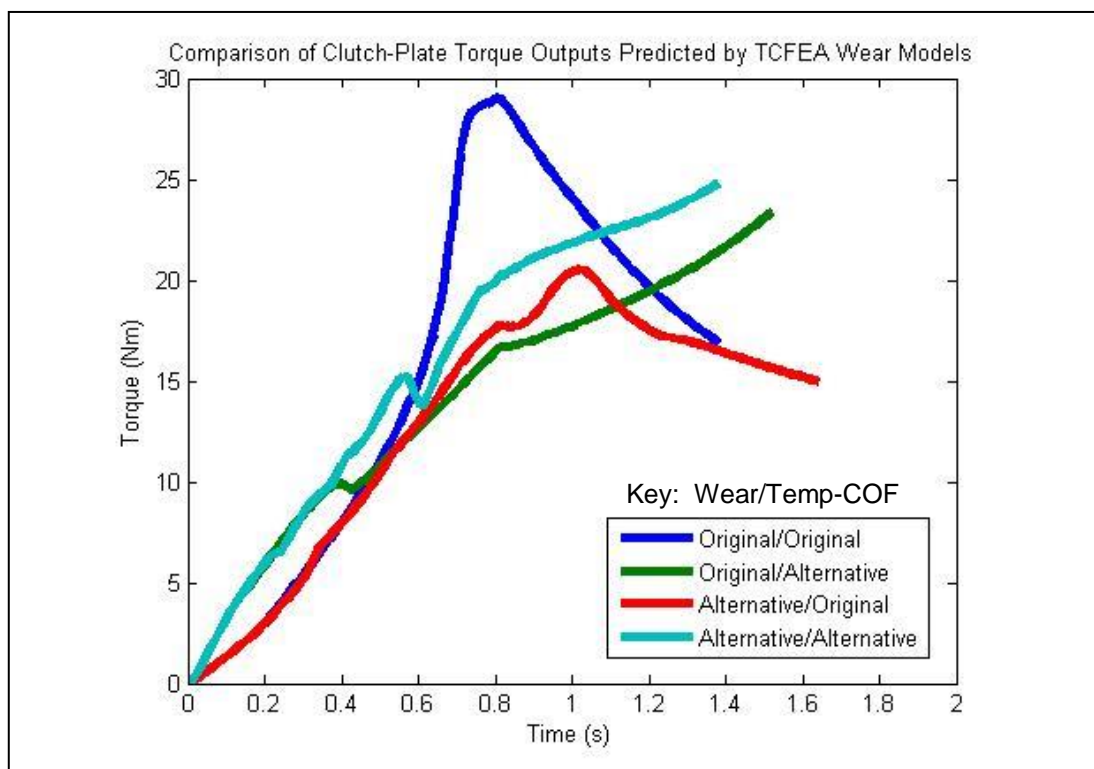


Figure 7.65 – Torque Outputs Predicted by TCFEA Wear Models

For the two models with the alternative wear equation, the effect of the lower friction surface temperatures on the torque output is clear. For the original temperature-COF relationship (alternative/original), the limited temperatures prevent the COF from rising to higher values and the torque output is low as a consequence. The opposite is true for the model with the alternative temperature-COF relationship (alternative/alternative) where the limited temperatures mean that the COF stays at a higher value and the torque output is thus greater leading to a shorter engagement time.

7.10 Summary

Matlab and Abaqus were coupled to create a thermomechanically coupled finite element analysis simulating clutch-plate engagements during SCID testing at 800rpm/1400N. Matlab was used to modify the Abaqus input file and as such a non-uniform heat flux distribution, based on the contact pressure distribution, could be applied to the finite element model.

For the non-wear model, initially flat surfaces predicted the formation of two hot bands either side of the mean geometric radius of the clutch plates resulting in peak temperatures of ~2000K (1700°C). The introduction of wear to the model predicted an increase in peak temperature to just over 2400K (~2150°C) as the two contact points in the non-wear model were worn away leaving only a central point of contact. A greater heat flux concentration therefore resulted in the higher maximum friction surface temperature.

Initially non-flat surfaces were simulated which showed that the initial surface profile can have a large effect on the contact localisation behaviour and therefore the peak friction surface temperatures. For Profile 0, the introduction of wear resulted in a lower maximum friction surface temperature as wear led to high pressure contact points becoming unstable and contact being restored elsewhere.

Despite the differences in friction surface behaviour as well as the torque output of the clutch-plate pairs, the migration of the effective friction radius was predicted to be insignificant. This was also the case for asymmetric surface profiles and consecutive clutch-plate engagement simulations, suggesting that any torque variation during a single clutch-plate engagement is due to COF variation as the result of surface morphology changes.

The simulations for initially flat surfaces (both non-wear and wear) were modified based on the results of SCID testing. The updated clamp load build-up and temperature-COF relationship led to lower maximum contact pressures, maximum friction surface temperatures and peak torque outputs and as a result, a longer engagement time. The maximum values also all occurred later in the engagement.

An alternative temperature-COF relationship and alternative wear equation was also investigated. For the non-wear model, the alternative temperature-COF relationship resulted in the formation of a single hot band as opposed to a twin-band regime

whereas the wear model behaved in a similar fashion to the original model. The alternative wear equation resulted in a greater level of contact region migration for both the original and alternative temperature-COF relationship which resulted in both single hot band and twin-band regimes during a single engagement. In all cases the alternative models resulted in lower maximum friction surface temperatures and lower torque outputs with the consequence of longer engagement times.

8. Discussion

8.1 Introduction

A combination of experimental and computer modelling techniques have been used to investigate the issue of carbon/carbon clutch-plate friction pair torque instability and inconsistency. The results of the experimental work have produced several key findings, some of which have corroborated the results of previous work. This experimental work has also discovered behaviour that was previously suspected but had not been directly observed or quantified. These findings have allowed the computational models to be validated and increase their potential to be used to inform design or race start procedure changes, reducing the need for extensive physical testing.

8.2 The Problem – Further Understanding

As discussed in the introduction chapter, the clutch torque inconsistency between successive engagements can lead to poor vehicle launch at a race start. The torque instability also contributes to the issue but if the instability followed the same trend for every engagement, the driver would know what to expect and could train themselves to manage the instability. At typical race start energy input and clamp load levels however, the torque output is both unstable and inconsistent. Figures 4.5 and 4.10 in Chapter 4.5 show that the SCID replicated this problem well. The torque outputs measured during the SCID tests at the lowest speed/load and highest speed/load combinations shown in these figures exhibit the same stability and consistency behaviour as shown in Figure 1.10 presented in Chapter 1.2.

The thermal imaging results recorded during SCID testing showed that the observed hot bands, and hence effective friction radius (EFR), do not move during a single clutch-plate engagement but do move between engagements. This suggests that torque inconsistency is due to a combination of EFR migration and surface morphology effects (due to contact moving to a different area which may have a different surface condition). Torque instability during a single engagement is due to surface morphology changes alone.

Despite no EFR migration during a single clutch-plate engagement, the estimation of the COF may be incorrect and have a detrimental effect on race start performance. In this investigation, it was possible to measure the radial position of the EFR using the thermal imaging camera but this of course is not possible within the F1 car itself. As such the COF calculated during the race start procedure is based on the assumption that the friction radius lies at the geometric centre of the friction surface. Figure 8.1 shows the torque output results from the seventh SCID engagement test carried out at the 8000rpm/1400N speed/load combination. The COF has been calculated based on both the mean geometric radius and EFR. The hot band during this engagement test existed towards the outer radius of the rotating clutch plate. For an equivalent torque, the COF predicted by the EFR analysis is lower than for the mean geometric radius assumption. The maximum COF values (occurring at the end of the engagement) are approximately 0.52 and 0.45 for the mean geometric and EFR cases respectively.

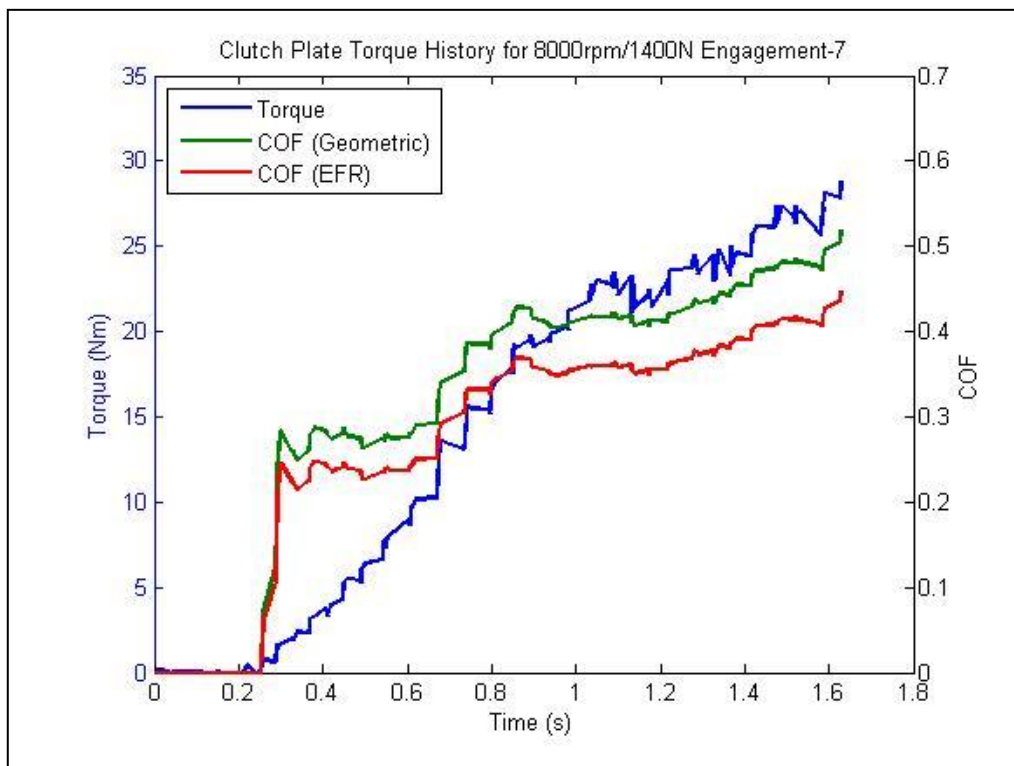


Figure 8.1 – Torque and COF Traces for Engagement7 at 8000rpm/1400N Speed/Load Combination

The geometric COF would be assumed for the race start which is higher than the true COF based on the EFR. The clamp load would therefore be set too low to produce the required torque output (Equation 4.2). Excess slip would occur and vehicle acceleration would be less than optimal as the true COF is lower than the calculated value. The torque generated would in fact be only 86.5% of the expected torque. This problem arises even before the effects of EFR migration and surface morphology effects are considered which will of course complicate the issue further and lead to poor vehicle launch performance.

8.3 Computational Modelling

Much of the TCFEA was developed prior to SCID testing so modifications to the temperature-COF relationship, clamp load build-up and inertia value used were subsequently made to the models based on the SCID test results. The modifications made little difference to the spatial evolution of the contact pressure distribution and hence hot band profiles showing that the hot banding is a result of the fundamental principle of TEI. The input levels simply influence the extent of the hot banding.

This finding was reiterated when an alternative temperature-COF and alternative wear equation were investigated which also predicted hot banding but to varying extents. Table 8.1 summarises the results of all the TCFEA simulations based on the modified TCFEA non-wear and wear models for the flat-to flat surface condition.

Model Type	Temperature-COF Relationship	Wear Equation	Banding Regime	Maximum Friction Surface Temperature (°C)
Non-Wear	Original	N/A	Twin	1541
Wear	Original	Original	Single	1535
Non-Wear	Alternative	N/A	Single	1327
Wear	Alternative	Original	Single	892
Wear	Original	Alternative	Single/Twin	709
Wear	Original	Alternative	Single/Twin	815

Table 8.1 – Summary of Results Based on Modified TCFEA Models
(Flat-to-Flat Surface Condition)

The TCFEA simulated the 8000rpm/1400N SCID engagement tests which showed the formation of single high-temperature (1300-1650°C) hot bands. With respect to this, the wear model with the original temperature-COF relationship and original wear equation and the non-wear model with the alternative temperature-COF relationship best approximate the SCID results. However, for the hot bands to migrate between engagements as observed during SCID testing, wear of the friction surfaces must occur and as such the wear model is the most appropriate of the two models.

Figure 8.2 shows the friction surface temperature profile predicted by the modified TCFEA wear model (original temperature-COF relationship and original wear equation) at the time when the maximum temperature occurs. It can clearly be seen that the temperature of the hot band (~1550°C) is comparable to those recorded during SCID testing (1300-1650°C). From the thermal imaging results the hot bands were approximately 2mm wide where the temperature outside the hot band was less than 450°C (lowest temperature the thermal imaging camera could measure). It can be seen from Figure 8.2 that the TCFEA predicts a hot band width of approximately 2mm agreeing well with the thermal imaging results.

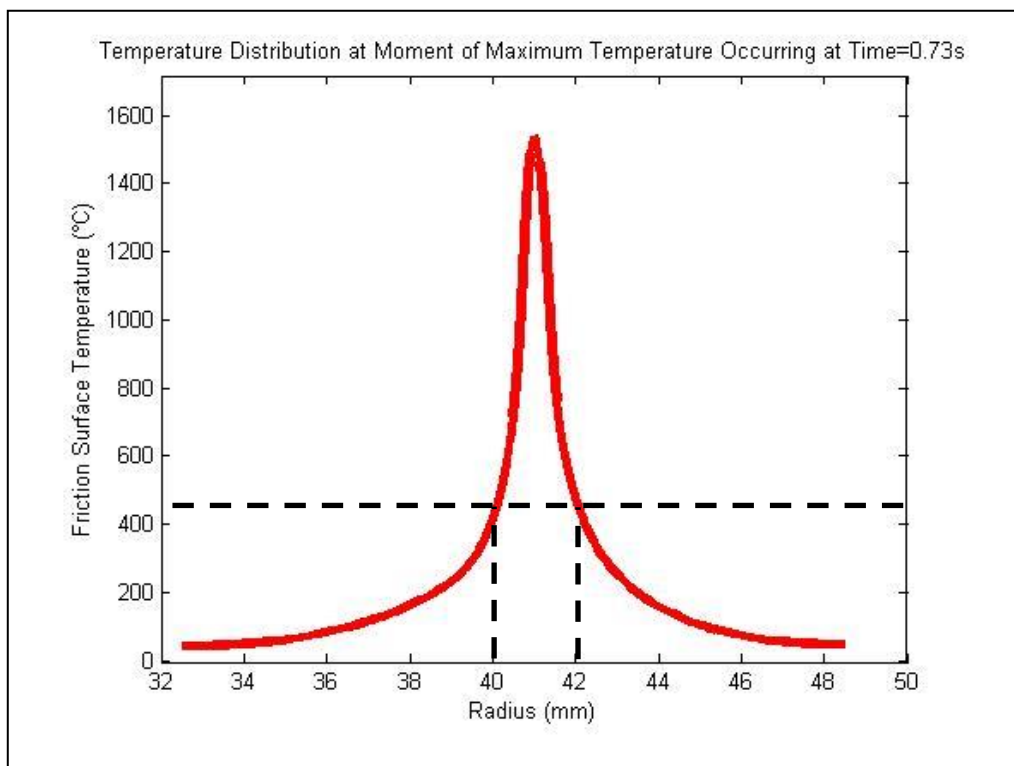


Figure 8.2 – Friction Surface Temperature Distribution Predicted by Modified TCFEA Wear Model at Time of Maximum Temperature Occurring (t=0.73s)

The time at which the maximum surface temperature occurs in the TCFEA is sooner than for the SCID tests. With the updated temperature-COF relationship and clamp load build-up, the maximum temperature predicted by the TCFEA occurs at 0.73s into the engagement whereas the maximum temperatures during SCID tests occur between approximately 0.9-1.6s with a large degree of variation between tests. The difference is likely to be due to the temperature-COF relationship used in the TCFEA in that the COF varies linearly from 25°C up to 1200°C and remains constant thereafter. In reality, the COF is known to rise sharply after the water desorption phase and then fall again as the temperature rises further. The TCFEA will initially overestimate the COF prior to the sudden rise resulting in a more rapid heat flux input such that the maximum surface temperature occurs earlier.

No significant effective friction radius migration was predicted during a single engagement which is also consistent with the results of SCID testing. Of primary concern in the F1 application is the torque output of the clutch. Figure 8.3 shows the torque output predicted by the TCFEA whilst Figure 8.4 shows the torque outputs recorded during SCID testing (discussed in Chapter 4.5). It is important to note that the time scales are different for each figure and, during the first 0.2s of the SCID tests, no clamp load is applied so no torque is generated.

It can be seen from Figures 8.3 and 8.4 that the TCFEA predicts a higher peak torque and as a result a shorter engagement time. The TCFEA uses a linear temperature-COF relationship in which a fall in COF above a certain temperature does not occur as would be expected with the formation of type III morphology. It may therefore overestimate the COF as the hot band rises above a certain temperature and hence overestimate the torque which will in turn exacerbate the hot banding effect. It is likely that the omission of the effect of type III morphology from the TCFEA is the cause of the differences in predicted and measured torque outputs. As shown in Figure 7.65, the torque outputs predicted by the wear models with the original wear equation are very different in profile to the wear models with the alternative wear equation. The original wear equation results in torque output profiles similar to those recorded during SCID testing with the original temperature-COF relationship most closely estimating the maximum friction surface temperature thus reiterating that the wear model with the original temperature-COF relationship and original wear equation is the most appropriate.

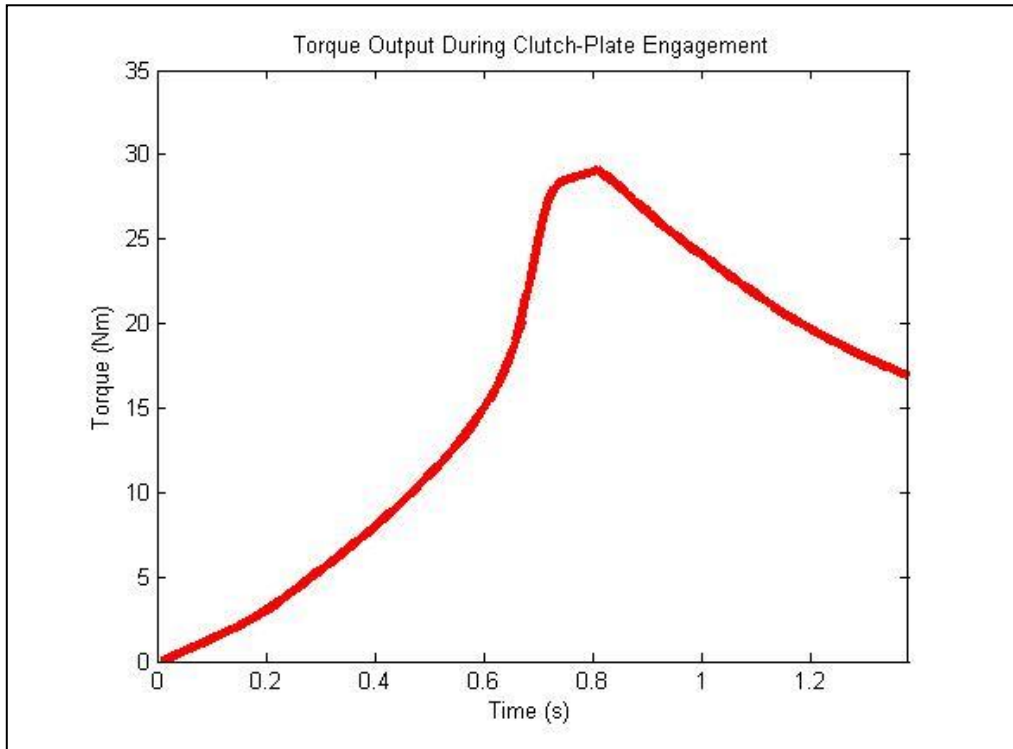


Figure 8.3 – Torque Output Predicted by Modified TCFEA Wear Model

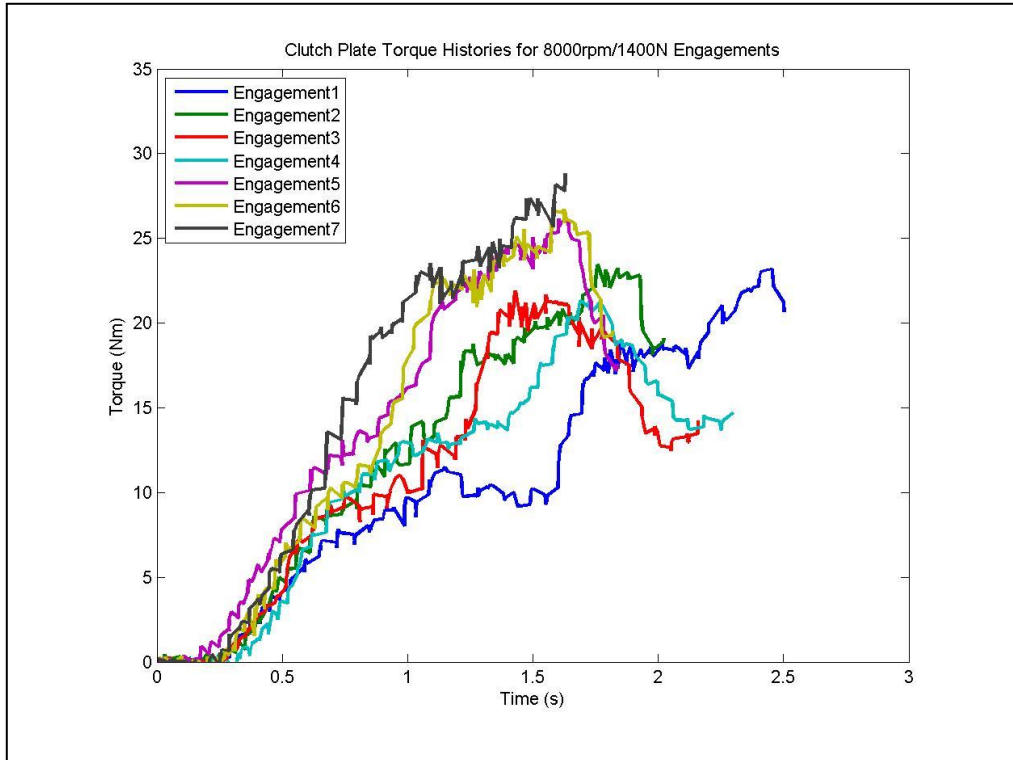


Figure 8.4 – Torque Output Traces for 8000rpm/1400N Speed/Load Combination SCID Tests

Figure 2.16 in the literature review showed the contact pressure distribution predicted by Thuresson [43] where a 2D finite element model was constructed simulating a block in sliding contact with a solid foundation. Wear was not included in the model and the contact pressure distribution shown in Figure 2.16 is very similar to the contact pressure distribution predicted by the TCFEA (Figure 7.16) for the equivalent non-wear scenario. Due to the higher energy input level involved with the F1 clutch-plate application, the contact pressure localisation is more extreme in Figure 7.16 due to the increased influence of TEI. Introduction of wear to the TCFEA led to the two contact points shown in Figure 7.16 being worn away and a single contact point being established near the central radius of the friction surface (Figure 7.36). However, work by Zhao et al. [13] and Abdullah et al. [17, 18] predicted a single band of high contact pressure and therefore high temperature in their axisymmetric finite element models of multi-plate clutches without the inclusion of wear (Figures 2.3 and 2.4). This may be due to the COF values used, as a single hot band was also predicted by the non-wear TCFEA model with the alternative temperature-COF relationship. The difference between the results presented by Zhao et al. [13] and Abdullah et al. [17, 18] and those of the TCFEA could also be due to the fact that the TCFEA simulates only a single clutch-plate pair whilst the whole clutch-plate pack is simulated by Zhao et al. [13] and Abdullah et al. [17, 18]. The physical effects of the deformation of all the clutch plates may lead to only a single contact point, and hot band, even without wear occurring. The results of the TCFEA did however agree with all the work of these authors in that it predicted hot banding even if the friction surfaces were initially perfectly flat.

Both the twin hot band and single hot band profiles were however observed during SCID tests. Figures 4.11, 4.12 and 4.13 show the three typical friction surface temperature profiles observed during SCID testing as the energy input and clamp load levels are increased. Figure 4.11 shows a small amount of temperature localisation but cannot be conclusively classed as being a hot band. As the energy input level and clamp load are increased, the twin hot band profile is established as shown in Figure 4.12 which is similar to the results of the non-wear TCFEA simulation. It is probable that at the temperatures shown in Figure 4.12, the wear rate is in fact so low that the two contact points are not worn away and persist, forming two hot bands. As the energy level input and clamp load are increased, the

temperatures produced are high enough for wear to be significant and a single contact point is established as predicted by the TCFEA simulations incorporating a wear model and shown in Figure 4.13.

The modified TCFEA wear model predicts that the twin contact point regime is initially established in the same way as for the non-wear model. Wear then eliminates these contact points and a single contact point is established. It is possible that the temperature profile shown in Figure 4.13 is formed after going through the twin contact point phase as predicted by the TCFEA simulations incorporating wear. If this occurs it must happen due to abrasion wear (as a result of the higher clamp load) before high temperatures are established and as the thermal imaging camera can only record temperatures above 450°C, this behaviour is not observed.

For the 1200N load case, both temperature profiles shown in Figures 4.12 and 4.13 were observed during different engagements with no apparent consistency. This was despite no change in energy input level or clamp load. This is likely due to two effects. Although at the temperatures shown in Figure 4.12 the wear rate may be low, enough wear may occur during some engagements to eliminate one of the two contact points. It is also possible that one of the contact points has a significantly different surface morphology with a higher COF causing immediate heat input concentration to one contact point which becomes dominant.

8.4 Contact Localisation

Both the modified TCFEA wear model and thermal imaging results from the SCID tests suggest that contact may only be occurring over a small proportion of the friction surface area. The 1D model developed in this investigation (which assumes full area contact) was carried out varying the area of the friction surface as a proportion of the total friction surface area. The inner and outer radii were adjusted accordingly such that the mean geometric radius was unaffected. As with the original 1D heat transfer model, only the uniform pressure model (see Chapter 6.9) was used (all material properties same as TCFEA). Figure 8.5 shows the results of this analysis where the friction surface temperatures during the engagement are plotted for a series of friction surface areas.

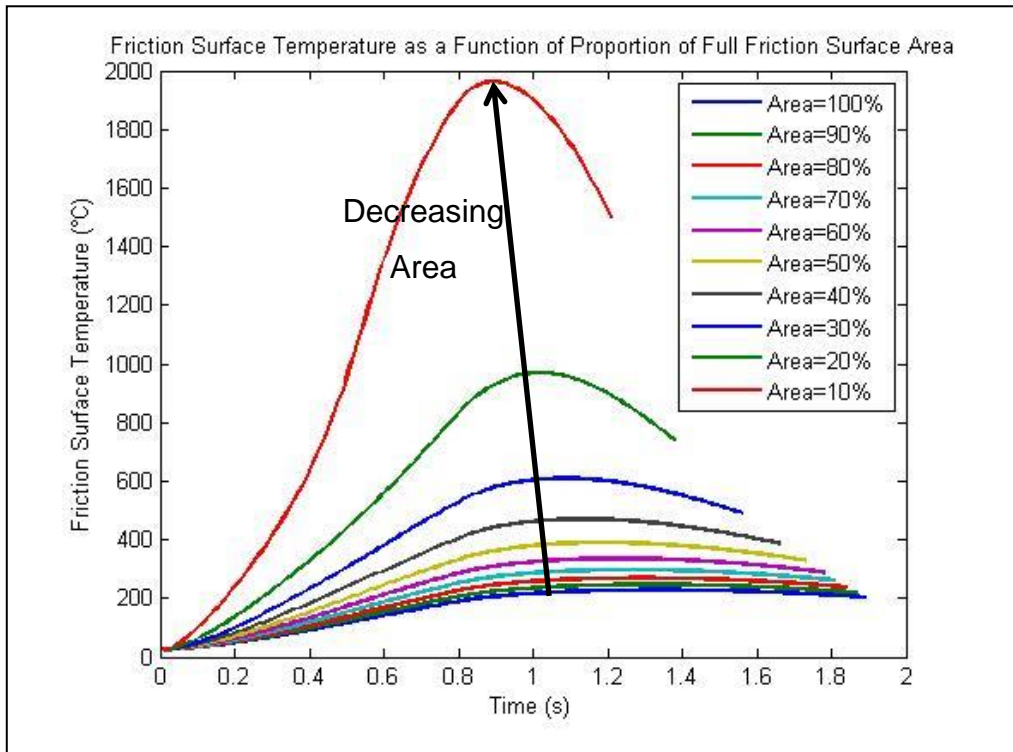


Figure 8.5 – Clutch-Plate Friction Surface Temperatures Predicted by 1D Heat Transfer Model as a Function of Proportion of Full Friction Surface Area

It can clearly be seen from Figure 8.5 that the maximum friction surface temperature increases significantly with decreasing friction surface area. Figure 8.6 suggests that the relationship between the friction surface area and maximum friction surface temperature is a negative exponential function.

The curve fitting tool within Matlab was used to fit a second order exponential equation to the curve shown in Figure 8.6 as defined in Equation 8.1.

$$T_{max} = 4228e^{-0.1105A\%} + 622.9e^{-0.01035A\%} \tag{8.1}$$

Where: T_{max} – Maximum Friction Surface Temperature (°C)

$A\%$ – Proportion of Full Friction Surface Area (%)

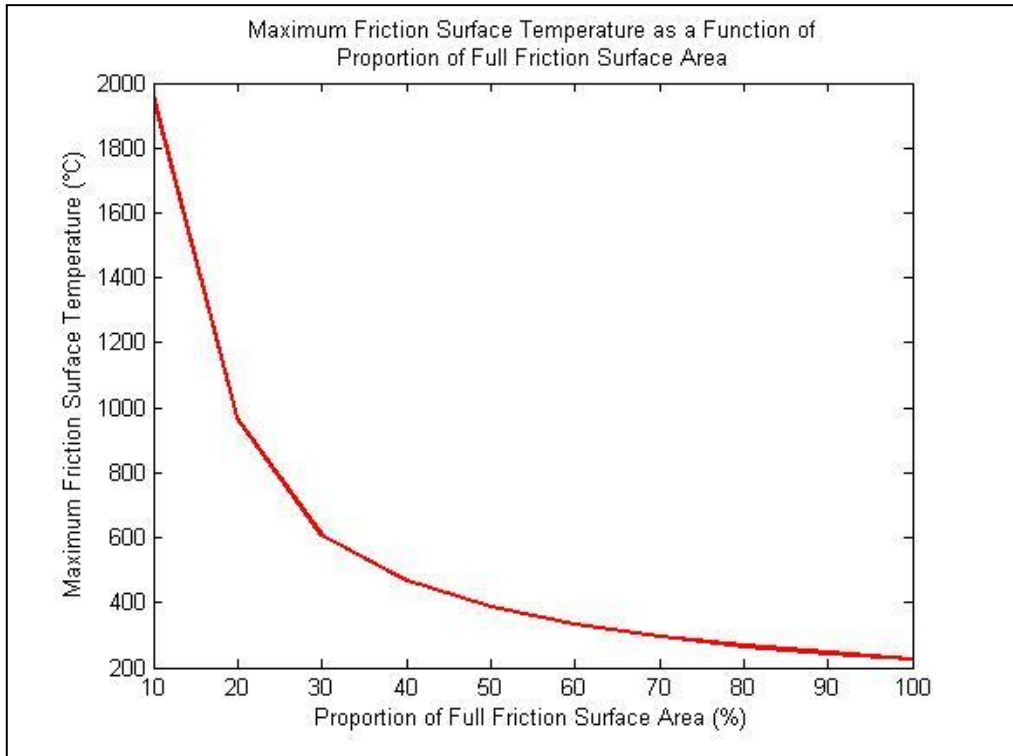


Figure 8.6 –Maximum Friction Surface Temperature-Proportion of Full Friction Surface Area in Contact Relationship Predicted by 1D Heat Transfer Model

The curve fit with a R^2 value of 0.9999 (unity is a perfect fit). A 2mm hot band equates to 12.5% of the full friction surface area. From Figure 8.6, using this value as an estimate of the proportion of area, Equation 8.1 calculates a maximum friction surface temperature of 1610°C which agrees well with both the modified TCFEA wear model and thermal imaging results.

However, the modified TCFEA wear model predicts that the contact localisation may be even more extreme than just 12.5% of the full friction surface area. Figure 8.7 shows the contact pressure distribution at the moment at which the maximum contact pressure is predicted. This level of contact localisation leading to high contact pressure is maintained for only a short period of time (~0.2s) but coincides with the formation of the hot band. The 2mm hot band may therefore in fact be a 1mm wide point of contact where some heat has conducted in the radial direction.

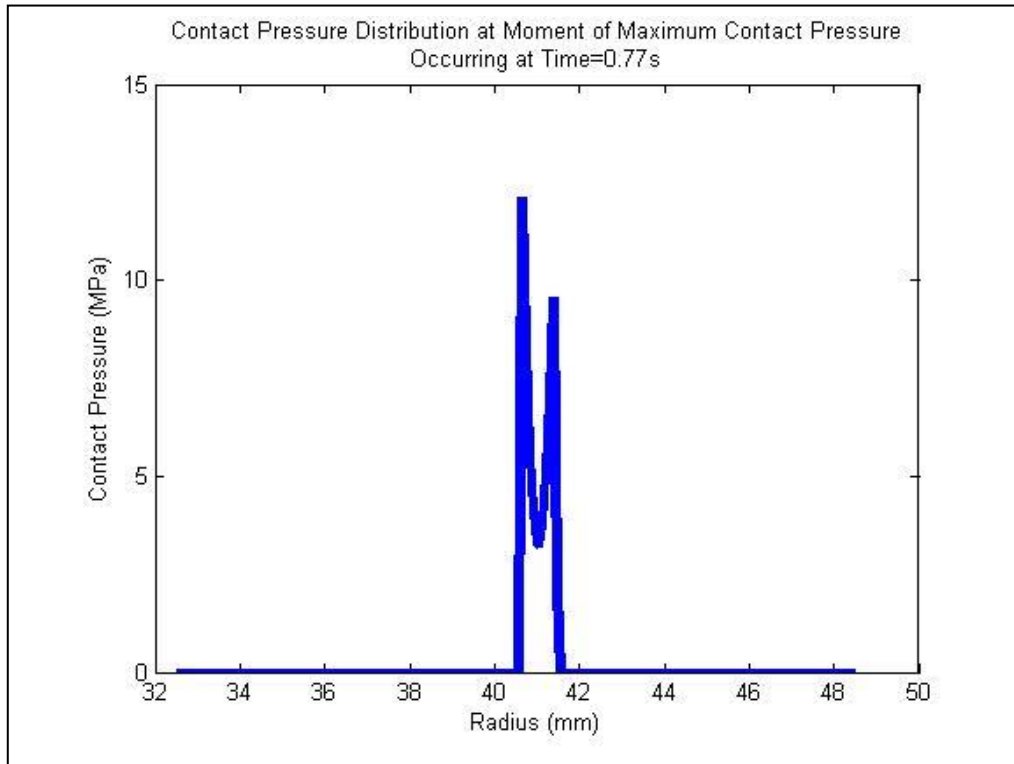


Figure 8.7 – Contact Pressure Distribution at Moment When Maximum Contact Pressure is Predicted by Modified TCFEA Wear Model

8.5 Wear Mechanism

Wear dust was observed on the friction surfaces of all the driving clutch plates but not the driven plates. This difference was attributed to the effect of the cleaning grooves in the driven plates. The driving clutch plates had $\text{\O}12\text{mm}$ holes drilled through them to allow the friction surface of the driven (rotating) clutch plates to be viewed with the thermal imaging camera. It was possible that the wear dust was being produced from burrs produced when the holes were drilled or perhaps from material being dragged out of the holes. To clarify the situation, an additional series of tests were carried out on a pair of clutch plates that had not been modified in any way. The tests were carried out at the 7000rpm/1400N speed/load combination. Figure 8.8 shows the torque output results for the engagements carried out at this speed/load combination for both sets of clutch plates (with and without holes). It can clearly be seen that the torque output behaviour is very similar suggesting that the viewing holes have no significant effect on the friction performance of the clutch-plate pairs. The time scales for each figure are not identical.

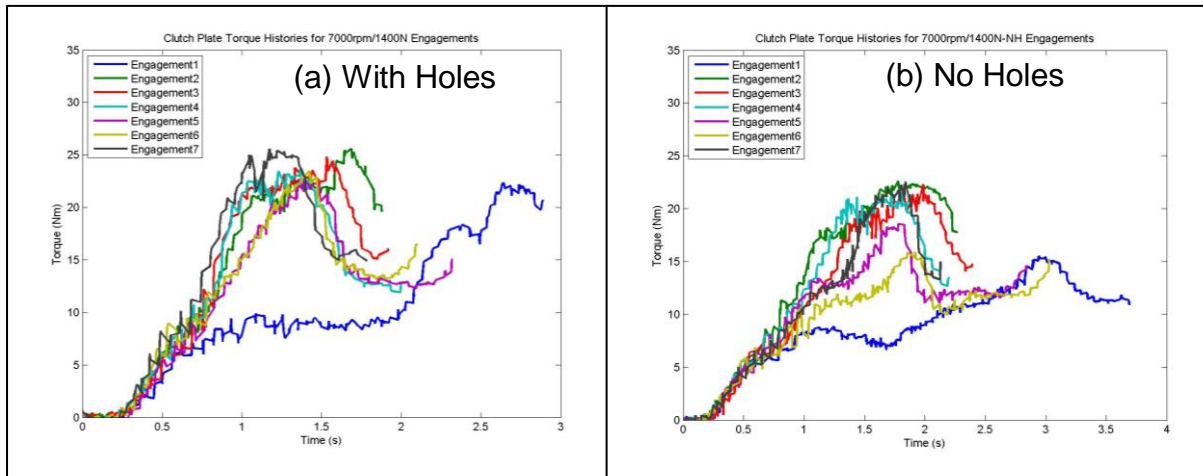


Figure 8.8 – Torque Output Results from SCID Tests Carried Out at 7000rpm/1400N Speed/Load Combination With (a) Holes and (b) No Holes Drilled Through Driving Clutch Plate

Wear dust was also observed on the friction surface of the driving plate without a viewing hole drilled through it. This result showed that the wear dust was not a product of the holes drilled through the clutch plates. The wear dust must therefore have been caused by abrasion of the friction surface. There appeared to be no correlation between the speed, loads and friction surface temperatures and the amount of wear dust present on the driving plate friction surfaces.

As distinct hot bands for all engagement tests were only produced for the 1400N load case (at both 7000rpm and 8000rpm), only the results for these tests could be used to conclusively show effective friction radius migration between tests. Wear of the friction surfaces must occur in order for the effective friction radius to migrate. Wear tracks were produced on the friction surfaces of the clutch plates used at a clamp load of 1400N. SEM images showed that the fibres in these regions were distorted but the actual wear mechanism is unclear. The high temperatures suggest that oxidation would occur but it is possible that increased levels of abrasion occur as the result of the hot bands leading to thermal expansion that greatly increases the normal loads in the area of the hot band.

8.6 Further Investigations

The results of this investigation have suggested that the clutch-plate torque output instability during a single engagement is due to surface morphology changes alone whilst the inconsistency between engagements is due to a combination of effective friction radius migration and surface morphology effects. Both factors will affect the torque output and as such their individual influence cannot be accurately assessed.

To isolate the surface morphology effects and assess their impact, either a very narrow clutch plate with an approximately 2mm wide friction surface or a clutch plate with a 2mm wide raised step on its friction surface could be tested. This would isolate contact to a very specific region so that, if any effective friction radius migration occurred, its effect would be minimal and it could be assumed that any torque inconsistency is then due only to surface morphology effects. The effective friction radius would be known, to within a small tolerance, and an accurate calculation of the COF could be made.

Increasing the wear resistance of the carbon/carbon clutch-plate material would also have the same effect in that contact would be isolated to any initial surface asperities. If these surface asperities did not wear away, the area of contact would remain the same in all successive engagements. If the initial area of contact was known, a correct calculation of the COF could be made.

Another potential solution would be to use a carbon/carbon material with a lower thermal expansion coefficient. A series of initial tests could first be used to wear away any large surface asperities. In subsequent clutch-plate engagements, lower levels of thermal expansion would lead to less contact localisation which would reduce the chance of extreme hot bands forming. This would reduce wear and limit the amount of effective friction radius migration.

8.7 Summary

This investigation has found that contact localisation is significant under typical race start conditions which causes a secondary, previously unconsidered issue of effective friction radius migration. The torque output of the clutch-plate pairs will be affected by this effective friction radius migration complicating the issue of isolating the surface morphology effects. The torque inconsistency between clutch-plate engagements is a function of both factors and as a result it is difficult to isolate and assess their individual effects with the current clutch-plate design.

9. Conclusions

The torque output of a multi-plate carbon/carbon clutch for a Formula One application can be both unstable and inconsistent. At low levels of energy input and clamp load, the torque output is low but stable and consistent between successive engagements. As either the energy input level, clamp load or both are increased, the peak torque output increases but the torque output evolution becomes less stable and also less consistent between engagements. The inconsistency between engagements is particularly problematic as the torque output can be very different from one engagement to the next despite no changes in energy or load inputs. This can have a significantly negative impact on race start performance.

Carbon/carbon composites are used as friction materials due to their low density, high strength, high thermal conductivity and ability to withstand temperatures of over 2000°C. Literature regarding the friction performance of carbon/carbon composites is limited due to their use being mostly in commercially sensitive applications. The typical coefficient of friction variation is however known to be related to the surface morphology. The surface morphology is related to the amount of work done at the friction surface which in turn affects the surface temperature. Oxidation of the carbon to carbon monoxide and carbon dioxide will occur at elevated temperatures.

To isolate and understand the performance of a single carbon/carbon clutch-plate pair, a unique single clutch-plate interface dynamometer was designed and commissioned. This dynamometer replicated the increase in torque output instability and inconsistency with increased energy input and clamp load levels. The use of a high-speed thermal imaging camera showed that extreme hot banding occurred on the friction surfaces of the clutch plates, the intensity of which became greater with increased energy input and clamp load. The hot bands formed during the highest clamp load tests were distinct in nature and approximately 2mm wide. The location of the hot band represents the location of the effective friction radius as the majority, if not all, of the frictional work must be done in the area of the hot band to produce the observed maximum temperatures of 1300-1650°C. The hot bands, and hence effective friction radius, do not migrate during individual engagements but do migrate between successive engagements. This can only occur if wear of the friction

surfaces causes the original contact point to be worn away, resulting in a recess once the clutch plates have cooled and contact is then established elsewhere during the next engagement. No effective radius migration occurs during a single engagement as the overall engagement time is too short for wear to become dominant over thermal expansion.

It has been shown that abrasion of the friction surfaces takes place during the clutch-plate engagement which produces wear dust. The friction film was observed to become thicker with increasing clamp load and at the highest clamp load combinations, wear tracks are formed in the areas where hot bands form where the carbon fibres are seen to be distorted. The friction surface roughness is reduced by frictional work whilst encouraging waviness profiles to form.

The fully coupled thermomechanical finite element analysis used to simulate the clutch plates during dynamometer testing showed that contact localisation occurs even if the friction surfaces are perfectly flat. Contact loss at the inner and outer radii of the clutch plates in the early stage of the clutch-plate engagements leads to the initiation of thermoelastic instabilities. The finite element analysis approximates the experimental results most accurately when the COF increases with temperature and when a wear model is included where the wear rate increases exponentially with friction surface temperature. The wear model manipulates the motion of friction surface nodes within the finite element model depending on the contact pressure and temperature at each node. The calculated wear rate is simulated by applying a velocity to the friction surface nodes whilst still allowing thermal expansion to take place. With the wear model included, extreme contact localisation is predicted by the finite element model leading to a single 2mm wide hot band with a peak temperature of approximately 1550°C, a result which is in strong agreement with SCID test results. The finite element analyses also agreed with experimental results in that no effective friction radius migration was predicted during single engagements. The initial friction surface profile of the clutch plates was shown to have a strong effect on the friction surface temperature which is known to affect friction performance.

At typical race start energy input and clamp load levels, thermoelastic instabilities lead to contact localisation and the formation of extreme hot bands regardless of the initial friction surface profile. Both the experimental and computational results show that the level of contact localisation results in as little as 12.5% (and briefly as little as

6.25%) of the friction surfaces remaining in contact with each other. The concentration in energy input to this small area causes hot bands to form.

The radial location of the hot bands and hence effective friction radius, vary between successive engagements. Estimation of the coefficient of friction of the clutch plates may be incorrect if the effective friction radius does not coincide with the mean geometric radius of the friction surface. Therefore in the race start application, the coefficient of friction may be incorrectly calculated and the clamp load setting may be either too low leading to clutch slippage, or too high leading to engine rpm falling rapidly and anti-stall mode temporarily disengaging the clutch

As the effective friction radius does not migrate during a single engagement, the instability of the clutch torque output is due to surface morphology effects alone. The inconsistency in torque output engagements however is due to a combination of both surface morphology effects and effective friction radius migration.

Recommendations for Further Work

1. Cleaning grooves in driving clutch plates

Wear dust was observed after SCID testing on the driving plates only. The cleaning grooves therefore remove dust from the friction surface of the driven plates effectively. By adding cleaning grooves to the driving plates, the impact of the wear dust on friction performance could be assessed and it could be determined if the wear dust is functional or superfluous. It is possible that the visible wear dust is simply wear dust that does not fill voids or form part of the friction film and can be ejected without affecting friction performance. This work could be carried out fairly quickly with the existing SCID as the grooves could be easily machined into the friction surfaces of the driving plates.

2. Effects of burnishing

A single pair of clutch plates was used during the commissioning of the SCID which was subjected to numerous low speed (3000-5000rpm) and low clamp load (500-1000N) engagements. After commissioning, these clutch plates were subjected to a series of engagement tests carried out at 7000rpm/1400N (identical to those discussed in Chapter 4). After the engagements, the friction surfaces of both plates showed no wear tracks or wear dust. The friction surfaces may have been conditioned during the SCID commissioning phase and became more resistant to wear by the formation of a protective friction film. The conditioning is known as burnishing and its effect on clutch-plate friction performance could be assessed using the existing SCID by executing a controlled series of burnishing (low speed/load) engagements before executing a full test programme at the speed/load combinations used in this investigation.

3. Stepped friction surface

Due to the effective friction radius migration, it is impossible to isolate the effect any surface morphology changes have on the torque inconsistency as both factors will affect the torque output. The surface morphology effects could be isolated by using a stepped friction surface (2mm wide) so that contact is forced to a small defined area. Any effective friction radius migration would therefore be

small and it could be assumed that any inconsistency in torque output between successive engagements is due to surface morphology effects alone. The comparative contributions of surface morphology effects and effective friction radius migration to torque inconsistency could then be quantified. The existing SCID could be used but producing a stepped clutch-plate friction surface may require more extensive machining or even possibly a clutch plate design change.

4. Establish accurate temperature-COF and temperature-wear relationships

Using a stepped friction surface would allow an accurate temperature-COF relationship to be established as the torque output would be influenced only by the surface morphology of the friction surface. By carrying out a constant speed slip test, the COF could be accurately calculated from the torque output and compared to the friction surface temperature in order to determine the temperature-COF relationship. By measuring the mass of the clutch plates and the height of the step on the friction surface before and after the slip tests, it may also be possible to establish an accurate temperature-wear relationship.

5. Further develop the TCFEA

The TCFEA shows promise in that it simulates the behaviour of the clutch plates quite closely. Improvements to the temperature-COF and temperature-wear relationships used could immediately improve its accuracy. The coupling between Matlab and Abaqus is a time consuming process and as such a new method would need to be developed, perhaps using Python instead of Matlab, in order to reduce the overall simulation time. Once this has been completed, a full parametric study could be carried out using the TCFEA to inform potential design or race start procedure changes.

References

- [1] Shigley, J.E., Mischke, C.R., Standard Handbook of Machine Design, 2nd Edition, New York, USA, McGraw-Hill, 1996

- [2] Garrett, T.K., Newton, K., Steeds, W., The Motor Vehicle, 13th Edition, Oxford, UK, Butterworth-Heinemann, 2000

- [3] Spotts, M.F., Design of Machine Elements, 6th Edition, Upper Saddle River, New Jersey, Pearson Education, 2004

- [4] How Dual-clutch Transmissions Work [Online], [Accessed 7th April 2011]. Available from World Wide Web:

<http://auto.howstuffworks.com/dual-clutch-transmission1.htm>

- [5] Gibson, D.W., Taccini, G.J., Carbon/Carbon Friction Materials for Dry and Wet Brake and Clutch Applications, Peoria, Illinois, April 11-13, 1989, SAE Technical Paper, 890950

- [6] Lawrence, G., Mace, G., Bowler, N., Goddard, G., Morrey, D., Measurement of the Interfacial Plate Temperature within a Carbon Clutch and Determination of Effects upon its Friction Characteristics, Motorsports Engineering Conference & Exhibition, Dearborn, Michigan, December 5-7, 2006, SAE Technical Paper 2006-01-3636, Warrendale, Pennsylvania, USA, 2006

- [7] Confidential Technical Document

- [8] Barber, J.R., Thermoelastic Instabilities in the Sliding of Conforming Solids, Proceedings of the Royal Society of London, Series A, Mathematical and Physical Sciences, 1969, Vol.312, No.1510, pp.381-394
- [9] Blanco, C., Bermejo, J., Marsh, H., Menendez, R., Chemical and physical properties of carbon as related to brake performance, Wear, 1997, Vol. 213, Issues 1-2, pp.1-12
- [10] Savage, G., Formula 1 Composites Engineering, Engineering Failure Analysis, 2009, Vol. 17, pp.92-115
- [11] Velardocchia.M., Amisano.F., Flora.R., A Linear Thermal Model for an Automotive Clutch, SAE 2000 World Congress, Detroit, Michigan, 2000, SAE Technical Papers, 2000-01-0834, Warrendale, Pennsylvania
- [12] Zagrodzki.P., Numerical Analysis of Temperature Fields and Thermal Stresses in the Friction Discs of a Multidisc Wet Clutch, Wear, 1985, Vol.101, pp.255-271
- [13] Zhao, S., Hilmas, G.E., Dharani, L.R., Behavior of a composite multi-plate clutch subjected to mechanical and frictionally excited thermal load, Wear, 2008, Vol. 264, pp.1059-1068
- [14] Zhao, S., Hilmas, G.E., Dharani, L.R., Numerical simulation of wear in a C/C composite multi-plate clutch, Carbon, 2009, Vol. 47, pp.2219-2225
- [15] Zagrodzki.P., Analysis of Thermomechanical Phenomena in Multidisc Clutches and Brakes, Wear, 1990, Vol.140, pp.291-308

- [16] Abdullah, O.I., Schlattmann, J., An Investigation of Heat Generation Due To Friction Using Finite Element Method, SAE Technical Paper 2014-01-0954, 2014
- [17] Abdullah, O.I., Al-Sahb, W.A., Al-Shabibi, A.M., THERMOELASTIC ANALYSIS OF MULTI-DISC CLUTCHES USING FINITE ELEMENT METHOD, Tribologia, 2014, Vol.5, pp. 9-24
- [18] Abdullah, O.I., Akhtar, M.J., Schlattmann, J., Investigation of Thermo-Elastic Behavior of Multidisk Clutches, Journal of Tribology, 2015, Vol. 137, pp. 1-9
- [19] Abdullah, O.I., An Investigation Into the Thermal Behavior of the Grooved Dry Friction Clutch, Journal of Tribology, 2014, Vol. 136, pp. 1-6
- [20] Inagaki, M., New Carbon: Control of Structure and Functions, First Edition, Oxford, Elsevier Science Ltd., 2000
- [21] Byrne, C., Modern Carbon Composite Brake Materials, Journal of Composite Materials, 2004, Vol. 38, No. 21
- [22] Luo, R., Huai, X., Qu, J., Ding, H., Xu, S., Effect of heat treatment on the tribological behavior of 2D carbon/carbon composites, Carbon, 2003, Vol. 41, pp.2693-2701
- [23] Marinkovic, S., Dimitrijevic, S., Carbon/Carbon Composites Prepared by Chemical Vapour Deposition, Carbon, 1985, Vol. 23, No.6, pp.691-699
- [24] Savage, G., Carbon-Carbon Composites, First Edition, London, Chapman & Hall, 1993

- [25] Kasem, H., Berthier, Y., Bonnamy, S., Jacquemard, P., Influence of sliding speed on wear of C/C composites under different controlled contact temperatures, 6th European Conference on Braking, Lille, France, 2010
- [26] Yen, B.K., Ishihara, T., An Investigation of Friction and Wear Mechanisms of Carbon-Carbon Composites in Nitrogen and Air at Elevated Temperatures, Carbon, 1996, Vol. 34, No.4, pp.489-498
- [27] Lee, K.J., Kuo, H.H., Chern Lin, J.H., Ju, C.P., Effect of surface condition on tribological behavior of PAN-CVI based carbon-carbon composite, Materials Chemistry and Physics, 1999, Vol. 57, pp.244-252
- [28] Chen, J.D., Chern Lin, J.H., Ju, C.P., Effect of humidity on the tribological behavior of carbon-carbon composites, Wear, 1996, Vol. 193, pp.38-47
- [29] Byrne.C, Wang.Z., Influence of Thermal Properties on Friction Performance of Carbon Composites, Carbon, 2001, Vol.39, pp.1789-1801
- [30] Krkoska, M., Filip, P., Humidity and Frictional Performance of C/C Composites, Developments in Advanced Ceramics and Composites: Ceramic Engineering and Science Proceedings, 2008, Vol. 26, No.8, Chapter 17
- [31] Kasem, H., Bonnamy, S., Berthier, Y., Dufrenoy, P., Jacquenard, P., Tribological, physiochemical, and thermal study of the abrupt friction transition during carbon/carbon composite friction, Wear, 2008, Vol. 267, pp. 846-852
- [32] Yen, B.K., Ishihara, T., The Surface Morphology and Structure of Carbon-Carbon Composites in High-Energy Sliding Contact, Wear, 1994, Vol. 174, pp.111-117

- [33] Hutton, T.J., McEnaney, B., Crelling, J.C., Structural studies of wear debris from carbon-carbon composite aircraft brakes, *Carbon*, 1998, Vol. 37, pp.907-916
- [34] Hutton, T.J., Johnson, D., McEnaney, B., Effects of fibre orientation on the tribology of a model carbon-carbon composite, *Wear*, 2001, Vol. 249, pp.647-655
- [35] Hao, M., Luo, R., Hou, Z., Yang, W., Xiang, Q., Yang, C., Effect of fiber-types on the braking performances of carbon/carbon composites, *Wear*, 2014, Vol. 319, pp. 145-149
- [36] Francois, M., Joly, J.P., Kapsa, P., Jacquemard, P., A temperature-programmed desorption and oxidation investigation of wear debris from carbon/carbon composite aircraft brakes, *Carbon*, 2007, Vol. 45, pp. 124-131
- [37] Kasem, H., Bonnamy, S., Rousseau, B., Estrade-Szwarcckopf, H., Berthier, Y., Jacquemard, P., Interdependence between wear process, size of detached particles and CO₂ production during carbon/carbon composite friction, *Wear*, 2007, Vol, 263, pp. 1220-1229
- [38] Kasem, H., Bonnamy, S., Berthier, Y., Jacquemard, P., Fiber-matrix unbonding and plastic deformation in C/C composites under tribological loading, *Wear*, 2010, Vol. 269, pp. 104-111
- [39] Kasem, H., Bonnamy, S., Berthier, Y., Jacquemard, P., Characterization of surface grooves and scratches induced by friction of C/C composites at low and high temperatures, *Tribology International*, 2010, Vol. 43, pp. 1951-1959

- [40] Tanner, J.A., Travis, M., Adsorption and Desorption Effects on Carbon Brake Material Friction and Wear Characteristics. Aerotech Congress & Exhibition, Grapevine, Texas, October 3-6, 2005, SAE Technical Paper 2005-01-3436, Warrendale, Pennsylvania, 2005
- [41] Yen, B.K., Ishihara, T., On Temperature-Dependent Tribological Regimes and Oxidation of Carbon-Carbon Composites up to 1800°C, *Wear*, 1996, Vol. 196, pp.254-262
- [42] Karmi Jr., R.J., A Preliminary Dynamic Model of Braking Friction Using Pressure and Temperature, SAE Technical Paper 2001-01-3150, 2001
- [43] Thuresson, D., Thermomechanical Analysis of Friction Brakes, SAE Technical Paper, 2000-01-2775, 2000
- [44] Vernersson, T., Lunden, R., Wear of Block Brakes and Disc Brakes for Repeated Brake Cycles, 6th European Conference on Braking, Lille, France, 2010
- [45] Graf, M., Ostermeyer, G-P., EFFICIENT COMPUTATION OF HOT BANDS AND HOT SPOTS, EB2013-TE-002, EuroBrake 2013, Dresden, Germany, 2013
- [46] Day, A.J., Tirovic, M., Newcomb, T.P., Thermal effects and pressure distribution in brakes, *Proceedings of The Institution of Mechanical Engineers*, 1991, Vol. 205, pp. 199-205
- [47] Day, A.J., *Braking of Road Vehicles*, Butterworth-Heinemann, 2014

- [48] Benham, P.P., Crawford, R.J., Armstrong, C.G., Mechanics of Engineering Materials, 2nd Edition, Essex, England, Pearson Education Limited, 1996
- [49] Bhandari. V.B., Design of Machine Elements, 3rd Edition, New Delhi, India, Tata Mcgraw-Hill, 2010
- [50] Samuel, A., Weir, J., Introduction to Engineering Design-Modelling, Synthesis and Problem Solving Strategies, Oxford, England, Butterworth Heinemann, 1999
- [51] Hamrock, B.J., Schmid, S.R., Jacobson, B.O., Fundamentals of Machine Elements, 3rd Edition, Florida, USA, CRC Press, 2014
- [52] Thevenet, J., Kasem, H., Siroux, M., Dufrenoy, P., Desmet, B., Thermal measurements by IR Camera and two-color pyrometer during railway braking tests, 6th European Conference on Braking, 2010, Lille, France
- [53] Williams, T., Thermal Imaging Cameras: Characteristics and Performance, 2009, Taylor & Francis
- [54] Veeco Wyko NT3300S interferometer User's Manual
- [55] Hariharan, P., Basics of Interferometry, 2nd Edition, Academic Press, 2006
- [56] Form Talysurf Intra, Operator's Handbook
- [57] Reimer, L., Scanning Electron Microscopy: Physics of Image Formation and Microanalysis, 2nd Edition, Springer, 1998

- [58] Pecharsky, V.K., Fundamentals of Powder Diffraction and Structural Characterization of Materials, Springer, 2005
- [59] Powder X-Ray Diffraction [Online], [Accessed 21st December 2014], Available from World Wide Web: http://chemwiki.ecdavis.edu/Analytical_Chemistry/Instrumental_Analysis/Diffraction/Powder_X-ray_Diffraction
- [60] Incropera, F.P., Dewitt, D.P., Fundamentals of heat and mass transfer, 5th Edition, Chichester, New York, Wiley, 2002
- [61] Limpert, R., Brake Design and Safety, 2nd Edition, Warrendale, Pennsylvania, Society of Automotive Engineers, 1999
- [62] Taguchi.G., System of Experimental Design, Volume One, White Plains/Dearborn, New York/Michigan, (UNIPUB/Kraus International Publications)/American Supplier Institute
- [63] Lee, K.J., Chern Lin, J.H., Ju, C.P., Simulated-stop tribological behaviour of pitch-resin-CVI carbon-carbon composite, Materials Chemistry and Physics, 1997, Vol. 49, pp. 217-224
- [64] Fowlkes.W.Y., Creveling.C.M., Engineering Methods for Robust Product Design: Using Taguchi Techniques and Product Development, Reading, Massachusetts, Corporate & Professional Publishing, 1995
- [65] Abaqus User's Manual...
- [66] Archard, J. F., Contact and Rubbing of Flat Surfaces, Journal of Applied Physics, 1953, Vol. 24, pp.981-988